Journal of METAMORPHIC GEOLOGY

Composite granite–quartz veins in the Sulu belt, China: evidence of supercritical fluid flow during exhumation of deeply subducted UHP continental crust

Journal:	*Journal of Metamorphic Geology*
Manuscript ID	JMG-16-0068.R1
Manuscript Type:	Original Article
Date Submitted by the Author:	04-Dec-2016
Complete List of Authors:	Wang, Songjie; China University of Geosciences, School of Earth Sciences; University of Maryland, Department of Geology Wang, Lu; China University of Geosciences, State Key Laboratory of Geological Processes and Mineral Resources Brown, Michael; University of Maryland, Department of Geology; Piccoli, Philip; University of Maryland, Department of Geology Johnson, Tim; Curtin University, Applied Geology; Feng, Peng; China University of Geosciences, School of Earth Sciences Deng, Hao; China University of Geosciences, School of Earth Sciences Kitajima, Kouki; University of Wisconsin Madison, Geoscience Huang, Yang; China University of Geosciences, School of Earth Sciences
Keywords:	composite granite–quartz veins, hydrous melt/aqueous fluid immiscibility, phase equilibria modeling, supercritical fluid, UHP/HP eclogite

Composite granite–quartz veins in the Sulu belt, China: evidence of supercritical fluid flow during exhumation of deeply subducted UHP continental crust

S.-J. WANG, [1,2] L. WANG, [1,*] M. BROWN, [2,1] P. M. PICCOLI, [2] T. E. JOHNSON, [3] P. FENG, [1] H. DENG, [1] K. KITAJIMA [4] AND Y. HUANG [1]

[1] *State Key Laboratory of Geological Processes and Mineral Resources, and Center for Global Tectonics, School of Earth Sciences, China University of Geosciences, Wuhan 430074, China*

[2] *Laboratory for Crustal Petrology, Department of Geology, University of Maryland, College Park, MD 20742, USA*

[3] *Department of Applied Geology, The Institute for Geoscience Research (TIGeR), Curtin University, GPO Box U1987, Perth, WA 6845, Australia*

[4] *The WiscSIMS Laboratory, Department of Geoscience, University of Wisconsin-Madison, Madison, WI 53706, USA*

*Corresponding author:

Lu Wang

wanglu@cug.edu.cn;

Tel: +86 189-7119-3667

Fax: 1-888-830-9167

ABSTRACT

Composite granite–quartz veins occur in retrogressed ultrahigh pressure (UHP) eclogite enclosed in gneiss at General's Hill in the central Sulu belt, eastern China. The granite in the veins has a high-pressure (HP) mineral assemblage of dominantly quartz + phengite + clinozoisite/epidote + garnet that yields temperatures around 820 ºC (Ti-in-zircon thermometry) at a pressure of 2.5 GPa (Si-in-phengite barometry). Zircon overgrowths on inherited cores and new grains of zircon from both components of the composite veins crystallized at *c.* 221 Ma. This age overlaps the timing of HP retrograde recrystallization dated at 225–215 Ma from multiple localities in the Sulu belt, consistent with the HP conditions retrieved from the granite. The $\varepsilon_{Hf}(t)$ values of new zircon from both components of the composite veins and the Sr–Nd isotope compositions of the granite consistently lie between values for gneiss and eclogite, whereas $\delta^{18}O$ values of new zircon are similar in the veins and the crustal rocks. These data are consistent with zircon growth from a mixed fluid generated internally within the gneiss and the eclogite, without any ingress of fluid from an external source. However, at the metamorphic peak the UHP rocks were likely fluid absent. Therefore, we propose that a grain boundary supercritical fluid was generated by exsolution of H_2O from nominally anhydrous minerals in both gneiss and eclogite during initial exhumation of deeply subducted continental crust. As exhumation progressed, the volume of fluid increased allowing it to migrate by diffuse porous flow from grain boundaries to fractures and from the dominant gneiss through the

subordinate eclogite. This process formed a blended fluid intermediate in its isotope composition between the two end members, as recorded by the composite veins. We further propose that as the solute-rich supercritical fluid in the fractures approached the critical curve for the granite–H_2O system, HP granite was precipitated preferentially in the eclogite because the fluid was not in equilibrium with the eclogite. The vein quartz in the composite veins precipitated from migrating aqueous fluid after phase separation across the critical curve. In both the granite and the gneiss, K-feldspar + plagioclase + biotite aggregates around phengite and K-feldspar veinlets along grain boundaries suggest minor phengite breakdown melting. Phase equilibria modeling of the granite indicates that the melting occurred during the transition from eclogite to amphibolite facies conditions towards the end of the decompression segment of the exhumation *P–T* path. Thus, the composite granite–quartz veins represent a rare example of a natural system that records how the fluid phase evolved during exhumation of continental crust. First a supercritical fluid generated internally at UHP conditions separated into immiscible hydrous melt and aqueous fluid at HP conditions, then low-volume hydrous melt was generated by phengite breakdown at lower pressures. The successive availability of different fluid phases attending retrograde metamorphism will affect the transport of trace elements through the continental crust and the role of these fluids as metasomatic agents interacting with the mantle wedge in the subduction channel.

Key words: composite granite–quartz veins; hydrous melt/aqueous fluid immiscibility; phase equilibria modeling; supercritical fluid; Sulu belt; UHP/HP eclogite.

INTRODUCTION

Aqueous fluid, supercritical fluid and hydrous melt exert an important influence on the composition and physical properties of their host rocks. Large-scale flow of these fluids, including hydrous melt, in subduction zones drives element recycling, and mass and heat transfer, leading to substantial crust–mantle interactions and arc magmatism (Manning, 2004; Kessel *et al*., 2005; Brown & Rushmer, 2006; Brown *et al*., 2011; Zheng, 2012; Spandler & Pirard, 2013; Bebout, 2014; Bebout & Penniston-Dorland, 2016). In addition, the liberation of fluid or melt during subduction may cause rheological weakening of the lithosphere, which may facilitate exhumation of subducted continental crust from high and ultrahigh pressure (HP–UHP) metamorphic conditions (e.g. Rosenberg & Handy, 2005; Gerya & Meilick, 2011; Labrousse *et al*., 2011, 2015; Sizova *et al.,* 2012; Ferrero *et al*., 2015).

Recent research into the fluid regime associated with subduction has focused on the possibility of hydrous melt–aqueous fluid supercriticality at UHP conditions (e.g. Mibe *et al*., 2011; Zheng *et al*., 2011; Zheng & Hermann, 2014). Supercritical fluid and hydrous melt have a greater capacity than aqueous fluid to transport trace elements (Hayden &

Manning, 2011; Sheng *et al*., 2013; Hermann & Rubatto, 2014; Schmidt & Poli, 2014). Indeed, supercritical fluid is increasingly argued to be the principal phase migrating from the subducting slab into the overlying mantle wedge deep beneath arcs, where it may separate during ascent into two immiscible phases—hydrous melt and aqueous fluid (e.g. Kawamoto *et al*., 2012, 2014; Liu *et al*., 2014). Similarly, during exhumation of deeply subducted continental crust, a syn-metamorphic supercritical fluid may separate into hydrous melt and aqueous fluid potentially leading to the precipitation of mineral deposits and/or complex vein systems (Zheng *et al*., 2011; Zheng & Hermann, 2014). To understand these fluid-related processes operating during deep subduction, it is important to characterize evidence of the generation and subsequent evolution of supercritical fluids as recorded by UHP metamorphic rocks preserved along intra-continental sutures, which represent sites of former continental subduction (e.g. Liou *et al*., 2009; Schertl & O'Brien, 2013; Brown, 2014).

The Sulu belt in eastern China is a well-studied example of continental crust that has been subducted to mantle depths. The Sulu belt reached peak pressure–temperature (*P–T*) conditions generally exceeding 3.5–4.5 GPa at 700–850 °C (e.g. Liu *et al*., 2006; Zhang *et al*., 2006; Wang L. *et al*., 2014; Wang S.J. *et al*., 2016), and may have reached pressures as high as 7 GPa at 1000 °C (Ye *et al*., 2000a). At these *P–T* conditions any remaining syn-metamorphic fluid will have been supercritical, which is consistent with the occurrence of multiphase solid inclusions interpreted to have precipitated from supercritical fluid trapped in UHP garnet and kyanite (e.g. Ferrando *et al*., 2005; Frezzotti

et al., 2007). Accordingly, the UHP metamorphic rocks in the Sulu belt provide an opportunity to investigate the origin and source of supercritical fluid attending metamorphism, the timing of hydrous melt/aqueous fluid phase separation, and the role of fluids in crust–mantle interactions during continental subduction and exhumation.

FLUIDS AND HP–UHP METAMORPHISM

Phase relations in silicate–H_2O systems

In silicate–H_2O systems, experimental studies have shown that the fluid phase attending metamorphism varies widely in composition and properties with *P–T* (Fig. 1). In particular, although aqueous fluid and hydrous melt are immiscible at low pressures they form a single miscible phase at pressures above the second critical endpoint (SCE), which is where the solvus between fluid and melt closes and a solidus may no longer be distinguished (Hermann *et al*., 2006; Hack *et al*., 2007). The SCEs for granite and basalt are located at approximately 3.0/3.4 GPa and 700/770 °C, respectively (Hermann *et al*., 2006; Hack *et al*., 2007; Mibe *et al*., 2011).

At temperatures lower than the SCE and the wet solidus, the phase in equilibrium with silicate minerals is an aqueous fluid in which dissolved solutes increase with increasing pressure (Fig. 1). By contrast, at temperatures above the wet solidus, but at pressures below the critical curve—the locus of points where the melt + fluid solvus closes, which extends from the SCE to higher temperatures and lower pressures with

changing solute content in silicate–H_2O systems (Fig. 1; Hermann *et al*., 2006; Hack *et al*., 2007)—two immiscible phases may be in equilibrium with silicate minerals, both an aqueous fluid and a hydrous melt (Fig. 1). In nature, unless the system is oversaturated with H_2O, with increasing temperature below the critical curve excess H_2O progressively dissolves into the melt until no free aqueous fluid remains at high temperatures. With increasing pressure at suprasolidus conditions, aqueous fluid and hydrous melt form a supercritical fluid at pressures above the critical curve (Fig. 1).

Hermann *et al*. (2006) argued that aqueous fluid and hydrous melt are compositionally well defined, and that there is only a narrow range of temperatures above the SCE (<100 °C) where transitional solute-rich fluid exists. Accordingly, they proposed that fluids with <30 wt% solutes be called aqueous, those with >65 wt% solutes be called hydrous melts, and those with intermediate compositions be called transitional supercritical fluids. However, as discussed by Frezzotti & Ferrando (2015), there are arguments against using an arbitrary concentration of solute to subdivide a supercritical fluid from a hydrous melt. In this study, at pressures above the SCE we follow Hermann *et al*. (2006) in separating aqueous fluid from supercritical fluid at 30 wt% solute. However, as solute content increases with temperature we do not distinguish high-solute fluids as hydrous melt, but at pressures above the SCE and the critical curve we refer to all compositions with >30 wt% solutes as supercritical fluid (Fig. 1).

Origin of fluids in exhuming continental crust

During progressive metamorphism, normally there is continuous release and loss of fluid. Ultimately, this process may lead to fluid absent conditions at the highest pressures and temperatures in the eclogite and granulite facies (Yardley & Valley, 1997), which may inhibit equilibration prior to peak *P–T* conditions (e.g. Young & Kylander-Clark, 2015). If rocks become fluid absent prior to peak *P*, what is the origin of fluids associated with retrogression during exhumation of UHP metamorphic rocks?

Multiple studies have shown that a large amount of H_2O may be stored in the continental crust in nominally anhydrous minerals (NAMs) as structural hydroxyl in point defects in the crystal lattice and as molecular water in clusters of molecules (Xia *et al*., 2005; Zheng, 2009). For example, the H_2O concentrations in garnet and omphacite from UHP eclogite in the Dabie–Sulu orogen are 1000–3000 ppm (reviewed by Zheng, 2009), and the total whole-rock H_2O content for phengite-free eclogite is ~2500 ppm (Chen *et al*., 2011a). Similarly, the H_2O concentrations in quartz, plagioclase and K-feldspar from UHP gneiss in the southern Sulu belt are 1500–3500 ppm, and the total whole-rock H_2O content for one hydrate-free gneiss is ~2400 ppm (Chen *et al*., 2011a). Addition of phengite, epidote, biotite or amphibole to the mineral assemblage increases the whole-rock H_2O content considerably, in proportion to the mode of these hydrous minerals.

Experimental studies have demonstrated increasing solubility of H_2O in NAMs with increasing pressure, potentially leaving little or no free fluid at the peak of UHP metamorphism (reviewed by Zheng, 2009). The converse of this relationship is the

171 decreasing solubility of H_2O in NAMs with decreasing pressure, leading to exsolution of
172 molecular H_2O and hydroxyl from NAMs during exhumation. In addition, the hydroxyl
173 in hydrous minerals in eclogite has been argued to facilitate destabilization of omphacite
174 to form symplectite without any requirement of fluid infiltration (Martin & Duchêne,
175 2015). Thus, continental crust metamorphosed at UHP conditions stores H_2O in NAMs
176 and hydrous minerals that will be made available during exhumation, providing an
177 internal source of fluids considered sufficient to facilitate retrogression (Zheng, 2009;
178 Chen *et al*., 2011a).
179
180 **Evidence of fluids in exhumed continental crust**
181 As reviewed in Table S1, although evidence of a grain-scale supercritical fluid
182 accompanying the late prograde to peak stage of UHP metamorphism has been presented
183 from several orogenic belts (e.g. Stöckhert *et al*., 2001, 2009; van Roermund *et al*., 2002;
184 Ferrando *et al*., 2005, 2009; Scambelluri *et al*., 2008; Vrijmoed *et al*., 2008; Malaspina et
185 al., 2010), our knowledge of the origin and subsequent evolution of supercritical fluids
186 during the retrograde evolution of rocks is limited (Hack *et al*., 2007; Xia *et al*., 2010;
187 Frezzotti & Ferrando, 2015). One issue in identifying the former presence of a
188 supercritical fluid in exhumed UHP crust is the changing composition of the fluid across
189 the range of *P–T* conditions (Hack *et al*., 2007; Hermann *et al*., 2013; Schmidt & Poli,
190 2014; Frezzotti & Ferrando, 2015). As a result, precipitates from a supercritical fluid at
191 pressures above the critical curve have a wide range of possible compositions, which may

192 make distinguishing them from the products of hydrous melts and/or aqueous fluids at
193 pressures below the critical curve challenging (Frezzotti & Ferrando, 2015). Studies of
194 multiphase solid inclusions trapped under UHP conditions suggest that compositions of
195 supercritical fluids typically are high in fluid-mobile element contents, such as K, Na,
196 LREE (Light Rare Earth Elements) and LILE (Large Ion Lithophile Elements), and also
197 HREE (Heavy Rare Earth Elements), HFSE (High Field Strength Elements) and
198 transition metals (Table S1). However, caution is necessary since multiphase solid
199 inclusions in UHP metamorphic rocks may represent an incomplete record or they may
200 have been modified in composition during exhumation (Hermann *et al*., 2013; Hermann
201 & Rubatto, 2014). In addition, the small size of multiphase solid inclusions, generally
202 only tens of microns in diameter, limits the information we can obtain from them
203 concerning the parent fluids, particularly with respect to the source of the fluids and the
204 timing of fluid availability.
205 The most visible evidence of channelized fluid flow during subduction and
206 exhumation is represented by HP–UHP vein systems that are common in eclogite facies
207 metamorphic rocks (Gao & Klemd, 2001; Rubatto & Hermann, 2003; Spandler &
208 Hermann, 2006; Zhang *et al*., 2008; Spandler *et al*., 2011; Guo *et al*., 2015). These
209 systems register information useful in deciphering the evolution of fluid attending
210 metamorphism.
211 Here, we present the results of a study of a well-exposed coastal outcrop in the
212 central Sulu belt, where composite granite–quartz veins occur within eclogite blocks in

the dominant gneiss of the subducted leading edge of the Yangtze Craton. We integrate observations from field relationships and petrography, with mineral and whole-rock compositions, including Sr–Nd isotopes, zircon U–Pb geochronology and Hf–O isotopes, and thermobarometry and phase equilibria modeling to develop a comprehensive understanding of the origin and source of fluid after the UHP metamorphic peak and its evolution during exhumation.

GEOLOGICAL SETTING

The Dabie–Sulu orogen in central–eastern China marks the site of northward subduction and collision of the Yangtze Craton beneath the North China Craton during the Triassic (Fig. S1a; e.g. Ernst *et al*., 2007; Liou *et al*., 2012). At the eastern end of the orogen, the Sulu belt was displaced to the northeast by approximately 500 km of sinistral offset along the NNE-trending Tan–Lu fault. Based on integrated field, petrological and geochemical studies, the Sulu belt is divided into a southern HP and a central and northern UHP zone (Liu *et al*., 2004; Xu *et al*., 2006). The UHP zone consists of mainly orthogneiss and paragneiss, with minor eclogite, garnet peridotite, quartzite and marble, all of which are intruded by post-orogenic granites (Hacker *et al*., 2000; Zhang *et al*., 2009). Eclogite occurs as blocks and lenses enclosed mainly in gneisses, but sometimes in garnet peridotite and marble. Coesite occurs in eclogite and as inclusions in zircons from eclogite, quartzite and gneiss (e.g. Zhang *et al*., 1995; Ye *et al*., 2000b; Liu & Liou, 2011;

234 Chen *et al*., 2013). SHRIMP U–Pb dating of coesite-bearing domains in zircons from
235 these rocks has yielded metamorphic ages from 234 ± 4 Ma to 225 ± 2 Ma (Liu & Liou,
236 2011), indicating that all these units record the Triassic UHP metamorphism.

237 This study area is located in the central Sulu belt at General's Hill (Fig. S1b), ~35 km
238 northeast of Qingdao, where a continuous outcrop 50–100 m wide extends along the
239 coast for approximately 1 km (the northern part of the outcrop is shown in Fig. 2). The
240 outcrop consists of strongly foliated, tight to isoclinally folded migmatitic eclogite
241 striking SSE–NNW with moderate to steep dips to the WSW (Fig. 2). The eclogite hosts
242 foliation-parallel centimeter-scale stromatic leucosomes and meter-scale sheets of
243 leucosome spaced 10–20 m apart and interpreted to be former melt ascent channels
244 (Wang *et al*., 2014). The leucosome is moderately to strongly foliated, with the foliation
245 mainly defined by phengite, elongated quartz and feldspar. The migmatitic eclogite is
246 surrounded by felsic gneiss and the outcrop is cut by quartz and feldspar porphyry dikes.

247 Based on structural mapping, and petrological and geochemical analysis, the
248 migmatitic eclogite was argued to record successive stages of generation and migration of
249 melt derived from the UHP eclogite by phengite-breakdown melting during exhumation
250 (Wang *et al*., 2014). LA-ICP-MS U–Pb dating of zircon overgrowth rims from leucosome,
251 retrogressed eclogite and migmatite yielded weighted mean $^{206}Pb/^{238}U$ ages (± 2σ) of 228
252 ± 6 Ma, 224 ± 4 Ma and 219 ± 5 Ma (Wang *et al*., 2014), suggesting that the melt
253 crystallization occurred during exhumation of the Sulu belt, shortly after the peak of UHP
254 metamorphism at *c.* 233 Ma (Zeng *et al*., 2011).

In this study, the regional mapping of Wang *et al*. (2014) was supplemented by 1:500 scale structural mapping that targeted centimeter- to decimeter-scale composite granite–quartz veins in the northern part of the outcrop adjacent to the enclosing gneiss (Fig. 2). The composite veins are irregular in shape but have sharp contacts with the host eclogite and are generally parallel to the foliation (Fig. 3a–c). The eclogite is fine-grained and variably retrogressed, while the enclosing gneiss is compositionally homogeneous, with a weak foliation that is gently folded.

Seventeen samples were collected at General's Hill, as summarized in Table S2 and illustrated in Figs 2 & 3, including two sets of granite–quartz samples from composite veins (YK1412-12 and YK1412-11; YK156-2 and YK156-1), the local host retrogressed eclogite (YK1412-13, YK156-3) and the adjacent gneiss (YK1412-14; YK156-4). Three other granite samples from composite veins (YK156-5, -6, -7), one additional eclogite (YK1510-2) and five other gneisses (YK137-12, -13, YK1412-9, -10, YK156-11) were sampled. Details of all analytical methods used in this study are provided in Appendix S1.

RESULTS

Petrography

In the composite veins, the granite is composed of quartz (45–49 vol%) + phengite (22–30 vol%) + clinozoisite/epidote (3–10 vol%) + rare garnet, with plagioclase (5–13 vol%) + K-feldspar (6–11 vol%), minor biotite (replacing phengite) and hornblende (replacing

garnet), and scarce apatite, zircon, rutile with thin rims of ilmenite (in phengite), and titanite (Fig. 4a–d). Phengite has 3.40–3.29 Si per formula unit (pfu; Table S3a, one analysis with 3.25 Si pfu). At the edges, phengite is surrounded by aggregates of variable thickness composed of biotite + plagioclase + K-feldspar from which thin films, cuspate veinlets and patches of K-feldspar with low dihedral angles extend along grain boundaries (Fig. 4e–i). Plagioclase occurs primarily in symplectites after phengite and garnet, and occasionally as subhedral grains (Fig. 4b,c). Garnet occurs as either subhedral grains showing minor retrogression or as relict fragments within symplectites of hornblende + plagioclase + opaque oxide (Fig. 4c). Millimeter-sized euhedral–subhedral epidote grains commonly have clinozoisite cores (Fig. 4d); in addition, they contain fine-grained inclusions of quartz, apatite and zircon (e.g. Fig. 4d). By contrast, the vein quartz in the composite veins is almost entirely composed of anhedral quartz (>99 vol%), with only rare biotite and zircon.

The host eclogite is strongly foliated with extensive amphibolite facies retrogression, where garnet, omphacite and phengite are almost entirely replaced by various symplectites (Fig. 5a,b). The symplectites comprise either hornblende + plagioclase after omphacite, or hornblende + plagioclase + opaque oxide after garnet, or biotite + plagioclase after phengite, and occur within a matrix of fine-grained garnet, hornblende, quartz, apatite, zircon and rutile/ilmenite (Fig. 5a,b).

The gneiss consists of quartz + plagioclase + K-feldspar + phengite + clinozoisite/epidote + zircon + titanite + apatite (Fig. 5c–f), without garnet. Coarse

297 phengite is retrogressed to biotite + plagioclase + K-feldspar at the edges (Fig. 5c,e,f).
298 Clinozoisite and epidote form anhedral grains up to 1 mm in diameter, and contain
299 inclusions including apatite, quartz and zircon (e.g. Fig. 5d). By contrast with the granite
300 in the composite veins, in the gneiss some subhedral plagioclase grains have retained
301 their primary magmatic features, such as multiple twinning and larger grain size (up to
302 several mm; Fig. 5c,e). K-feldspar occurs as subhedral grains, and also as cuspate veinlets
303 along grain boundaries between plagioclase and quartz (Fig. 5f). Large quartz grains
304 exhibit subgrain structure, otherwise quartz forms the major phase with minor feldspar in
305 a finer-grained, anastomosing matrix, where it exhibits granoblastic-polygonal
306 microstructure.
307
308 **Whole-rock major and trace element compositions**
309 The major and trace element compositions of the composite granite–quartz veins, the host
310 eclogites and the surrounding gneisses are summarized in Table S3b, and Figs S2 & 6.
311 Granite in the veins has high SiO_2 (73.01–75.61 wt%) and K_2O (3.79–4.26 wt%), but low
312 Na_2O (0.99–1.35 wt%), FeO_t (1.44–2.43 wt%) and MgO (0.52–1.14 wt%). The granites
313 are characterized by high REE contents (∑REE = 170–276 ppm), and on a
314 chondrite-normalized plot show enriched LREE and flat HREE patterns [$(La/Yb)_N$ =
315 21.80–42.26; $(Gd/Yb)_N$ = 2.02–3.39; Fig. 6a] with weakly negative to negligible Eu
316 anomalies (Eu/Eu* = 0.74–0.91). In a primitive mantle-normalized multi-element
317 diagram (Fig. 6b), the granite shows enrichment in LILE, notably Sr, but a moderate

depletion in HFSE, including Nb and Ta.

The vein quartz of the composite veins has 99.10 wt% SiO_2 and very low abundances of all other oxides, reflecting the dominance of modal quartz. The sample also has low concentrations of all trace elements. It is characterized by a relatively flat chondrite-normalized REE pattern [$(La/Yb)_N$ = 14.56; Fig. 6a], with slight LREE enrichment [$(La/Sm)_N$ = 8.39] and a moderately negative Eu anomaly (Eu/Eu* = 0.33). In a primitive mantle-normalized multi-element diagram (Fig. 6b), the sample shows weak depletion of Nb and Sr with a significant positive anomaly for Pb.

The host eclogites contain moderate SiO_2 (49.09–54.34 wt%) and MgO (4.72–5.07 wt%), but high FeO_t (9.15–13.10 wt%) and Na_2O (3.30–4.79 wt%) contents. They have moderate REE abundances (∑REE = 85–173 ppm) and exhibit mildly enriched to flat chondrite-normalized LREE [$(La/Sm)_N$ = 2.82–3.56] and flat HREE [$(Gd/Yb)_N$ = 1.16–1.56] patterns with negligible Eu anomalies (Eu/Eu* = 0.90–1.00; Fig. 6a). In a primitive mantle-normalized multi-element diagram, the eclogites are generally enriched in HFSE and LILE such as Zr, Hf and Ba (Fig. 6c).

The gneisses have high SiO_2 (69.70–74.92 wt%), Na_2O (3.48–4.94 wt%) and K_2O (2.11–4.83 wt%) contents. They also contain high REE concentrations (∑REE = 167–222 ppm), and in chondrite-normalized REE plot are seen to be enriched in LREE and flat in HREE [$(La/Yb)_N$ = 11.58–22.69; $(Gd/Yb)_N$ = 1.07–1.96] with slightly negative Eu anomalies (Eu/Eu* = 0.62–0.81; Fig. 6a). In a primitive mantle-normalized multi-element diagram, the gneisses are depleted in Nb, Ta, Sr and enriched in Th, U and Pb (Fig. 6d).

339 The high Na_2O and low Sr contents distinguish the gneiss from the granite in the
340 composite veins (Fig. S2).
341
342 **Whole-rock Sr–Nd isotopes**
343 The whole-rock Sr–Nd isotope compositions of granite from the composite veins, the
344 host eclogites and the surrounding gneisses are given in Table S4 and shown in Fig. 7,
345 including, for comparison, the Sr–Nd isotope compositions of UHP eclogites from
346 Yangkou (Chen *et al*., 2002), a few kilometers to the north of General's Hill. Initial
347 $^{87}Sr/^{86}Sr$ ratios and $\varepsilon_{Nd}(t)$ values (for definition of $\varepsilon_{Nd}(t)$ see table S4) were corrected to
348 the metamorphic age of t = 221 Ma for all samples based on the U–Pb zircon ages
349 reported below. The granite has moderate initial $^{87}Sr/^{86}Sr$ ratios of 0.7078–0.7110 and
350 negative $\varepsilon_{Nd}(t)$ values ranging from -21.9 to -15.6, yielding two-stage depleted mantle Nd
351 model ages of 2776–2259 Ma. The eclogites exhibit moderate and consistent initial
352 $^{87}Sr/^{86}Sr$ ratios of 0.7068–0.7088 and negative $\varepsilon_{Nd}(t)$ values of -16.5 to -11.6, while the
353 gneisses have variably high initial $^{87}Sr/^{86}Sr$ ratios of 0.7093–0.7168 and much more
354 negative $\varepsilon_{Nd}(t)$ values of -22.2 to -18.1.
355
356 **Zircon microstructure**
357 Zircon grains from both components of the composite veins show similar microstructural
358 features. They are generally colorless and transparent in plane light, euhedral to subhedral
359 and equant to prismatic, with crystal lengths varying from 50 to 300 μm and aspect ratios

(length/width) of 1:1 to 4:1. Most grains show a distinct core–rim structure in cathodoluminescence (CL) images (Fig. S3a,b). The cores show rhythmic oscillatory or sector zoning with weak to moderate luminescence, whereas the overgrowth rims, which have sharp contacts against the cores, are unzoned or weakly zoned with moderate luminescence. In some cases, the rims are incompletely surrounded by a thin outer edge (<5 μm) that is CL-bright (Fig. S3a,b). In addition, there are zircon grains that are unzoned or weakly zoned and exhibit moderate luminescence in CL images (Fig. S3a,b), similar to the rim domains. These grains also may have thin CL-bright edges.

Zircon grains from the host eclogite are mostly yellowish or murky-brown to colorless in plane light, whereas those from the gneiss are mostly colorless and transparent in plane light. Zircons from both are subhedral to anhedral and oval (in the eclogite), equant or prismatic (in both), with lengths ranging from 50 to 300 μm and aspect ratios of 1:1 to 4:1. In CL images, most zircon grains from eclogite and gneiss display overgrowth rims in sharp contact with cores (Fig. S3c,d). In the eclogite, the zircon cores are irregular with weak oscillatory, patchy or planar zoning and weak to moderate luminescence, whereas the overgrowth rims are unzoned or weakly zoned with relatively homogeneous moderate luminescence. In addition, some zircon grains in the eclogite are unzoned and resemble the overgrowth rims in CL images (Fig. S3c). In the gneiss, the zircon cores exhibit oscillatory or sector zoning, whereas the rims are unzoned; they exhibit homogeneous weak to moderate luminescence. In addition, the rims may have thin (<5 μm) CL-bright edges, similar to those on zircons from the composite vein.

The outermost CL-bright edges on zircons from the composite vein and the gneiss are similar to those commonly seen in HP–UHP metamorphic rocks elsewhere in the Sulu belt (e.g. Xu *et al*., 2013; Gao *et al*., 2014). They may represent recrystallization of the outermost part of the rim or new zircon growth (Corfu *et al*., 2003). However, they are too thin to be analyzed by LA-ICP-MS or SIMS, and consequently are not discussed further.

Zircon U–Pb ages and trace element compositions

Eclogite

Zircon from two host eclogites (YK1412-13 and YK156-3; Tables S5a & S6a) was analyzed for U–Pb isotope and trace element compositions. Zircon cores from YK1412-13 (n = 18) are characterized by high Th/U ratios (0.27–2.19, Fig. S4a,b) and record $^{206}Pb/^{238}U$ dates varying from 778 ± 9 to 398 ± 7 Ma (Fig. 8a). By contrast, overgrowth rims and new grains (n = 19) have low Th/U ratios (0.004–0.030, Fig. S4a,b); a subset of 9 analyses with >90% concordance yields $^{206}Pb/^{238}U$ dates of 223 ± 7 to 214 ± 9 Ma and gives a weighted mean age of 217 ± 2 Ma (2σ, MSWD = 0.75, Fig. 8a). Similarly, zircon cores from YK156-3 (n = 13) have high Th/U ratios (0.08–1. 91, Fig. S4a,b) and yield $^{206}Pb/^{238}U$ dates ranging from 776 ± 9 to 462 ± 13 Ma (Fig. 8b). By contrast, overgrowth rims and new grains (n = 16) have low Th/U ratios (0.004–0.021, Fig. S4a,b); a subset of 8 analyses with >90% concordance yields $^{206}Pb/^{238}U$ dates of 222 ± 5 to 215 ± 5 Ma and gives a weighted mean age of 217 ± 2 Ma (2σ, MSWD = 1.3, Fig.

8b).

Trace element compositions of zircons are illustrated in Fig. 9a,b. The cores with variably low Hf/Y ratios (1.0–100.2) have high total REE abundances (∑REE = 343–13702 ppm) and elevated chondrite-normalized HREE patterns [$(Gd/Lu)_N$ = 0.012–0.520], with positive Ce (Ce/Ce* = 2.3–641.9) and negative Eu (Eu/Eu* = 0.23–0.81) anomalies. By contrast, the overgrowth rims and new grains have higher Hf/Y ratios (110.9–478.0) but lower total REE abundances (∑REE = 38–161 ppm) and flatter chondrite-normalized HREE patterns [$(Gd/Lu)_N$ = 0.579–2.898]; most have negligible to weakly positive Eu anomalies (Fig. S5, Eu/Eu* = 0.67–2.02).

Granite

U–Pb isotope and trace element compositions were determined for zircon from two samples of granite from the composite veins (YK1412-12 and YK156-2; Tables S5b & S6b). Zircon cores from YK1412-12 (n = 34) are characterized by high Th/U ratios (0.17–1.62, Fig. S4c,d). They yield $^{206}Pb/^{238}U$ dates varying from 786 ± 5 to 333 ± 5 Ma, while a subset of 15 analyses with with >90% concordance yields $^{206}Pb/^{238}U$ dates of 784 ± 12 to 747 ± 4 Ma and gives a weighted mean age of 769 ± 8 Ma (2σ, MSWD = 20.0, Fig. 8c). Similarly, cores from YK156-2 (n = 19) have high Th/U ratios (0.18–2.78, Fig. S4c,d) and yield $^{206}Pb/^{238}U$ dates ranging from 782 ± 8 to 414 ± 7 Ma. Nine analyses with >90% concordance yield $^{206}Pb/^{238}U$ dates from 782 ± 8 to 763 ± 10 Ma that give a weighted mean age of 777 ± 5 Ma (2σ, MSWD = 1.4, Fig. 8d).

Overgrowth rims and new grains of zircon from YK1412-12 (n = 21) and YK156-2

(n = 18) have low Th/U ratios of 0.003–0.027 and 0.004–0.014, respectively (Fig. S4c,d). New zircon with >90% concordance yields $^{206}Pb/^{238}U$ dates of 229 ± 5 to 211 ± 5 Ma and 222 ± 6 to 218 ± 8 Ma, respectively. These dates give consistent weighted mean ages of 221 ± 2 Ma (2σ, MSWD = 0.69, Fig. 8c; n = 21) and 220 ± 2 Ma (2σ, MSWD = 0.19, Fig. 8d; n = 7).

Zircons from the two samples have similar trace element compositions for the cores, overgrowth rims and new grains (Table S6b). The cores contain high total REE abundances (∑REE = 134–9231 ppm) and show variably low Hf/Y ratios of 1.3–66.5. In chondrite-normalized REE diagrams (Fig. 9c,d), they are characterized by steep HREE patterns [$(Gd/Lu)_N$ = 0.076–0.858], and pronounced positive Ce (Ce/Ce* = 6.0–438.1) and negative Eu (Eu/Eu* = 0.08–0.41) anomalies. By contrast, the overgrowth rims and new grains have lower total REE abundances (∑REE = 21–288 ppm) than the cores, with higher Hf/Y ratios of 76.32–479.27. They exhibit flatter chondrite-normalized HREE patterns [$(Gd/Lu)_N$ = 0.031–1.958], with similar positive Ce (Ce/Ce* = 0.7–152.1), but mostly weakly negative Eu anomalies (Fig. S5, Eu/Eu* = 0.09–1.67; Fig. 9c,d).

Vein quartz

U–Pb isotope and trace element compositions were determined for zircon from two samples of the vein quartz (YK1412-11 and YK156-1; Tables S5c & S6c). Cores from YK1412-11 (n = 32) have high Th/U ratios (0.05–1.81, Fig. S4e,f) and give $^{206}Pb/^{238}U$ dates varying from 794 ± 6 to 328 ± 4 Ma, with a subset of 7 analyses with >90% concordance yielding $^{206}Pb/^{238}U$ dates of 794 ± 6 to 758 ± 4 Ma and a weighted mean age

444 of 772 ± 12 Ma (2σ, MSWD = 18.0, Fig. 8e). Similarly, cores from YK156-1 (n = 20)
445 have high Th/U ratios (0.24–1.78, Fig. S4e,f) and give $^{206}Pb/^{238}U$ dates ranging from 782
446 ± 14 to 281 ± 9 Ma; the 10 least recrystallized spots have concordant $^{206}Pb/^{238}U$ dates of
447 782 ± 14 to 748 ± 8 Ma that yield a weighted mean age of 773 ± 8 Ma (2σ, MSWD = 5.7,
448 Fig. 8f).
449 Overgrowth rims and new grains of zircon from the two samples (n = 33 and 31,
450 respectively) have low Th/U ratios of 0.003–0.029 and 0.005–0.060 (Fig. S4c,d). New
451 zircon domains with >90% concordance record $^{206}Pb/^{238}U$ dates of 231 ± 4 to 215 ± 5 Ma
452 and 233 ± 4 to 215 ± 6 Ma, respectively, and yield weighted mean ages of 222 ± 1 Ma
453 (2σ, MSWD = 2.7, Fig. 8e; n = 33) and 221 ± 1 Ma (2σ, MSWD = 4.5, Fig. 8f; n = 28).
454 Zircon cores with low Hf/Y ratios (2.6–185.0) are characterized by high total REE
455 contents (∑REE = 55–7199 ppm) and steep chondrite-normalized HREE patterns
456 [$(Gd/Lu)_N$ = 0.109–0.402], with positive Ce (Ce/Ce* = 10.3–184.1) and negative Eu
457 (Eu/Eu* = 0.04–0.80) anomalies (Fig. 9e,f). By contrast, the overgrowth rims and new
458 grains have high Hf/Y ratios of 69.9–400.9. They are depleted in REE abundances
459 (∑REE = 21–215 ppm) and exhibit flatter chondrite-normalized HREE patterns
460 [$(Gd/Lu)_N$ = 0.056–3.609] than the cores, mostly with positive Ce (Ce/Ce* = 0.3–101.7)
461 and weakly negative to moderately positive Eu anomalies (Fig. S5, Eu/Eu* = 0.27–4.30).
462 *Gneiss*
463 Zircons from two gneiss samples were analyzed for U–Pb isotope and trace element
464 compositions (YK1412-14 and YK156-4; Tables S5d & S6d). Zircon cores from

YK1412-14 (n = 37) show high Th/U ratios (0.06–1.96, Fig. S4g,h) and record $^{206}Pb/^{238}U$ dates ranging from 787 ± 7 to 274 ± 2 Ma; 17 analyses with >90% concordance yield $^{206}Pb/^{238}U$ dates from 787 ± 7 to 731 ± 5 Ma that give a weighted mean age of 762 ± 9 Ma (2σ, MSWD = 36.0, Fig. 8g). Similarly, cores from YK156-4 (n = 34) give $^{206}Pb/^{238}U$ dates varying from 784 ± 10 to 267 ± 3 Ma; the 12 least recrystallized zircons with >90% concordance record $^{206}Pb/^{238}U$ dates from 784 ± 10 to 776 ± 13 Ma that give a weighted mean age of 779 ± 3 Ma (2σ, MSWD = 0.66, Fig. 8h). By contrast, overgrowth rims (n = 16 and 17, respectively) from zircon in the gneisses are characterized by low Th/U ratios (0.007–0.026 and 0.008–0.075, Fig. S4g,h). Analyses with >90% concordance yield $^{206}Pb/^{238}U$ dates of 228 ± 3 to 213 ± 2 Ma and 229 ± 4 to 216 ± 2 Ma, respectively that give weighted mean ages of 223 ± 2 (2σ, MSWD = 11.1, Fig. 8g; n = 16) and 222 ± 2 Ma (2σ, MSWD = 5.7, Fig. 8h; n = 14).

Trace element compositions of zircons are shown in Fig. 9g,h. The cores have variably low Hf/Y ratios (1.2–95.4) and high total REE concentrations (∑REE = 229–16263 ppm). They show steep chondrite-normalized HREE patterns [$(Gd/Lu)_N$ = 0.086–0.499], and strongly positive Ce (Ce/Ce* = 2.3–347.3) and negative Eu (Eu/Eu* = 0.07–0.67) anomalies. Compared to the cores, the overgrowth rims have higher Hf/Y ratios (43.7–253.4) and lower total REE abundances (∑REE = 114–492 ppm; Table S6d), but exhibit similar sloping chondrite-normalized HREE patterns [$(Gd/Lu)_N$ = 0.066–0.451] mostly with weakly to moderately negative Eu anomalies (Fig. S5, Eu/Eu* = 0.1–1.32).

Zircon Hf–O isotope compositions

Eclogite

For zircons from one of the eclogite samples (YK1412-13), the cores (n = 13) record high $^{176}Lu/^{177}Hf$ ratios of 0.000347–0.003385 but low $^{176}Hf/^{177}Hf$ ratios of 0.281853–0.282169 (Table S7; Fig. S6a,b). At t_1 = 780 Ma, the calculated $\varepsilon_{Hf}(t_1)$ values (for definition and calculation of $\varepsilon_{Hf}(t)$ see Appendix S1 & Table S7) are -16.1 to -4.3 with a weighted mean of -12.4 ± 2.1 (MSWD = 22; Fig. 10a), yielding T_{DM1} (for definition and calculation of T_{DM} see Appendix S1 & Table S7) ages varying from 1980 ± 29 to 1500 ± 39 Ma. On the other hand, the overgrowth rims and new grains (n = 19) exhibit low $^{176}Lu/^{177}Hf$ ratios of 0.000006–0.001883 but high $^{176}Hf/^{177}Hf$ ratios of 0.282124–0.282265 (Table S7; Fig. S6a,b), which yield initial $^{176}Hf/^{177}Hf$ ratios of 0.282116 to 0.282265 and $\varepsilon_{Hf}(t_2)$ values of -18.4 to -13.1 at 221 Ma (Figs 10a & 11). The zircon cores (n = 24) record $\delta^{18}O$ values from 5.61 ‰ to 6.82 ‰, whereas the overgrowth rims and new grains (n = 36) show slightly lower $\delta^{18}O$ values of 5.33 ‰ to 5.93 ‰ (Table S8; Fig. 12a,b).

Composite vein

For zircons from one of the granite samples (YK1412-12), the cores (n = 21) have relatively high $^{176}Lu/^{177}Hf$ ratios of 0.000355–0.001778 and low $^{176}Hf/^{177}Hf$ ratios of 0.281845–0.282054 (Table S7; Fig. S6c,d). Assuming t_1 = 780 Ma, the calculated $\varepsilon_{Hf}(t_1)$ values are -16.5 to -8.5 (Fig. 10b), yielding T_{DM2} of 2706 ± 102 to 2209 ± 63 Ma. By contrast, the overgrowth rims and new zircon grains (n = 18) have lower $^{176}Lu/^{177}Hf$ ratios of 0.000014–0.000903 but higher $^{176}Hf/^{177}Hf$ ratios of 0.282015–0.282245

compared to those of the cores (Table S7; Fig. S6c,d). At t_2 = 221 Ma, the calculated initial $^{176}Hf/^{177}Hf$ ratios and $\varepsilon_{Hf}(t_2)$ values are 0.282013 to 0.282244 and -22.0 to -14.4, respectively (Figs 10b & 11). The overgrowth rims and new grains of zircon (n = 51) have $\delta^{18}O$ values of 5.25 to 5.98 ‰, slightly lower than the cores (n = 25), which have homogeneous $\delta^{18}O$ values from 5.47 ‰ to 6.41 ‰ (Table S8; Fig. 12c,d).

For zircons from one of the vein quartz samples (YK1412-11), the cores (n = 23) have high $^{176}Lu/^{177}Hf$ ratios of 0.000443–0.002185, but variably low $^{176}Hf/^{177}Hf$ ratios of 0.281861–0.282193 (Table S7; Fig. S6c,d). At t_1 = 780 Ma, their $\varepsilon_{Hf}(t_1)$ values are -16.9 to -4.0 with a weighted mean of -9.5 ± 1.6 (MSWD = 16; Fig. 11c), corresponding to T_{DM2} ages of 2669 ± 76 to 1930 ± 105 Ma. By contrast, overgrowth rims and new grains (n = 18) have relatively low $^{176}Lu/^{177}Hf$ ratios of 0.000020–0.001000 and high $^{176}Hf/^{177}Hf$ ratios of 0.281991–0.282258 (Table S7; Fig. S6e,f). At t_2 = 221 Ma, the calculated initial $^{176}Hf/^{177}Hf$ ratios are 0.281988 to 0.282258 (Fig. 11), corresponding to $\varepsilon_{Hf}(t_2)$ values of -22.9 to -13.3 with a weighted mean of -18.2 ± 1.5 (MSWD = 10.2; Fig. 10c). The zircon cores (n = 25) record $\delta^{18}O$ values of 5.46 ‰–6.67 ‰, whereas the overgrowth rims and new grains (n = 44) have slightly lower $\delta^{18}O$ values of 5.19–6.06 ‰ (Table S8; Fig. 12e,f).

Gneiss

For zircons from one of the gneiss samples (YK1412-14), the cores (n = 8) have $^{176}Lu/^{177}Hf$ ratios of 0.000992–0.002155 and $^{176}Hf/^{177}Hf$ ratios of 0.281807–0.281951 (Table S7; Fig. S6g,h). The calculated $\varepsilon_{Hf}(t_1)$ values at 780 Ma are -18.0 to -12.4 with a

528 weighted mean of -14.8 ± 1.6 (MSWD = 4.3; Fig. 10d), yielding T_{DM2} ages from 2801 ±
529 95 to 2451 ± 85 Ma. By contrast, the overgrowth rims (n = 9) record lower $^{176}Lu/^{177}Hf$
530 ratios of 0.000115–0.001077 but variably high $^{176}Hf/^{177}Hf$ ratios of 0.281894–0.282027
531 when compared to the cores (Table S7; Fig. S6g,h). At t_2 = 221 Ma, the calculated initial
532 $^{176}Hf/^{177}Hf$ ratios and $\varepsilon_{Hf}(t_2)$ values are 0.281890 to 0.282026 and -26.4 to -21.5,
533 respectively (Figs 10d & 11). The cores (n = 23) have $\delta^{18}O$ values of 5.82 ‰–6.67 ‰,
534 slightly higher than those of the overgrowth rims (n = 38) with $\delta^{18}O$ values of 5.30–6.29 ‰
535 (Table S8; Fig. 11g,h).
536
537 **Ti-in-zircon thermometry**
538 The solubility of Ti in zircon shows strong dependence on temperature. For zircon that
539 grew in equilibrium with an appropriate mineral assemblage to buffer the activity of Ti
540 (a_{TiO2}; buffered by rutile, titanite or ilmenite) and silica (a_{SiO2}; buffered by a SiO_2 phase),
541 the Ti concentration has been calibrated as a thermometer (Ferry & Watson, 2007).
542 Because zircon is extremely retentive of Ti, the Ti-in-zircon thermometer is robust in
543 preserving temperatures of zircon growth (Cherniak & Watson, 2007).
544 We use the Ti-in-zircon thermometer of Ferry & Watson (2007) to constrain the
545 crystallization temperature of overgrowth rims and/or new grains of zircon in the host
546 eclogite, the granite and vein quartz from the composite veins, and the surrounding gneiss.
547 This thermometer was calibrated at 1.0 GPa and has a positive pressure dependence of
548 approximately 50 °C/GPa (Ferry & Watson, 2007, p. 711). The Si content of phengite has

549 been calibrated as a barometer by Caddick & Thompson (2008, equation 8). Pressures
550 calculated using the Si content of phengite in the granite from the composite veins (3.40–
551 3.29 Si pfu) are summarized in a box-and-whisker plot in Fig. S7a. The interquartile
552 range is 2.5–2.1 GPa; based on these data, we have corrected the calculated temperatures
553 to 2.5 GPa.

554 Overgrowth rims and/or new grains of zircon from the eclogite, the granite and vein
555 quartz, and the gneiss have Ti concentrations that vary from 3 to 38 ppm, 1 to 33 ppm,
556 0.2 to 65 ppm, and 0.7 to 60 ppm, respectively (Table S6). As quartz is a major mineral in
557 all samples, a_{SiO2} is taken as 1. Rutile is the major Ti-rich mineral in the eclogite; in the
558 granite from the composite veins, rutile occurs included in phengite, although titanite is
559 the Ti-bearing mineral outside phengite. Therefore, we take a_{TiO2} in the eclogite and
560 granite to be 1.0 (Watson *et al*., 2006). However, the a_{TiO2} in the vein quartz is
561 unconstrained, so temperatures calculated with a_{TiO2} of 1.0 may underestimate
562 temperature by up to 70 °C at 750 °C (Ferry & Watson, 2007). By contrast, titanite is the
563 only Ti-rich mineral in the gneiss, which suggests that a_{TiO2} was likely <1.0. Since the
564 plausible lower limit of a_{TiO2} in typical crustal rocks is 0.5 (Hayden & Watson, 2007;
565 Ferry & Watson, 2007), we use this value in calculating temperatures from the gneiss.

566 The Ti-in-zircon temperatures are summarized in box-and-whisker plots in Fig. S7b.
567 For the granite, the interquartile range is 851–777 °C, while the interquartile range for the
568 vein quartz is 864–763 °C. Similarly, for the host eclogite, the interquartile range is 839–
569 784 °C, consistent with that of 901–744 °C for the gneiss. The median temperatures for all

samples are ~820 °C.

Phase equilibria modeling

Figure 13 shows a *P–T* pseudosection calculated in the $MnO–Na_2O–CaO–K_2O–FeO–MgO–Al_2O_3–SiO_2–H_2O–TiO_2–O$ (MnNCKFMASHTO) model system for the composition of a granite sample (YK1412-12) from one composite vein. Phase equilibria calculations use the major element oxide bulk composition as determined by XRF analysis, assuming all loss on ignition as H_2O and an $Fe^{3+}/\Sigma Fe$ ratio of 0.2. Calculations were undertaken using THERMOCALC (Powell & Holland, 1988) and the end-member thermodynamic data of Holland & Powell (2011; ds62 dataset as generated on 06/02/14). Activity–composition models used are those calibrated for pelitic systems (White *et al*., 2014a,b). For clinopyroxene we use the suprasolidus 'augite' model of Green *et al*. (2016). Although this was calibrated against a different ('mafic') thermodynamic model for melt, it is the only high-*T* clinopyroxene model available. Similarly, the high-*T* hornblende model is from Green *et al*. (2016). The original thermodynamic model for haplogranite melt was formally calibrated up to only 1.0 GPa (Holland & Powell, 2001). Extrapolation of the thermodynamic model for melt to very high pressures may introduce errors, so we have limited the pressure range of the *P–T* pseudosection to < 1.5 GPa, which is lower that the fluid-absent solidus for phengite breakdown. Phase abbreviations in Fig. 13 follow Whitney & Evans (2010).

The fields appropriate to the development of the microstructures interpreted to record

591 phengite breakdown melting and melt crystallization (Fig. 4e–i), and replacement of
592 garnet by hornblende + plagioclase + opaque oxide (Fig. 4c) during decompression are
593 indicated by the heavy black lines. These fields all contain garnet, epidote, phengitic
594 white mica (Ms) and melt, and are bound to lower *T* by the H_2O-saturated solidus (Fig.
595 13). In Fig. 13, at higher *P*/lower *T* clinopyroxene (omphacite) is predicted and at higher
596 *T*/lower *P*, epidote is not calculated to be stable (at higher *T/P*) and rutile does not occur
597 at lower *T/P*.

598 The observed petrographic features constrain the retrograde *P–T* evolution of the
599 granite to this central swath in which both *P* and *T* decline, similar to the *P–T* path shown
600 by the white arrow (Fig. 13). The evidence of rutile included in phengite, titanite outside
601 of phengite and phengite breakdown, combined with the phase equilibria shown in Fig.
602 13, including the calculated isopleths for melt and phengite, suggests limited melt
603 production by reactions consuming phengite. Phengite breakdown likely began at $P > 1.5$
604 GPa, outside of the range of the calculations, and may have continued during cooling
605 along the upper pressure part of the white arrow, as suggested by crossing the mol% melt
606 isopleths,. However, along the exemplar *P–T* path the modeled amount of melt is small,
607 being ~3–4 mol% from 1.5 to 1.1 GPa, before decreasing to the solidus; the predicted
608 amount of phengite decreases by a few mol.% from 1.5 GPa to the solidus. The final
609 subsolidus phase assemblage of Grt + Bt + Ep + Ms + Ttn + H_2O (+ Qz + Pl + Kfs) is
610 shown in bold in Fig. 13. Thus, the best estimate for final equilibration of the granite in
611 the composite veins, assuming H_2O saturation was attained, is 0.7–1.1 GPa at T <670 °C

612 (Fig. 13).

613

614 # DISCUSSION

615

616 **Age and nature of the protoliths at General's Hill**

617 The cores of zircons in the eclogite show weak oscillatory, patchy or planar zoning,
618 variable but high Th/U and low Hf/Y ratios, and steep HREE patterns with negative Eu
619 anomalies. These features all point to a magmatic origin, indicating that the cores were
620 inherited from the protolith of the eclogite (Hoskin & Ireland, 2000; Wu & Zheng, 2004).
621 The cores yield $^{206}Pb/^{238}U$ dates from *c*. 780 to *c*. 400 Ma, suggesting various degrees of
622 solid-state recrystallization (e.g. Zheng *et al*., 2004; Xia *et al*., 2009). The oldest
623 $^{206}Pb/^{238}U$ dates of 778 ± 9 Ma and 776 ± 9 Ma, respectively, from the two samples are
624 concordant and are consistent with the extensively reported protolith ages of *c.* 780–750
625 Ma for UHP metamorphic rocks in the Sulu belt (e.g. Zheng et al., 2005, 2006, 2009).
626 Based on these results, we interpret the crystallization age of the protolith of the eclogite
627 to be *c.* 780 Ma.

628 Solid-state recrystallization of zircon should not disturb the original magmatic Lu–Hf
629 isotope signature (Zheng *et al*., 2005; Xia *et al*., 2009; Chen *et al*., 2010), so we may use
630 the initial Hf isotope systematics of the zircon cores to characterize the protolith. The
631 eclogites are basaltic in composition and the zircon cores have negative $\varepsilon_{Hf}(t_1)$ values of
632 -16.1 to -4.3, corresponding to T_{DM1} ages of 1980–1500 Ma. The enriched signature

633 suggests that ancient lithospheric mantle was involved in the source of the magmas
634 (Zheng *et al*., 2006, 2009; Chen *et al*., 2014). This interpretation is reinforced by the O
635 isotope composition of the zircon cores, which yield $\delta^{18}O$ values of 5.61–6.82 ‰ that are
636 higher than the normal mantle zircon value of 5.3 ± 0.3 ‰ (Valley *et al*., 1998, 2005).
637 Thus, we conclude that the protolith magmas were derived from enriched mantle,
638 possibly as old as Paleoproterozoic.

639 The cores of zircons in the gneiss exhibit similar features to those of the eclogites
640 and also indicate a magmatic origin. The cores yield variable $^{206}Pb/^{238}U$ dates from *c*. 780
641 to *c*. 255 Ma, suggesting various degrees of Pb loss, whereas the least recrystallized
642 zircons in the two gneisses give weighted mean ages of 762 ± 9 Ma and 779 ± 6 Ma,
643 respectively. Thus, the crystallization age of the protolith of the gneiss is similar to the
644 eclogite.

645 The gneisses are granitic in composition, enriched in LREE with flat HREE patterns,
646 and depleted in Nb, Ta, Sr but enriched in Th, U and Pb. These features resemble those of
647 rocks from more extensive outcrops of granitic gneiss elsewhere in the Sulu belt (Tang *et*
648 *al*., 2008; Zong *et al.,* 2010; Xu *et al*., 2013), suggesting the protolith of the gneiss at
649 General's Hill was similar throughout the belt. Furthermore, the $\delta^{18}O$ values of 5.82–
650 6.67 ‰ from the zircon cores are inconsistent with a metasedimentary protolith
651 [$\delta^{18}O$(WR) = 10–20 ‰; Eiler, 2001] or with granite derived from a metasedimentary
652 source [$\delta^{18}O$(Zircon) >8 ‰, considering the fractionation of $\Delta^{18}O$(Zircon–WR) of ~-2 ‰
653 for granite; O'Neil & Chappell, 1977; Valley *et al*., 2005].

654 The zircon cores from the gneiss have a limited range of $\varepsilon_{Hf}(t_1)$ values of -18.0 to
655 -12.4 at 780 Ma, corresponding to T_{DM2} ages of 2801–2451 Ma (6 of 8 are >2500 Ma).
656 This indicates that the protolith originated from a predominantly Neoarchean crustal
657 source. Thus, the protoliths of the eclogites and gneisses were probably generated
658 contemporaneously during an episode of bimodal magmatism along the periphery of the
659 Yangtze Craton at *c.* 780 Ma, most likely as a response to the breakup of the
660 supercontinent Rodinia (e.g. Li *et al*., 2003; Zheng *et al*., 2004, 2006, 2007).
661 In the composite veins, zircon cores from both granite and vein quartz exhibit
662 well-developed zoning, have $^{206}Pb/^{238}U$ dates varying from *c*. 790 to *c*. 330 Ma and *c*. 790
663 to *c*. 280 Ma, respectively, with corresponding $\varepsilon_{Hf}(t_1)$ values ranging from -16.5 to -8.5
664 and -16.9 to -4.0, and $\delta^{18}O$ values of 5.47–6.51 ‰ and 5.46–6.67 ‰. These features
665 resemble those of the inherited zircon cores from the host eclogite and the surrounding
666 gneiss. Similar inherited magmatic zircon cores are commonly recognized in HP–UHP
667 veins from elsewhere in the Dabie–Sulu orogen (e.g. Zong *et al*., 2010; Chen *et al*., 2012;
668 Sheng *et al*., 2012), where they have been interpreted as xenocrysts transported by melt
669 and/or aqueous fluid. We interpret the zircon cores in the composite veins to have been
670 derived in a similar manner.
671
672 **Fluid flow at General's Hill**
673 *Timing of fluid flow*
674 Resorption and new growth of zircon generally reflect the presence of fluids during

675 metamorphism (Corfu *et al*., 2003; Rubatto & Hermann, 2003; Li *et al*., 2004; Wu *et al*.,
676 2006). Thus, new zircon growth in the composite veins, the host eclogite and the
677 surrounding gneiss likely records important information concerning the timing and source
678 of fluids responsible for vein formation (Hoskin, 2005; Wu *et al*., 2009).

679 Overgrowth rims on inherited cores and new grains of zircon in both the granite and
680 vein quartz in the composite veins are euhedral, exhibit homogeneous moderate
681 luminescence in CL images and have sharp boundaries against the cores. This zircon
682 consistently has lower Th/U (mostly <0.1) and $^{176}Lu/^{177}Hf$ ratios but variably higher
683 $^{176}Hf/^{177}Hf$ compared to the cores, implying that the new zircon grew in association with
684 the attending fluid and was not simply recrystallized *in situ* (Zheng *et al*., 2005; Xia *et al*.,
685 2009; Chen *et al*., 2010). The new zircon from both the granite and vein quartz has low
686 HREE contents with high Hf/Y ratios, and shows shallowly sloping to relatively flat
687 HREE patterns with weakly negative (granite) to moderately positive (vein quartz) Eu
688 anomalies. These features suggest that the new zircon grew in the presence of garnet but
689 not feldspar, consistent with crystallization under eclogite facies conditions (Rubatto,
690 2002; Rubatto & Hermann, 2003, 2007; Whitehouse & Platt, 2003). Moreover, when
691 compared to the magmatic zircon cores, the consistently low $^{176}Lu/^{177}Hf$ but variably high
692 $^{176}Hf/^{177}Hf$ ratios of all the new zircons also indicate co-precipitation with garnet (Zheng
693 *et al*., 2005), consistent with the presence of garnet in the granite.

694 The new zircon from both granite and vein quartz yields weighted mean $^{206}Pb/^{238}U$
695 ages of 222–220 Ma, identical within uncertainty. Because this zircon crystallized from

the fluids that precipitated the composite veins, the ages are interpreted as registering the timing of an episode of fluid flow at *c.* 221 Ma. The age is younger than the peak UHP coesite eclogite facies metamorphism in the Sulu belt, which occurred between *c*. 235 Ma and *c*. 225 Ma, but is synchronous with the HP quartz eclogite facies recrystallization at *c.* 225 to *c*. 215 Ma (Liu *et al*., 2006; Zhao *et al*., 2006; Liu & Liou, 2011). Therefore, the fluid event recorded by these ages is inferred to have occurred during exhumation of the Sulu belt from coesite eclogite to quartz eclogite facies conditions.

The new zircon from the host eclogites and surrounding gneisses yields weighted mean $^{206}Pb/^{238}U$ ages of 223–217 Ma that are identical within uncertainty, and consistent with the age of *c.* 221 Ma obtained from the composite veins, implying that fluid was present in the eclogite and gneiss contemporaneously with that forming the veins. This zircon also has contrasting trace element and Lu–Hf isotope compositions compared to the magmatic cores, consistent with growth related to Triassic metamorphism.

The source of the fluid

Multiple studies have documented that robust isotope systems are credible in determining the source of fluids attending metamorphism, which is essential to constrain the length scale of fluid flow during subduction and exhumation and the formation of HP–UHP vein systems (e.g. Philippot & Selverstone, 1991; Scambelluri & Philippot, 2001; Verlaguet *et al*., 2011; Liu *et al*., 2014; Zhao *et al*., 2016). The range of initial $^{176}Hf/^{177}Hf$ ratios and the mean $\varepsilon Hf(t_2)$ values of the new zircon in both components of the composite vein are consistent at $t_2 = 221$ Ma, and lie between values recorded by new zircon in the host

717 eclogite and the surrounding gneiss (Figs 10 & 11). This observation suggests that zircon
718 in the composite veins crystallized from a fluid intermediate in composition between the
719 fluid expected to have been in equilibrium with eclogite and that in equilibrium with
720 gneiss. From this inference we conclude that the composite veins were precipitated from
721 a blended fluid derived by mixing of fluids derived from the eclogite and gneiss, rather
722 than from an exotic fluid, which implies that fluid flow was restricted within the exhumed
723 continental crust.

724 In addition, the εHf(t_2) values of the new zircon from the composite veins show an
725 approximately negative linear relationship with the corresponding $^{176}Lu/^{177}Hf$ ratios (Fig.
726 S8), with the lowest $^{176}Lu/^{177}Hf$ and the highest εHf(t_2) values similar to those of the host
727 eclogite, and the highest $^{176}Lu/^{177}Hf$ and the lowest εHf(t_2) values approaching those of
728 the surrounding gneiss. This relationship supports the intepretation that the zircon, and by
729 implication the composite veins, was precipitated from a hybrid fluid, with one end
730 member being in equilibrium with the eclogite with low $^{176}Lu/^{177}Hf$ ratios but high εHf(t_2)
731 values and the other end member being in equilibrium with the gneiss with high
732 $^{176}Lu/^{177}Hf$ but low εHf(t_2) values.

733 The whole-rock Nd and zircon O isotope compositions are fully consistent with this
734 conclusion. The granite in the composite veins shows variable εNd(t) values between
735 -15.6 and -21.9 at 221 Ma, spanning the range from those of the eclogite to those the
736 gneiss (Fig. 7). Further, new zircon from both components of the composite vein yields
737 consistent $\delta^{18}O$ values of 5.25–5.98 ‰ and 5.19–6.06 ‰, respectively, which are

738 indistinguishable from those of the eclogite ($\delta^{18}O$ values of 5.33 ‰–5.93 ‰) and the
739 gneiss ($\delta^{18}O$ values of 5.30–6.29 ‰; Fig. 12).

740 The new zircon from all samples in this study consistently shows positive $\delta^{18}O$
741 values that are similar to or slightly lower than the corresponding core domains (Fig. 12).
742 However, these values do not match the large-scale O isotope depletion signature for
743 igneous and metamorphic zircon from other UHP metamorphic rocks exposed in the Sulu
744 belt (e.g. Zheng *et al*., 2003, 2004; Tang *et al*., 2008; Chen *et al*., 2011b; He *et al*., 2016).
745 This difference implies that the gabbroic protoliths of the UHP eclogites at General's Hill
746 may have been emplaced deep enough in the crust to have escaped the high-temperature
747 meteoric–hydrothermal alteration that affected other rocks in the belt during the
748 Neoproterozoic.

749 In combination, these various lines of evidence suggest that the composite granite–
750 quartz veins were precipitated from a hybrid fluid derived by mixing of primary fluids
751 derived from eclogite and gneiss. The lack of a depleted O isotope signature requires that
752 the fluid be locally sourced as well as internally (rock) buffered.

753 *Constraints on the formation of the composite veins*

754 The *P–T* evolution of the central Sulu belt is summarized in Fig. 14. The prograde to peak
755 *P–T* path follows Wang S.J. *et al*. (2016; see also Wang L. *et al*., 2014); the estimated
756 peak UHP conditions were well in excess of the SCE for crustal compositions (Fig. 14).
757 The presence of intergranular coesite in eclogite and the relict igneous mineralogy of the
758 gabbro and gneiss at Yangkou only a few kilometers to the north of General's Hill (Liou

759 & Zhang, 1996; Wallis *et al*., 1997; Zhang & Liou, 1997), and the relict igneous textures
760 in the gneiss in this study indicate that at the metamorphic peak these rocks were very
761 likely fluid absent (cf. Mosenfelder *et al*., 2005; Young & Kylander-Clark, 2015).
762 Given this fluid absent condition at the metamorphic peak and the likelihood that
763 both eclogite and gneiss have similar total H_2O contents (Chen *et al*., 2011a), we infer
764 that during initial decompression H_2O was exsolved from NAMs in both the eclogite and
765 the gneiss to generate a grain-boundary solute-rich supercritical fluid (cf. Wang, S.J. *et al*.,
766 2016). We postulate that as this supercritical fluid increased in volume with continuing
767 decompression, it created a permeable, interconnected grain boundary network through
768 the solid infrastructure. The formation of this network enabled migration of the
769 supercritical fluid by diffuse porous flow (cf. Turcotte & Ahern, 1978). Initially, the
770 supercritical fluid likely maintained equilibrium with the host silicate mineral assemblage
771 via dissolution as it migrated through the grain boundary network to fractures. Once in
772 fractures, the fluid passed from one rock type to the other, resulting in blending of the
773 compositionally different supercritical fluids generated by exsolution of H_2O from the
774 NAMs in each rock type. This process led to development of the hybrid isotope
775 composition of the ascending fluid as it evolved down pressure to the critical curve.
776 The granite in the composite veins has high SiO_2, K_2O, moderate Al_2O_3 and low
777 Na_2O concentrations, and is enriched in LILE and LREE, but depleted in HFSE and
778 HREE, indicating that it was likely crystallized from a hydrous melt derived from a
779 crustal source (cf. Zheng & Hermann, 2014). However, when the mineralogy is compared

780 to leucosomes inferred to represent the crystallized products of hydrous melts derived
781 from crustal protoliths (e.g. Lang & Gilotti, 2007; Liu *et al*., 2010; Yakymchuk *et al*.,
782 2013; 2015; Wang *et al*., 2014), the granite in the composite veins has lower modal
783 feldspar and higher modal quartz, phengite and clinozoisite/epidote. In addition, the
784 Ti-in-zircon temperatures of ~820 ºC calculated at 2.5 GPa, based on the phengite
785 compositions, indicate that the granite crystallized at temperatures well above the wet
786 solidus at HP metamorphic conditions (Fig. 14).

787 For these reasons, we posit that the HP granite was precipitated from supercritical
788 fluid as it approached the critical curve, consistent with the *P–T* conditions calculated
789 based on phengite and new zircon from the granite, rather than from a hydrous melt
790 formed by phengite breakdown as proposed for other UHP localities (cf. Hermann *et al*.,
791 2013). We infer that HP granite was precipitated preferentially in the eclogite because the
792 supercritical fluid was not in thermodynamic equilibrium with it, whereas we take the
793 absence of composite granite–quartz veins in the surrounding gneiss to indicate that the
794 supercritical fluid was likely in equilibrium with the dominant rock type by volume.

795 By contrast, the vein quartz in the composite veins contains 99.10 wt% SiO_2, with
796 very low abundances of other oxides and all trace elements, consistent with precipitation
797 from an aqueous fluid (cf. Hermann *et al*., 2006). Thus, we interpret the vein quartz to
798 have precipitated after separation of the migrating supercritical fluid as it decompressed
799 through the critical curve around the transition from UHP to HP conditions. Continued
800 migration of hydrous melt and/or aqueous fluid at *P–T* conditions below the critical curve

led to extensive retrogression of the eclogite at General's Hill.

As our study demonstrates, exhumation is a highly dynamic process in which both solid and fluid compositions and proportions change with the evolving *P–T* conditions. Thus, the supercritical fluid generated by exsolution of H_2O from NAMs with decreasing pressure evolves by dissolution of the silicate mineral matrix, becoming increasingly solute-rich as it approaches the critical curve. Further, the supercritical fluid, once channelized in fractures, flowed faster than the rate of decompression of the host crust, perhaps preventing it from maintaining thermodynamic equilibrium with the subordinate eclogite.

Partial melting of the granite in the composite veins during ongoing exhumation of the continental crust

Partial melting during exhumation of UHP rocks has been widely proposed in several orogenic belts (see reviews by Hermann & Rubatto, 2014; Zheng & Hermann, 2014), where it is inferred to have been triggered mainly by breakdown of hydrous minerals, including phengite and zoisite (Skjerlie & Patiño Douce, 2002; Schmidt *et al*., 2004; Auzanneau *et al*., 2006; Hermann & Spandler, 2008; Liu *et al*., 2009).

Microstructural evidence in the granite from the composite veins—aggregates of biotite + plagioclase + K-feldspar at the edges of phengite and thin films, cuspate veinlets and patches of K-feldspar along grain boundaries (Fig. 4e–i)—are consistent with the former presence of an intergranular melt (Sawyer, 1999; Holness *et al*., 2011; Vernon,

2011). Consequently, we interpret K-feldspar in the granite to be largely a product of low volume partial melting due to phengite breakdown. Similar microstructures are also present in the gneiss (Fig. 5f). These features suggest that during exhumation from HP eclogite to amphibolite facies conditions (Fig. 14), minor phengite-breakdown melting occurred in both the granite and the gneiss. The microstructures are consistent with the sequence of phase assemblage fields in the *P–T* pseudosection calculated for the composition of the granite from a composite vein and discussed above (Fig. 13). Thus, we propose a low *P* retrograde *P–T* path similar to the exemplar white arrow (Fig. 13), with final melt crystallization recording conditions of 0.7–1.1 GPa and <670 °C.

Implications for multistage fluid interactions between continental crust and mantle in the subduction channel

Subduction zones are important sites for the exchange of mass and energy between the mantle and crust (e.g. Brown & Rushmer, 2006; Hermann *et al*., 2006; Mibe *et al*., 2011; Zheng, 2012). Although arc magmatism generally does not accompany continental subduction (Rumble *et al*., 2003; Zheng, 2012), the development of syn-exhumation and post-collisional magmatic rocks with distinct chemical signatures indicates that crust–mantle interactions nonetheless occur during continental subduction and exhumation (Guo *et al*., 2004; Yang *et al*., 2012; Zhao *et al*., 2012, 2013; Dai *et al*., 2015).

In this study, we have shown that composite granite–quartz veins formed during phase separation of supercritical fluid as it crossed the critical curve around the transition

from UHP to HP metamorphic conditions, and that the granite experienced minor phengite-breakdown melting during ongoing exhumation. This represents a rare natural example of the variety of fluids that could be transferred to the subduction channel to interact with the mantle wedge during exhumation of continental crust from UHP metamorphic conditions.

The importance of a crustal component in the mantle at UHP pressures is supported, for example, by information from majorite-hosted diamond-bearing multiphase solid inclusions in websterite from the island of Fjørtoft in the northernmost UHP terrane of the Western Gneiss Region of Norway (Table S1; van Roermund *et al*., 2002; Carswell & van Roermund, 2005; Malaspina *et al*., 2010). Here, the multiphase solid inclusions were interpreted to have precipitated from an oxidized supercritical fluid derived from the deeply subducted continental crust that infiltrated into the mantle wedge at depths ≥130 km.

CONCLUSIONS

This study of composite granite–quartz veins in eclogite provides new information that contributes to our growing understanding of the origin and evolution of supercritical fluid during exhumation of deeply subducted continental crust. We posit that eclogite and gneiss at General's Hill in the central Sulu belt were likely fluid absent at the peak of UHP metamorphism, and argue that a supercritical fluid was generated by exsolution of

H_2O stored in NAMs during exhumation from the peak UHP conditions. This fluid migrated by diffuse porous flow into fractures enabling it to pass from one fluid source to another. This conclusion is supported by a variety of isotope data that require the supercritical fluid to be a hybrid derived by mixing of fluids produced in both eclogite and gneiss.

As the blended supercritical fluid passed through the exhuming crust, it approached the critical curve, where it precipitated a HP silicate mineral assemblage corresponding to the granite in the composite veins preferentially in the eclogite with which it was not in thermodynamic equilibrium. By contrast, the vein quartz was precipitated from aqueous fluid after phase separation of the supercritical fluid as it crossed the critical curve. At *P*–*T* conditions below the critical curve, migration of hydrous melt and/or aqueous fluid led to extensive retrogression of the eclogite. Lastly, the granite in the composite veins and the surrounding gneisses experienced minor partial melting due to phengite breakdown during exhumation from HP eclogite to amphibolite facies *P*–*T* conditions.

The results of this study demonstrate that different fluid phases were available successively in continental crust undergoing exhumation after ultradeep subduction, changing from supercritical fluid at UHP conditions to coexisting hydrous melt and aqueous fluid at HP conditions, and then hydrous melt derived by hydrate-breakdown at lower pressures. This succession shows that the crustal component that may interact with the mantle at the slab–mantle interface evolves with changing *P*–*T* conditions. Thus, supercritical fluid is dominant at UHP conditions, whereas hydrous melts play the major

role at shallower depths in the subduction channel.

ACKNOWLEDGEMENTS

The first author is grateful to the China Scholarship Council for funding a 12-month PhD joint supervision at the University of Maryland, College Park (CSC No. 201506410003). This research was funded by the National Natural Science Foundation of China (Nos. 41272225, 41572182) and the Fundamental Research Funds for National University, China University of Geosciences, Wuhan (No. CUG–G1323511572); the WiscSIMS Laboratory is funded by the US National Science Foundation (EAR03-19230, EAR10-53466, EAR13-55590). We thank Y.S. Liu and Z.C. Hu for help with LA(MC)-ICP-MS analysis, H.H. Chen for help with whole-rock trace element analysis, L. Zhou for help with whole-rock Sr–Nd isotope analysis, J. Valley, J. Kern and A. Ishida for assistance with SIMS analysis, and B. Hess for sample preparation. We acknowledge Y.B. Wu, M. Tang and H. Yang for useful suggestions concerning interpretation of the geochemical data, two anonymous reviewers for insightful comments and Katy Evans for editorial handling.

REFERENCES

Auzanneau, E., Vielzeuf, D. & Schmidt, M.W., 2006. Experimental evidence of decompression melting during exhumation of subducted continental crust. *Contributions to Mineralogy and Petrology*, **152,** 125–148.

Bebout, G.E., 2014. Chemical and isotopic cycling in subduction zones. *Treatise on Geochemistry*, **4,** 703–747.

Bebout, G.E. & Penniston-Dorland, S.C., 2016. Fluid and mass transfer at subduction interfaces—The field metamorphic record. *Lithos*, **240,** 228–258.

Brown, M., 2014. The contribution of metamorphic petrology to understanding lithosphere evolution and geodynamics. *Geoscience Frontiers*, **5,** 553–569.

Brown, M. & Rushmer, T., 2006. Evolution and differentiation of the continental crust. Cambridge University Press.

Brown, M., Korhonen, F.J. & Siddoway, C.S., 2011. Organizing melt flow through the crust. *Elements*, **7,** 261–266.

Caddick, M.J. & Thompson, A.B., 2008. Quantifying the tectono-metamorphic evolution of pelitic rocks from a wide range of tectonic settings: mineral compositions in equilibrium. Contributions to Mineralogy and Petrology, **156,** 177–195.

Carswell, D.A. & van Roermund, H.L., 2005. On multi-phase mineral inclusions associated with microdiamond formation in mantle-derived peridotite lens at Bardane on Fjørtoft, west Norway. *European Journa of Mineralogy*, **17,** 31–42.

Chen, B., Ye, K. & Liu, J., 2002. Cogenetic relationship of the Yangkou gabbro-to-granite unit, Su-Lu terrane, eastern China, and implications for UHP metamorphism. *Journal of the Geological Society*, **159,** 457–467.

Chen, R.X., Zheng, Y.F. & Xie, L., 2010. Metamorphic growth and recrystallization of zircon: distinction by simultaneous in-situ analyses of trace elements, U–Th–Pb and Lu–Hf isotopes in zircons from eclogite-facies rocks in the Sulu orogen. *Lithos*, **114,** 132–154.

Chen, R.X., Zheng, Y.F. & Gong, B., 2011a. Mineral hydrogen isotopes and water contents in ultrahigh-pressure metabasite and metagranite: constraints on fluid flow during continental subduction-zone metamorphism. *Chemical Geology*, **281,** 103–124.

Chen, Y.X., Zheng, Y.F., Chen, R.X. *et al.,* 2011b. Metamorphic growth and recrystallization of zircons in extremely ^{18}O-depleted rocks during eclogite-facies metamorphism: evidence from U–Pb ages, trace elements, and O–Hf isotopes. *Geochimica et Cosmochimica Acta*, **75,** 4877–4898.

Chen, R.X., Zheng, Y.F. & Hu, Z.C., 2012. Episodic fluid action during exhumation of deeply subducted continental crust: geochemical constraints from zoisite–quartz vein and host metabasite in the Dabie orogen. *Lithos*, **155,** 146–166.

Chen, Y.X., Zheng, Y.F. & Hu, Z.C., 2013. Petrological and zircon evidence for anatexis of UHP quartzite during continental collision in the Sulu orogen. *Journal of Metamorphic Geology*, **31,** 389–413.

Chen, Y.X., Zheng, Y.F., Li, L. & Chen, R.X., 2014. Fluid-rock interaction and geochemical transport during protolith emplacement and continental collision: A tale from Qinglongshan ultrahigh-pressure

metamorphic rocks in the Sulu orogen. *American Journal of Sciences*, **314,** 357–399.
Cherniak, D.J. & Watson, E.B., 2007. Ti diffusion in zircon. *Chemical Geology*, **242**, 473–483.
Corfu, F., Hanchar, J.M., Hoskin, P.W. & Kinny, P., 2003. Atlas of zircon textures. *Reviews in mineralogy and Geochemistry*, **53,** 469–500.
Dai, L.Q., Zhao, Z.F., Zheng, Y.F. & Zhang, J., 2015. Source and magma mixing processes in continental subduction factory: Geochemical evidence from postcollisional mafic igneous rocks in the Dabie orogen. *Geochemistry, Geophysics, Geosystems*, **16,** 659–680.
Eiler, J.M., 2001. Oxygen isotope variations of basaltic lavas and upper mantle rocks. *Reviews in mineralogy and Geochemistry*, **43,** 319–364.
Ernst, W., Tsujimori, T., Zhang, R.Y. & Liou, J.G., 2007. Permo-Triassic collision, subduction-zone metamorphism, and tectonic exhumation along the East Asian continental margin. *Annual Review of Earth and Planetary Sciences*, **35,** 73–110.
Ferrando, S., Frezzotti, M., Dallai, L. & Compagnoni, R., 2005. Multiphase solid inclusions in UHP rocks (Su-Lu, China): remnants of supercritical silicate-rich aqueous fluids released during continental subduction. *Chemical Geology*, **223,** 68–81.
Ferrando, S., Frezzotti, M.L., Petrelli, M. & Compagnoni, R., 2009. Metasomatism of continental crust during subduction: the UHP whiteschists from the Southern Dora-Maira Massif (Italian Western Alps). *Journal of Metamorphic Geology*, **27,** 739–756.
Ferrero, S., Wunder, B., Walczak, K., O'Brien, P.J. & Ziemann, M.A., 2015. Preserved near ultrahigh-pressure melt from continental crust subducted to mantle depths. *Geology*, **43(5),** 447–450.
Ferry, J.M. & Watson, E.B., 2007. New thermodynamic models and revised calibrations for the Ti-in-zircon and Zr-in-rutile thermometers. *Contributions to Mineralogy and Petrology*, **154,** 429–437.
Frezzotti, M.L. & Ferrando, S., 2015. The chemical behavior of fluids released during deep subduction based on fluid inclusions. *American Mineralogist*, **100,** 352–377.
Frezzotti, M.L., Ferrando, S., Dallai, L. & Compagnoni, R., 2007. Intermediate alkali–alumino-silicate aqueous solutions released by deeply subducted continental crust: fluid evolution in UHP OH-Rich topaz–kyanite quartzites from Donghai (Sulu, China). *Journal of Petrology*, **48,** 1219–1241.
Gao, J. & Klemd, R., 2001. Primary fluids entrapped at blueschist to eclogite transition: evidence from the Tianshan meta-subduction complex in northwestern China. *Contributions to Mineralogy and Petrology*, **142,** 1–14.
Gao, X.Y., Zheng, Y.F., Xia, X.P. & Chen, Y.X., 2014. U–Pb ages and trace elements of metamorphic rutile from ultrahigh-pressure quartzite in the Sulu orogen. *Geochimica et Cosmochimica Acta*, **143,** 87–114.
Gerya, T. & Meilick, F., 2011. Geodynamic regimes of subduction under an active margin: effects of rheological weakening by fluids and melts. *Journal of Metamorphic Geology*, **29,** 7–31.
Green, E. C. R., White, R. W., Diener, J. F. A., Powell, R. & Holland, T. J. B. (2016). Activity–composition relations for the calculation of partial melting equilibria in metabasic rocks. *Journal of Metamorphic Geology*, **34**, 845–869.
Guo, F., Fan, W., Wang, Y. & Zhang, M., 2004. Origin of early Cretaceous calc-alkaline lamprophyres from the Sulu orogen in eastern China: implications for enrichment processes beneath continental collisional belt. *Lithos*, **78,** 291–305.
Guo, S., Chen, Y., Ye, K. *et al.,* 2015. Formation of multiple high-pressure veins in ultrahigh-pressure

eclogite (Hualiangting, Dabie terrane, China): Fluid source, element transfer, and closed-system metamorphic veining. *Chemical Geology*, **417,** 238–260.

Hack, A.C., Thompson, A.B. & Aerts, M., 2007. Phase relations involving hydrous silicate melts, aqueous fluids, and minerals. *Reviews in Mineralogy and Geochemistry*, **65,** 129–185.

Hacker, B.R., Ratschbacher, L., Webb, L. *et al.,* 2000. Exhumation of ultrahigh-pressure continental crust in east central China: Late Triassic–Early Jurassic tectonic unroofing. *Journal of Geophysical Research: Solid Earth*, **105,** 13339–13364.

Hayden, L.A. & Watson, E.B., 2007. Rutile saturation in hydrous siliceous melts and its bearing on Ti-thermometry of quartz and zircon. *Earth and Planetary Science Letters*, **258**, 561–568.

Hayden, L.A. & Manning, C.E., 2011. Rutile solubility in supercritical $NaAlSi_3O_8$–H_2O fluids. *Chemical Geology*, **284,** 74–81.

He, Q., Zhang, S.B. & Zheng, Y.F., 2016. High temperature glacial meltwater-rock reaction in the Neoproterozoic: evidence from zircon in-situ oxygen isotopes in granitic gneiss from the Sulu orogen. *Precambrian Research*, **284,** 1–13.

Hermann, J., 2002. Experimental constraints on phase relations in subducted continental crust. *Contributions to Mineralogy and Petrology*, **143,** 219–235.

Hermann, J. & Spandler, C.J., 2008. Sediment melts at sub-arc depths: an experimental study. *Journal of Petrology*, **49,** 717–740.

Hermann, J. & Rubatto, D., 2014. Subduction of continental crust to mantle depth: geochemistry of ultrahigh-pressure rocks. *Treatise on Geochemistry*, **4,** 309–340.

Hermann, J., Spandler, C., Hack, A. & Korsakov, A.V., 2006. Aqueous fluids and hydrous melts in high-pressure and ultra-high pressure rocks: implications for element transfer in subduction zones. *Lithos*, **92,** 399–417.

Hermann, J., Zheng, Y.F. & Rubatto, D., 2013. Deep fluids in subducted continental crust. *Elements*, **9,** 281–287.

Holland, T. & Powell, R., 2001. Calculation of phase relations involving haplogranitic melts using an internally consistent thermodynamic dataset. *Journal of Petrology*, **42**, 673–683.

Holland, T.J.B. & Powell, R., 2011. An improved and extended internally consistent thermodynamic dataset for phases of petrological interest, involving a new equation of state for solids. *Journal of Metamorphic Geology*, **29**, 333–383.

Holness, M.B., Cesare, B. & Sawyer, E.W., 2011. Melted rocks under the microscope: microstructures and their interpretation. *Elements*, **7,** 247–252.

Holtz, F., Becker, A., Freise, M. & Johannes, W., 2001. The water-undersaturated and dry Qz-Ab-Or system revisited. Experimental results at very low water activities and geological implications. *Contributions to Mineralogy and Petrology*, **141,** 347–357.

Hoskin, P.W., 2005. Trace-element composition of hydrothermal zircon and the alteration of Hadean zircon from the Jack Hills, Australia. *Geochimica et Cosmochimica Acta*, **69,** 637–648.

Hoskin, P.W. & Ireland, T.R., 2000. Rare earth element chemistry of zircon and its use as a provenance indicator. *Geology*, **28,** 627–630.

Kawamoto, T., Kanzaki, M., Mibe, K., Matsukage, K.N. & Ono, S., 2012. Separation of supercritical slab-fluids to form aqueous fluid and melt components in subduction zone magmatism. *Proceedings of*

1024 *the National Academy of Sciences*, **109,** 18695–18700.
1025 Kawamoto, T., Mibe, K., Bureau, H. *et al*., 2014. Large-ion lithophile elements delivered by saline fluids to
1026 the sub-arc mantle. *Earth, Planets and Space*, **66,** 1–11.
1027 Kessel, R., Schmidt, M.W., Ulmer, P. & Pettke, T., 2005. Trace element signature of subduction-zone fluids,
1028 melts and supercritical liquids at 120–180 km depth. *Nature*, **437,** 724–727.
1029 Labrousse, L., Prouteau, G. & Ganzhorn, A.C., 2011. Continental exhumation triggered by partial melting
1030 at ultrahigh pressure. *Geology*, **39,** 1171–1174.
1031 Labrousse, L., Duretz, T. & Gerya, T., 2015. H_2O-fluid-saturated melting of subducted continental crust
1032 facilitates exhumation of ultrahigh-pressure rocks in continental subduction zones. *Earth and Planetary*
1033 *Science Letters*, **428,** 151–161.
1034 Lang, H. & Gilotti, J., 2007. Partial melting of metapelites at ultrahigh-pressure conditions, Greenland
1035 Caledonides. *Journal of Metamorphic Geology*, **25,** 129–147.
1036 Li, X.P., Zheng, Y.F., Wu, Y.B., Chen, F., Gong, B. & Li, Y.L., 2004. Low-T eclogite in the Dabie terrane of
1037 China: petrological and isotopic constraints on fluid activity and radiometric dating. *Contributions to*
1038 *Mineralogy and Petrology*, **148,** 443–470.
1039 Li, Z.X., Li, X., Kinny, P., Wang, J., Zhang, S. & Zhou, H., 2003. Geochronology of Neoproterozoic
1040 syn-rift magmatism in the Yangtze Craton, South China and correlations with other continents: evidence
1041 for a mantle superplume that broke up Rodinia. *Precambrian Research*, **122,** 85–109.
1042 Liou, J.G. & Zhang, R.Y., 1996. Occurrences of intergranular coesite in ultrahigh-P rocks from the Sulu
1043 region, eastern China: implications for lack of fluid during exhumation. *American Mineralogist*, **81**,
1044 1217–1221.
1045 Liou, J.G., Ernst, W., Zhang, R., Tsujimori, T. & Jahn, B., 2009. Ultrahigh-pressure minerals and
1046 metamorphic terranes–the view from China. *Journal of Asian Earth Sciences*, **35,** 199–231.
1047 Liou, J.G., Zhang, R.Y., Liu, F.L., Zhang, Z.M. & Ernst, W.G., 2012. Mineralogy, petrology, U–Pb
1048 geochronology, and geologic evolution of the Dabie-Sulu classic ultrahigh-pressure metamorphic
1049 terrane, East–Central China. *American Mineralogist*, **97,** 1533–1543.
1050 Liu, F.L. & Liou, J.G., 2011. Zircon as the best mineral for P–T–time history of UHP metamorphism: a
1051 review on mineral inclusions and U–Pb SHRIMP ages of zircons from the Dabie–Sulu UHP rocks.
1052 *Journal of Asian Earth Sciences*, **40,** 1–39.
1053 Liu, F.L., Xu, Z.Q. & Liou, J.G., 2004. Tracing the boundary between UHP and HP metamorphic belts in
1054 the southwestern Sulu terrane, eastern China: evidence from mineral inclusions in zircons from
1055 metamorphic rocks. *International Geological Review*, **46,** 409–425.
1056 Liu, D.Y., Jian, P., Kröner, A. & Xu, S.T., 2006. Dating of prograde metamorphic events deciphered from
1057 episodic zircon growth in rocks of the Dabie–Sulu UHP complex, China. *Earth and Planetary Science*
1058 *Letters*, **250,** 650–666.
1059 Liu, F.L., Gerdes, A., Liou, J.G., Xue, H.M. & Liang, F.H., 2006. SHRIMP U-Pb zircon dating from
1060 Sulu-Dabie dolomitic marble, eastern China: Constrains on prograde, ultrahigh-pressure and retrograde
1061 metamorphic ages. *Journal of Metamorphic Geology*, **24,** 569–589.
1062 Liu, Q., Jin, Z.M. & Zhang, J.F., 2009. An experimental study of dehydration melting of phengite-bearing
1063 eclogite at 1.5–3.0 GPa. *Chinese Science Bulletin*, **54,** 2090–2100.
1064 Liu, F.L., Robinson, P.T., Gerdes, A. *et al.,* 2010. Zircon U–Pb ages, REE concentrations and Hf isotope

compositions of granitic leucosome and pegmatite from the north Sulu UHP terrane in China: constraints on the timing and nature of partial melting. *Lithos*, **117,** 247–268.

Liu, X.C., Wu, Y.B., Gao, S. *et al.,* 2014. Record of multiple stage channelized fluid and melt activities in deeply subducted slab from zircon U–Pb age and Hf–O isotope compositions. *Geochimica et Cosmochimica Acta*, **144,** 1–24.

Malaspina, N., Scambelluri, M., Poli, S., Van Roermund, H.L.M. & Langenhorst, F., 2010. The oxidation state of mantle wedge majoritic garnet websterites metasomatised by C-bearing subduction fluids. *Earth and Planetary Science Letters*, **298,** 417–426.

Manning, C.E., 2004. The chemistry of subduction-zone fluids. *Earth and Planetary Science Letters*, **223,** 1–16.

Martin, C. & Duchêne, S., 2015. Residual water in hydrous minerals as a kinetic factor for omphacite destabilization into symplectite in the eclogites of Vårdalsneset (WGR, Norway). *Lithos*, **232,** 162–173.

Mibe, K., Kawamoto, T., Matsukage, K.N., Fei, Y. & Ono, S., 2011. Slab melting versus slab dehydration in subduction-zone magmatism. *Proceedings of the National Academy of Sciences*, **108,** 8177–8182.

Mosenfelder, J.L., Schertl, H.P., Smyth, J.R. & Liou, J.G., 2005. Factors in the preservation of coesite: The importance of fluid infiltration. *American Mineralogist*, **90,** 779–789.

Naemura, K., Hirajima, T. & Svojtka, M., 2009. The pressure–temperature path and the origin of phlogopite in spinel–garnet peridotites from the Blanský Les Massif of the Moldanubian Zone, Czech Republic. *Journal of Petrology*, **50,** 1795–1827.

O'Neil, J. & Chappell, B., 1977. Oxygen and hydrogen isotope relations in the Berridale batholith. *Journal of the Geological Society*, **133,** 559–571.

Philippot, P. & Selverstone, J., 1991. Trace-element-rich brines in eclogitic veins: implications for fluid composition and transport during subduction. *Contributions to Mineralogy and Petrology*, **106,** 417−430.

Powell, R. & Holland, T. J. B., 1988. An internally consistent dataset with uncertainties and correlations: 3. Applications to geobarometry, worked examples and a computer program. *Journal of metamorphic Geology*, **6(2),** 173−204.

Rosenberg, C.L. & Handy, M.R., 2005. Experimental deformation of partially melted granite revisited: implications for the continental crust. Journal of Metamorphic Geology, **23,** 19−28.

Rubatto, D., 2002. Zircon trace element geochemistry: partitioning with garnet and the link between U–Pb ages and metamorphism. *Chemical Geology*, **184,** 123−138.

Rubatto, D. & Hermann, J., 2003. Zircon formation during fluid circulation in eclogites (Monviso, Western Alps): implications for Zr and Hf budget in subduction zones. *Geochimica et Cosmochimica Acta*, **67,** 2173−2187.

Rubatto, D. & Hermann, J., 2007. Zircon behaviour in deeply subducted rocks. *Elements*, **3,** 31−35.

Rumble, D., Liou, J.G. & Jahn, B.M., 2003. Continental crust subduction and ultrahigh pressure metamorphism. *Treatise on Geochemistry*, **3,** 293−319.

Sawyer, E., 1999. Criteria for the recognition of partial melting. *Physics and Chemistry of the Earth, Part A: Solid Earth and Geodesy*, **24,** 269−279.

Scambelluri, M. & Philippot, P., 2001. Deep fluids in subduction zones. *Lithos*, **55,** 213−227.

Scambelluri, M., Pettke, T. & Van Roermund, H., 2008. Majoritic garnets monitor deep subduction fluid

flow and mantle dynamics. *Geology*, **36,** 59−62.
Schertl, H.P. & O'Brien, P.J., 2013. Continental crust at mantle depths: key minerals and microstructures. *Elements*, **9,** 261−266.
Schmidt, M.W. & Poli, S., 2014. Devolatilization during subduction. The Crust, *Treatise on Geochemistry* (eds. HD Holland and KK Turekian, Second Edition), Elsevier-Pergamon, Oxford, **4,** 669−701.
Schmidt, M.W., Vielzeuf, D. & Auzanneau, E., 2004. Melting and dissolution of subducting crust at high pressures: the key role of white mica. *Earth and Planetary Science Letters*, **228,** 65−84.
Sheng, Y.M., Zheng, Y.F., Chen, R.X., Li, Q. & Dai, M., 2012. Fluid action on zircon growth and recrystallization during quartz veining within UHP eclogite: insights from U–Pb ages, O–Hf isotopes and trace elements. *Lithos*, **136,** 126−144.
Sheng, Y.M., Zheng, Y.F., Li, S.N. & Hu, Z., 2013. Element mobility during continental collision: insights from polymineralic metamorphic vein within UHP eclogite in the Dabie orogen. *Journal of Metamorphic Geology*, **31,** 221−241.
Sizova, E., Gerya, T. & Brown, M., 2012. Exhumation mechanisms of melt-bearing ultrahigh pressure crustal rocks during collision of spontaneously moving plates. *Journal of Metamorphic Geology*, **30,** 927−955.
Skjerlie, K.P. & Douce, A.E.P., 2002. The fluid-absent partial melting of a zoisite-bearing quartz eclogite from 1.0 to 3.2 GPa; Implications for melting in thickened continental crust and for subduction-zone processes. *Journal of Petrology*, **43,** 291−314.
Spandler, C. & Hermann, J., 2006. High-pressure veins in eclogite from New Caledonia and their significance for fluid migration in subduction zones. *Lithos*, **89,** 135−153.
Spandler, C. & Pirard, C., 2013. Element recycling from subducting slabs to arc crust: A review. *Lithos*, **170,** 208−223.
Spandler, C., Pettke, T. & Rubatto, D., 2011. Internal and external fluid sources for eclogite-facies veins in the Monviso meta-ophiolite, Western Alps: implications for fluid flow in subduction zones. *Journal of Petrology*, **52,** 1207−1236.
Stöckhert, B., Duyster, J., Trepmann, C. & Massonne, H.J., 2001. Microdiamond daughter crystals precipitated from supercritical COH+ silicate fluids included in garnet, Erzgebirge, Germany. *Geology*, **29,** 391−394.
Stöckhert, B., Trepmann, C. & Massonne, H.J., 2009. Decrepitated UHP fluid inclusions: about diverse phase assemblages and extreme decompression rates (Erzgebirge, Germany). *Journal of Metamorphic Geology*, **27,** 673−684.
Sun, S.S. & McDonough, W.F., 1989. Chemical and isotopic systematics of oceanic basalts: implications for mantle composition and processes. *Geological Society, London, Special Publications*, **42,** 313−345.
Tang, J., Zheng, Y.F., Gong, B. *et al.,* 2008. Extreme oxygen isotope signature of meteoric water in magmatic zircon from metagranite in the Sulu orogen, China: implications for Neoproterozoic rift magmatism. *Geochimica et Cosmochimica Acta*, **72,** 3139−3169.
Turcotte, D.L. & Ahern, J.L., 1978. A porous flow model for magma migration in the asthenosphere. *Journal of Geophysical Research*, **83(B2)**, 767–772.
Valley, J.W., Kinny, P.D., Schulze, D.J. & Spicuzza, M.J., 1998. Zircon megacrysts from kimberlite: oxygen isotope variability among mantle melts. *Contributions to Mineralogy and Petrology*, **133,** 1−11.

1147 Valley, J.W., Lackey, J., Cavosie, A. *et al.,* 2005. 4.4 billion years of crustal maturation: oxygen isotope
1148 ratios of magmatic zircon. *Contributions to Mineralogy and Petrology*, **150,** 561−580.
1149 van Roermund, H.L., Carswell, D.A., Drury, M.R. & Heijboer, T.C., 2002. Microdiamonds in a megacrystic
1150 garnet websterite pod from Bardane on the island of Fjørtoft, western Norway: evidence for diamond
1151 formation in mantle rocks during deep continental subduction. *Geology*, **30,** 959−962.
1152 Verlaguet, A., Goffé, B., Brunet, F. *et al.,* 2011. Metamorphic veining and mass transfer in a chemically
1153 closed system: a case study in Alpine metabauxites (western Vanoise). *Journal of Metamorphic Geology*,
1154 **29,** 275−300.
1155 Vernon, R., 2011. Microstructures of melt-bearing regional metamorphic rocks. *Geological Society of*
1156 *America Memoirs*, **207,** 1−11.
1157 Vrijmoed, J.C., Smith, D.C. & Van Roermund, H.L.M., 2008. Raman confirmation of microdiamond in the
1158 Svartberget Fe-Ti type garnet peridotite, Western Gneiss Region, Western Norway. *Terra Nova*, **20,**
1159 295−301.
1160 Wallis, S.R., Ishiwatari, A., Hirajima, T. *et al.,* 1997. Occurrence and field relationships of
1161 ultrahigh-pressure metagranitoid and coesite eclogite in the Su-Lu terrane, eastern China. *Journal of the*
1162 *Geological Society*, **154**, 45–54.
1163 Wang, L., Kusky, T.M. & Li, S.Z., 2010. Structural geometry of an exhumed UHP terrane in the eastern
1164 Sulu Orogen, China: implications for continental collisional processes. *Journal of Structural Geology*,
1165 **32,** 423−444.
1166 Wang, L., Kusky, T.M., Polat, A. *et al.,* 2014. Partial melting of deeply subducted eclogite from the Sulu
1167 orogen in China. *Nature Communications*, **5**.
1168 Wang, S.J., Wang, L., Brown, M. & Feng, P., 2016. Multi-stage barite crystallization in partially melted
1169 UHP eclogite from the Sulu belt, China. *American Mineralogist*, **101,** 564−579.
1170 Watson, E.B., Wark, D.A. & Thomas, J.B., 2006. Crystallization thermometers for zircon and rutile.
1171 *Contributions to Mineralogy and Petrology*, **151,** 413–433.
1172 White, R.W., Powell, R., Holland, T.J.B., Johnson, T.E. & Green, E.C.R., 2014a. New mineral
1173 activity-composition relations for thermodynamic calculations in metapelitic systems. *Journal of*
1174 *Metamorphic Geology*, **32**, 261–286.
1175 White, R.W., Powell, R. & Johnson, T.E., 2014b. The effect of Mn on mineral stability in metapelites
1176 revisited: new *a–x* relations for manganese-bearing minerals. *Journal of Metamorphic Geology*, **32**,
1177 809–828.
1178 Whitehouse, M.J. & Platt, J.P., 2003. Dating high-grade metamorphism−constraints from rare-earth
1179 elements in zircon and garnet. *Contributions to Mineralogy and Petrology*, **145,** 61−74.
1180 Whitney, D.L. & Evans, B.W., 2010. Abbreviations for names of rock-forming minerals. *American*
1181 *Mineralogist*, **95,** 185.
1182 Wu, Y.B. & Zheng, Y.F., 2004. Genesis of zircon and its constraints on interpretation of U−Pb age. *Chinese*
1183 *Science Bulletin*, **49,** 1554−1569.
1184 Wu, Y.B., Zheng, Y.F., Zhao, Z.F., Gong, B., Liu, X. & Wu, F.Y., 2006. U–Pb, Hf and O isotope evidence
1185 for two episodes of fluid-assisted zircon growth in marble-hosted eclogites from the Dabie orogen.
1186 *Geochimica et Cosmochimica Acta*, **70,** 3743−3761.
1187 Wu, Y.B., Gao, S., Zhang, H.F. *et al*., 2009. U−Pb age, trace-element, and Hf-isotope compositions of

zircon in a quartz vein from eclogite in the western Dabie Mountains: Constraints on fluid flow during early exhumation of ultrahigh-pressure rocks. *American Mineralogist*, **94,** 303−312.

Xia, Q.K., Sheng, Y.M., Yang, X.Z. & Yu, H.M., 2005. Heterogeneity of water in garnets from UHP eclogites, eastern Dabieshan, China. *Chemical Geology*, **224,** 237–246.

Xia, Q.X., Zheng, Y.F., Yuan, H. & Wu, F.Y., 2009. Contrasting Lu–Hf and U–Th–Pb isotope systematics between metamorphic growth and recrystallization of zircon from eclogite-facies metagranites in the Dabie orogen, China. *Lithos*, **112,** 477−496.

Xia, Q.X., Zheng, Y.F. & Hu, Z.C., 2010. Trace elements in zircon and coexisting minerals from low-T/UHP metagranite in the Dabie orogen: implications for action of supercritical fluid during continental subduction-zone metamorphism. *Lithos*, **114,** 385−412.

Xu, Z.Q., Wang, Q., Ji, S.C. *et al.,* 2006. Petrofabrics and seismic properties of garnet peridotite from the UHP Sulu terrane (China): implications for olivine deformation mechanism in a cold and dry subducting continental slab. *Tectonophysics*, **421,** 111−127.

Xu, H.J., Ye, K., Song, Y.R. *et al.,* 2013. Prograde metamorphism, decompressional partial melting and subsequent melt fractional crystallization in the Weihai migmatitic gneisses, Sulu UHP terrane, eastern China. *Chemical Geology*, **341,** 16−37.

Yakymchuk, C., Brown, M., Ivanic, T. & Korhonen, F., 2013. Leucosome distribution in migmatitic paragneisses and orthogneisses: A record of self-organized melt migration and entrapment in a heterogeneous partially-molten crust. *Tectonophysics*, **603,** 136−154.

Yakymchuk, C., Brown, M., Clark, C. *et al.,* 2015. Decoding polyphase migmatites using geochronology and phase equilibria modelling. *Journal of Metamorphic Geology*, **33,** 203−230.

Yang, Q.L., Zhao, Z.F. & Zheng, Y.F., 2012. Slab–mantle interaction in continental subduction channel: Geochemical evidence from Mesozoic gabbroic intrusives in southeastern North China. *Lithos*, **155,** 442−460.

Yardley, B.W.D. & Valley, J.W., 1997. The petrologic case for a dry lower crust. *Journal of Geophysical Research: Solid Earth*, **102**, 12173–12185.

Ye, K., Cong, B.L. & Ye, D.N., 2000a. The possible subduction of continental material to depths greater than 200 km. *Nature*. **407,** 734–736.

Ye, K., Yao, Y.P., Katayama, I., Cong, B.L., Wang, Q. & Maruyama, S., 2000b. Large areal extent of ultrahigh-pressure metamorphism in the Sulu ultrahigh-pressure terrane of East China: new implications from coesite and omphacite inclusions in zircon of granitic gneiss. *Lithos*, **52,** 157–164.

Young, D.J. & Kylander-Clark, A.R.C., 2015. Does continental crust transform during eclogite facies metamorphism? *Journal of Metamorphic Geology*, **33**, 331–357.

Zeng, L.S., Gao, L.E., Yu, J.J. & Hu, G.Y., 2011. SHRIMP zircon U/Pb dating on ultrahigh pressure rocks from Yangkou: Implications for the timing of partial melting in the Sulu UHP metamorphic belt. *Acta Petrologica Sinica*, **27,** 1085–1094. (In Chinese with English abstract)

Zhang, R.Y. & Liou, J.G., 1997. Partial transformation of gabbro to coesite-bearing eclogite from Yangkou, the Sulu terrane, eastern China. *Journal of Metamorphic Geology*, **15,** 183–202.

Zhang, R.Y., Liou, J.G. & Ernst, W., 1995. Ultrahigh-pressure metamorphism and decompressional P−T paths of eclogites and country rocks from Weihai, eastern China. *Island Arc*, **4,** 293−309.

Zhang, R.Y., Liou, J.G. & Ernst, W., 2009. The Dabie–Sulu continental collision zone: a comprehensive

review. *Gondwana Research*, **16,** 1−26.
Zhang, Z.M., Xiao, Y.L., Hoefs, J., Liou, J.G. & Simon, K., 2006. Ultrahigh pressure metamorphic rocks from the Chinese Continental Scientific Drilling Project: I. Petrology and geochemistry of the main hole (0–2,050 m). *Contributions to Mineralogy and Petrology*, **152,** 421−441.
Zhang, Z.M., Shen, K., Sun, W.D. *et al.,* 2008. Fluids in deeply subducted continental crust: petrology, mineral chemistry and fluid inclusion of UHP metamorphic veins from the Sulu orogen, eastern China. *Geochimica et Cosmochimica Acta*, **72,** 3200−3228.
Zhao, Z.F., Zheng, Y.F., Gao, T.S. *et al.,* 2006. Isotopic constraints on age and duration of fluid-assisted high-pressure eclogite-facies recrystallization during exhumation of deeply subducted continental crust in the Sulu orogen. *Journal of Metamorphic Geology*, **24,** 687–702.
Zhao, Z.F., Zheng, Y.F., Zhang, J. Dai, L.Q., Li, Q. & Liu, X., 2012. Syn-exhumation magmatism during continental collision: Evidence from alkaline intrusives of Triassic age in the Sulu orogen. *Chemical Geology*, **328,** 70–88.
Zhao, Z.F., Dai, L.Q. & Zheng, Y.F., 2013. Postcollisional mafic igneous rocks record crust-mantle interaction during continental deep subduction.*Scientific Reports*, **3**.
Zhao, Y.J., Wu, Y.B., Liu, X.C. *et al.,* 2016. Distinct zircon U–Pb and O–Hf–Nd–Sr isotopic behaviour during fluid flow in UHP metamorphic rocks: evidence from metamorphic veins and their host eclogite in the Sulu Orogen, China. *Journal of Metamorphic Geology*, **34,** 343–362.
Zheng, Y.F., 2009. Fluid regime in continental subduction zones: petrological insights from ultrahigh-pressure metamorphic rocks. *Journal of the Geological Society*, **166,** 763–782.
Zheng, Y.F., 2012. Metamorphic chemical geodynamics in continental subduction zones. *Chemical Geology*, **328,** 5–48.
Zheng, Y.F. & Hermann, J., 2014. Geochemistry of continental subduction-zone fluids. *Earth, Planets and Space*, **66,** 1–16.
Zheng, Y.F., Fu, B., Gong, B. & Li, L., 2003. Stable isotope geochemistry of ultrahigh pressure metamorphic rocks from the Dabie–Sulu orogen in China: implications for geodynamics and fluid regime. *Earth-Science Reviews*, **62,** 105–161.
Zheng, Y.F., Wu, Y.B., Chen, F.K., Gong, B., Li, L. & Zhao, Z.F., 2004. Zircon U–Pb and oxygen isotope evidence for a large-scale ^{18}O depletion event in igneous rocks during the Neoproterozoic. *Geochimica et Cosmochimica Acta*, **68,** 4145–4165.
Zheng, Y.F., Wu, Y.B., Zhao, Z.F., Zhang, S.B., Xu, P. & Wu, F.Y., 2005. Metamorphic effect on zircon Lu–Hf and U–Pb isotope systems in ultrahigh-pressure eclogite-facies metagranite and metabasite. *Earth and Planetary Science Letters*, **240,** 378–400.
Zheng, Y.F., Zhao, Z.F., Wu, Y.B., Zhang, S.B., Liu, X. & Wu, F.Y., 2006. Zircon U–Pb age, Hf and O isotope constraints on protolith origin of ultrahigh-pressure eclogite and gneiss in the Dabie orogen. *Chemical Geology*, **231,** 135–158.
Zheng, Y.F., Zhang, S.B., Zhao, Z.F. *et al.,* 2007. Contrasting zircon Hf and O isotopes in the two episodes of Neoproterozoic granitoids in South China: implications for growth and reworking of continental crust. *Lithos*, **96,** 127–150.
Zheng, Y.F., Chen, R.X. & Zhao, Z.F., 2009. Chemical geodynamics of continental subduction-zone metamorphism: insights from studies of the Chinese Continental Scientific Drilling (CCSD) core

samples. *Tectonophysics*, **475,** 327–358.
Zheng, Y.F., Xia, Q.X., Chen, R.X. & Gao, X.Y., 2011. Partial melting, fluid supercriticality and element mobility in ultrahigh-pressure metamorphic rocks during continental collision. *Earth-Science Reviews*, **107,** 342–374.
Zong, K.Q., Liu, Y.S., Hu, Z.C. *et al.,* 2010. Melting-induced fluid flow during exhumation of gneisses of the Sulu ultrahigh-pressure terrane. *Lithos*, **120,** 490–510.

SUPPORTING INFORMATION

Additional Supporting Information may be found in the online version of this article at the publisher's web site:

Appendix S1. Analytical methods.

Figure S1. (a) Metamorphic facies map of the Dabie–Sulu orogen in central–eastern China; (b) Simplified geological map of the General's Hill locality (after Wang *et al*., 2010).

Figure S2. (a) Major and (b) trace element compositions for the granite in the composite veins, the host eclogite and the surrounding gneiss at General's Hill. Major oxides and trace elements are plotted as weight percent and parts per million, respectively.

Figure S3. Cathodoluminescence images of representative zircon grains from one composite vein, the host eclogite and the surrounding gneiss. Circles mark the locations of LA(MC)-ICP-MS U–Pb (red) and Hf (light blue) isotope analyses.

Figure S4. Plots of Th *vs.* U and Th/U vs. REE contents for zircon from the host eclogites (a, b), the granite (c, d) and vein quartz (e, f) from the composite veins, and the surrounding gneisses (g, h).

1295 **Figure S5.** Box-and-whisker plots to show the Eu/Eu* ratios for overgrowth rims
1296 and/or new zircon grains from the granite and vein quartz in the composite veins, the host
1297 eclogites and the surrounding gneisses.

1298 **Figure S6.** $^{176}Hf/^{177}Hf$ ratios and $^{176}Lu/^{177}Hf$ ratios *vs.* U–Pb ages for zircon from the
1299 host eclogite (a, b), the granite (c, d) and vein quartz (e, f) of the composite vein, and the
1300 surrounding gneiss (g, h).

1301 **Figure S7.** Box-and-whisker plots for the granite in the composite veins to show: (a)
1302 the distribution of pressures calculated at *T* of 800 °C based on the Si-in-phengite
1303 barometer of Caddick & Thompson (2008, equation 8), and (b) the distribution of
1304 temperatures calculated at 2.5 GPa for overgrowth rims and/or new grains of zircon from
1305 the host eclogite, the composite veins, and the surrounding gneiss, based on the
1306 Ti-in-zircon thermometer of Ferry & Watson (2007).

1307 **Figure S8.** Covariation diagram of $^{176}Lu/^{177}Hf$ ratios *vs.* $\varepsilon Hf(t)$ values (corrected to *t*
1308 = 221 Ma) of overgrowth rims and new grains of zircon from the composite veins; (a)
1309 granite and (b) vein quartz.

1310 **Table S1.** Summary of published data on the characterization of supercritical fluids
1311 in subduction zones.

1312 **Table S2.** Sample numbers, lithology, GPS coordinates and mineral assemblages.

1313 **Table S3.** (a) Major element compositions of phengite in granite from the composite
1314 veins; (b) Major and trace element compositions of the granite and vein quartz from the
1315 composite veins, the host eclogite and the surrounding gneiss.

1316 **Table S4** Whole-rock Sr and Nd isotope compositions of the granite from the
1317 composite veins, the host eclogites and the surrounding gneisses.

1318 **Table S5.** LA-ICP-MS U–Th–Pb data for zircon from the host eclogites (a), the
1319 granite and vein quartz of the composite veins (b,c), and the surrounding gneisses (d).

1320 **Table S6.** LA-ICP-MS trace element compositions of zircon from the host eclogites
1321 (a), the granite (b) and vein quartz (c) from the composite veins, and the surrounding
1322 gneisses (d).

1323 **Table S7.** LA(MC)-ICP-MS Lu–Hf isotope compositions of zircon from the granite
1324 and vein quartz from the composite veins, the host eclogite and the surrounding gneiss.

1325 **Table S8.** *In situ* SIMS O isotope compositions of zircon from the granite and vein
1326 quartz from the composite veins, the host eclogite and the surrounding gneiss.

FIGURE CAPTIONS

Fig. 1. *P–T* phase diagram for silicate–H_2O systems. The wet solidus for calcium granite (Ca Gr; plagioclase An_{20}) terminates at the second critical endpoint (SCE); the approximate position of the critical curve is shown by the gray band. The finer gray lines are isopleths of wt% solute in the fluid phase (Hermann *et al*., 2006, 2013). The *P–T* fields for aqueous fluid, immiscible hydrous melt + aqueous fluid and supercritical fluid in equilibrium with silicate minerals are shown.

Fig. 2. Geological map of the coastal outcrop at General's Hill, with sample locations marked in solid circles, squares and stars representing composite granite–quartz veins, the host eclogite and the surrounding gneiss, respectively (detailed map based on the regional mapping of Wang *et al*., 2014). For location of the General's Hill outcrop in relation to the Sulu belt as a whole, see Fig. S1.

Fig. 3. Field occurrence of the composite granite–quartz veins at General's Hill, with locations of samples marked; the irregularly shaped composite veins are centimeter to decimeter in width within retrogressed eclogite.

Fig. 4. Representative photomicrographs to show the mineralogy and microstructures of the granite in the composite veins. (a–d) Images to show the main mineral assemblage of

Qz + Ph + Pl + Grt + Czo/Ep + Kfs (a, b, d in cross-polarized light and c in plane-polarized light). Garnet mostly occurs as relict grains surrounded by Hb + Pl + Opq symplectite (c); clinozoisite and epidote exhibit distinct core–rim structure (d). (e–i) Images to show the occurrence of K-feldspar as interstitial cuspate veinlets and films with low dihedral angles along grain boundaries of phengite and quartz (e–h in cross-polarized light and i backscattered electrons). Mineral names are abbreviated according to the recommendations of Whitney & Evans (2010).

Fig. 5. Representative images to show the mineralogy and microstructures of the eclogite (a, b) and gneiss (c–f). (a, b) Eclogite showing the mineral assemblage of Hb + Qz + Ap + Grt + Rt/Ilm and Hb + Pl symplectite after Omp, Hb + Pl + Opq symplectite after Grt and Bt + Pl symplectite after Ph; rutile is mostly retrogressed to ilmenite at the rim (plane-polarized light). (c–e) Gneiss showing the mineral assemblage of Qz + Pl + Kfs + Ph + Ep/Czo + Ttn; phengite is retrogressed to Bt + Pl + Kfs at the edges (cross-polarized light). (f) In addition to subhedral grains, Kfs also occurs as cuspate veinlets and patches along grain boundaries of plagioclase and quartz (backscattered electrons). Mineral names are abbreviated according to the recommendations of Whitney & Evans (2010).

Fig. 6. Whole-rock chondrite-normalized rare earth element patterns (a) and primitive mantle-normalized trace element patterns (b–d) of the granite and vein quartz from the

1368 composite veins (a, b), the host eclogites (a, c) and the surrounding gneisses (a, d).
1369 Normalization values are from Sun & McDonough (1989).
1370
1371 **Fig. 7.** εNd(t) *vs.* initial $^{87}Sr/^{86}Sr$ plot at t = 221 Ma for granite in the composite veins, the
1372 host eclogites and the surrounding gneisses. Whole-rock Sr–Nd isotope compositions of
1373 UHP eclogite at Yangkou, a few kilometers to the north of General's Hill, are shown for
1374 comparison (from Chen *et al*., 2002). The two gray lines show results of modeling simple
1375 binary Sr–Nd isotope mixing of exemplar end members of the eclogite and gneiss. Tick
1376 marks along mixing curve are at 10% increments.
1377
1378 **Fig. 8.** U–Pb concordia diagrams for zircon from the host eclogites (a, b), the granite (c, d)
1379 and vein quartz (e, f) from the composite veins, and the surrounding gneisses (g, h); the
1380 red circles represent analytical spots with <90% concordance. The inserts are U–Pb
1381 concordia diagrams for concordant new zircon domains; the mean $^{206}Pb/^{238}U$ ages are
1382 given with 2σ uncertainty.
1383
1384 **Fig. 9.** Chondrite-normalized rare earth element patterns of zircons from the host
1385 eclogites (a, b), the granite (c, d) and vein quartz (e, f) from the composite veins, and the
1386 surrounding gneisses (g, h). Normalization values are from Sun & McDonough (1989).
1387
1388

Fig. 10. Histogram of εHf(t) values at t_1 = 780 Ma for zircon cores and at t_2 = 221 Ma for new zircon grains and/or overgrowth rims from the host eclogite (a), the granite (b) and vein quartz (c) from one composite vein, and the surrounding gneiss (d).

Fig. 11. Comparison of initial $^{176}Hf/^{177}Hf$ ratios [$(^{176}Hf/^{177}Hf)_i$] at t_2 = 221 Ma for new zircon grains and/or overgrowth rims from the host eclogite, the granite and vein quartz from one composite vein, and the surrounding gneiss.

Fig. 12. Histograms of $\delta^{18}O$ values for zircons from the host eclogite (a, b), the granite (c, d) and vein quartz (e, f) from one composite vein, and the surrounding gneiss (g, h). The $\delta^{18}O$ value of the mantle (5.3 ± 0.3 ‰) is from Valley *et al*. (1998). VSMOW—Vienna standard mean ocean water.

Fig. 13. Phase equilibria modelling results in the MnNCKFMASHTO model system based on the composition of the granite vein sample YK1412-12. The bulk composition assumes an H_2O content equivalent to the loss on ignition and $Fe^{3+}/\Sigma Fe$ of 0.2. The fields appropriate to development of the microstructures interpreted to record decompression melting of phengite (Fig. 4e–i) are enclosed within the bold lines and bounded by the H_2O-saturated solidus. These fields are contoured for the calculated abundance (in mol.%) of melt (red dashes) and phengitic white mica (Ms; blue dashes). The white arrow shows a segment of the retrograde *P–T* path consistent with petrographic observations.

Fig. 14. Inferred *P–T* path at General's Hill in the central Sulu belt. Dashed boxes 1 and 2 represent Zr-in-rutile temperatures calculated at pressures from 2.5 to 4.5 GPa for rutile inclusions in garnet (from Wang S.J. *et al*., 2016) and the range of peak Grt–Cpx temperatures calculated at pressures of 3.5 to 6 GPa (from Wang L. *et al*., 2014), respectively, for UHP eclogite. Solid box 3 shows the range of Ti-in-zircon temperatures calculated at pressures of 2.5–2.1 GPa for granite from the composite veins (this study). Solid box 4 represents the calculated *P–T* conditions for phengite breakdown melting in the granite and melt crystallization (from Fig. 13). The solid black curve denotes the wet solidus for granite (from Holtz *et al*., 2001). The solid circle represents the second critical endpoint (SCE) for the calcium granite (Ca Gr)–H_2O system (from Hack *et al*., 2007), and the gray band shows the approximate position of the critical curve. Arrows show possible late prograde to peak and retrograde *P–T* path segments consistent with the thermobarometric data. Mineral names are abbreviated according to the recommendations of Whitney & Evans (2010).

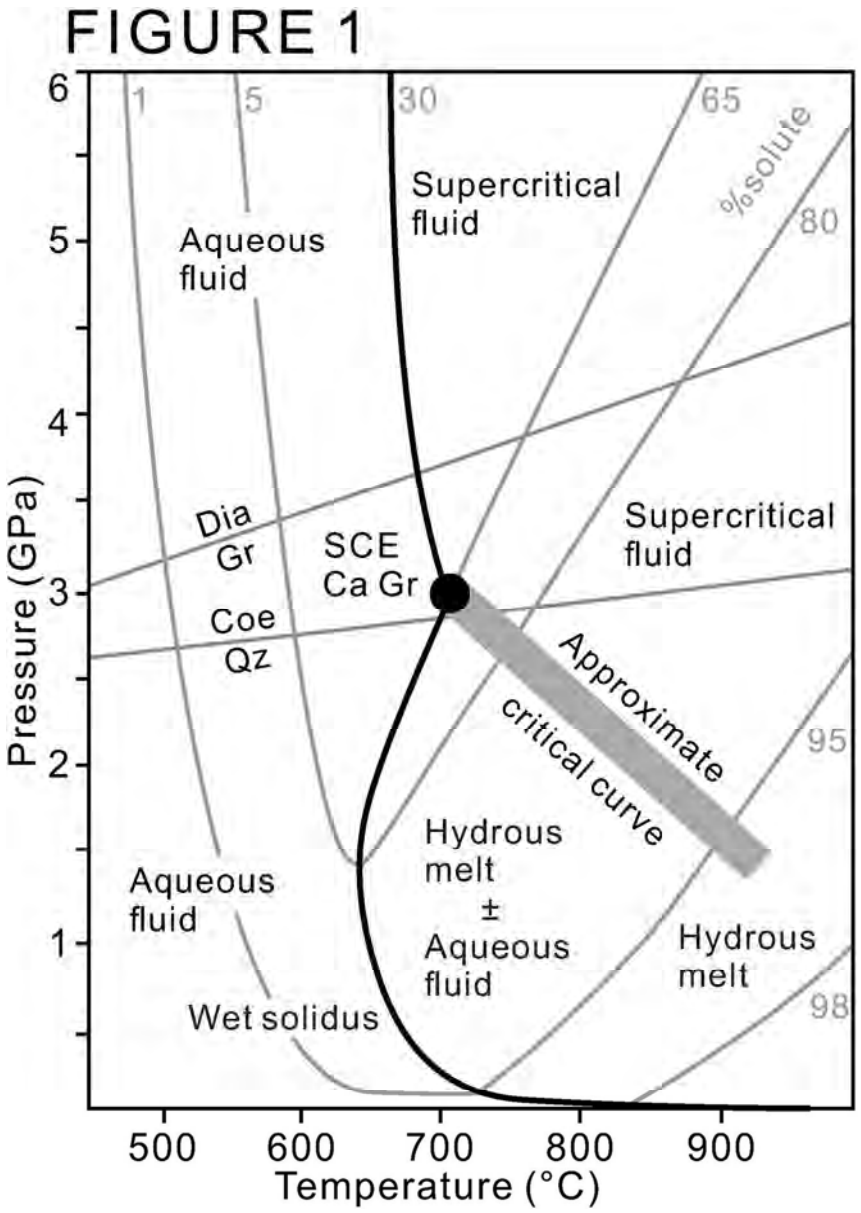

Fig. 1. P–T phase diagram for silicate–H2O systems. The wet solidus for calcium granite (Ca Gr; plagioclase An20) terminates at the second critical endpoint (SCE); the approximate position of the critical curve is shown by the gray band. The finer gray lines are isopleths of wt% solute in the fluid phase (Hermann et al., 2006, 2013). The P–T fields for aqueous fluid, immiscible hydrous melt + aqueous fluid and supercritical fluid in equilibrium with silicate minerals are shown.

109x154mm (300 x 300 DPI)

FIGURE 2

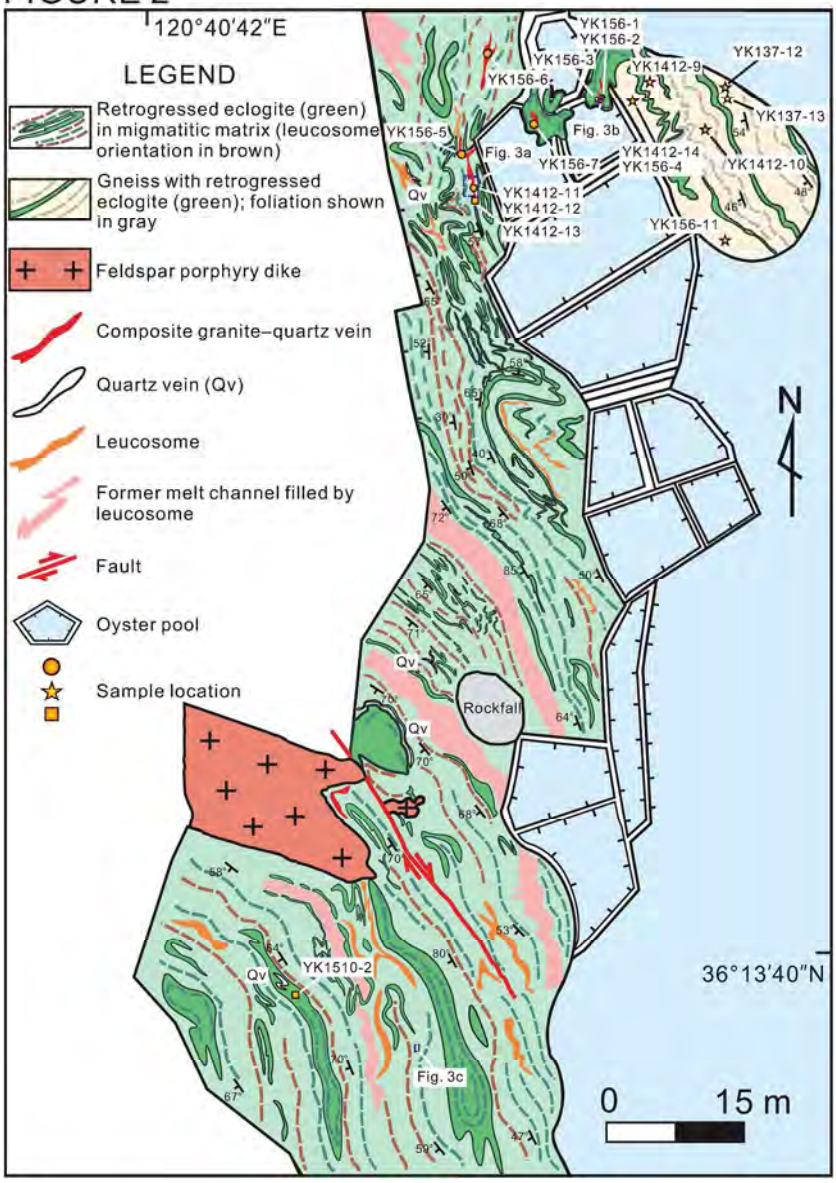

Fig. 2. Geological map of the coastal outcrop at General's Hill, with sample locations marked in solid circles, squares and stars representing composite granite–quartz veins, the host eclogite and the surrounding gneiss, respectively (detailed map based on the regional mapping of Wang et al., 2014). For location of the General's Hill outcrop in relation to the Sulu belt as a whole, see Fig. S1.

231x333mm (300 x 300 DPI)

FIGURE 3

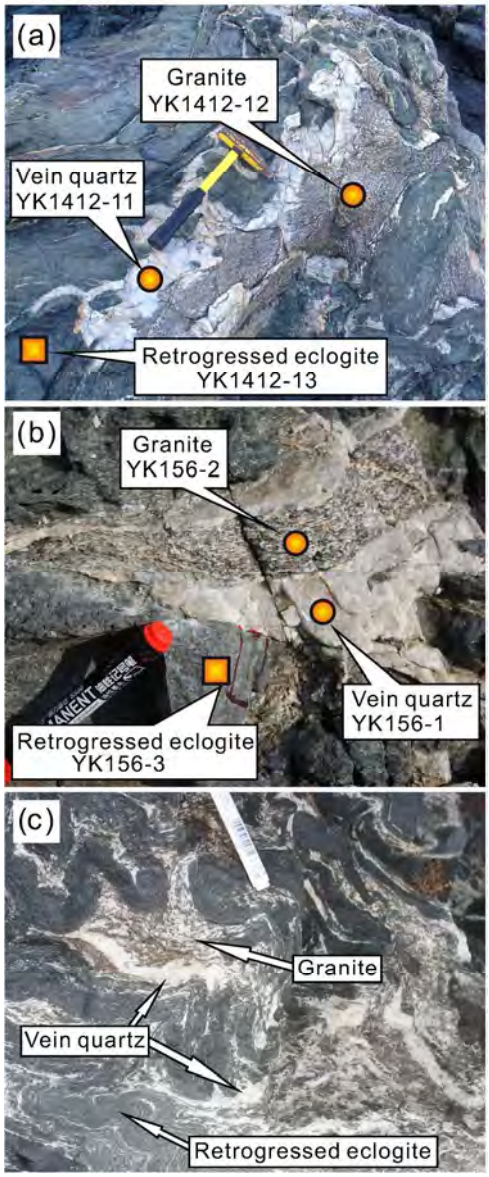

Fig. 3. Field occurrence of the composite granite–quartz veins at General's Hill, with locations of samples marked; the irregularly shaped composite veins are centimeter to decimeter in width within retrogressed eclogite.

198x492mm (300 x 300 DPI)

FIGURE 4

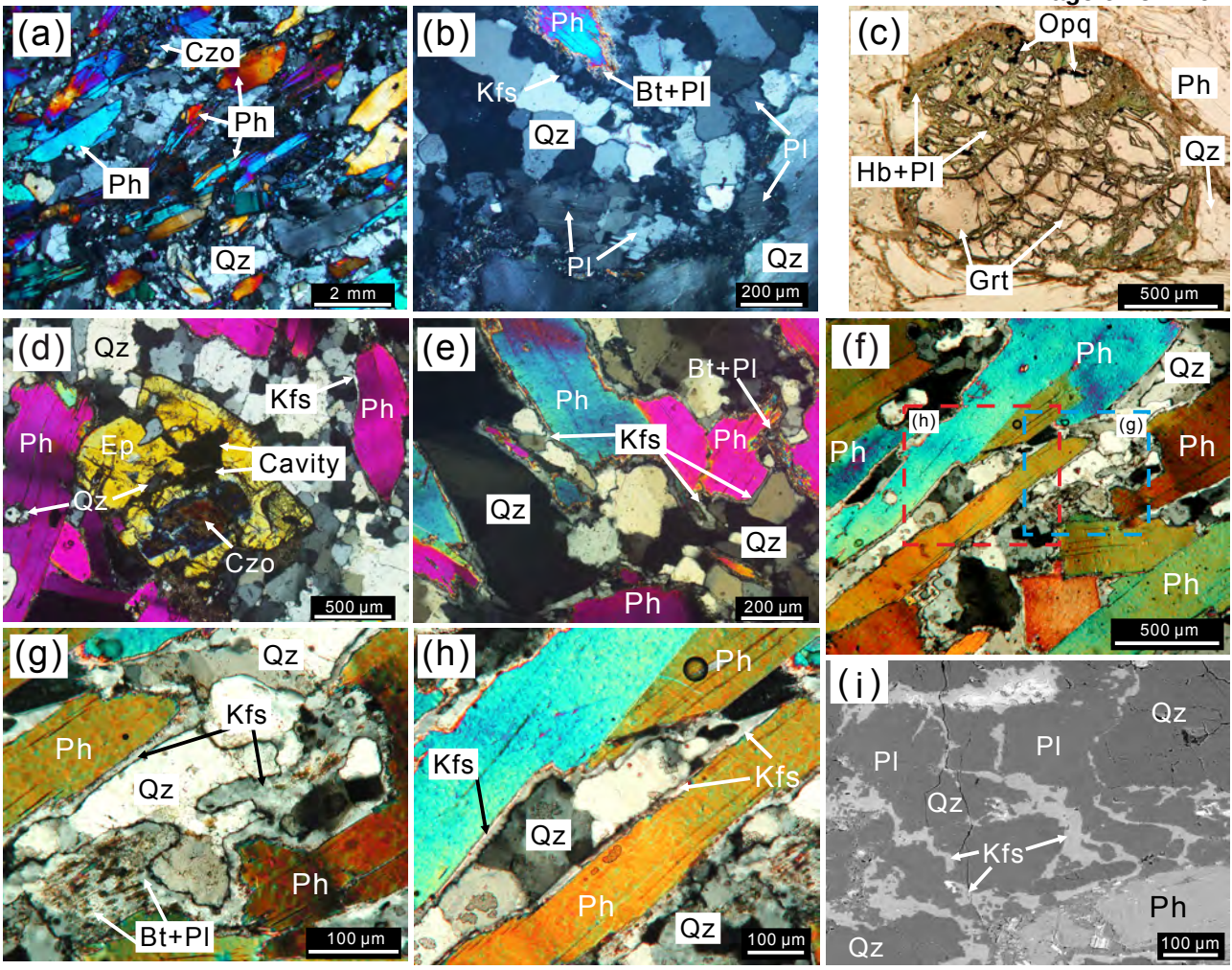
(a)
Czo
Ph
Ph
Qz
2 mm
(b)
Ph
Kfs
Bt+Pl
Qz
Pl
Pl
Qz
200 µm
(c)
Opq
Ph
Qz
Hb+Pl
Grt
500 µm
(d)
Qz
Kfs
Ph
Ph
Ep
Cavity
Qz
Czo
500 µm
(e)
Bt+Pl
Ph
Kfs
Ph
Qz
Qz
Ph
200 µm
(f)
Ph
Qz
(h)
(g)
Ph
Ph
Ph
500 µm
(g)
Qz
Kfs
Ph
Qz
Ph
Bt+Pl
100 µm
(h)
Ph
Kfs
Kfs
Qz
Ph
Qz
100 µm
(i)
Qz
Pl
Pl
Qz
Kfs
Ph
Qz
100 µm

FIGURE 5

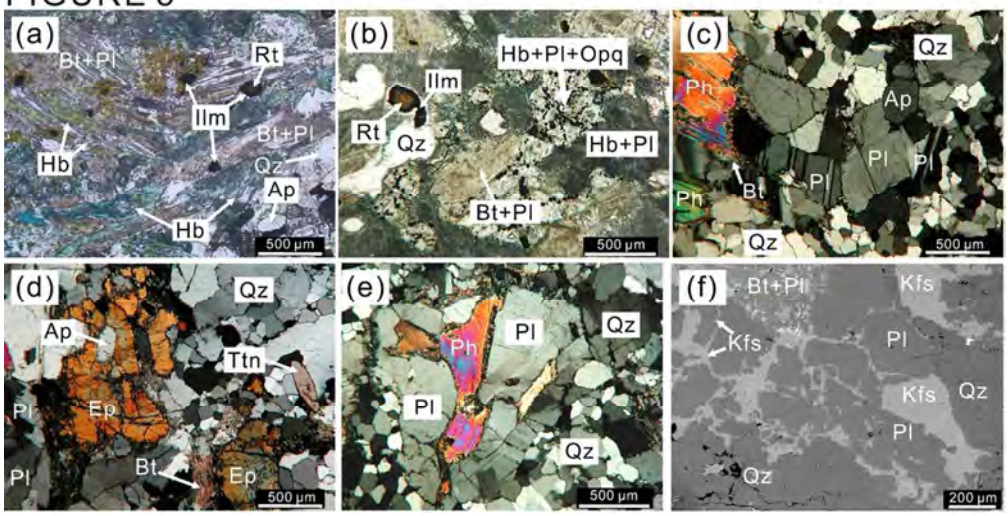

Fig. 5. Representative images to show the mineralogy and microstructures of the eclogite (a, b) and gneiss (c–f). (a, b) Eclogite showing the mineral assemblage of Hb + Qz + Ap + Grt + Rt/Ilm and Hb + Pl symplectite after Omp, Hb + Pl + Opq symplectite after Grt and Bt + Pl symplectite after Ph; rutile is mostly retrogressed to ilmenite at the rim (plane-polarized light). (c–e) Gneiss showing the mineral assemblage of Qz + Pl + Kfs + Ph + Ep/Czo + Ttn; phengite is retrogressed to Bt + Pl + Kfs at the edges (cross-polarized light). (f) In addition to subhedral grains, Kfs also occurs as cuspate veinlets and patches along grain boundaries of plagioclase and quartz (backscattered electrons). Mineral names are abbreviated according to the recommendations of Whitney & Evans (2010).

90x48mm (300 x 300 DPI)

FIGURE 6

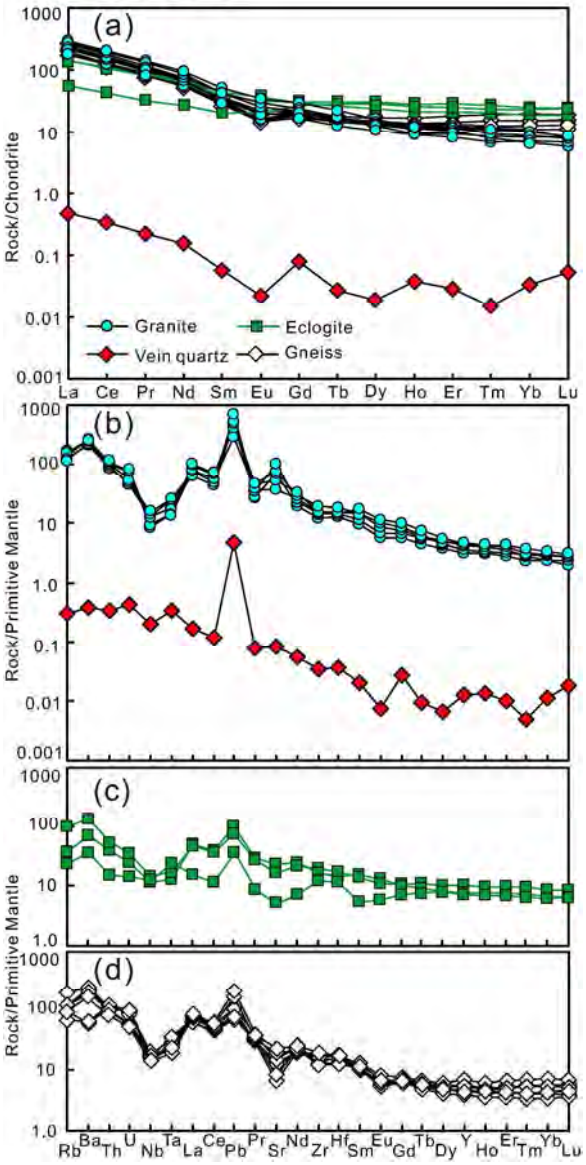

Fig. 6. Whole-rock chondrite-normalized rare earth element patterns (a) and primitive mantle-normalized trace element patterns (b–d) of the granite and vein quartz from the composite veins (a, b), the host eclogites (a, c) and the surrounding gneisses (a, d). Normalization values are from Sun & McDonough (1989).

166x344mm (300 x 300 DPI)

FIGURE 7

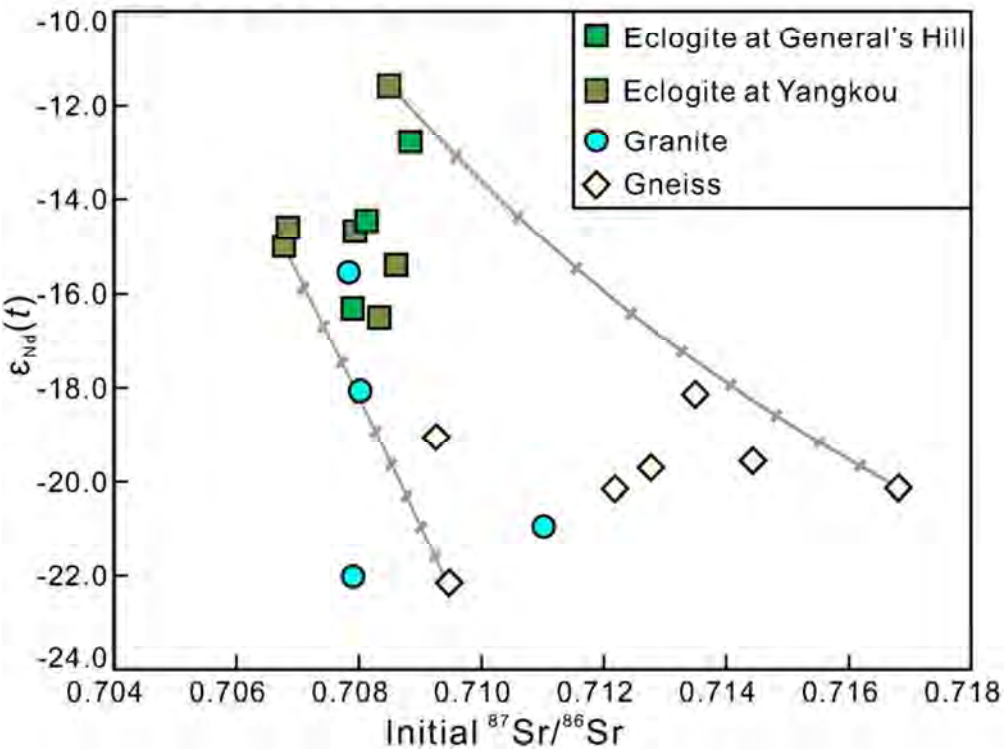

Fig. 7. εNd(t) vs. initial $^{87}Sr/^{86}Sr$ plot at t = 221 Ma for granite in the composite veins, the host eclogites and the surrounding gneisses. Whole-rock Sr–Nd isotope compositions of UHP eclogite at Yangkou, a few kilometers to the north of General's Hill, are shown for comparison (from Chen et al., 2002). The two gray lines show results of modeling simple binary Sr–Nd isotope mixing of exemplar end members of the eclogite and gneiss. Tick marks along mixing curve are at 10% increments.

65x53mm (300 x 300 DPI)

FIGURE 8

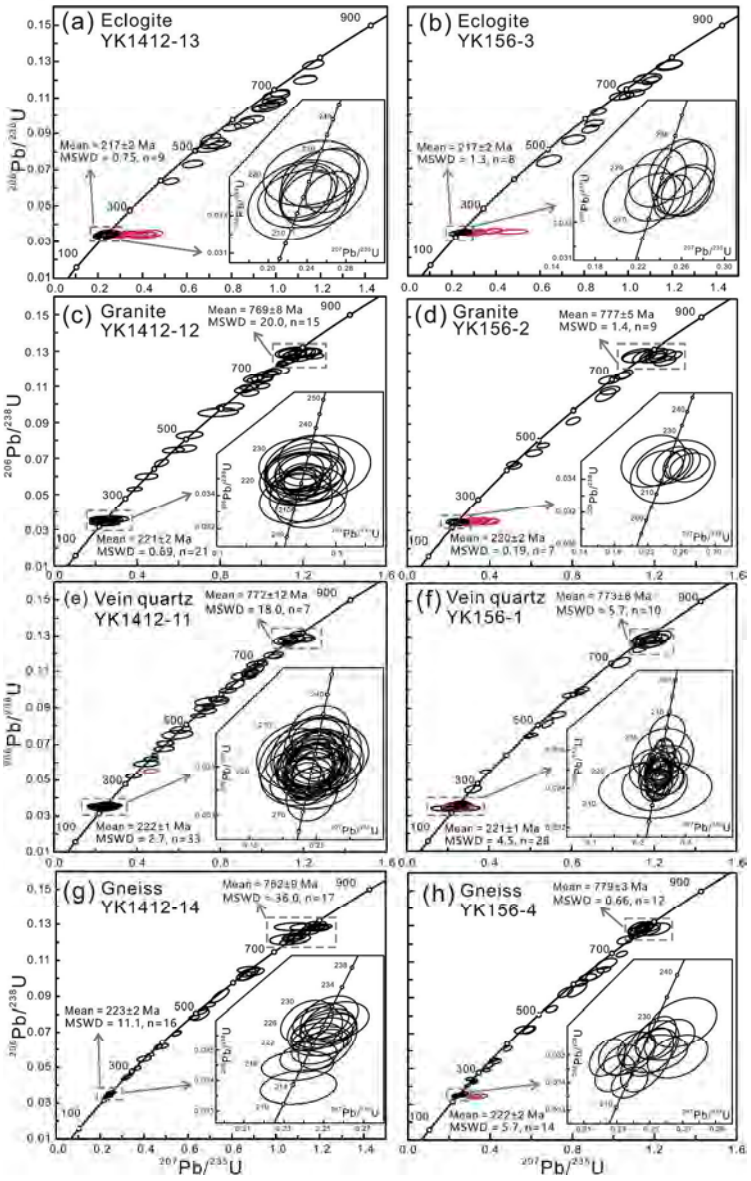

Fig. 8. U–Pb concordia diagrams for zircon from the host eclogites (a, b), the granite (c, d) and vein quartz (e, f) from the composite veins, and the surrounding gneisses (g, h); the red circles represent analytical spots with <90% concordance. The inserts are U–Pb concordia diagrams for concordant new zircon domains; the mean $^{206}Pb/^{238}U$ ages are given with 2σ uncertainty.

234x378mm (300 x 300 DPI)

FIGURE 9

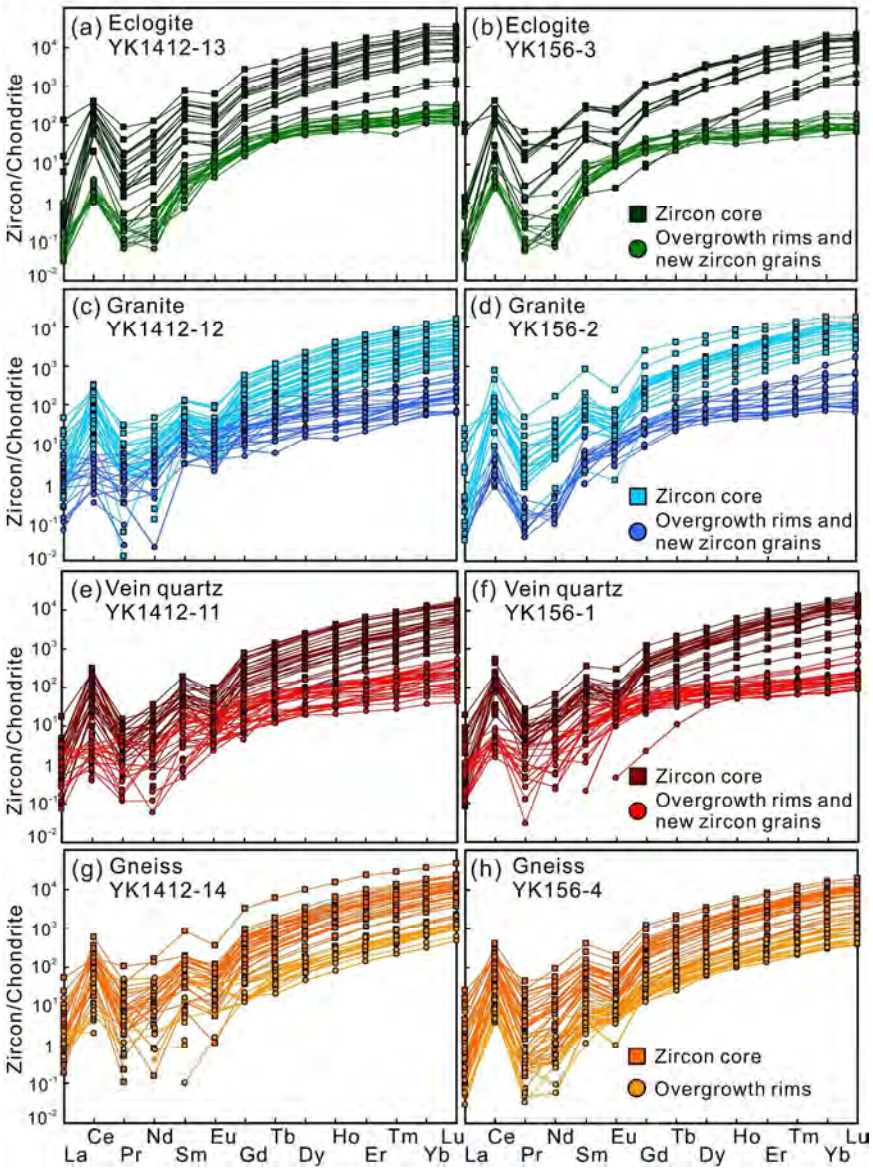

Fig. 9. Chondrite-normalized rare earth element patterns of zircons from the host eclogites (a, b), the granite (c, d) and vein quartz (e, f) from the composite veins, and the surrounding gneisses (g, h). Normalization values are from Sun & McDonough (1989).

188x261mm (300 x 300 DPI)

FIGURE 10

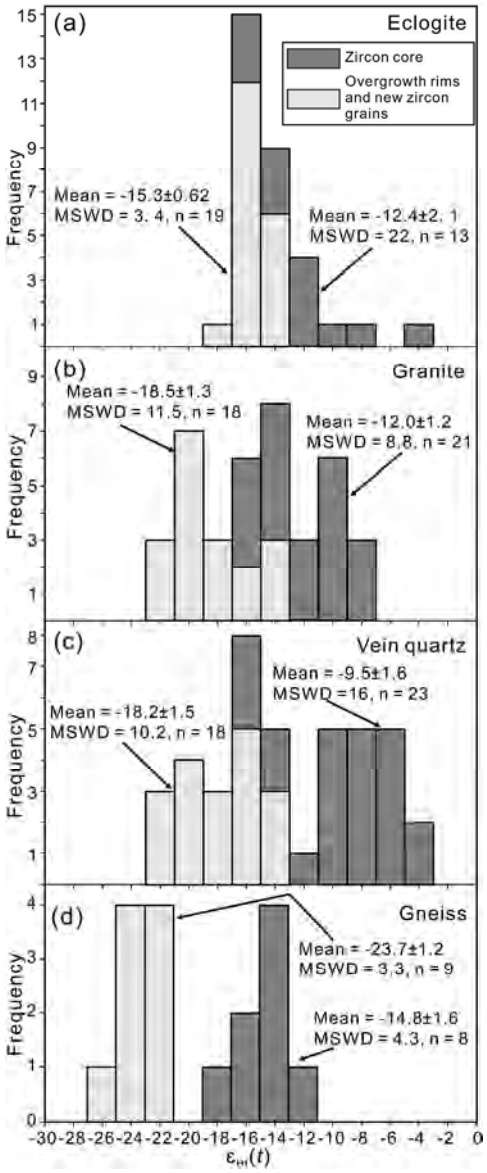

Fig. 10. Histogram of εHf(t) values at t_1 = 780 Ma for zircon cores and at t_2 = 221 Ma for new zircon grains and/or overgrowth rims from the host eclogite (a), the granite (b) and vein quartz (c) from one composite vein, and the surrounding gneiss (d).

202x509mm (300 x 300 DPI)

FIGURE 11

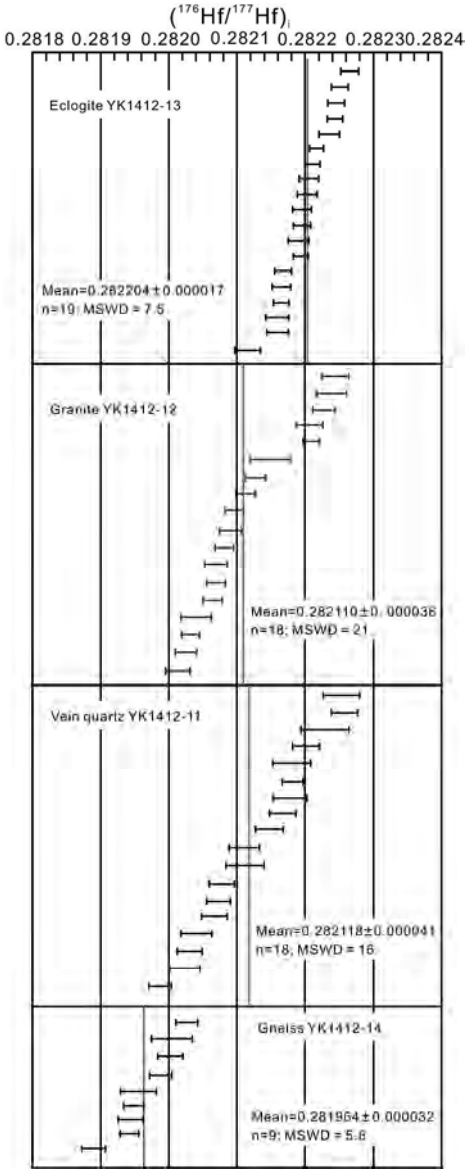

Fig. 11. Comparison of initial $^{176}Hf/^{177}Hf$ ratios [$(^{176}Hf/^{177}Hf)i$] at t_2 = 221 Ma for new zircon grains and/or overgrowth rims from the host eclogite, the granite and vein quartz from one composite vein, and the surrounding gneiss.

191x498mm (300 x 300 DPI)

FIGURE 12

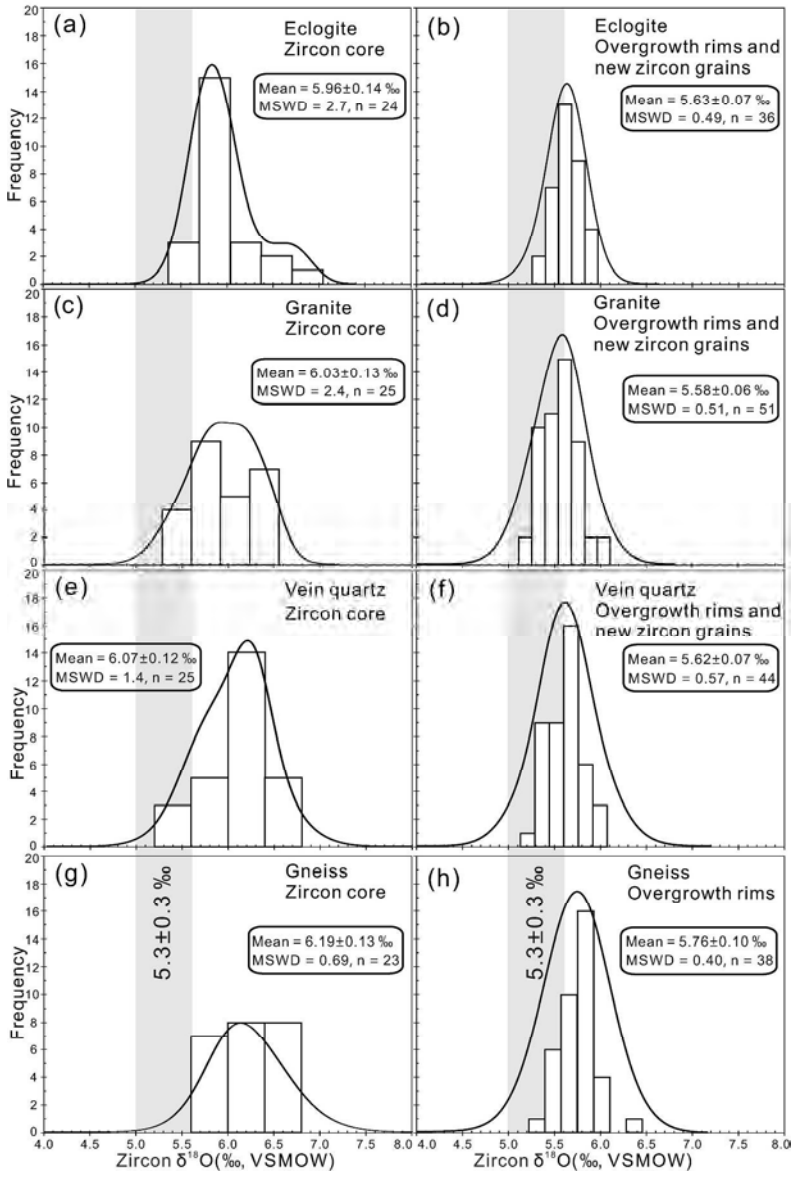

Fig. 12. Histograms of $\delta^{18}O$ values for zircons from the host eclogite (a, b), the granite (c, d) and vein quartz (e, f) from one composite vein, and the surrounding gneiss (g, h). The $\delta^{18}O$ value of the mantle (5.3 ± 0.3 ‰) is from Valley et al. (1998). VSMOW—Vienna standard mean ocean water.

211x323mm (300 x 300 DPI)

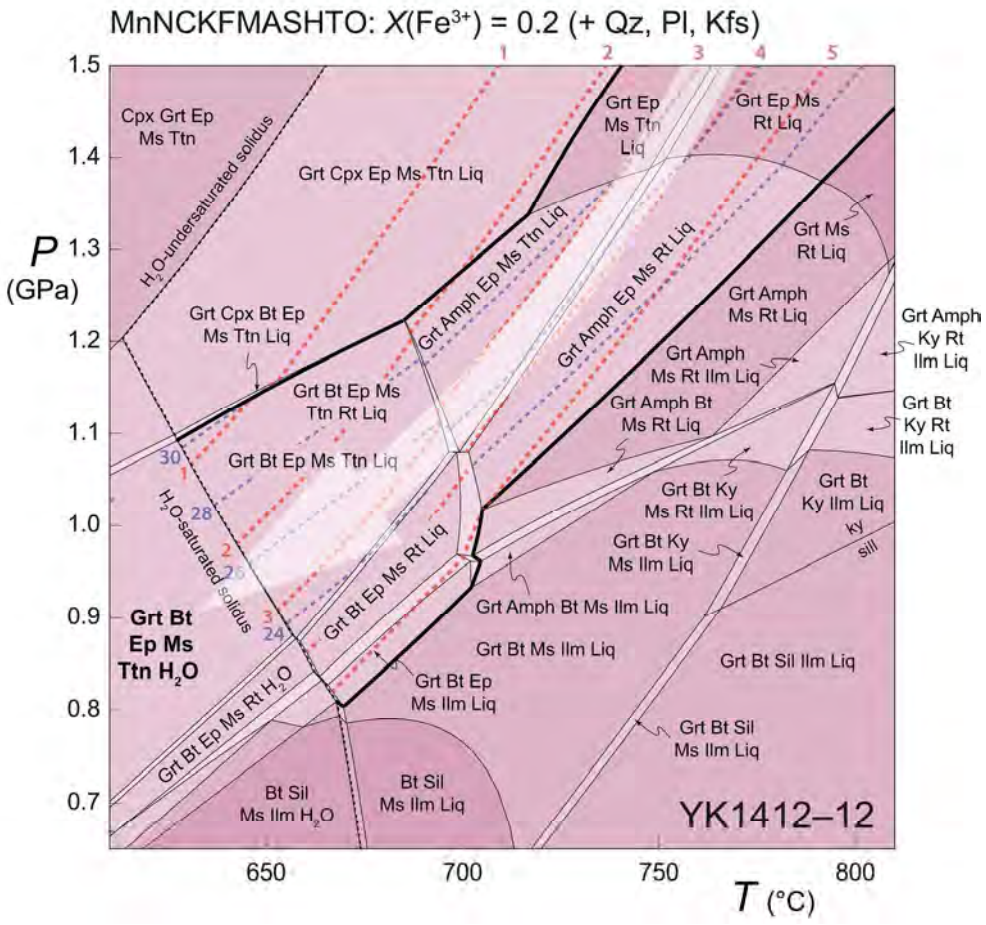

Fig. 13. Phase equilibria modelling results in the MnNCKFMASHTO model system based on the composition of the granite vein sample YK1412-12. The bulk composition assumes an H_2O content equivalent to the loss on ignition and $Fe^{3+}/\Sigma Fe$ of 0.2. The fields appropriate to development of the microstructures interpreted to record decompression melting of phengite (Fig. 4e–i) are enclosed within the bold lines and bounded by the H2O-saturated solidus. These fields are contoured for the calculated abundance (in mol.%) of melt (red dashes) and phengitic white mica (Ms; blue dashes). The white arrow shows a segment of the retrograde P–T path consistent with petrographic observations.

191x177mm (300 x 300 DPI)

FIGURE 14

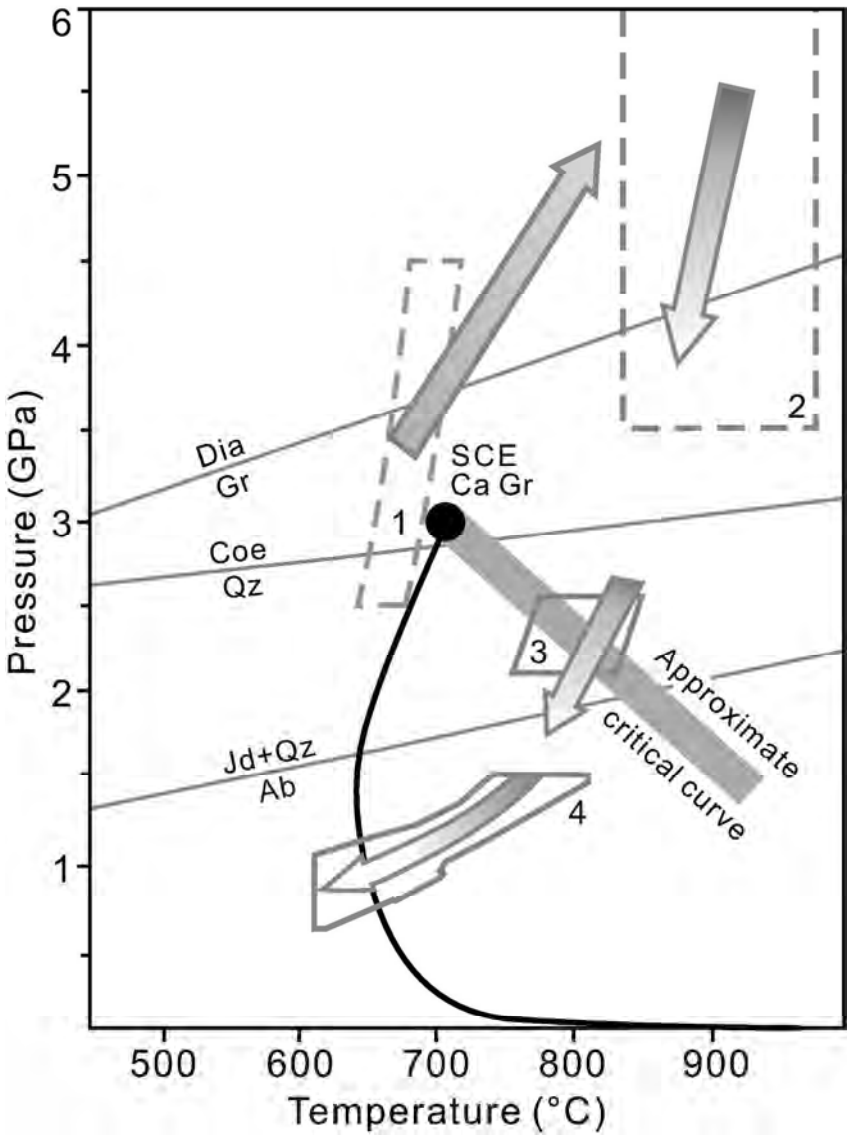

Fig. 14. Inferred *P–T* path at General's Hill in the central Sulu belt. Dashed boxes 1 and 2 represent Zr-in-rutile temperatures calculated at pressures from 2.5 to 4.5 GPa for rutile inclusions in garnet (from Wang S.J. et al., 2016) and the range of peak Grt–Cpx temperatures calculated at pressures of 3.5 to 6 GPa (from Wang L. et al., 2014), respectively, for UHP eclogite. Solid box 3 shows the range of Ti-in-zircon temperatures calculated at pressures of 2.5–2.1 GPa for granite from the composite veins (this study). Solid box 4 represents the calculated P–T conditions for phengite breakdown melting in the granite and melt crystallization (from Fig. 13). The solid black curve denotes the wet solidus for granite (from Holtz et al., 2001). The solid circle represents the second critical endpoint (SCE) for the calcium granite (Ca Gr)–H2O system (from Hack et al., 2007), and the gray band shows the approximate position of the critical curve. Arrows show possible late prograde to peak and retrograde P–T path segments consistent with the thermobarometric data. Mineral names are abbreviated according to the recommendations of Whitney & Evans (2010).

111x159mm (300 x 300 DPI)

SUPPORTING INFORMATION

Composite granite–quartz veins in the Sulu belt, China: evidence of supercritical fluid flow during exhumation of deeply subducted UHP continental crust

S.-J. WANG, [1,2] L. WANG, [1,*] M. BROWN, [2, 1] P. M. PICCOLI, [2] T.M. JOHNSON, [3] P. FENG, [1] H. DENG, [1] K. KITAJIMA [4] AND Y. HUANG [1]

[1] *State Key Laboratory of Geological Processes and Mineral Resources, and Center for Global Tectonics, School of Earth Sciences, China University of Geosciences, Wuhan 430074, China*

[2] *Laboratory for Crustal Petrology, Department of Geology, University of Maryland, College Park, MD 20742, USA*

[3] *Department of Applied Geology, The Institute for Geoscience Research (TIGeR), Curtin University, GPO Box U1987, Perth, WA 6845, Australia*

[4] *The WiscSIMS Laboratory, Department of Geoscience, University of Wisconsin-Madison, Madison, WI 53706, USA*

Appendix S1. Analytical methods.

Figure S1. (a) Metamorphic facies map of the Dabie–Sulu orogen in central–eastern China; (b) Simplified geological map of the General's Hill locality (after Wang *et al*., 2010).

Figure S2. (a) Major and (b) trace element compositions for the granite in the composite veins,

the host eclogite and the surrounding gneiss at General's Hill. Major oxides and trace elements are plotted as weight percent and parts per million, respectively.

Figure S3. Cathodoluminescence images of representative zircon grains from one composite vein, the host eclogite and the surrounding gneiss. Circles mark the locations of LA(MC)-ICP-MS U–Pb (red) and Hf (light blue) isotope analyses.

Figure S4. Plots of Th *vs.* U and Th/U vs. REE contents for zircon from the host eclogites (a, b), the granite (c, d) and vein quartz (e, f) from the composite veins, and the surrounding gneisses (g, h).

Figure S5. Box-and-whisker plots to show the Eu/Eu* ratios for overgrowth rims and/or new zircon grains from the granite and vein quartz in the composite veins, the host eclogites and the surrounding gneisses.

Figure S6. $^{176}Hf/^{177}Hf$ ratios and $^{176}Lu/^{177}Hf$ ratios *vs.* U–Pb ages for zircon from the host eclogite (a, b), the granite (c, d) and vein quartz (e, f) of the composite vein, and the surrounding gneiss (g, h).

Figure S7. Box-and-whisker plots for the granite in the composite veins to show: (a) the distribution of pressures calculated at T of 800 ^{o}C based on the Si-in-phengite barometer of Caddick & Thompson (2008, equation 8), and (b) the distribution of temperatures calculated at 2.5 GPa for overgrowth rims and/or new grains of zircon from the host eclogite, the composite veins, and the surrounding gneiss, based on the Ti-in-zircon thermometer of Ferry & Watson (2007).

Figure S8. Covariation diagram of $^{176}Lu/^{177}Hf$ ratios *vs.* $\varepsilon Hf(t)$ values (corrected to t = 221 Ma)

of overgrowth rims and new grains of zircon from the composite veins; (a) granite and (b) vein quartz.

Table S1. Summary of published data on the characterization of supercritical fluids in subduction zones.

Table S2. Sample numbers, lithology, GPS coordinates and mineral assemblages.

Table S3. (a) Major element compositions of phengite in granite from the composite veins; (b) Major and trace element compositions of the granite and vein quartz from the composite veins, the host eclogite and the surrounding gneiss.

Table S4 Whole-rock Sr and Nd isotope compositions of the granite from the composite veins, the host eclogites and the surrounding gneisses.

Table S5. LA-ICP-MS U–Th–Pb data for zircon from the host eclogites (a), the granite and vein quartz of the composite veins (b,c), and the surrounding gneisses (d).

Table S6. LA-ICP-MS trace element compositions of zircon from the host eclogites (a), the granite (b) and vein quartz (c) from the composite veins, and the surrounding gneisses (d).

Table S7. LA(MC)-ICP-MS Lu–Hf isotope compositions of zircon from the granite and vein quartz from the composite veins, the host eclogite and the surrounding gneiss.

Table S8. *In situ* SIMS O isotope compositions of zircon from the granite and vein quartz from the composite veins, the host eclogite and the surrounding gneiss.

Appendix S1: Analytical methods

Backscattered electron (BSE) imaging and energy-dispersive spectroscopy (EDS) were undertaken for mineral identification and microstructural investigation using a FEI Quanta 450 field emission gun scanning electron microscope (SEM) at the State Key Laboratory of Geological Processes and Mineral Resources (GPMR), China University of Geosciences (CUG), Wuhan. The operating conditions were an accelerating voltage of 20 kV and a working distance of ~12 mm.

Point counting for mode calculation was performed on polished thin sections for three samples of granite from the composite veins. Analyses were performed using a JEOL 8900R electron probe microanalyzer (EPMA) at the Advanced Imaging and Microscopy Laboratory (AIMLab) at the University of Maryland, College Park. BSE imaging was used in conjunction with EDS analysis to aid in mineral identification. A minimum of 1000 points was counted on each sample. Spacing between adjacent points was determined by the size of the sample and the grain size, as follows: YK156-2 (1000 μm, 46 x 27 grids), YK156-5 (910 μm, 50 x 23 grids), and YK156-6 (700 μm, 35 x 32 grids).

Major elements of phengite were measured using the JEOL 8900R EPMA at the AIMLab at the University of Maryland, College Park. Operating conditions were as follows: 15 kV accelerating voltage, 10 nA cup current, and a 10 μm beam. Natural muscovite, amphibole, microcline and rhodonite were used as primary standards. Raw data were corrected using a ZAF algorithm.

Fresh rock samples free of alteration were crushed in a corundum jaw crusher to <60 mesh. For each sample, approximately 70 g was further powdered in an agate ring mill to <200 mesh for whole-rock major and trace element, and Sr–Nd isotope analyses. Major elements were analyzed at the Comprehensive Rock and Mineral Test Center, Wuhan, using a wet chemical method according to the GB/T 14506.28-1993 standard, whereas LOI was measured according to the LY/T 1253-1999 standard. The analytical uncertainty is generally <5%. After digestion of powdered samples in HF + HNO_3 acids in Teflon bombs, trace element concentrations were determined at the State Key Laboratory of GPMR, CUG, Wuhan using an Agilent 7500a ICP-MS. International standards AGV-2, BHVO-2, BCR-2 and RGM-2 were used as reference materials to evaluate analytical precision. The detailed sample digestion procedure for inductively coupled plasma mass spectrometry (ICP-MS) analysis and analytical precision and accuracy for trace element analysis are similar to those of Liu *et al*. (2008b). Whole-rock Sr and Nd isotope compositions were acquired at the State Key Laboratory of GPMR, CUG, Wuhan using a Neptune Plus multi-collector (MC) ICP-MS. $^{87}Rb/^{86}Sr$ and $^{147}Sm/^{144}Nd$ ratios were calculated from Rb, Sr, Sm and Nd concentrations measured by ICP-MS. The measured Sr and Nd isotope ratios were normalized to $^{86}Sr/^{88}Sr = 0.1194$ and $^{146}Nd/^{144}Nd = 0.7219$, respectively. During the course of analysis, the Chinese GBW04411 standard gave an average $^{87}Sr/^{86}Sr$ value of 0.759909 ± 6 (2ζ) and the international BCR-2 standard gave an average $^{143}Nd/^{144}Nd$ of 0.512592 ± 0.000003 (2ζ). Detailed sample preparation, chemical separation and analytical procedures for the Sr and Nd isotope analysis were similar to those given by Gao *et al.* (2004).

Zircons were extracted from the two sets of composite vein samples following standard

crushing, sieving, heavy liquid and magnetic methods. After extraction, zircon grains were handpicked from the heavy fraction using a binocular microscope. For LA(MC)-ICP-MS zircon trace element, U–Pb dating and Lu–Hf isotope analyses, a portion of the zircon separate was mounted in 16 mm diameter epoxy resin and the zircons were polished to approximately half thickness. Before LA(MC)-ICP-MS analysis, BSE and cathodoluminescence (CL) imaging was conducted at the State Key Laboratory of GPMR, CUG, Wuhan using a FEI Quanta 450 field emission gun SEM with a Gatan Mono CL4+ CL system attached (acceleration voltage 10 kV, spot size 5 μm and working distance of 13.9–14.1 mm).

Synchronous U–Pb and trace element analysis was undertaken by LA-ICP-MS at the State Key Laboratory of GPMR, CUG, Wuhan; operating conditions and data reduction were similar to those described by Liu *et al*. (2008a, 2010). Samples were ablated using a GeoLas 2005 with a spot size of 32 μm, which was connected to an Agilent 7500a ICP-MS instrument to acquire ion-signal intensities. Each analysis incorporated a background acquisition of approximately 20 s (gas blank) followed by 50 s of data acquisition from the sample. Zircon 91500 was used as an external standard for U–Pb dating, and was analyzed twice bracketing every batch of 6 analyses of unknowns. Preferred U–Th–Pb isotopic ratios adopted for 91500 were from Wiedenbeck *et al*. (1995), and uncertainty of the preferred values was propagated through the calculation of final results for the unknowns. Trace element compositions of zircons were calibrated against multiple-reference materials (BCR-2G and BIR-1G) combined with internal standardization. Off-line selection and integration of background and analyte signals, and time-drift correction and quantitative calibration for trace element and U–Pb analysis were performed using

ICPMSDataCal (Liu *et al*., 2008a). The data were processed using the program *ISOPLOT/Ex_ver3* developed by Ludwig (2003).

Following zircon U–Pb and trace element analysis, *in-situ* Lu–Hf isotope analysis of zircon was conducted for one set of samples (YK1412-11, -12, -13 and -14) using a Neptune Plus MC-ICP-MS in combination with a Geolas 2005 excimer ArF laser ablation system also at the State Key Laboratory of GPMR, CUG, Wuhan. All data were acquired in single spot ablation mode with a spot size of 44 μm over the same laser ablation spots used for dating. Each measurement incorporated a background acquisition of 20 s followed by 50 s of signal acquisition from the unknowns. Zircon 91500, GJ-1 and Temora were used as reference standards. Detailed operating conditions for the laser ablation system and the MC-ICP-MS instrument, and the analytical method are given by Hu *et al*. (2012). Mass bias of Hf and Yb were calculated using an exponential correction law and normalized values of $^{179}Hf/^{177}Hf = 0.7325$ and $^{173}Yb/^{171}Yb = 1.1248$ (Blichert-Toft *et al*., 1997), respectively. Interference of ^{176}Yb on ^{176}Hf and ^{176}Lu on ^{176}Hf were corrected by measuring the interference-free ^{173}Yb and ^{175}Lu isotopes and using the recommended ratios of $^{176}Yb/^{173}Yb = 0.7876$ (McCulloch *et al*., 1977) and $^{176}Lu/^{175}Lu = 0.02656$ (Blichert-Toft *et al*., 1997), respectively. A decay constant of 1.867×10^{-11} $year^{-1}$ for ^{176}Lu was adopted (Söderlund *et al*., 2004). Initial $^{176}Hf/^{177}Hf$ ratios were calculated according to the determined $^{206}Pb/^{238}U$ age, and $\varepsilon_{Hf}(t)$ values (defined as the part in 10,000 difference in the initial $^{176}Hf/^{177}Hf$ ratio between the sample and the chondritic reservoir at the time of zircon growth) were calculated relative to a chondritic reservoir with a $^{176}Hf/^{177}Hf$ ratio of 0.282772 and $^{176}Lu/^{177}Hf$ of 0.0332 (Blichert-Toft & Albarède, 1997). Single-stage Hf model

ages (T_{DM1}) were calculated relative to a model depleted mantle with a present day $^{176}Hf/^{177}Hf$ ratio of 0.28325 and $^{176}Lu/^{177}Hf$ ratio of 0.0384 (Vervoort & Blichert-Toft, 1999), and two-stage Hf model ages (T_{DM2}) were calculated by assuming a mean $^{176}Lu/^{177}Hf$ ratio of 0.015 for the average continental crust (Griffin *et al*., 2002).

Zircons from the same set of samples used for Lu–Hf isotope analysis were selected for O isotope analysis. Zircon grains were soaked in cold HF for 24 h to remove any metamict material, and then mounted within 7.5 mm of the center of a 25 mm diameter epoxy resin puck with chips of O isotope standard zircon KIM-5 (Valley *et al*., 1998; Valley, 2003). The zircons were polished to expose their midsections but with low relief for accurate O isotope analysis. To guide O isotope analysis, the internal texture of zircons and location of microcracks and inclusions was characterized using reflected and transmitted light optical microscopy, and CL imaging. The CL images of zircons were acquired individually using the JEOL 8900R EPMA equipped with a Gatan CL system at the AIMLab at the University of Maryland, College Park. The analytical conditions were an acceleration voltage of 7 kV and a low beam current of 2 nA.

The O isotope composition of these zircons was determined using a CAMECA IMS 1280 hosted in the Wisconsin Secondary Ion Mass Spectrometer Laboratory at the University of Wisconsin-Madison. Analytical procedures and operating conditions are the same as those given by Kita *et al*. (2009). Measurements were conducted using a focused 2.5 nA Cs^+ primary ions (+10 kV) with an average beam size of 10 μm. Secondary ^{16}O, $^{16}O^1H$ and ^{18}O were detected simultaneously using multicollection Faraday Cup detectors. The KIM-5 zircon standard ($\delta^{18}O$ = 5.09 ‰ Vienna Standard Mean Ocean Water (VSMOW); Valley, 2003) was used to calibrate the

$\delta^{18}O$(zircon) VSMOW of the unknowns. A set of 4–5 analyses of the KIM-5 was performed bracketing each 10–20 analyses of unknowns to evaluate instrument bias and external reproducibility. The precision of zircon O isotope analysis, expressed as two standard deviations (±2 SD), was defined by the external precision of the spot-to-spot analyses on the standard KIM-5.

REFERENCES

Blichert-Toft, J. & Albarède, F., 1997. The Lu–Hf isotope geochemistry of chondrites and the evolution of the mantle–crust system. *Earth and Planetary Science Letters*, **148,** 243–258.

Blichert-Toft, J., Chauvel, C. & Albarède, F., 1997. Separation of Hf and Lu for high-precision isotope analysis of rock samples by magnetic sector-multiple collector ICP-MS. *Contributions to Mineralogy and Petrology*, **127,** 248–260.

Caddick, M.J. & Thompson, A.B., 2008. Quantifying the tectono-metamorphic evolution of pelitic rocks from a wide range of tectonic settings: mineral compositions in equilibrium. Contributions to Mineralogy and Petrology, **156,** 177–195.

Gao, S., Rudnick, R.L., Yuan, H.L. *et al.,* 2004. Recycling lower continental crust in the North China craton. *Nature* **432,** 892–897.

Griffin, W.L., Wang, X., Jackson, S.E. *et al*., 2002. Zircon chemistry and magma mixing, SE China: in-situ analysis of Hf isotopes, Tonglu and Pingtan igneous complexes. *Lithos*, **61(3)**, 237–269.

Ferry, J.M. & Watson, E.B., 2007. New thermodynamic models and revised calibrations for the Ti-in-zircon and Zr-in-rutile thermometers. *Contributions to Mineralogy and Petrology*, **154,** 429–437.

Hu, Z.C., Liu, Y.S., Gao, S. *et al.,* 2012. Improved in situ Hf isotope ratio analysis of zircon using newly designed X skimmer cone and jet sample cone in combination with the addition of nitrogen by laser ablation multiple collector ICP-MS. *Journal of Analytical Atomic Spectrometry*, **27,** 1391–1399.

Kita, N.T., Ushikubo, T., Fu, B. & Valley, J.W., 2009. High precision SIMS oxygen isotope analysis and the effect of sample topography. *Chemical Geology*, **264,** 43–57.

Liu, Y.S., Hu, Z.C., Gao, S. *et al.,* 2008a. In situ analysis of major and trace elements of anhydrous minerals by LA-ICP-MS without applying an internal standard. *Chemical Geology*, **257,** 34–43.

Liu, Y.S., Zong, K.Q., Kelemen, P.B. & Gao, S., 2008b. Geochemistry and magmatic history of eclogites and ultramafic rocks from the Chinese continental scientific drill hole: subduction and ultrahigh-pressure metamorphism of lower crustal cumulates. *Chemical Geology*, **247,** 133–153.

Liu, Y.S., Gao, S., Hu, Z. C., Gao, C., Zong, K. & Wang, D., 2010. Continental and oceanic crust recycling-induced melt–peridotite interactions in the Trans-North China Orogen: U–Pb dating, Hf isotopes and trace elements in zircons from mantle xenoliths. *Journal of Petrology*, **51,** 537–571.

Ludwig, K., 2003. *User's manual for Isoplot 3.00: a geochronological toolkit for Microsoft Excel*. Berkeley Geochronology Center, Special Publications **1,** 1–55.

McCulloch, M.T., Rosman, K.J. & De Laeter, J.R., 1977. The isotopic and elemental abundance of ytterbium in meteorites and terrestrial samples. *Geochimica et Cosmochimica Acta*, **41,** 1703–1707.

Söderlund, U., Patchett, J.P., Vervoort, J.D. & Isachsen, C.E., 2004. The Lu-176 decay constant determined by Lu−Hf and U−Pb isotope systematics of Precambrian mafic intrusions. *Earth and Planetary Science Letters*, **219,** 311−324.

Valley, J.W., 2003. Oxygen isotopes in zircon. *Reviews in mineralogy and Geochemistry*, **53,** 343−385.

Valley, J.W., Kinny, P.D., Schulze, D.J. & Spicuzza, M.J., 1998. Zircon megacrysts from kimberlite: oxygen isotope variability among mantle melts. *Contributions to Mineralogy and Petrology*, **133,** 1−11.

Vervoort, J.D. & Blichert-Toft, J., 1999. Evolution of the deleted mantle: Hf isotope evidence from juvenile rocks through time. *Geochimica et Cosmochimica Acta*, **63,** 533−556.

Wang, L., Kusky, T.M. & Li, S.Z., 2010. Structural geometry of an exhumed UHP terrane in the eastern Sulu Orogen, China: implications for continental collisional processes. *Journal of Structural Geology*, **32,** 423−444.

Wiedenbeck, M., Alle, P., Corfu, F. et al., 1995. Three natural zircon standards for U−Th−Pb, Lu−Hf, trace element and REE analyses. *Geostandards newsletter*, **19,** 1−23.

FIGURE S1

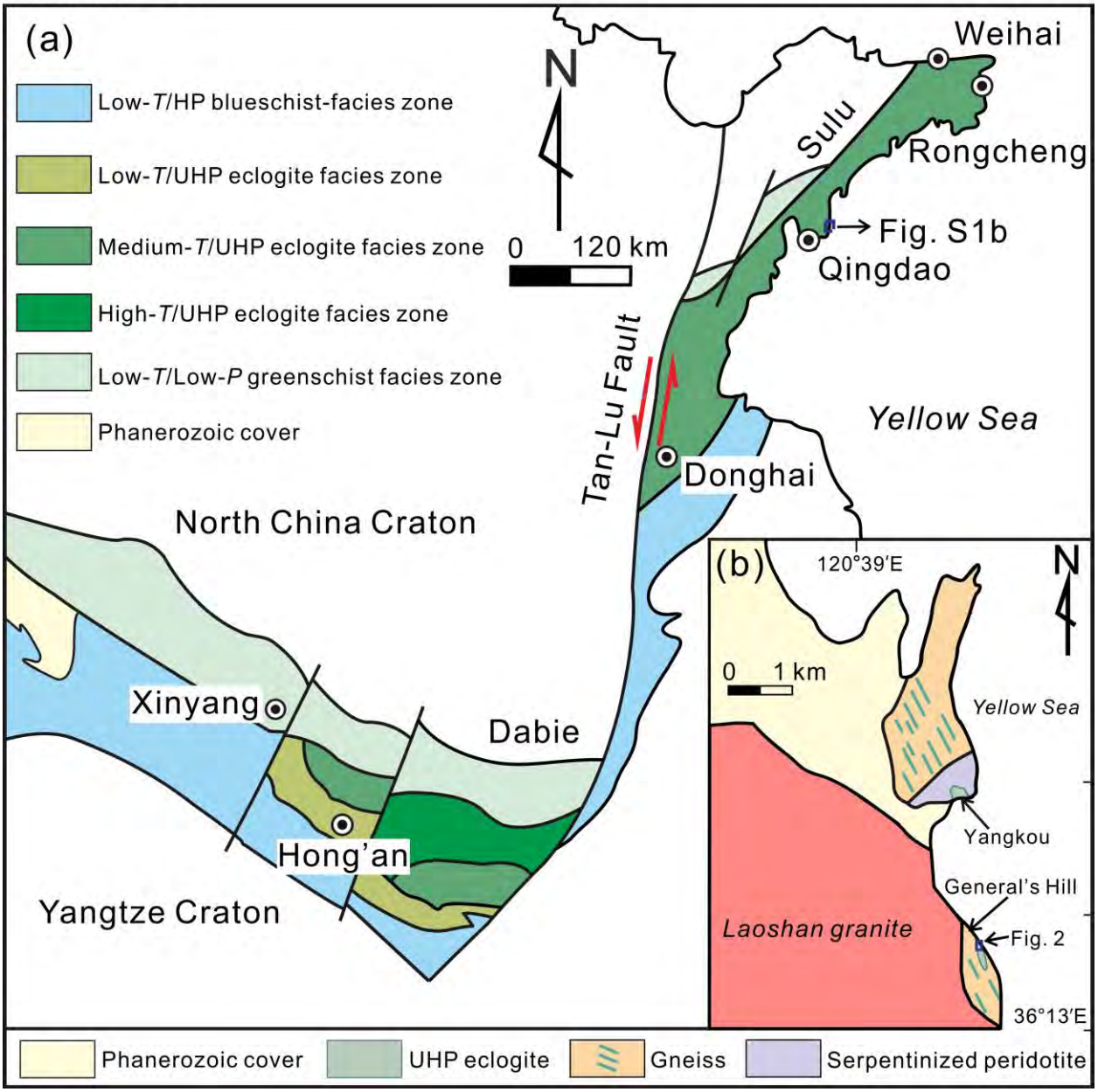

Figure S1. (a) Metamorphic facies map of the Dabie–Sulu orogen in central–eastern China; (b) Simplified geological map of the General's Hill locality (after Wang *et al*., 2010).

Figure S2a

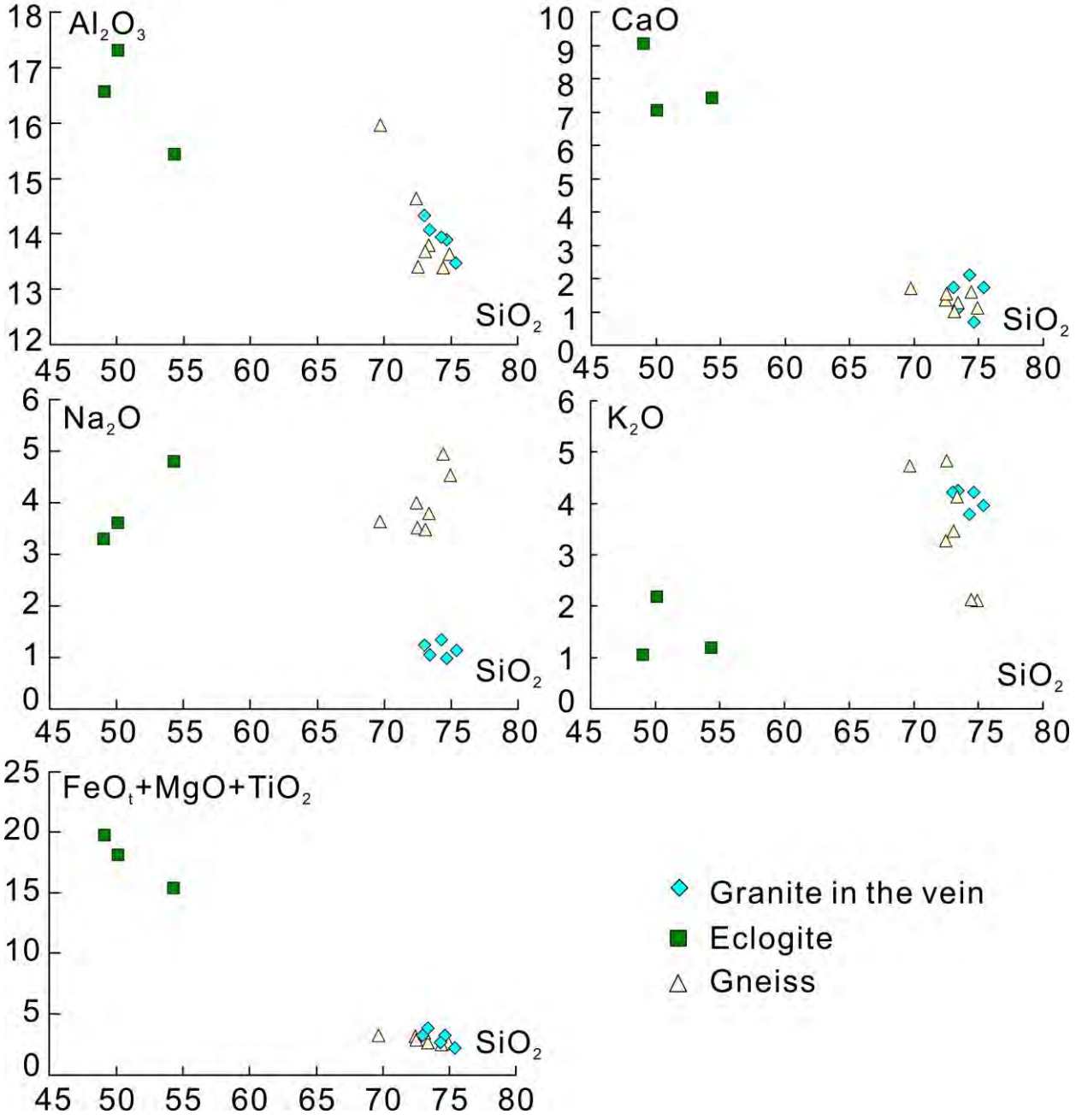

Figure S2. (a) Major element compositions for the granite in the composite veins, the host eclogite and the surrounding gneiss at General's Hill. Major oxides are plotted as weight percent.

CONTINUED

Figure S2b

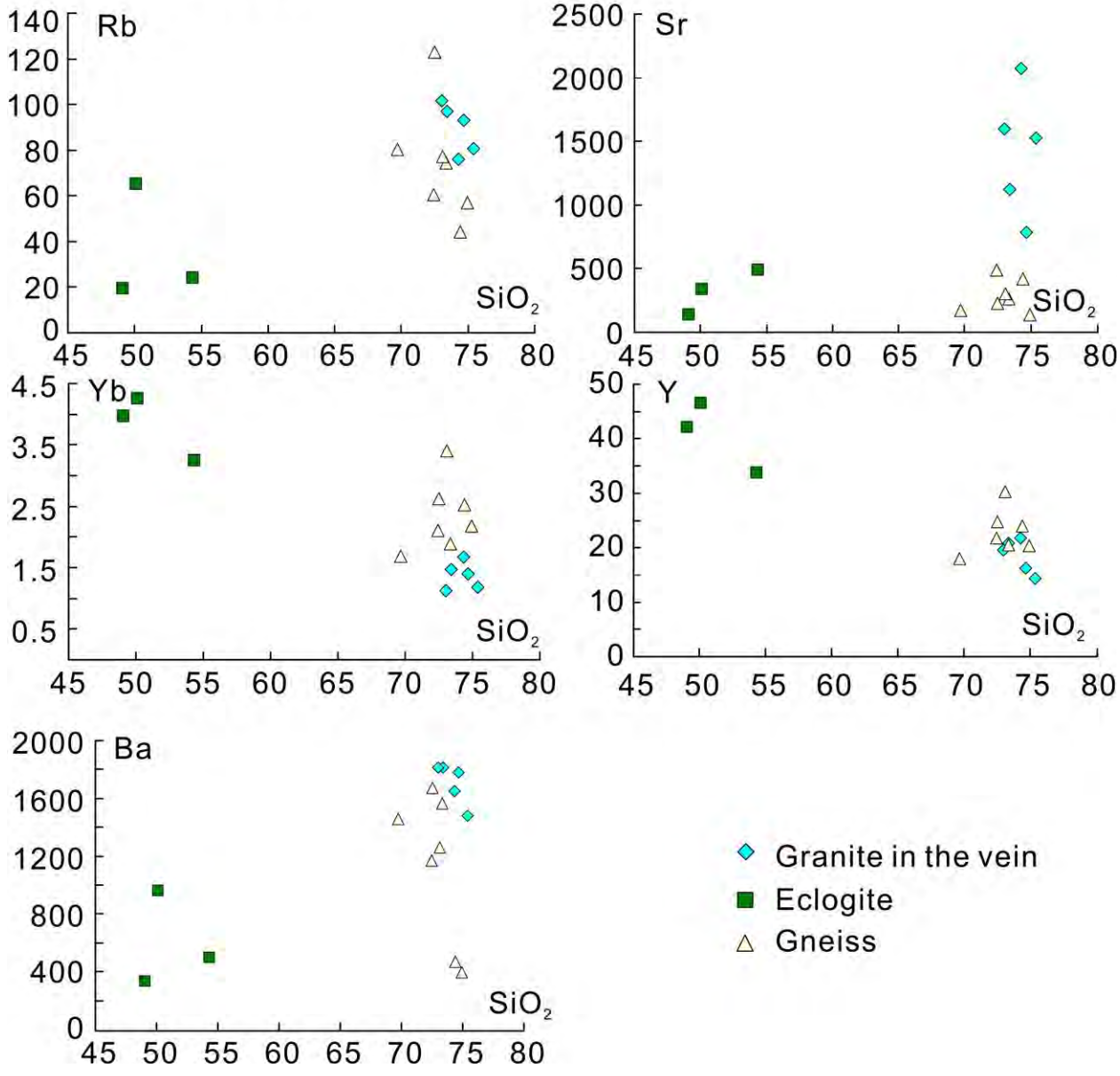

Figure S2. (b) Trace element compositions for the granite in the composite veins, the host eclogite and the surrounding gneiss at General's Hill. Trace elements are plotted as parts per million.

FIGURE S3

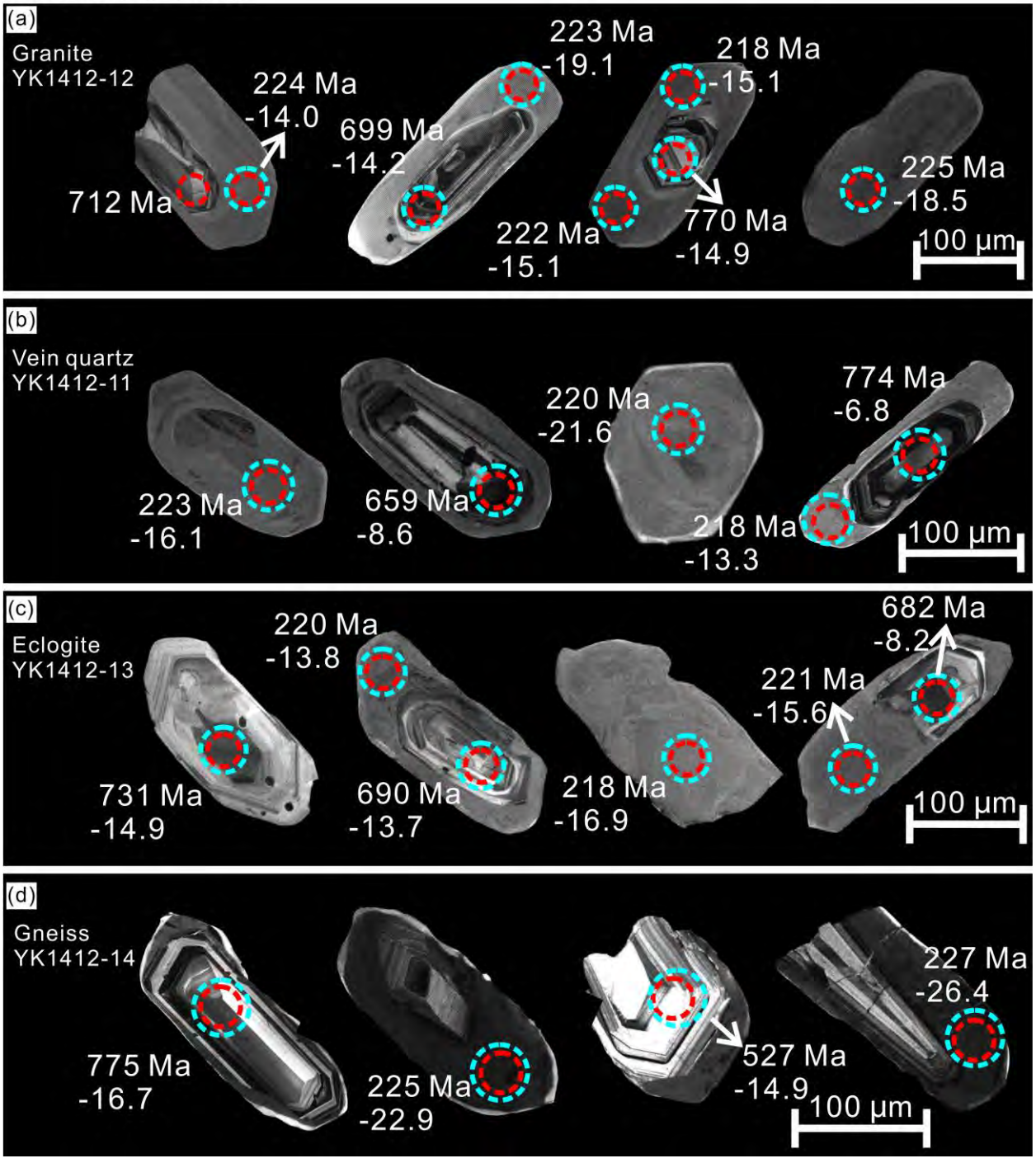

Figure S3. Cathodoluminescence images of representative zircon grains from one composite vein, the host eclogite and the surrounding gneiss. Circles mark the locations of LA(MC)-ICP-MS U–Pb (red) and Hf (light blue) isotope analyses.

FIGURE S4

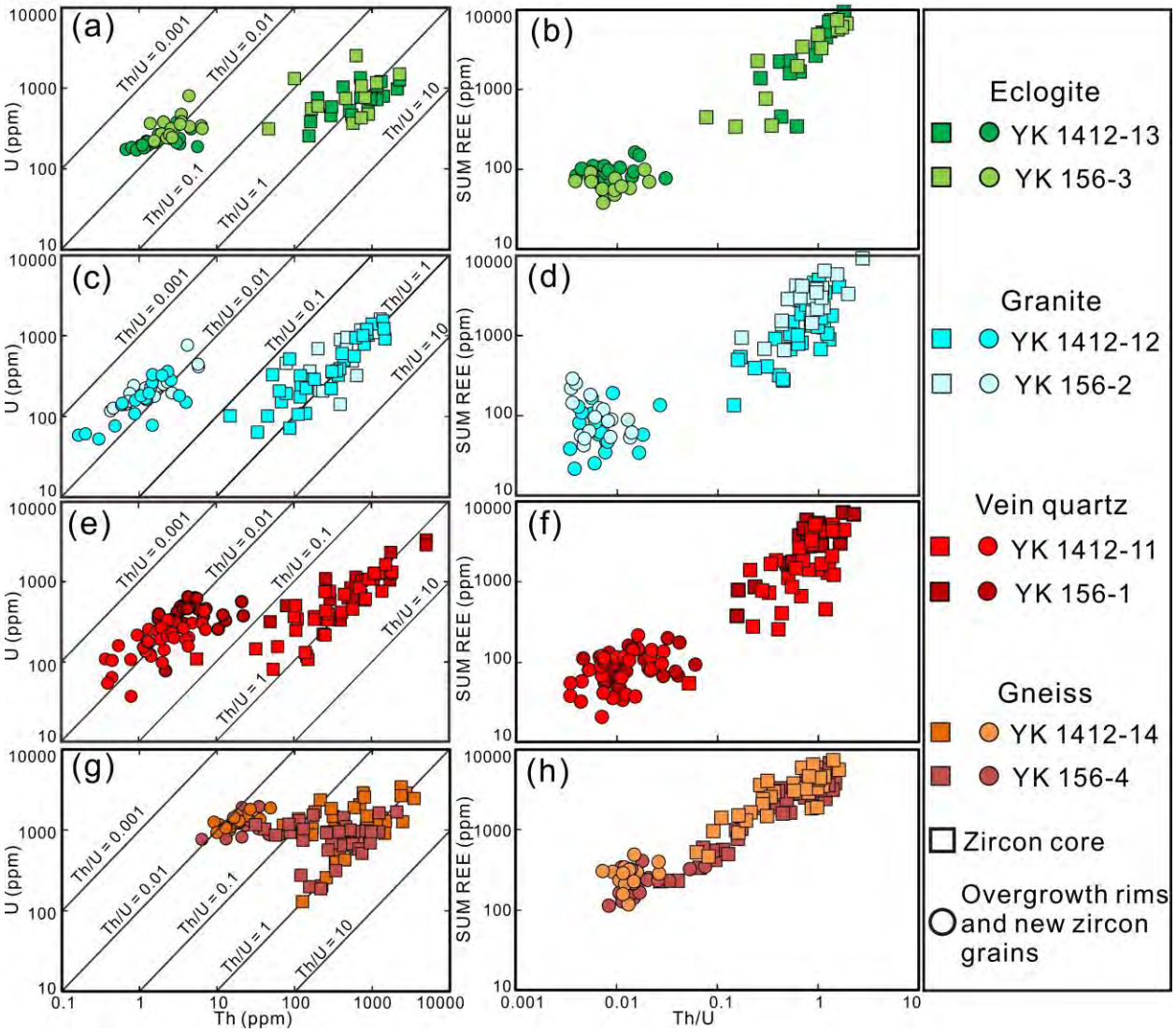

Figure S4. Plots of Th *vs.* U and Th/U vs. REE contents for zircon from the host eclogites (a, b), the granite (c, d) and vein quartz (e, f) from the composite veins, and the surrounding gneisses (g, h).

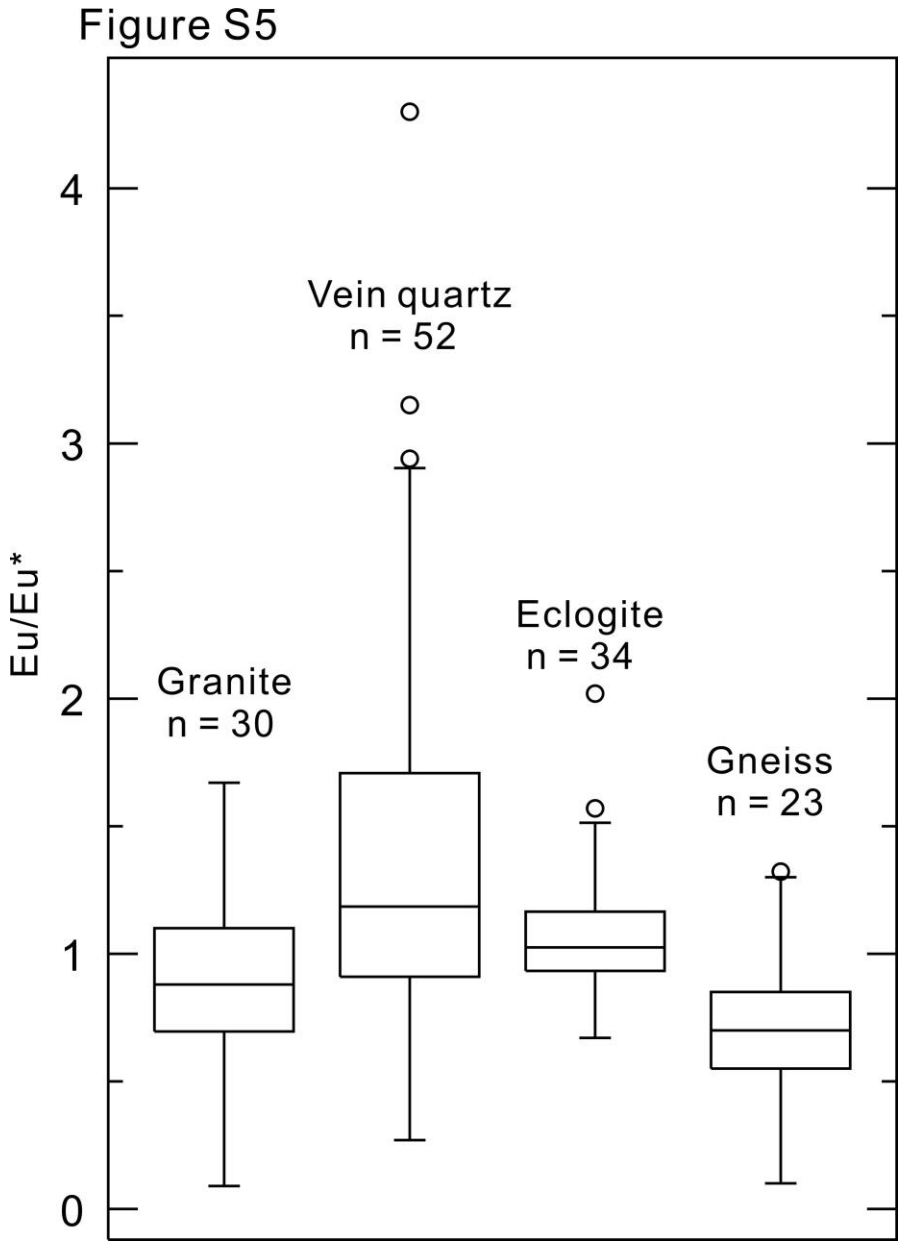

Figure S5. Box-and-whisker plots to show the Eu/Eu* ratios for overgrowth rims and/or new zircon grains from the granite and vein quartz in the composite veins, the host eclogites and the surrounding gneisses.

FIGURE S6

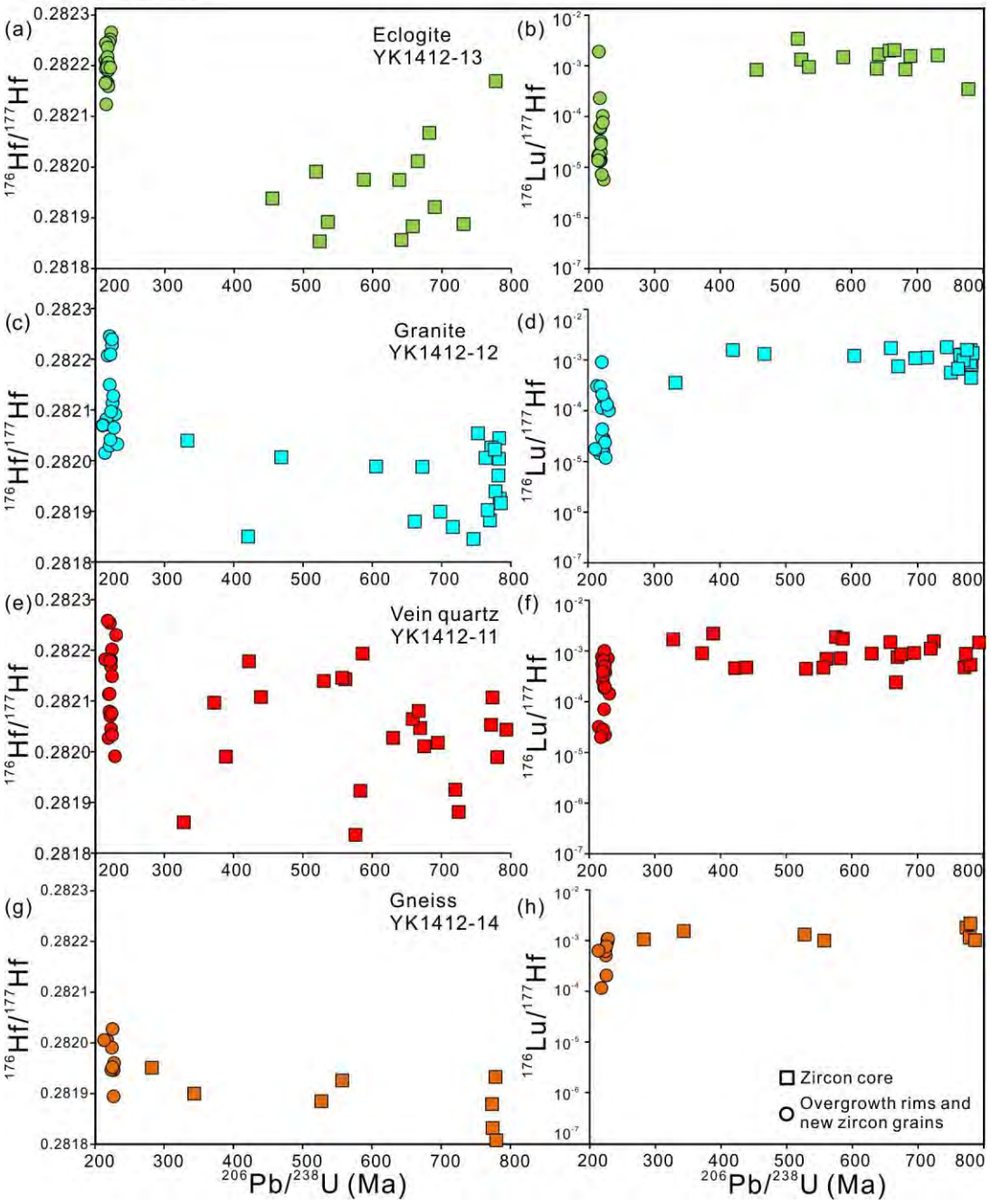

Figure S6. $^{176}Hf/^{177}Hf$ ratios and $^{176}Lu/^{177}Hf$ ratios *vs.* U–Pb ages for zircon from the host eclogite (a, b), the granite (c, d) and vein quartz (e, f) of the composite vein, and the surrounding gneiss (g, h).

FIGURE S7

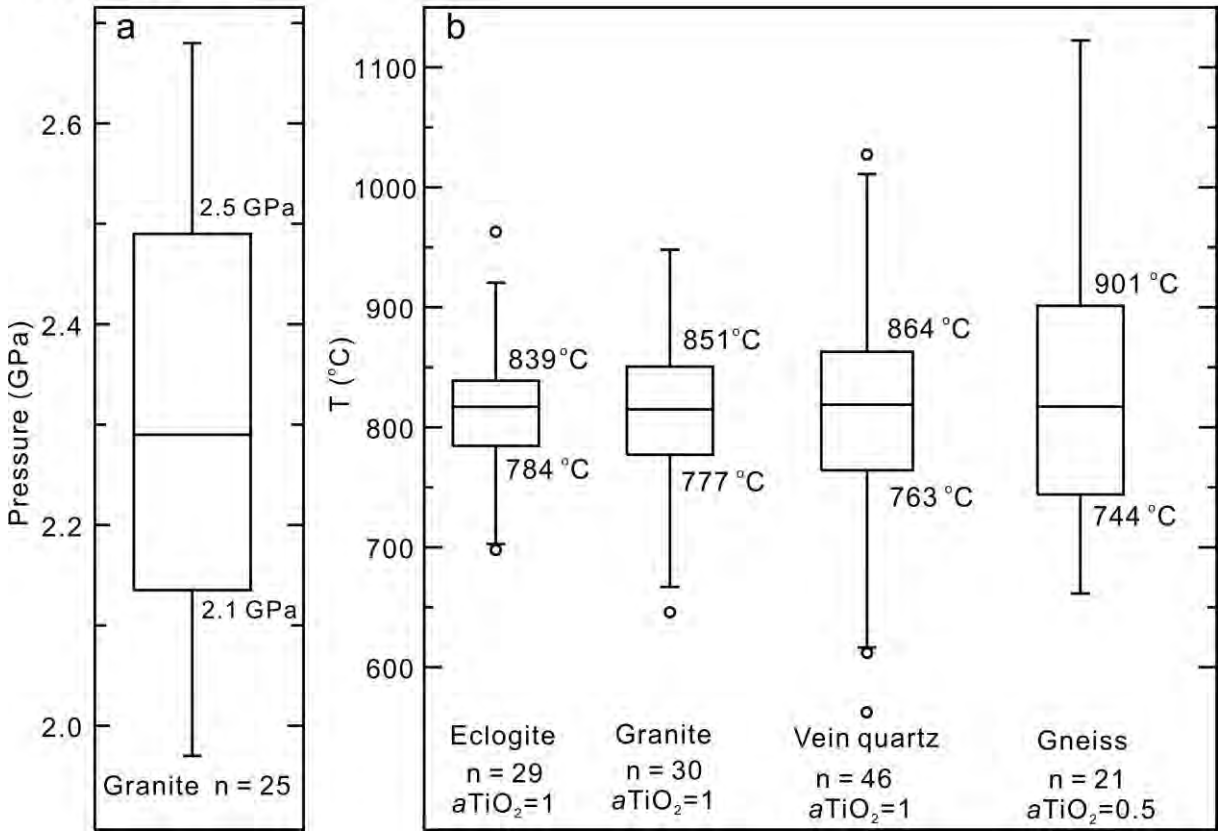

Figure S7. Box-and-whisker plots for the granite in the composite veins to show: (a) the distribution of pressures calculated at *T* of 800 °C based on the Si-in-phengite barometer of Caddick & Thompson (2008, equation 8), and (b) the distribution of temperatures calculated at 2.5 GPa for overgrowth rims and/or new grains of zircon from the host eclogite, the composite veins, and the surrounding gneiss, based on the Ti-in-zircon thermometer of Ferry & Watson (2007).

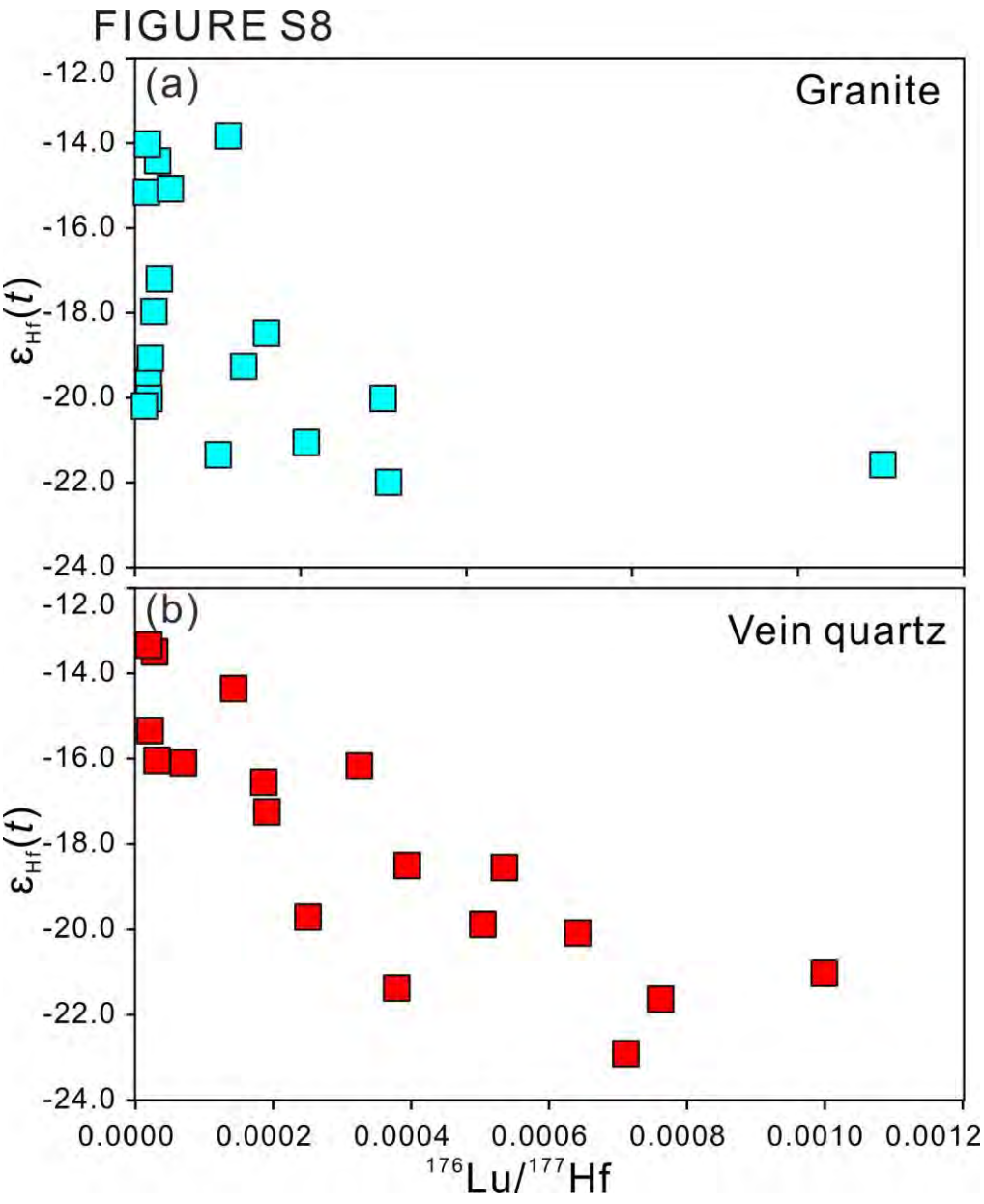

Figure S8. Covariation diagram of $^{176}Lu/^{177}Hf$ ratios *vs.* εHf(*t*) values (corrected to *t* = 221 Ma) of overgrowth rims and new grains of zircon from the composite veins; (a) granite and (b) vein quartz.

Table S1. Summary of published data on the characterization of supercritical fluids in subduction zones.

Metamorphic belt	Lithology	Host mineral	Peak P–T conditions	Stage of crystallization	Mineral association	Fluid nature	Fluid source	Reference
Dabie belt								
Matrix Rutile grains	UHP quartzite	*n.a.*	P = 3.0–4.5 GPa, T = 750–850 °C	Retrograde amphibolite facies metamorphism	*n.a.*	Separation of a supercritical fluid	Regionally generated in the local subducted slice	Gao et al., 2014
Multiphase solid inclusions	Amphibolite (retrogressed from eclogite)	UHP garnet	P = ~3.3 GPa, T = ~670 °C	Peak metamorphism	Kfs + Qz + Cal + Zrn ± Amp ± Cpx ± Grt ± Ap	Silicate-rich supercritical fluid	Penetrating from country rock gneiss	Huang & Xiao, 2015
Sulu belt								
Multiphase solid inclusions	Kyanite quartzite	UHP kyanite	P = ~3.5–4.0 GPa, T = 840 ± 50 °C	Peak metamorphism	Pg + Ms + Anh ± Crn ± "Alu-type" sulphate ± Zrn ± Cal ± Chl ± SiO_2 ± Brt ± Py ± Ap	Supercritical silicate-rich aqueous fluid/intermediate alkali-alumino-silicate aqueous solutions	Internally derived by dehydration of host rocks	Ferrando et al. 2005; Frezzotti et al., 2007
Multiphase solid inclusions	Eclogite	UHP Garnet and kyanite	P = ~3.5–4.0 GPa, T = 840 ± 50 °C	Peak metamorphism	Pg + Rt + Ap ± Amp ± Zn-St ± Mag ± Pl ± Zrn ± Py ± "Aln-type" sulphate ± Zn–Mg–Fe–Al–Ti Spl	Supercritical silicate-rich aqueous fluid	Internally derived by dehydration of host rocks	Ferrando et al. 2005; Frezzotti et al., 2007
Multiphase solid inclusions	Eclogite	UHP Kyanite, zoisite and allanite	P = 3.0–4.5 GPa, T = 700–800 °C	Peak metamorphism	Ms + Cal + Anh + Mag+ Py + Ap + Clt with liquid and gas phase	Supercritical silicate-rich aqueous fluid	Internally derived from eclogite	Zhang Z.M. et al., 2008
Fluid inclusions and mineral exsolutions	Eclogite	UHP omphacite	P = 3.0–4.5 GPa, T = 700–800 °C	Peak metamorphism	Hl + Qz + Cal + unknown silicates +Opq + a gas bubble + a liquid phase	High-salinity supercritical fluid	Internally derived from dissolutioin of norminally anhydrous minerals	Zhang Z.M. et al., 2007
Multiphase solid inclusions	Eclogite	UHP garnet	P = ~4.5 GPa, T = ~800 °C	Late prograde to peak of UHP metamorphism	Brt + Bt ± Kfs ± Ep ± Ab ± Zrn	Silicate-rich supercritical fluid	Internally buffered by dehydration	Wang et al., 2016
Western Gneiss Region, Norway								
Multiphase solid inclusions in mantle rock	Garnet websterite	UHP spinel in turn enclosed in garnet	P = 3.9–4.3 GPa, T = 850–900 °C	Peak metamorphism	Micro-Dia + Ap + Mnz + Zrn + Kls + Ti-Pg + KTiCrOx + $(BaCaMg)CO_3$ + Mgs + Dol + Crn + Per + barium sulfide + iron-nickel sulfide	COH-, sulfide-, and silicate-rich supercritical fluids	No specific source has been mentioned	van Roermund et al., 2002; Carswell & van Roermund, 2005; Malaspina et al., 2010
Polyphase solid inclusions in mantle rock	Garnet-phlogopite websterite	UHP garnet	P = 5.5 GPa, T = 800 °C	Peak metamorphism	Amp + Chl + Al-silicate + Fe-Pb-sulfides + Y-phosphate + Al-Fe-Mg oxides + Al-Spl + Dia + C-phase	H-C-N-O-F-P-S-Cl metal-bearing supercritical fluid	No conclusion in the original paper	Vrijmoed et al., 2008
Erzgebirge, Germany								
Multiphase solid inclusions	UHP gneiss	Garnet	P >4.5 GPa, T = 1000 °C	Peak metamorphism	Micro-Dia + Phl + Qz+ Pg + Ph + Ap + Rt	supercritical COH fluid rich in alkalies and silica	not strengthened	Stöckhert et al., 2001; Stöckhert et al., 2009
nanometric inclusions	Garnet–quartz–feldspathic gneiss	Diamond included in zircon	P = 7–8 GPa, T = 1100 °C	Peak metamorphism	SiO_2, $CaCO_3$, KCl, $KAlSi_3O_8$, $BaCO_3$, TiO_2, Fe_xO_y, H_2O	Silicic-hydrous-saline high-density fuid	Originated from their host rocks	Dobrzhinetskaya et al., 2013
nanometric inclusions	Quartzo-feldspatic rocks	Microdiamond	P = 7–8 GPa, T = 1100 oC	Peak metamorphism	SiO_2 + Kfs+ Ky + archerite	COH-rich multicomponent supercritical fluid rich in K, Al, Si, P, Ti	Derived from a local crustal source	Dobrzhinetskaya et al., 2003b
Kokchetav Massif								
nanometer-size inclusions	Dolomite marble and garnet–quartz–pyroxene rock	Microdiamond	P = 4.0–6.0 GPa, T = ~1000 °C	Peak metamorphism	Phosphate + Chl + sulfate/sulfide	SiO_2-poor, ultrapotassic COH fluid	Crustal derived	Hwang et al., 2005, 2006
Multiple inclusion pockets	Felsic gneiss	UHP garnet, zircon	P = 4.0–6.0 GPa, T = ~1000 °C	Peak metamorphism	Dia + Qz + Ph + Phl + Ab + Kfs + Rt + Ap + Ttn + Bt + Chl + Gr	COH-rich multicomponent supercritical fluid	Derived from the subducted metasediments and interacted with mantle-derived fluid	Dobrzhinetskaya et al., 2003a
Nanometric inclusions	Felsic gneiss	Microdiamond	P = 4.0–6.0 GPa, T = ~1000 °C	Peak metamorphism	SiO_2 + Rt + Zrn + Brt + Mgs + Fe_xO_y + Cr_2O_3 +ThxOy + FeCr2O4 + Fe-rich Py	COH-rich multicomponent supercritical fluid	Derived from the subducted metasediments and interacted with mantle-derived fluid	Dobrzhinetskaya et al., 2003a
Doria Maira								
Multiphase solid inclusions	Pyrope whiteschist	UHP garnet	P = 4.0–4.3 GPa, T = ~730 °C	Peak metamorphism	Mg-Chl + Na-K-Phl + Cl-rich Ap + Zn-rich Py + fluid phase as daughter minerals, Talc and magnesite as step-daughter minerals	Intermediate Al-Si aqueous solutions enriched in Mg, Fe, Na, K, Ca, P, Cl, S, CO_3^{2-}, LILE, U, Th	Internal origin, likely originated by dehydration reactions	Ferrando et al., 2009
Moldanubian Zone								
Multiphase solid inclusions in mantle rocks	Phlogopite- and apatite-bearing spinel–garnet perodotite	UHP chromian spinel	P = 2.3–3.5 GPa, T = 850– 1030 °C	Peak metamorphism	Phl + Dol + Ap + Cal + Chl + Fe-Ni sulfide + Gn + Mnz + Th-oxide + Rt + Gr + Mhb	Carbonatite melt or supercritical fluid	Metasomatized from subducted crustal rocks as a result of prograde dehydration or dehydration melting	Naemura et al., 2009

Note: mineral names are abbreviated according to the recommendations of Whitney & Evans (2010).

REFERENCES

Carswell, D.A. & van Roermund, H.L., 2005. On multi-phase mineral inclusions associated with microdiamond formation in mantle-derived peridotite lens at Bardane on Fjørtoft, west Norway. *European Journa of Mineralogy*, **17,** 31–42.

Dobrzhinetskaya, L.F., Green, H.W., Bozhilov, K.N., Mitchell, T.E. & Dickerson, R.M., 2003a. Crystallization environment of Kazakhstan microdiamond: evidence from nanometric inclusions and mineral associations. *Journal of Metamorphic Geology*, **21,** 425–437.

Dobrzhinetskaya, L.F., Green, H.W., Weschler, M. *et al.,* 2003b. Focused ion beam technique and transmission electron microscope studies of microdiamonds from the Saxonian Erzgebirge, Germany. *Earth and Planetary Science Letters*, **210,** 399–410.

Dobrzhinetskaya, L.F., Wirth,R., Green,H.W., Schreiber,A. & O'Bannon, E., 2013. First find of polycrystalline diamond in ultrahigh‐pressure metamorphic terrane of Erzgebirge, Germany. *Journal of Metamorphic Geology*, **31,** 5–18.

Ferrando, S., Frezzotti, M., Dallai, L. & Compagnoni, R., 2005. Multiphase solid inclusions in UHP rocks (Su-Lu, China): remnants of supercritical silicate-rich aqueous fluids released during continental subduction. *Chemical Geology*, **223,** 68–81.

Ferrando, S., Frezzotti, M.L., Petrelli, M. & Compagnoni, R., 2009. Metasomatism of continental crust during subduction: the UHP whiteschists from the Southern Dora-Maira Massif (Italian Western Alps). *Journal of Metamorphic Geology*, **27,** 739–756.

Frezzotti, M.L., Ferrando, S., Dallai, L. & Compagnoni, R., 2007. Intermediate alkali–alumino-silicate aqueous solutions released by deeply subducted continental crust: fluid evolution in UHP OH-Rich topaz–kyanite quartzites from Donghai (Sulu, China). *Journal of Petrology*, **48,** 1219–1241.

Gao, X.Y., Zheng, Y.F., Xia, X.P. & Chen, Y.X., 2014. U–Pb ages and trace elements of metamorphic rutile from ultrahigh-pressure quartzite in the Sulu orogen. *Geochimica et Cosmochimica Acta*, **143,** 87–114.

Huang, J. & Xiao, Y., 2015. Element mobility in mafic and felsic ultrahigh-pressure metamorphic rocks from the Dabie UHP Orogen, China: insights into supercritical liquids in continental subduction zones. *International Geological Review*, **57,** 1103–1129.

Hwang, S.L., Shen, P., Chu, H.T. *et al.,* 2005. Crust-derived potassic fluid in metamorphic microdiamond. *Earth and Planetary Science Letters*, **231,** 295–306.

Hwang, S.L., Chu, H.T., Yui, T.F. *et al.,* 2006. Nanometer-size P/K-rich silica glass (former melt) inclusions in microdiamond from the gneisses of Kokchetav and Erzgebirge massifs: Diversified characteristics of the formation media of metamorphic microdiamond in UHP rocks due to host-rock buffering. *Earth and Planetary Science Letters*, **243,** 94–106.

Malaspina, N., Scambelluri, M., Poli, S., Van Roermund, H.L.M. & Langenhorst, F., 2010. The oxidation state of mantle wedge majoritic garnet websterites metasomatised by C-bearing subduction fluids. *Earth and Planetary Science Letters*, **298,** 417–426.

Naemura, K., Hirajima, T. & Svojtka, M., 2009. The pressure–temperature path and the origin of phlogopite in spinel–garnet peridotites from the Blanský Les Massif of the Moldanubian Zone, Czech Republic. *Journal of Petrology*, **50,** 1795–1827.

Naemura, K., Hirajima, T. & Svojtka, M., 2009. The pressure–temperature path and the origin of phlogopite in spinel–garnet peridotites from the Blanský Les Massif of the Moldanubian Zone, Czech Republic. *Journal of Petrology*, **50,** 1795–1827.

Stöckhert, B., Duyster, J., Trepmann, C. & Massonne, H.J., 2001. Microdiamond daughter crystals precipitated

from supercritical COH+ silicate fluids included in garnet, Erzgebirge, Germany. *Geology*, **29,** 391−394.

Stöckhert, B., Trepmann, C. & Massonne, H.J., 2009. Decrepitated UHP fluid inclusions: about diverse phase assemblages and extreme decompression rates (Erzgebirge, Germany). *Journal of Metamorphic Geology*, **27,** 673−684.

van Roermund, H.L., Carswell, D.A., Drury, M.R. & Heijboer, T.C., 2002. Microdiamonds in a megacrystic garnet websterite pod from Bardane on the island of Fjørtoft, western Norway: evidence for diamond formation in mantle rocks during deep continental subduction. *Geology*, **30,** 959−962.

Vrijmoed, J.C., Smith, D.C. & Van Roermund, H.L.M., 2008. Raman confirmation of microdiamond in the Svartberget Fe-Ti type garnet peridotite, Western Gneiss Region, Western Norway. *Terra Nova*, **20,** 295−301.

Wang, S.J., Wang, L., Brown, M. & Feng, P., 2016. Multi-stage barite crystallization in partially melted UHP eclogite from the Sulu belt, China. *American Mineralogist*, **101,** 564−579.

Whitney, D.L. & Evans, B.W., 2010. Abbreviations for names of rock-forming minerals. *American Mineralogist*, **95,** 185.

Zhang, Z.M., Shen, K., Liou, J.G. & Zhao, X., 2007. Fluid inclusions associated with exsolved quartz needles in omphacite of UHP eclogites, Chinese Continental Scientific Drilling Main Drill Hole. *International Geological Review*, **49,** 479−486.

Zhang, Z.M., Shen, K., Sun, W.D. *et al.,* 2008. Fluids in deeply subducted continental crust: petrology, mineral chemistry and fluid inclusion of UHP metamorphic veins from the Sulu orogen, eastern China. *Geochimica et Cosmochimica Acta*, **72,** 3200−3228.

Table S2. Sample numbers, lithology, GPS coordinates and mineral assemblages.

Sample	Lithology	Latitude (°N)	Longitude (°E)	Mineral assemblage	Remarks
YK1412-11	Vein quartz of the composite veins	36°13′43. 1″	120°40′42.7″	Qz + rare Bt and Zrn	Rock set 1
YK1412-12	Granite of the composite veins	36°13′43.1″	120°40′42.7″	Qz + Ph + Pl + Kfs + Ep/Czo + Grt + Bt + Ap + Zrn + Ttn + Rare Ilm and Rt	
YK1412-13	Eclogite	36°13′43.1″	120°40′42.7″	Hb + Grt + Qz + Ap + Zrn + Symplectites after Omp, Grt and Ph	
YK1412-14	Gneiss	36°13′43.1″	120°40′43.2″	Qz + Pl + Kfs + Ph + Ep/Czo + Zrn + Ttn + Ap	
YK156-1	Vein quartz of the composite veins	36°13′43. 4″	120°40′43.2″	Qz + minor Ph, Bt and Zrn	Rock set 2
YK156-2	Granite of the composite veins	36°13′43.4″	120°40′43.2″	Qz + Ph + Pl + Kfs + Ep/Czo + Grt + Bt + Ap + Zrn + Ttn + Rare Ilm and Rt	
YK156-3	Eclogite	36°13′43.4″	120°40′43.2″	Hb + Grt + Qz + Ap + Zrn + Symplectites after Omp, Grt and Ph	
YK156-4	Gneiss	36°13′43.2″	120°40′43.7″	Qz + Pl + Kfs + Ph + Ep/Czo + Zrn + Ttn + Ap	
YK156-5	Granite of the composite veins	36°13′43.2″	120°40′42.6″	Qz + Ph + Pl + Kfs + Ep/Czo + Grt + Bt + Ap + Zrn + Ttn + Rare Ilm and Rt	
YK156-6	Granite of the composite veins	36°13′43.6″	120°40′42.9″	Qz + Ph + Pl + Kfs + Ep/Czo + Grt + Bt + Ap + Zrn + Ttn + Rare Ilm and Rt	
YK156-7	Granite of the composite veins	36°13′42.0″	120°40′43.1″	Qz + Ph + Pl + Kfs + Ep/Czo + Grt + Bt + Ap + Zrn + Ttn + Rare Ilm and Rt	
YK1510-2	Eclogite	36°13′40.1″	120°40′42.3″	Hb + Grt + Qz + Ap + Zrn + Symplectites after Omp, Grt and Ph	
YK137-12	Gneiss	36°13′43.3″	120°40′43.5″	Qz + Pl + Kfs + Ph + Ep/Czo + Zrn + Ttn + Ap	
YK137-13	Gneiss	36°13′43.3″	120°40′43.5″	Qz + Pl + Kfs + Ph + Ep/Czo + Zrn + Ttn + Ap	
YK1412-9	Gneiss	36°13′43.4″	120°40′43.2″	Qz + Pl + Kfs + Ph + Ep/Czo + Zrn + Ttn + Ap	
YK1412-10	Gneiss	36°13′43.4″	120°40′43.2″	Qz + Pl + Kfs + Ph + Ep/Czo + Zrn + Ttn + Ap	
YK156-11	Gneiss	36°13′43.0″	120°40′43.5″	Qz + Pl + Kfs + Ph + Ep/Czo + Zrn + Ttn + Ap	

Note: mineral names are abbreviated according to the recommendations of Whitney & Evans (2010).

REFERENCE

Whitney, D.L. & Evans, B.W., 2010. Abbreviations for names of rock-forming minerals. *American Mineralogist*, **95,** 185.

Table S3a. Major element compositions of phengite in the granite of the composite veins.

Spot No.	1	2	3	4	5	6	7	8	9	10	11	12	13	14	15	16	17	18	19	20	21	22	23	24	25
SiO_2	48.95	49.14	49.11	48.59	47.46	48.87	48.45	48.63	49.19	48.77	49.00	48.62	48.60	47.39	49.13	49.22	49.62	49.53	49.73	49.37	49.31	49.55	49.59	49.66	49.78
TiO_2	0.63	0.50	0.62	0.61	0.41	0.36	0.48	0.48	0.53	0.41	0.51	0.53	0.60	0.41	0.52	0.67	0.50	0.53	0.54	0.53	0.58	0.70	0.56	0.63	0.60
Al_2O_3	30.42	29.43	30.18	30.26	30.27	30.59	29.12	29.41	29.95	29.94	29.19	29.92	30.33	30.17	29.22	29.91	29.11	29.17	28.88	28.98	28.40	28.90	28.09	27.73	27.42
FeO_t	2.84	3.21	3.26	3.14	3.00	3.01	3.31	4.11	2.76	3.24	3.52	3.13	3.01	3.40	2.90	2.95	3.05	2.91	2.94	3.05	3.31	3.23	3.03	3.26	3.51
MnO	0.00	0.02	0.00	0.00	0.00	0.03	0.04	0.07	0.10	0.00	0.07	0.03	0.07	0.00	0.00	0.06	0.09	0.03	0.01	0.00	0.03	0.04	0.03	0.00	0.00
MgO	1.89	2.14	1.78	1.94	1.77	1.72	2.16	1.89	2.23	1.97	2.16	1.92	1.94	2.12	2.23	2.08	2.45	2.33	2.20	2.48	2.65	2.46	2.59	2.64	2.73
CaO	0.03	0.00	0.00	0.01	0.00	0.00	0.00	0.00	0.02	0.00	0.00	0.02	0.01	0.00	0.00	0.00	0.02	0.00	0.00	0.00	0.00	0.00	0.01	0.03	0.01
Na_2O	0.49	0.41	0.43	0.41	0.46	0.40	0.35	0.41	0.36	0.43	0.33	0.34	0.41	0.44	0.46	0.40	0.41	0.43	0.45	0.31	0.28	0.39	0.37	0.38	0.33
K_2O	9.50	9.45	9.49	9.56	9.05	9.74	9.53	9.24	9.40	9.27	9.41	9.41	9.26	9.47	9.45	9.64	9.34	9.19	9.37	9.41	9.53	9.44	9.37	9.56	9.61
Total	94.75	94.30	94.86	94.52	92.43	94.73	93.44	94.25	94.54	94.03	94.19	93.93	94.23	93.41	93.92	94.93	94.58	94.11	94.12	94.14	94.10	94.70	93.64	93.89	94.01
O	11	11	11	11	11	11	11	11	11	11	11	11	11	11	11	11	11	11	11	11	11	11	11	11	11
Si	3.31	3.34	3.32	3.30	3.29	3.31	3.33	3.32	3.33	3.32	3.34	3.32	3.31	3.25	3.35	3.32	3.36	3.37	3.39	3.36	3.36	3.36	3.40	3.39	3.40
Ti	0.03	0.03	0.03	0.03	0.02	0.02	0.02	0.02	0.03	0.02	0.03	0.03	0.03	0.02	0.03	0.03	0.03	0.03	0.03	0.03	0.03	0.04	0.03	0.03	0.03
Al	2.42	2.36	2.41	2.42	2.47	2.44	2.36	2.37	2.39	2.41	2.35	2.41	2.43	2.44	2.35	2.38	2.32	2.34	2.32	2.33	2.28	2.31	2.27	2.23	2.21
Fe^{3+}	0.00	0.00	0.00	0.00	0.00	0.00	0.00	0.00	0.00	0.00	0.00	0.00	0.00	0.00	0.00	0.00	0.00	0.00	0.00	0.00	0.00	0.00	0.00	0.00	0.00
Fe^{2+}	0.16	0.18	0.18	0.18	0.17	0.17	0.19	0.23	0.16	0.18	0.20	0.18	0.17	0.19	0.17	0.17	0.17	0.17	0.17	0.17	0.19	0.18	0.17	0.19	0.20
Mn	0.00	0.00	0.00	0.00	0.00	0.00	0.00	0.00	0.01	0.00	0.00	0.00	0.00	0.00	0.00	0.00	0.01	0.00	0.00	0.00	0.00	0.00	0.00	0.00	0.00
Mg	0.19	0.22	0.18	0.20	0.18	0.17	0.22	0.19	0.22	0.20	0.22	0.20	0.20	0.22	0.23	0.21	0.25	0.24	0.22	0.25	0.27	0.25	0.26	0.27	0.28
Ca	0.00	0.00	0.00	0.00	0.00	0.00	0.00	0.00	0.00	0.00	0.00	0.00	0.00	0.00	0.00	0.00	0.00	0.00	0.00	0.00	0.00	0.00	0.00	0.00	0.00
Na	0.06	0.05	0.06	0.05	0.06	0.05	0.05	0.05	0.05	0.06	0.04	0.05	0.05	0.06	0.06	0.05	0.05	0.06	0.06	0.04	0.04	0.05	0.05	0.05	0.04
K	0.82	0.82	0.82	0.83	0.80	0.84	0.83	0.80	0.81	0.81	0.82	0.82	0.80	0.83	0.82	0.83	0.81	0.80	0.81	0.82	0.83	0.82	0.82	0.83	0.84
Cation	7.00	7.00	7.00	7.00	7.00	7.00	7.00	7.00	7.00	7.00	7.00	7.00	7.00	7.00	7.00	7.00	7.00	7.00	7.00	7.00	7.00	7.00	7.00	7.00	7.00

Table S3b. Major and trace element compositions of the composite granite–quartz veins, the host eclogite and the surrounding gneiss. Unit is wt% for major elements and ppm for trace elements, respectively.

Rock type	Granite					Vein quartz	Eclogite			Gneiss						
Sample	YK1412-12	YK156-2	YK156-5	YK156-6	YK156-7	YK1412-11	YK1412-13	YK156-3	YK1510-2	YK1412-14	YK156-4	YK156-11	YK137-12	YK137-13	YK1412-9	YK1412-10
SiO_2	75.39	74.66	74.31	73.40	73.01	99.10	54.34	50.13	49.09	74.92	73.36	72.44	72.51	73.11	74.43	69.70
TiO_2	0.19	0.23	0.23	0.23	0.28	0.01	1.45	1.46	1.80	0.24	0.25	0.31	0.31	0.26	0.22	0.31
Al_2O_3	13.47	13.89	13.94	14.07	14.33	0.14	15.43	17.31	16.56	13.63	13.80	14.63	13.40	13.68	13.40	15.96
FeO_t	1.44	1.91	1.81	2.43	2.10	0.02	9.15	11.56	13.10	1.64	1.81	2.23	1.93	2.31	1.74	1.85
MnO	0.02	0.02	0.01	0.02	0.01	0.01	0.15	0.18	0.22	0.04	0.03	0.03	0.04	0.05	0.03	0.04
MgO	0.52	1.03	0.59	1.14	0.79	0.07	4.72	5.07	4.86	0.65	0.51	0.59	0.59	0.83	0.46	1.01
CaO	1.72	0.68	2.11	1.10	1.73	0.28	7.41	7.05	9.03	1.11	1.29	1.36	1.54	1.01	1.60	1.71
Na_2O	1.13	0.99	1.35	1.06	1.25	0.07	4.79	3.60	3.30	4.54	3.79	4.00	3.52	3.48	4.94	3.64
K_2O	3.96	4.21	3.79	4.26	4.21	0.03	1.19	2.17	1.05	2.11	4.13	3.28	4.83	3.46	2.12	4.74
P_2O_5	0.05	0.08	0.06	0.10	0.09	0.01	0.44	0.30	0.18	0.08	0.08	0.10	0.09	0.08	0.06	0.09
LOI	1.53	2.06	1.48	1.84	1.78	0.07	0.92	1.04	0.46	0.70	0.74	1.04	0.73	1.30	0.60	0.48
Total	99.44	99.77	99.69	99.65	99.58	99.81	99.99	99.87	99.65	99.66	99.78	100.01	99.49	99.57	99.62	99.53
Li	10.5	19.4	13.6	22.6	15.7	0.18	8.6	13.8	5.1	7.6	6.5	9.7	8.7	14.8	5.2	4.7
Be	1.5	1.6	1.0	1.5	1.4	0.08	1.4	1.4	1.2	1.9	1.7	1.5	2.6	2.0	1.1	1.7
Sc	3.2	3.3	2.9	4.0	3.6	0.28	24.9	27.8	34.7	4.1	3.7	4.0	3.7	3.7	3.6	4.2
V	14.2	25.3	17.3	29.9	25.2	2.22	189.2	190.0	250.3	20.4	19.5	24.8	19.4	21.6	14.9	22.4
Cr	4.3	6.5	3.9	6.5	5.2	0.34	93.6	93.5	44.8	3.9	4.0	6.8	4.9	4.4	3.8	4.2
Co	69.8	85.1	75.1	54.7	72.5	271.56	55.7	62.1	98.6	60.9	105.9	104.8	154.2	123.6	73.0	76.1
Ni	3.6	10.3	4.5	6.9	6.7	3.66	44.9	51.3	71.0	4.7	4.8	5.2	4.5	5.5	3.2	4.4
Cu	1.0	0.8	0.9	0.7	13.6	0.53	24.0	50.6	45.2	3.1	1.5	3.1	3.6	4.4	1.3	19.0
Zn	29.5	35.2	23.3	37.0	32.3	0.71	86.9	90.0	89.4	30.0	18.3	28.0	24.2	36.7	26.5	26.6
Ga	16.7	16.6	16.0	16.5	17.6	0.42	18.7	20.1	18.2	14.3	15.0	16.3	16.1	16.5	17.0	16.1
Rb	80.5	92.9	76.2	96.9	101.4	0.19	24.0	65.1	19.5	56.8	74.6	60.4	123.0	77.1	44.0	80.3
Sr	1525.9	785.9	2075.6	1125.4	1598.2	1.76	486.8	338.9	137.1	138.6	261.2	488.6	226.8	300.1	418.7	172.3
Y	14.3	16.3	21.8	20.8	19.6	0.06	33.8	46.6	42.0	20.3	20.5	21.8	24.8	30.3	23.9	17.9
Zr	137.9	170.1	167.1	175.7	213.9	0.38	179.4	221.9	177.3	166.2	157.5	220.4	194.5	141.3	188.0	140.6
Nb	10.9	6.2	9.2	6.9	9.1	0.14	8.4	10.2	11.4	9.8	11.1	10.6	12.4	10.2	12.1	10.3
Sn	1.0	0.9	0.8	1.2	1.2	0.03	1.4	1.6	1.4	1.1	1.3	1.5	2.1	1.2	1.5	1.2
Cs	0.6	0.9	0.7	0.9	0.8	0.01	0.4	1.4	0.4	0.5	0.5	0.4	0.8	0.7	0.5	0.6
Ba	1478.1	1779.0	1647.7	1816.1	1811.0	2.72	495.5	960.4	333.5	394.5	1562.6	1171.8	1671.9	1259.2	471.5	1457.2
La	43.4	54.0	50.7	69.8	66.4	0.11	33.3	33.2	13.6	46.2	42.3	62.5	42.5	55.0	50.3	53.5
Ce	77.1	98.3	91.0	123.7	118.2	0.21	68.3	65.8	26.6	80.0	73.7	110.6	76.8	98.6	87.3	93.4
Pr	7.8	10.3	9.5	13.4	12.7	0.02	8.2	7.8	3.0	8.4	7.8	11.1	8.0	9.9	8.9	9.5
Nd	26.4	36.0	31.2	44.0	40.6	0.07	32.4	30.0	12.5	28.1	25.6	35.3	27.1	33.5	29.9	31.2
Sm	4.4	6.6	5.1	7.8	6.5	0.01	6.8	6.0	3.1	4.7	4.3	5.5	4.8	5.6	4.9	4.8
Eu	0.9	1.7	1.1	2.0	1.5	0.00	2.1	1.8	1.3	0.9	0.9	1.2	1.0	1.3	0.9	1.0
Gd	3.4	5.0	4.1	6.1	4.5	0.02	6.1	6.4	5.6	3.8	3.5	4.0	4.1	4.4	4.2	4.0
Tb	0.5	0.7	0.6	0.8	0.6	0.00	1.0	1.2	1.1	0.6	0.6	0.6	0.6	0.7	0.6	0.5
Dy	2.7	3.3	3.5	4.1	3.6	0.00	6.0	7.7	7.5	3.4	3.3	3.6	3.9	4.3	3.7	3.1
Ho	0.5	0.5	0.7	0.7	0.6	0.00	1.2	1.6	1.5	0.7	0.7	0.7	0.8	1.0	0.7	0.6
Er	1.4	1.6	2.0	1.9	1.7	0.00	3.6	4.7	4.3	2.0	2.0	2.2	2.4	3.1	2.3	1.7
Tm	0.2	0.2	0.3	0.2	0.2	0.00	0.5	0.7	0.6	0.3	0.3	0.3	0.4	0.5	0.4	0.3
Yb	1.2	1.4	1.7	1.5	1.1	0.01	3.2	4.3	4.0	2.2	1.9	2.1	2.6	3.4	2.5	1.7
Lu	0.2	0.2	0.2	0.2	0.1	0.00	0.5	0.6	0.6	0.3	0.3	0.3	0.4	0.5	0.4	0.3
Hf	4.0	4.9	4.6	4.6	5.6	0.01	4.5	5.4	4.5	4.7	4.6	5.5	5.4	3.9	5.6	4.0
Ta	1.1	0.6	1.0	0.6	0.8	0.01	0.5	0.7	1.3	1.1	1.0	1.0	1.4	1.2	1.5	0.8
Tl	0.3	0.4	0.3	0.4	0.4	0.00	0.1	0.3	0.1	0.2	0.3	0.2	0.4	0.3	0.2	0.3
Pb	38.0	20.2	50.5	29.6	34.6	0.34	7.1	5.4	3.4	7.4	5.0	16.6	5.6	7.5	5.4	11.9
Th	7.4	8.5	8.3	9.3	8.6	0.03	3.4	4.8	1.7	8.9	7.9	7.4	9.1	10.1	10.8	8.0
U	1.1	1.6	0.9	1.7	1.2	0.01	0.5	0.7	0.4	1.8	1.2	1.1	1.9	1.7	2.2	1.2
∑REE	170	220	202	276	258	0.46	173	171	85	181	167	168	175	222	197	206
Eu/Eu*	0.74	0.91	0.76	0.88	0.83	0.33	1.00	0.90	0.92	0.66	0.67	0.75	0.66	0.81	0.62	0.73
$(La/Yb)_N$	26.18	27.53	21.80	33.91	42.26	14.56	7.36	5.59	2.46	15.22	16.10	21.32	11.63	11.58	14.25	22.69
$(La/Sm)_N$	6.43	5.28	6.36	5.78	6.61	8.39	3.17	3.56	2.82	6.41	6.42	7.33	5.68	6.28	6.62	7.17
$(Gd/Yb)_N$	2.37	2.93	2.02	3.39	3.32	2.35	1.56	1.23	1.16	1.45	1.55	1.57	1.28	1.07	1.37	1.96

Note: FeO_t=Fe_2O_3*0.8998+FeO.

Table S4. Whole-rock Sr and Nd isotope compositions of the granite in the composite veins, the host eclogite and the surrounding gneiss.

Lithology	Sample	Rb (ppm)	Sr (ppm)	$^{87}Rb/^{86}Sr$	$^{87}Sr/^{86}Sr$	±2σ	$(^{87}Sr/^{86}Sr)i$	Sm (ppm)	Nd (ppm)	$^{147}Sm/^{144}Nd$	$^{143}Nd/^{144}Nd$	±2σ	εNd(*t*)	T_{DM2} (Ma)
Granite	YK156-2	92.94	785.9	0.34244	0.70897	6	0.7079	6.59	35.97	0.11122	0.511590	0.000004	-18.0	2364
	YK156-5	76.20	2075.6	0.10631	0.71131	5	0.7110	5.15	31.23	0.10000	0.511435	0.000002	-20.7	2679
	YK156-6	96.92	1125.4	0.24939	0.70856	5	0.7078	7.80	43.98	0.10759	0.511712	0.000003	-15.6	2259
	YK156-7	101.44	1598.2	0.18379	0.70836	5	0.7078	6.48	40.63	0.09674	0.511369	0.000002	-21.9	2776
Eclogite	YK1412-13	65.09	338.9	0.55620	0.70964	6	0.7079	6.02	30.03	0.12160	0.511695	0.000005	-16.3	2319
	YK156-3	24.00	486.8	0.41300	0.70858	6	0.7081	6.77	32.43	0.12669	0.511796	0.000003	-14.5	2166
	YK1510-2	19.47	137.1	0.41143	0.71013	6	0.7088	3.12	12.54	0.15139	0.511918	0.000004	-12.8	2026
	*YK-6	15.05	607.5	0.0715	0.70883	17	0.7086	5.65	29.36	0.1165	0.511731	9	-15.4	2248
	*YK-18	39.00	385.8	0.2930	0.70770	20	0.7068	5.34	29.51	0.1094	0.511742	14	-15.0	2215
	*YK-26	32.76	193.7	0.4900	0.70838	20	0.7068	4.23	21.70	0.1180	0.511775	4	-14.6	2182
	*YK-33	2.60	168.0	0.0449	0.70865	16	0.7085	3.72	13.87	0.1621	0.511995	10	-11.6	1926
	*CF92-103	36.11	396.0	0.2640	0.70918	8	0.7084	7.50	39.84	0.1138	0.511673	5	-16.5	2333
	*CF92-105	36.10	343.4	0.3040	0.70929	8	0.7083	6.35	33.20	0.1157	0.511675	3	-16.5	2334
	*CF92-106	13.52	238.9	0.1640	0.70846	9	0.7080	3.98	21.21	0.1135	0.511764	4	-14.7	2189
Gneiss	YK1412-14	56.83	138.6	1.1876	0.71649	4	0.7128	4.66	28.07	0.1007	0.511491	0.000005	-19.7	2593
	YK156-4	74.57	261.2	0.8266	0.71608	6	0.7135	4.25	25.61	0.1008	0.511571	0.000011	-18.1	2467
	YK156-11	60.40	489.0	0.3577	0.71057	5	0.7095	5.50	35.30	0.0945	0.511354	0.000004	-22.2	2796
	YK137-12	123.00	226.8	1.5705	0.72173	7	0.7168	4.83	27.14	0.1080	0.511479	0.000006	-20.1	2626
	YK137-13	77.08	300.1	0.7437	0.71159	6	0.7093	5.65	33.53	0.1022	0.511526	0.000009	-19.0	2540
	YK1412-9	44.02	418.7	0.3044	0.71539	5	0.7144	4.90	29.86	0.0995	0.511496	0.000011	-19.5	2582
	YK1412-10	80.27	172.3	1.3494	0.71640	6	0.7122	4.82	31.19	0.0938	0.511457	0.000005	-20.2	2632

$(^{87}Sr/^{86}Sr)i$, and εNd(*t*) were calculated with the timing of metamorphism at *c.* 221 Ma;

$^{87}Rb/^{86}Sr$ and $^{144}Sm/^{147}Nd$ ratios were calculated using Rb, Sr and Sm, Nd contents, respectively, measured by ICP-MS; εNd(t) (the part per 10,000 deviation of a $^{143}Nd/^{144}Nd$ ratio from the chondritic ratio at any time) values were calculated based on present-day $(^{147}Sm/^{144}Nd)_{CHUR}$=0.1967; $(^{143}Nd/^{144}Nd)_{CHUR}$ = 0.512638; T_{DM2} values were calculated with present-day $(^{147}Sm/^{144}Nd)_{DM}$=0.2137, and $(^{143}Nd/^{144}Nd)_{DM}$=0.51315.

Where subscript CHUR=chondritic uniform reservoir; i=initial.

Samples with asterisk were from Yangkou, a few kilometers to the north of General's Hill, which were reported by Chen et al. (2002) and quoted for comparison. $(^{87}Sr/^{86}Sr)i$ ratios and εNd(*t*) were recalculated at t = 221 Ma, with corresponding T_{DM2} ages.

REFERENCE

Chen, B., Ye, K. & Liu, J., 2002. Cogenetic relationship of the Yangkou gabbro-to-granite unit, Su-Lu terrane, eastern China, and implications for UHP metamorphism. *Journal of the Geological Society*, **159,** 457–467.

Table S5a. LA-ICP-MS zircon U–Th–Pb data of the host eclogites.

Eclogite YK1412-13

Spot No.	Domain	Element Content (ppm)			Th/U	Isotopic ratio						Ages						
		Pb	Th	U		$^{206}Pb/^{207}Pb$	1σ	$^{207}Pb/^{235}U$	1σ	$^{206}Pb/^{238}U$	1σ	$^{206}Pb/^{207}Pb$	1σ	$^{207}Pb/^{235}U$	1σ	$^{206}Pb/^{238}U$	1σ	Concordance
YK1412-13-01	Core	313	721	766	0.94	0.0641	0.0029	0.7456	0.0339	0.0837	0.0012	746	96	566	20	518	7	91%
YK1412-13-02		399	893	579	1.54	0.0662	0.0028	0.9537	0.0406	0.1047	0.0018	813	90	680	21	642	11	94%
YK1412-13-03		617	1415	788	1.80	0.0647	0.0025	1.0022	0.0394	0.1116	0.0017	765	81	705	20	682	10	96%
YK1412-13-04		514	1163	715	1.63	0.0674	0.0023	0.9986	0.0327	0.1075	0.0014	850	64	703	17	658	8	93%
YK1412-13-05		133	155	254	0.61	0.0634	0.0037	0.7174	0.0385	0.0846	0.0018	724	124	549	23	524	11	95%
YK1412-13-06		544	1172	1063	1.10	0.0659	0.0024	0.9904	0.0344	0.1088	0.0014	806	76	699	18	666	8	95%
YK1412-13-07		655	1321	1202	1.10	0.0676	0.0019	1.1324	0.0345	0.1201	0.0015	854	64	769	16	731	9	95%
YK1412-13-08		284	428	1024	0.42	0.0653	0.0016	1.1679	0.0312	0.1283	0.0016	783	51	786	15	778	9	99%
YK1412-13-09		894	2130	971	2.19	0.0649	0.0020	0.8587	0.0293	0.0954	0.0018	770	65	629	16	587	11	93%
YK1412-13-10		393	713	1334	0.53	0.0648	0.0018	1.0185	0.0278	0.1130	0.0013	769	62	713	14	690	7	96%
YK1412-13-11		167	297	454	0.65	0.0626	0.0031	0.6258	0.0305	0.0732	0.0013	694	106	493	19	455	8	91%
YK1412-13-12		956	2277	1259	1.81	0.0642	0.0015	0.9320	0.0224	0.1041	0.0011	750	50	669	12	639	6	95%
YK1412-13-13		173	304	582	0.52	0.0596	0.0026	0.7060	0.0302	0.0866	0.0021	587	90	542	18	535	12	98%
YK1412-13-14		240	518	525	0.99	0.0622	0.0023	0.8016	0.0281	0.0933	0.0013	683	78	598	16	575	8	96%
YK1412-13-15		254	553	463	1.19	0.0658	0.0024	0.8938	0.0352	0.0975	0.0015	1200	78	648	19	600	9	92%
YK1412-13-16		457	962	730	1.32	0.0656	0.0021	0.9708	0.0316	0.1059	0.0016	794	67	689	16	649	9	94%
YK1412-13-17		115	201	754	0.27	0.0610	0.0029	0.5291	0.0227	0.0637	0.0012	639	69	431	15	398	7	92%
YK1412-13-18		143	163	382	0.43	0.0613	0.0031	0.6953	0.0354	0.0820	0.0014	650	107	536	21	508	9	94%
YK1412-13-19	Overgrowth rims and new zircon grains	15.80	1.32	195	0.007	0.0657	0.0184	0.2321	0.0351	0.0338	0.0014	798	608	212	29	214	9	98%
YK1412-13-20		10.04	0.68	173	0.004	0.0650	0.0116	0.2446	0.0329	0.0352	0.0011	776	388	222	27	223	7	99%
YK1412-13-21		16.28	4.69	311	0.015	0.0558	0.0063	0.2536	0.0265	0.0349	0.0010	443	254	230	21	221	6	96%
YK1412-13-26		21.61	1.78	266	0.007	0.0520	0.0066	0.2351	0.0303	0.0339	0.0010	283	267	214	25	215	6	99%
YK1412-13-30		10.20	1.80	229	0.008	0.0553	0.0050	0.2414	0.0185	0.0340	0.0008	433	202	220	15	215	5	98%
YK1412-13-31		8.84	3.32	237	0.014	0.0546	0.0043	0.2389	0.0174	0.0341	0.0009	394	176	218	14	216	6	99%
YK1412-13-32		7.32	1.30	216	0.006	0.0521	0.0060	0.2340	0.0247	0.0343	0.0009	300	297	214	20	217	6	98%
YK1412-13-33		7.88	0.93	170	0.005	0.0634	0.0090	0.2570	0.0302	0.0344	0.0013	720	306	232	24	218	8	93%
YK1412-13-35		10.72	3.08	378	0.008	0.0578	0.0038	0.2638	0.0168	0.0342	0.0007	524	144	238	13	217	4	90%
YK1412-13-22		19.83	5.67	187	0.030	0.0831	0.0073	0.3753	0.0339	0.0346	0.0011	1272	168	324	25	220	7	61%
YK1412-13-23		17.03	1.25	219	0.006	0.0653	0.0067	0.2856	0.0277	0.0339	0.0009	787	217	255	22	215	5	82%
YK1412-13-24		16.69	1.06	195	0.005	0.1126	0.0145	0.4204	0.0301	0.0340	0.0011	1843	235	356	21	215	7	50%
YK1412-13-25		17.74	3.37	203	0.017	0.0623	0.0049	0.2831	0.0211	0.0344	0.0009	687	173	253	17	218	6	85%
YK1412-13-27		12.91	0.81	183	0.004	0.0957	0.0095	0.4069	0.0311	0.0343	0.0009	1543	188	347	22	218	6	54%
YK1412-13-28		24.30	1.58	211	0.007	0.0913	0.0104	0.4166	0.0497	0.0344	0.0015	1454	219	354	36	218	10	52%
YK1412-13-29		5.72	2.52	237	0.011	0.0639	0.0051	0.2891	0.0227	0.0343	0.0008	737	166	258	18	217	5	83%
YK1412-13-34		11.35	1.17	180	0.006	0.0879	0.0164	0.3145	0.0291	0.0345	0.0012	1381	366	278	22	218	8	76%
YK1412-13-36		5.80	1.11	196	0.006	0.0731	0.0051	0.3138	0.0201	0.0338	0.0009	1017	138	277	15	214	6	74%
YK1412-13-37		6.20	3.07	210	0.015	0.0771	0.0056	0.3410	0.0231	0.0349	0.0009	1124	146	298	17	221	6	70%

Eclogite YK156-3

Spot No.	Domain	Element Content (ppm)			Th/U	Isotopic ratio						Ages						
		Pb	Th	U		$^{206}Pb/^{207}Pb$	1σ	$^{207}Pb/^{235}U$	1σ	$^{206}Pb/^{238}U$	1σ	$^{206}Pb/^{207}Pb$	1σ	$^{207}Pb/^{235}U$	1σ	$^{206}Pb/^{238}U$	1σ	Concordance
YK156-3-01	Core	266	569	365	1.56	0.0647	0.0034	1.0299	0.0515	0.1162	0.0022	765	109	719	26	708	13	98%
YK156-3-02		391	903	473	1.91	0.0649	0.0025	1.0880	0.0419	0.1206	0.0016	769	81	748	20	734	9	98%
YK156-3-03		373	818	761	1.07	0.0638	0.0020	0.8458	0.0282	0.0950	0.0012	744	67	622	16	585	7	93%
YK156-3-04		510	1156	1164	0.99	0.0614	0.0016	0.8645	0.0235	0.1016	0.0012	654	56	633	13	624	7	98%
YK156-3-05		120	167	554	0.30	0.0673	0.0020	1.1901	0.0360	0.1280	0.0016	848	63	796	17	776	9	97%
YK156-3-06		124	204	593	0.34	0.0627	0.0020	0.9627	0.0309	0.1109	0.0015	698	69	685	16	678	9	98%
YK156-3-07		455	628	2513	0.25	0.0645	0.0014	0.9926	0.0219	0.1108	0.0012	767	239	700	11	677	7	96%
YK156-3-08		332	732	426	1.72	0.0669	0.0022	1.1872	0.0395	0.1277	0.0019	835	69	795	18	775	11	97%
YK156-3-09		1018	2282	1484	1.54	0.0660	0.0016	1.1027	0.0259	0.1196	0.0015	807	45	755	13	728	8	96%
YK156-3-10		287	460	741	0.62	0.0641	0.0031	0.7524	0.0351	0.0860	0.0016	744	102	570	20	532	10	93%
YK156-3-11		130.1	101	1304	0.08	0.0645	0.0018	0.8297	0.0260	0.0919	0.0015	767	57	613	14	567	9	92%
YK156-3-12		386	734	1056	0.69	0.0659	0.0018	1.0310	0.0285	0.1125	0.0013	1200	56	719	14	687	8	95%
YK156-3-13		53.5	46.8	311	0.15	0.0638	0.0038	0.6406	0.0371	0.0743	0.0021	744	124	503	23	462	13	91%
YK156-3-14	Overgrowth rims and new zircon grains	17.51	2.77	297	0.009	0.0531	0.0043	0.2375	0.0176	0.0347	0.0007	345	183	216	14	220	5	98%
YK156-3-15		9.30	2.07	379	0.005	0.0519	0.0040	0.2355	0.0183	0.0340	0.0006	280	178	215	15	215	4	99%
YK156-3-16		14.09	3.51	470	0.007	0.0581	0.0035	0.2657	0.0161	0.0342	0.0007	532	132	239	13	217	4	90%
YK156-3-18		8.04	4.46	333	0.013	0.0571	0.0036	0.2621	0.0162	0.0342	0.0006	498	141	236	13	217	4	91%
YK156-3-19		21.41	4.43	800	0.006	0.0544	0.0026	0.2524	0.0116	0.0340	0.0006	387	110	229	9	215	3	94%
YK156-3-23		14.98	6.54	314	0.021	0.0496	0.0053	0.2209	0.0221	0.0339	0.0009	176	237	203	18	215	5	94%
YK156-3-26		12.30	3.39	356	0.010	0.0561	0.0040	0.2568	0.0179	0.0350	0.0008	457	155	232	14	222	5	95%
YK156-3-29		6.50	2.69	244	0.011	0.0587	0.0050	0.2618	0.0193	0.0347	0.0009	554	182	236	15	220	6	92%
YK156-3-17		10.72	3.53	382	0.009	0.0669	0.0057	0.2889	0.0182	0.0342	0.0008	835	174	258	14	217	5	82%
YK156-3-20		8.24	2.60	314	0.008	0.0650	0.0078	0.2751	0.0205	0.0346	0.0007	772	254	247	16	219	5	88%
YK156-3-21		10.05	6.35	340	0.019	0.0693	0.0076	0.3054	0.0286	0.0346	0.0011	907	226	271	22	219	7	79%
YK156-3-22		16.18	1.96	270	0.007	0.0766	0.0046	0.3543	0.0212	0.0348	0.0008	1122	120	308	16	220	5	66%
YK156-3-24		19.48	1.40	365	0.004	0.0644	0.0038	0.2976	0.0171	0.0342	0.0007	754	121	265	13	217	4	80%
YK156-3-25		8.57	1.58	222	0.007	0.0730	0.0115	0.2956	0.0378	0.0343	0.0011	1015	324	263	30	217	7	81%
YK156-3-27		14.43	2.28	241	0.009	0.0852	0.0076	0.3823	0.0309	0.0351	0.0011	1320	170	329	23	222	7	61%
YK156-3-28		21.76	2.48	263	0.009	0.0971	0.0083	0.4693	0.0473	0.0347	0.0008	1569	155	391	33	220	5	44%

Table S5b. LA-ICP-MS zircon U–Th–Pb data of the granite of the composite veins.

Granite YK1412-12

Spot No.	Domain	Element Content (ppm)			Th/U	Isotopic ratio						Ages						
		Pb	Th	U		$^{206}Pb/^{207}Pb$	1σ	$^{207}Pb/^{235}U$	1σ	$^{206}Pb/^{238}U$	1σ	$^{206}Pb/^{207}Pb$	1σ	$^{207}Pb/^{235}U$	1σ	$^{206}Pb/^{238}U$	1σ	Concordance
YK1412-12-01	Core	52.6	68.4	151	0.45	0.0563	0.0036	0.5751	0.0346	0.0746	0.0011	461	144	461	22.3	464	6	99%
YK1412-12-02		22.8	33.7	63.7	0.53	0.0618	0.0053	0.7916	0.0641	0.0956	0.0015	733	183	592	36.3	588	9	99%
YK1412-12-03		57.8	79.1	192	0.41	0.0633	0.0026	0.9910	0.0403	0.1138	0.0012	717	89	699	20.6	694	7	99%
YK1412-12-04		192	371	323	1.15	0.0620	0.0020	0.9405	0.0305	0.1096	0.0010	672	67	673	15.9	670	6	99%
YK1412-12-05		232	435	499	0.87	0.0642	0.0018	1.0527	0.0293	0.1183	0.0010	750	53	730	14.5	721	6	98%
YK1412-12-06		75	140	109	1.29	0.0651	0.0032	1.1561	0.0590	0.1293	0.0021	789	104	780	27.8	784	12	99%
YK1412-12-07		102	162	288	0.56	0.0654	0.0020	1.1588	0.0389	0.1281	0.0019	787	65	781	18.3	777	11	99%
YK1412-12-08		76	120	318	0.38	0.0646	0.0019	0.9446	0.0281	0.1061	0.0011	761	68	675	14.7	650	7	96%
YK1412-12-09		14.4	14.9	101	0.15	0.0548	0.0045	0.4453	0.0357	0.0600	0.0010	406	190	374	25.1	376	6	99%
YK1412-12-10		79	122	231	0.53	0.0653	0.0022	1.0762	0.0384	0.1187	0.0015	787	66	742	18.8	723	9	97%
YK1412-12-11		72	119	174	0.69	0.0632	0.0024	1.0047	0.0350	0.1148	0.0015	722	80	706	17.7	700	8	99%
YK1412-12-12		84	143	225	0.64	0.0634	0.0022	1.0219	0.0347	0.1168	0.0014	720	68	715	17.4	712	8	99%
YK1412-12-13		29.6	45.3	101	0.45	0.0582	0.0039	0.6530	0.0424	0.0830	0.0014	539	148	510	26.1	514	8	99%
YK1412-12-14		102	182	288	0.63	0.0611	0.0020	0.9158	0.0299	0.1081	0.0013	643	69	660	15.9	661	7	99%
YK1412-12-15		162	300	220	1.37	0.0681	0.0022	1.2293	0.0405	0.1294	0.0014	872	67	814	18.5	784	8	96%
YK1412-12-16		39.9	64.3	206	0.31	0.0608	0.0030	0.6374	0.0323	0.0754	0.0013	632	106	501	20.0	469	8	93%
YK1412-12-17		62	112	106	1.06	0.0631	0.0035	0.8491	0.0438	0.0985	0.0014	722	121	624	24.1	606	8	97%
YK1412-12-18		53.2	88.0	71.5	1.23	0.0653	0.0036	1.1856	0.0685	0.1292	0.0019	785	115	794	31.8	783	11	98%
YK1412-12-19		222	386	389	0.99	0.0674	0.0017	1.2102	0.0326	0.1290	0.0015	850	52	805	15.0	782	9	97%
YK1412-12-20		321	591	555	1.07	0.0646	0.0014	1.1134	0.0242	0.1239	0.0009	761	44	760	11.6	753	5	99%
YK1412-12-21		60.2	353	366	0.96	0.0655	0.0020	1.1594	0.0342	0.1283	0.0012	791	64	782	16	778	7	99%
YK1412-12-22		201.9	1009	1393	0.72	0.0641	0.0014	1.0464	0.0224	0.1176	0.0008	746	48	727	11	717	4	98%
YK1412-12-23		168	1473	912	1.62	0.0651	0.0015	1.1485	0.0272	0.1269	0.0010	777	49	777	13	770	6	99%
YK1412-12-24		240.5	1386	1518	0.91	0.0646	0.0012	1.1012	0.0199	0.1228	0.0007	761	240	754	10	747	4	99%
YK1412-12-25		37.77	87.5	515	0.17	0.0546	0.0021	0.5182	0.0220	0.0675	0.0013	394	85	424	15	421	8	99%
YK1412-12-26		18.99	52.6	327	0.16	0.0529	0.0033	0.3887	0.0239	0.0531	0.0007	324	136	333	17	333	5	99%
YK1412-12-27		87.7	413	603	0.68	0.0604	0.0020	0.9643	0.0330	0.1144	0.0015	617	72	686	17	699	8	98%
YK1412-12-28		169.9	865	1055	0.82	0.0647	0.0013	1.1639	0.0226	0.1297	0.0009	765	41	784	11	786	5	99%
YK1412-12-29		207.7	1429	1214	1.18	0.0653	0.0013	1.1448	0.0231	0.1264	0.0008	783	47	775	11	767	5	98%
YK1412-12-30		142.6	800	780	1.02	0.0691	0.0016	1.2367	0.0314	0.1293	0.0015	903	49	817	14	784	9	95%
YK1412-12-31		158.2	622	940	0.66	0.0712	0.0016	1.2558	0.0292	0.1272	0.0009	962	45	826	13	772	5	93%
YK1412-12-32		200.7	856	1192	0.72	0.0664	0.0013	1.1511	0.0244	0.1258	0.0016	820	35	778	12	764	9	98%
YK1412-12-33		152.7	767	1004	0.76	0.0663	0.0013	1.0063	0.0219	0.1100	0.0010	817	42	707	11	673	6	95%
YK1412-12-34		61.4	306	360	0.85	0.0684	0.0023	1.2085	0.0444	0.1281	0.0024	881	70	804	20	777	14	96%
YK1412-12-35	Overgrowth rims and new zircon grains	2.90	0.17	58.4	0.003	0.0540	0.0111	0.2427	0.0466	0.0350	0.0010	369	407	221	38.1	222	6	99%
YK1412-12-36		1.72	0.49	76.3	0.006	0.0617	0.0119	0.2331	0.0404	0.0338	0.0010	661	424	213	33.2	214	6	99%
YK1412-12-37		2.52	1.49	77.7	0.019	0.0567	0.0078	0.2546	0.0335	0.0362	0.0008	480	312	230	27.1	229	5	99%
YK1412-12-38		4.36	1.25	161	0.008	0.0504	0.0047	0.2440	0.0234	0.0351	0.0005	213	204	222	19.1	222	3	99%
YK1412-12-39		2.96	0.30	52.5	0.006	0.0554	0.0114	0.2558	0.0500	0.0353	0.0012	428	405	231	40.4	224	7	96%
YK1412-12-40		2.29	0.20	60.8	0.003	0.0549	0.0095	0.2495	0.0440	0.0354	0.0009	409	344	226	35.7	224	6	99%
YK1412-12-41		6.37	1.12	175	0.006	0.0544	0.0076	0.2410	0.0337	0.0345	0.0007	387	317	219	28	218	4	99%
YK1412-12-42		6.64	1.22	168	0.007	0.0500	0.0085	0.2442	0.0390	0.0353	0.0007	195	352	222	32	224	4	99%
YK1412-12-43		5.50	0.90	158	0.006	0.0646	0.0097	0.2578	0.0385	0.0333	0.0008	761	320	233	31	211	5	90%
YK1412-12-44		5.19	0.60	139	0.004	0.0572	0.0103	0.2484	0.0452	0.0354	0.0007	498	406	225	37	224	5	99%
YK1412-12-45		9.38	1.48	261	0.006	0.0462	0.0052	0.2288	0.0300	0.0346	0.0006	6	252	209	25	219	4	95%
YK1412-12-46		11.49	1.49	329	0.005	0.0526	0.0047	0.2443	0.0209	0.0349	0.0005	322	204	222	17	221	3	99%
YK1412-12-47		6.63	1.07	180	0.006	0.0533	0.0064	0.2500	0.0295	0.0355	0.0006	339	274	227	24	225	4	99%
YK1412-12-48		10.22	2.59	281	0.009	0.0530	0.0061	0.2499	0.0275	0.0348	0.0006	328	267	227	22	221	4	97%
YK1412-12-49		5.29	0.61	145	0.004	0.0589	0.0094	0.2553	0.0374	0.0352	0.0008	561	352	231	30	223	5	96%
YK1412-12-50		13.59	2.34	360	0.006	0.0507	0.0038	0.2401	0.0180	0.0349	0.0005	233	168	219	15	221	3	98%
YK1412-12-51		7.38	1.34	193	0.007	0.0515	0.0060	0.2388	0.0271	0.0354	0.0007	265	257	217	22	224	4	97%
YK1412-12-52		6.19	4.03	149	0.027	0.0508	0.0092	0.2320	0.0403	0.0358	0.0010	232	374	212	33	227	6	93%
YK1412-12-53		4.19	0.88	108	0.008	0.0507	0.0116	0.2696	0.0589	0.0356	0.0012	228	456	242	47	226	8	92%
YK1412-12-54		7.04	3.31	181	0.018	0.0588	0.0109	0.2540	0.0429	0.0340	0.0011	561	413	230	35	216	7	93%
YK1412-12-55		12.68	1.99	321	0.006	0.0517	0.0049	0.2344	0.0220	0.0345	0.0006	272	217	214	18	218	3	97%

Granite YK156-2

Spot No.	Domain	Element Content (ppm)			Th/U	Isotopic ratio						Ages						
		Pb	Th	U		$^{206}Pb/^{207}Pb$	1σ	$^{207}Pb/^{235}U$	1σ	$^{206}Pb/^{238}U$	1σ	$^{206}Pb/^{207}Pb$	1σ	$^{207}Pb/^{235}U$	1σ	$^{206}Pb/^{238}U$	1σ	Concordance
YK156-2-01		40.2	213	208	1.02	0.0633	0.0026	1.1150	0.0464	0.1279	0.0020	717	88	761	22	776	12	97%
YK156-2-02		56.7	312	353	0.88	0.0657	0.0021	0.9834	0.0315	0.1086	0.0015	798	67	695	16	664	9	95%
YK156-2-03		65.8	640	320	2.00	0.0624	0.0022	0.9796	0.0337	0.1146	0.0016	687	76	693	17	699	9	99%
YK156-2-04		92.3	393	890	0.44	0.0609	0.0018	0.6586	0.0198	0.0780	0.0009	635	63	514	12	484	6	94%
YK156-2-05		41.0	234	206	1.14	0.0702	0.0029	1.2279	0.0488	0.1284	0.0025	1000	82	813	22	779	14	95%
YK156-2-06		33.7	159	363	0.44	0.0552	0.0021	0.5118	0.0197	0.0676	0.0010	420	85	420	13	422	6	99%
YK156-2-07		40.9	79.0	451	0.18	0.0607	0.0026	0.6151	0.0260	0.0738	0.0013	628	94	487	16	459	8	94%
YK156-2-08		93.7	563	485	1.16	0.0673	0.0024	1.1942	0.0444	0.1288	0.0027	856	75	798	21	781	15	97%
YK156-2-09		164.4	904	1005	0.90	0.0638	0.0014	1.0440	0.0253	0.1173	0.0013	744	47	726	13	715	8	98%

YK156-2-10	Core	36.0	392	141	2.78	0.0639	0.0032	1.1241	0.0554	0.1287	0.0025	739	106	765	26	781	14	97%
YK156-2-11		59.5	204	687	0.30	0.0572	0.0021	0.5248	0.0197	0.0664	0.0011	502	86	428	13	414	7	96%
YK156-2-12		143.1	766	1145	0.67	0.0629	0.0014	0.8048	0.0225	0.0917	0.0014	702	48	600	13	566	8	94%
YK156-2-13		207.9	1204	1089	1.11	0.0680	0.0014	1.2125	0.0266	0.1291	0.0013	878	38	806	12	782	8	96%
YK156-2-14		121.9	472	696	0.68	0.0725	0.0021	1.2509	0.0351	0.1257	0.0017	1000	58	824	16	763	10	92%
YK156-2-15		158.7	798	895	0.89	0.0684	0.0015	1.2143	0.0287	0.1278	0.0014	883	46	807	13	776	8	96%
YK156-2-16		162.9	767	1169	0.66	0.0654	0.0020	0.9621	0.0329	0.1059	0.0023	787	64	684	17	649	13	94%
YK156-2-17		205.5	720	1175	0.61	0.0722	0.0017	1.2894	0.0285	0.1286	0.0016	992	46	841	13	780	9	92%
YK156-2-18		149.0	479	948	0.50	0.0635	0.0015	1.1422	0.0324	0.1285	0.0023	724	50	774	15	779	13	99%
YK156-2-19		256.1	1286	1594	0.81	0.0642	0.0014	1.0539	0.0264	0.1176	0.0018	750	46	731	13	717	11	98%
YK156-2-23		9.26	1.78	239	0.007	0.0543	0.0042	0.2494	0.0160	0.0348	0.0007	383	168	226	13	221	4	97%
YK156-2-24		9.83	2.07	248	0.008	0.0509	0.0043	0.2343	0.0182	0.0346	0.0007	235	193	214	15	219	4	97%
YK156-2-27		8.53	1.21	224	0.005	0.0510	0.0058	0.2261	0.0252	0.0350	0.0010	239	244	207	21	222	6	92%
YK156-2-29		5.30	0.68	140	0.005	0.0653	0.0106	0.2493	0.0332	0.0344	0.0012	783	351	226	27	218	8	96%
YK156-2-32		29.82	4.22	761	0.006	0.0540	0.0029	0.2540	0.0105	0.0348	0.0005	372	116	230	9	221	3	95%
YK156-2-35		15.94	5.86	410	0.014	0.0555	0.0031	0.2615	0.0136	0.0349	0.0006	432	126	236	11	221	4	93%
YK156-2-36		16.89	5.80	442	0.013	0.0562	0.0031	0.2697	0.0158	0.0347	0.0006	461	122	242	13	220	3	90%
YK156-2-20	Overgrowth	7.05	1.58	177	0.009	0.0802	0.0076	0.3508	0.0253	0.0349	0.0010	1203	193	305	19	221	6	67%
YK156-2-21	rims and	8.20	0.94	210	0.004	0.0679	0.0040	0.3128	0.0177	0.0346	0.0009	865	122	276	14	220	5	77%
YK156-2-22	new zircon	9.53	1.72	254	0.007	0.0683	0.0046	0.3011	0.0195	0.0336	0.0007	877	141	267	15	213	5	77%
YK156-2-25	grains	4.49	0.43	117	0.004	0.1021	0.0104	0.4036	0.0267	0.0347	0.0010	1663	191	344	19	220	7	55%
YK156-2-26		4.92	0.47	126	0.004	0.0736	0.0076	0.3487	0.0328	0.0350	0.0012	1031	209	304	25	222	8	68%
YK156-2-28		9.06	1.42	230	0.006	0.0650	0.0072	0.3076	0.0323	0.0351	0.0012	776	234	272	25	222	7	79%
YK156-2-30		9.12	0.86	240	0.004	0.0716	0.0059	0.3126	0.0250	0.0347	0.0008	973	175	276	19	220	5	77%
YK156-2-31		7.15	0.76	191	0.004	0.0616	0.0053	0.2897	0.0251	0.0351	0.0009	661	185	258	20	223	6	85%
YK156-2-33		10.31	2.33	266	0.009	0.0670	0.0053	0.3038	0.0201	0.0348	0.0007	839	165	269	16	220	4	80%
YK156-2-34		7.25	2.67	194	0.014	0.0643	0.0047	0.2960	0.0231	0.0346	0.0008	752	157	263	18	219	5	81%
YK156-2-37		6.32	0.73	154	0.005	0.0977	0.0121	0.3885	0.0294	0.0350	0.0011	1583	234	333	21	221	7	59%

Table S5c. LA-ICP-MS zircon U–Th–Pb data of the vein quartz of the composite veins.

Vein quartz YK1412-11

Spot No.	Domain	Element Content (ppm)			Th/U	Isotopic ratio						Ages						
		Pb	Th	U		$^{206}Pb/^{207}Pb$	1σ	$^{207}Pb/^{235}U$	1σ	$^{206}Pb/^{238}U$	1σ	$^{206}Pb/^{207}Pb$	1σ	$^{207}Pb/^{235}U$	1σ	$^{206}Pb/^{238}U$	1σ	Concordance
YK1412-11-01		62.3	107	245	0.44	0.0595	0.0017	0.7478	0.0204	0.0910	0.0008	587	65.7	567	12	562	5	99%
YK1412-11-02		77	147	118	1.25	0.0644	0.0019	1.0570	0.0312	0.1191	0.0012	754	58.3	732	15	725	7	99%
YK1412-11-03		238	415	415	1.00	0.0646	0.0014	1.1727	0.0254	0.1311	0.0011	761	45.2	788	12	794	6	99%
YK1412-11-04		139	255	215	1.19	0.0585	0.0027	0.7226	0.0306	0.0902	0.0013	550	106	552	18	557	8	99%
YK1412-11-05		333	578	452	1.28	0.0640	0.0018	1.1259	0.0319	0.1272	0.0011	740	260.2	766	15	772	6	99%
YK1412-11-06		157	272	334	0.82	0.0608	0.0024	0.7935	0.0315	0.0947	0.0009	632	87.0	593	18	583	5	98%
YK1412-11-07		92	153	107	1.43	0.0660	0.0030	1.1693	0.0521	0.1288	0.0015	806	94.4	786	24	781	9	99%
YK1412-11-08		119	185	366	0.51	0.0628	0.0018	0.9447	0.0265	0.1095	0.0011	702	61.1	675	14	670	7	99%
YK1412-11-09		166	279	394	0.71	0.0627	0.0020	0.9570	0.0357	0.1105	0.0023	698	67.7	682	19	675	14	99%
YK1412-11-10		77	142	131	1.08	0.0646	0.0028	1.1327	0.0496	0.1276	0.0019	761	60.2	769	24	774	11	99%
YK1412-11-11		47.0	62.1	154	0.40	0.0618	0.0028	0.9141	0.0393	0.1076	0.0013	665	98.1	659	21	659	8	99%
YK1412-11-12		31.9	54.7	80.6	0.68	0.0587	0.0043	0.7599	0.0538	0.0935	0.0016	554	159	574	31	576	10	99%
YK1412-11-13		11.0	5.63	108	0.05	0.0530	0.0048	0.4450	0.0408	0.0594	0.0011	328	206	374	29	372	7	99%
YK1412-11-14		75.0	290	758	0.38	0.0588	0.0020	0.6944	0.0230	0.0858	0.0007	567	74	535	14	530	4	99%
YK1412-11-15		29.5	185	337	0.55	0.0573	0.0037	0.5289	0.0322	0.0677	0.0010	506	138	431	21	422	6	97%
YK1412-11-16	Core	103.3	710	829	0.86	0.0595	0.0018	0.7856	0.0237	0.0953	0.0008	583	65	589	13	587	5	99%
YK1412-11-17		128.2	1370	757	1.81	0.0610	0.0018	0.8717	0.0293	0.1028	0.0017	639	63	636	16	631	10	99%
YK1412-11-18		22.0	111	341	0.33	0.0530	0.0035	0.3827	0.0249	0.0522	0.0007	328	150	329	18	328	4	99%
YK1412-11-19		30.0	102	365	0.28	0.0549	0.0028	0.5356	0.0276	0.0706	0.0008	406	117	436	18	440	5	99%
YK1412-11-20		150.2	929	1071	0.87	0.0628	0.0015	0.9502	0.0218	0.1091	0.0007	702	50	678	11	667	4	98%
YK1412-11-21		211	1555	1290	1.21	0.0651	0.0014	1.0662	0.0220	0.1182	0.0008	776	44	737	11	720	5	97%
YK1412-11-22		35.5	259	429	0.60	0.0548	0.0027	0.4685	0.0227	0.0622	0.0007	467	105	390	16	389	4	99%
YK1412-11-23		97.8	816	587	1.39	0.0620	0.0020	0.9779	0.0326	0.1139	0.0013	672	66	693	17	695	7	99%
YK1412-11-24		12.3	32.6	145	0.23	0.0598	0.0055	0.5941	0.0488	0.0752	0.0016	598	198	473	31	468	10	98%
YK1412-11-26		78.1	452	695	0.65	0.0607	0.0022	0.7406	0.0270	0.0882	0.0010	632	78	563	16	545	6	96%
YK1412-11-27		88.9	840	610	1.38	0.0609	0.0019	0.8366	0.0267	0.0997	0.0009	635	69	617	15	613	5	99%
YK1412-11-28		43.6	107	504	0.21	0.0557	0.0030	0.6090	0.0329	0.0780	0.0013	439	116	483	21	484	8	99%
YK1412-11-29		231	1780	1260	1.41	0.0642	0.0014	1.1372	0.0250	0.1274	0.0010	746	44	771	12	773	6	99%
YK1412-11-30		256	1846	1316	1.40	0.0687	0.0013	1.2208	0.0233	0.1279	0.0011	889	40	810	11	776	6	95%
YK1412-11-31		214.3	1093	1274	0.86	0.0654	0.0010	1.1290	0.0165	0.1247	0.0007	787	33	767	8	758	4	98%
YK1412-11-32		264	1528	1627	0.94	0.0626	0.0011	0.9924	0.0185	0.1150	0.0011	694	39	700	9	702	6	99%
YK1412-11-25		47.8	253	747	0.34	0.0612	0.0029	0.4651	0.0223	0.0555	0.0008	656	102	388	15	348	5	89%
YK1412-11-33		3.83	2.04	97.9	0.021	0.0513	0.0052	0.2474	0.0240	0.0354	0.0006	257	36.1	224	20	224	4	99%
YK1412-11-34		2.02	0.45	63.8	0.007	0.0519	0.0064	0.2548	0.0294	0.0364	0.0007	280	263	230	24	231	4	99%
YK1412-11-35		1.14	0.80	37.2	0.022	0.0541	0.0114	0.2476	0.0481	0.0352	0.0009	376	415	225	39	223	5	99%
YK1412-11-36		2.94	1.42	124	0.011	0.0507	0.0061	0.2453	0.0294	0.0352	0.0007	228	256	223	24	223	4	99%
YK1412-11-37		2.90	1.45	118	0.012	0.0537	0.0060	0.2435	0.0253	0.0339	0.0007	361	254	221	21	215	5	97%
YK1412-11-38		4.21	1.23	135	0.009	0.0521	0.0053	0.2408	0.0242	0.0347	0.0008	300	235	219	20	220	5	99%
YK1412-11-39		10.69	2.16	141	0.015	0.0523	0.0054	0.2522	0.0257	0.0361	0.0006	298	240	228	21	229	3	99%

YK1412-11-40	Overgrowth rims and new zircon grains	5.37	0.80	107	0.007	0.0517	0.0065	0.2463	0.0326	0.0352	0.0008	333	267	224	27	223	5	99%
YK1412-11-41		4.61	0.38	108	0.003	0.0538	0.0062	0.2404	0.0262	0.0347	0.0007	365	263	219	21	220	4	99%
YK1412-11-42		2.52	0.40	54.3	0.007	0.0536	0.0107	0.2497	0.0447	0.0355	0.0010	354	398	226	36	225	6	99%
YK1412-11-43		2.40	0.46	104	0.004	0.0523	0.0061	0.2441	0.0279	0.0349	0.0007	298	268	222	23	221	4	99%
YK1412-11-44		8.68	1.36	254	0.005	0.0516	0.0053	0.2416	0.0239	0.0351	0.0006	333	237	220	20	222	4	98%
YK1412-11-45		5.32	1.16	152	0.008	0.0537	0.0087	0.2446	0.0387	0.0354	0.0008	367	320	222	32	224	5	99%
YK1412-11-46		7.69	4.46	200	0.022	0.0525	0.0114	0.2444	0.0552	0.0354	0.0010	306	439	222	45	224	6	98%
YK1412-11-47		7.49	0.97	215	0.004	0.0547	0.0064	0.2455	0.0280	0.0350	0.0006	467	267	223	23	221	4	99%
YK1412-11-48		11.65	2.38	332	0.007	0.0500	0.0043	0.2332	0.0188	0.0344	0.0005	195	189	213	16	218	3	97%
YK1412-11-49		6.86	4.08	189	0.022	0.0573	0.0100	0.2454	0.0365	0.0350	0.0009	502	395	223	30	222	6	99%
YK1412-11-50		6.56	1.30	186	0.007	0.0546	0.0074	0.2435	0.0333	0.0349	0.0007	394	309	221	27	221	4	99%
YK1412-11-51		8.57	1.74	244	0.007	0.0513	0.0060	0.2461	0.0281	0.0351	0.0007	254	248	223	23	222	4	99%
YK1412-11-52		6.21	1.33	175	0.008	0.0519	0.0078	0.2417	0.0354	0.0350	0.0006	280	311	220	29	222	4	99%
YK1412-11-53		7.22	1.92	191	0.010	0.0464	0.0076	0.2198	0.0366	0.0351	0.0010	17	352	202	31	222	6	90%
YK1412-11-54		10.95	4.91	303	0.016	0.0532	0.0045	0.2449	0.0202	0.0348	0.0005	345	193	222	16	220	3	99%
YK1412-11-55		6.38	1.34	180	0.007	0.0496	0.0092	0.2298	0.0415	0.0346	0.0008	176	385	210	34	219	5	95%
YK1412-11-56		9.30	1.99	266	0.007	0.0530	0.0053	0.2390	0.0236	0.0345	0.0006	328	230	218	19	219	4	99%
YK1412-11-57		5.64	0.55	159	0.003	0.0506	0.0076	0.2441	0.0348	0.0350	0.0007	233	306	222	28	222	5	99%
YK1412-11-58		11.02	6.65	300	0.022	0.0496	0.0043	0.2276	0.0192	0.0346	0.0005	176	189	208	16	219	3	94%
YK1412-11-59		8.19	2.34	210	0.011	0.0536	0.0068	0.2510	0.0321	0.0359	0.0008	354	289	227	26	227	5	99%
YK1412-11-60		9.90	7.31	251	0.029	0.0502	0.0082	0.2457	0.0428	0.0343	0.0007	206	341	223	35	217	4	97%
YK1412-11-61		8.32	2.70	228	0.012	0.0554	0.0055	0.2562	0.0242	0.0354	0.0007	432	220	232	20	224	4	96%
YK1412-11-62		9.26	3.79	263	0.014	0.0518	0.0056	0.2489	0.0289	0.0354	0.0007	276	246	226	24	224	5	99%
YK1412-11-63		7.67	2.88	199	0.014	0.0608	0.0106	0.2590	0.0376	0.0349	0.0007	635	381	234	30	221	5	94%
YK1412-11-64		6.11	4.40	157	0.028	0.0568	0.0068	0.2569	0.0292	0.0348	0.0007	483	268	232	24	220	4	94%
YK1412-11-65		15.79	7.02	430	0.016	0.0509	0.0034	0.2365	0.0160	0.0343	0.0004	235	153	216	13	217	2	99%

Vein quartz YK156-1

Spot No.	Domain	Element Content (ppm)			Th/U	Isotopic ratio						Ages						
		Pb	Th	U		$^{206}Pb/^{207}Pb$	1σ	$^{207}Pb/^{235}U$	1σ	$^{206}Pb/^{238}U$	1σ	$^{206}Pb/^{207}Pb$	1σ	$^{207}Pb/^{235}U$	1σ	$^{206}Pb/^{238}U$	1σ	Concordance
YK156-1-01	Core	623	5107	3287	1.55	0.0664	0.0013	1.1324	0.0233	0.1230	0.0014	820	34	769	11	748	8	97%
YK156-1-02		105.2	500	620	0.81	0.0643	0.0014	1.1302	0.0237	0.1273	0.0009	750	44	768	11	772	5	99%
YK156-1-03		111.5	545	834	0.65	0.0613	0.0015	0.8520	0.0224	0.1002	0.0010	650	54	626	12	616	6	98%
YK156-1-04		73.5	294	596	0.49	0.0593	0.0019	0.7927	0.0238	0.0973	0.0009	576	75	593	14	598	5	99%
YK156-1-05		121.4	741	679	1.09	0.0674	0.0015	1.1977	0.0282	0.1281	0.0011	850	-152	800	13	777	6	97%
YK156-1-06		16.39	49.8	316	0.16	0.0518	0.0043	0.3215	0.0264	0.0445	0.0014	276	189	283	20	281	9	99%
YK156-1-07		30.75	80.9	500	0.16	0.0509	0.0022	0.3832	0.0166	0.0547	0.0007	235	72	329	12	343	5	95%
YK156-1-08		403	5073	2853	1.78	0.0601	0.0011	0.6845	0.0191	0.0815	0.0015	609	44	529	11	505	9	95%
YK156-1-09		208.7	1086	1219	0.89	0.0657	0.0013	1.1703	0.0262	0.1284	0.0014	798	43	787	12	779	8	98%
YK156-1-10		114.2	635	1136	0.56	0.0583	0.0016	0.6070	0.0172	0.0750	0.0006	539	59	482	11	466	4	96%
YK156-1-11		97.8	259	1090	0.24	0.0572	0.0015	0.5918	0.0152	0.0744	0.0008	498	57	472	10	463	5	98%
YK156-1-12		307	1788	2310	0.77	0.0611	0.0012	0.8413	0.0160	0.0990	0.0009	643	36	620	9	608	6	98%
YK156-1-13		166	1732	1039	1.67	0.0613	0.0021	0.7334	0.0238	0.0864	0.0012	650	74	559	14	534	7	95%
YK156-1-14		349	584	638	0.92	0.0676	0.0022	1.2076	0.0400	0.1287	0.0020	857	65.9	804	18	780	11	97%
YK156-1-15		527	1060	1082	0.98	0.0653	0.0018	1.1635	0.0326	0.1283	0.0017	783	58.2	784	15	778	10	99%
YK156-1-16		767	1259	1255	1.00	0.0646	0.0019	1.1587	0.0408	0.1288	0.0031	761	61.1	781	19	781	18	99%
YK156-1-17		406	748	1033	0.72	0.0653	0.0020	1.0381	0.0303	0.1151	0.0019	785	68	723	15	702	11	97%
YK156-1-18		197	399	331	1.21	0.0679	0.0028	1.1880	0.0542	0.1274	0.0027	865	87.0	795	25	773	16	97%
YK156-1-19		182	293	352	0.83	0.0681	0.0024	1.2082	0.0504	0.1287	0.0033	872	72.22	804	23	780	19	96%
YK156-1-20		123	240	221	1.09	0.0654	0.0026	1.1653	0.0477	0.1289	0.0024	787	88.0	784	22	782	14	99%
YK156-1-22	Overgrowth rims and new zircon grains	22.29	5.39	628	0.009	0.0464	0.0027	0.2217	0.0124	0.0352	0.0005	16.8	133.3	203	10	223	3	90%
YK156-1-23		18.13	3.62	494	0.007	0.0517	0.0034	0.2515	0.0165	0.0357	0.0006	272	147	228	13	226	4	99%
YK156-1-24		17.54	3.46	479	0.007	0.0519	0.0032	0.2456	0.0153	0.0351	0.0004	280	143	223	12	222	3	99%
YK156-1-25		7.83	2.17	219	0.010	0.0526	0.0068	0.2282	0.0307	0.0350	0.0007	322	267	209	25	222	4	94%
YK156-1-26		12.22	3.25	326	0.010	0.0521	0.0052	0.2387	0.0229	0.0348	0.0006	287	230	217	19	220	3	98%
YK156-1-27		13.41	13.2	327	0.041	0.0527	0.0052	0.2614	0.0249	0.0368	0.0007	317	226	236	20	233	4	98%
YK156-1-28		13.79	6.88	367	0.019	0.0551	0.0060	0.2569	0.0271	0.0344	0.0005	417	238	232	22	218	3	93%
YK156-1-29		9.06	2.39	235	0.010	0.0533	0.0092	0.2526	0.0426	0.0357	0.0009	343	357	229	35	226	5	98%
YK156-1-30		21.58	21.4	560	0.038	0.0518	0.0029	0.2450	0.0133	0.0349	0.0004	276	128	223	11	221	3	99%
YK156-1-31		17.26	7.41	458	0.016	0.0506	0.0035	0.2443	0.0169	0.0348	0.0004	220	159	222	14	221	3	99%
YK156-1-32		15.14	22.5	374	0.060	0.0545	0.0062	0.2646	0.0289	0.0356	0.0005	391	256	238	23	225	3	94%
YK156-1-33		2.73	2.23	77.3	0.029	0.0572	0.0182	0.2367	0.0789	0.0340	0.0010	498	581	216	65	215	6	99%
YK156-1-35		10.64	3.28	282	0.012	0.0516	0.0051	0.2509	0.0240	0.0350	0.0006	333	223	227	19	222	4	97%
YK156-1-36		16.01	3.17	417	0.008	0.0522	0.0036	0.2525	0.0178	0.0357	0.0006	300	156	229	14	226	3	98%
YK156-1-37		12.88	2.69	337	0.008	0.0522	0.0049	0.2393	0.0221	0.0342	0.0006	300	217	218	18	217	3	99%
YK156-1-38		16.71	5.94	452	0.013	0.0512	0.0032	0.2401	0.0146	0.0343	0.0005	250	143	218	12	217	3	99%
YK156-1-39		14.54	12.3	383	0.032	0.0509	0.0042	0.2421	0.0192	0.0348	0.0005	235	193	220	16	221	3	99%
YK156-1-40		16.68	3.84	458	0.008	0.0521	0.0037	0.2412	0.0163	0.0341	0.0004	300	168	219	13	216	3	98%
YK156-1-41		13.04	1.81	342	0.005	0.0516	0.0042	0.2434	0.0200	0.0347	0.0005	333	189	221	16	220	3	99%
YK156-1-42		14.77	1.83	393	0.005	0.0539	0.0048	0.2515	0.0220	0.0346	0.0006	369	208	228	18	219	4	96%
YK156-1-43		17.81	4.60	479	0.010	0.0497	0.0030	0.2423	0.0147	0.0355	0.0005	189	141	220	12	225	3	97%
YK156-1-44		8.90	2.67	250	0.011	0.0507	0.0049	0.2336	0.0215	0.0346	0.0006	228	207	213	18	220	4	97%
YK156-1-45		9.45	10.7	255	0.042	0.0514	0.0111	0.2351	0.0453	0.0342	0.0009	257	443	214	37	217	5	98%

YK156-1-46		9.98	3.44	276	0.012	0.0539	0.0043	0.2439	0.0187	0.0342	0.0005	369	181	222	15	217	3	97%
YK156-1-47		23.35	4.36	644	0.007	0.0512	0.0036	0.2436	0.0179	0.0347	0.0006	250	193	221	15	220	4	99%
YK156-1-48		17.48	4.27	460	0.009	0.0546	0.0047	0.2609	0.0202	0.0354	0.0005	394	201	235	16	224	3	95%
YK156-1-50		11.61	3.02	313	0.010	0.0573	0.0048	0.2616	0.0218	0.0345	0.0005	502	185	236	18	218	3	92%
YK156-1-51		22.08	5.62	618	0.009	0.0535	0.0025	0.2532	0.0118	0.0346	0.0005	350	107	229	10	219	3	95%
YK156-1-21		10.90	2.06	298	0.007	0.0473	0.0054	0.2174	0.0250	0.0349	0.0006	61	261	200	21	221	4	89%
YK156-1-34		11.27	3.90	298	0.013	0.0619	0.0062	0.2817	0.0299	0.0342	0.0008	733	217	252	24	217	5	85%
YK156-1-49		11.76	2.55	315	0.008	0.0615	0.0064	0.2750	0.0262	0.0350	0.0006	657	224	247	21	222	4	89%

Table S5d. LA-ICP-MS zircon U–Th–Pb data of the surrounding gneisses.

Gneiss YK1412-14

Spot No.	Domain	Element Content (ppm)			Th/U	Isotopic ratio						Ages						
		Pb	Th	U		$^{206}Pb/^{207}Pb$	1σ	$^{207}Pb/^{235}U$	1σ	$^{206}Pb/^{238}U$	1σ	$^{206}Pb/^{207}Pb$	1σ	$^{207}Pb/^{235}U$	1σ	$^{206}Pb/^{238}U$	1σ	Concordance
YK1412-14-01		255.8	770	2882	0.27	0.0598	0.0014	0.7473	0.0265	0.0903	0.0025	594	56	567	15	557	15	98%
YK1412-14-02		55.4	319	874	0.37	0.0524	0.0023	0.3999	0.0205	0.0547	0.0011	306	134	342	15	344	7	99%
YK1412-14-03		74.4	381	568	0.67	0.0637	0.0019	0.9060	0.0270	0.1036	0.0014	731	65	655	14	635	8	96%
YK1412-14-04		231.6	1321	1402	0.94	0.0684	0.0014	1.2068	0.0246	0.1276	0.0010	880	43	804	11	774	6	96%
YK1412-14-05		53.1	71.8	1145	0.06	0.0524	0.0018	0.3242	0.0115	0.0448	0.0006	302	78	285	9	282	4	99%
YK1412-14-06		62.9	336	387	0.87	0.0666	0.0022	1.1794	0.0387	0.1277	0.0011	828	64	791	18	775	6	97%
YK1412-14-07		257.4	2483	1266	1.96	0.0682	0.0015	1.2145	0.0271	0.1284	0.0009	876	46	807	12	779	5	96%
YK1412-14-08		34.8	225	203	1.11	0.0606	0.0032	1.0805	0.0576	0.1286	0.0014	633	113	744	28	780	8	95%
YK1412-14-09		380.1	2743	2862	0.96	0.0607	0.0013	0.8623	0.0193	0.1022	0.0008	628	42	631	11	627	5	99%
YK1412-14-10		189.5	692	2041	0.34	0.0585	0.0012	0.6661	0.0162	0.0820	0.0012	546	44	518	10	508	7	98%
YK1412-14-11		376.6	2367	3414	0.69	0.0592	0.0012	0.7014	0.0151	0.0852	0.0008	576	44	540	9	527	4	97%
YK1412-14-12		126.3	651	808	0.81	0.0639	0.0017	1.0778	0.0285	0.1218	0.0011	739	56	743	14	741	6	99%
YK1412-14-13		225.0	1486	1286	1.16	0.0656	0.0014	1.1621	0.0251	0.1279	0.0011	794	44	783	12	776	6	99%
YK1412-14-14		127.2	473	827	0.57	0.0657	0.0017	1.1814	0.0312	0.1299	0.0011	796	54	792	15	787	7	99%
YK1412-14-15		183.3	1100	1124	0.98	0.0643	0.0014	1.0865	0.0242	0.1221	0.0010	750	46	747	12	742	6	99%
YK1412-14-16		117.6	215	2352	0.09	0.0533	0.0012	0.3394	0.0077	0.0460	0.0004	343	45	297	6	290	2	97%
YK1412-14-17		66.4	170	1043	0.16	0.0546	0.0014	0.4300	0.0113	0.0570	0.0005	394	53	363	8	358	3	98%
YK1412-14-18		125.2	332	1169	0.28	0.0612	0.0016	0.8646	0.0290	0.1021	0.0022	656	56	633	16	627	13	99%
YK1412-14-19	Core	84.9	265	938	0.28	0.0591	0.0018	0.6565	0.0267	0.0798	0.0020	569	67	512	16	495	12	96%
YK1412-14-20		36.7	257	256	1.00	0.0605	0.0024	0.8765	0.0343	0.1049	0.0011	633	53	639	19	643	6	99%
YK1412-14-21		154.4	586	1882	0.31	0.0568	0.0012	0.5481	0.0143	0.0695	0.0010	483	48	444	9	433	6	97%
YK1412-14-22		130.4	316	1469	0.21	0.0580	0.0015	0.6281	0.0158	0.0785	0.0009	528	56	495	10	487	5	98%
YK1412-14-23		174.0	1453	906	1.60	0.0634	0.0014	1.1001	0.0237	0.1253	0.0009	720	47	753	11	761	5	99%
YK1412-14-24		175.5	845	1117	0.76	0.0636	0.0013	1.0836	0.0224	0.1228	0.0008	728	44	745	11	746	4	99%
YK1412-14-25		61.5	344	398	0.86	0.0640	0.0020	1.0835	0.0357	0.1227	0.0016	743	65	745	17	746	9	99%
YK1412-14-26		191.4	1140	1216	0.94	0.0632	0.0014	1.0514	0.0225	0.1200	0.0008	717	14	730	11	731	5	99%
YK1412-14-27		425.1	2372	2654	0.89	0.0649	0.0011	1.1249	0.0205	0.1250	0.0010	772	32	765	10	759	6	99%
YK1412-14-28		20.9	127	130	0.98	0.0641	0.0036	1.0650	0.0612	0.1217	0.0019	746	120	736	30	740	11	99%
YK1412-14-29		74.1	445	426	1.05	0.0629	0.0019	1.1183	0.0350	0.1284	0.0012	706	67	762	17	779	7	97%
YK1412-14-30		174.6	879	1081	0.81	0.0668	0.0014	1.1895	0.0255	0.1286	0.0010	831	44	796	12	780	6	98%
YK1412-14-31		79.3	184	1672	0.11	0.0519	0.0015	0.3120	0.0093	0.0435	0.0004	280	69	276	7	274	2	99%
YK1412-14-32		181.2	853	1482	0.58	0.0618	0.0014	0.8789	0.0284	0.1023	0.0023	665	50	640	15	628	13	98%
YK1412-14-33		443.6	3470	2456	1.41	0.0668	0.0013	1.1613	0.0216	0.1256	0.0009	831	44	783	10	763	5	97%
YK1412-14-34		63.5	168	868	0.19	0.0569	0.0019	0.4842	0.0171	0.0618	0.0009	487	77	401	12	387	6	96%
YK1412-14-35		75.9	113	1371	0.08	0.0538	0.0014	0.3696	0.0110	0.0494	0.0008	365	57	319	8	311	5	97%
YK1412-14-36		211.9	803	2546	0.32	0.0570	0.0012	0.5480	0.0123	0.0694	0.0007	494	42	444	8	433	4	97%
YK1412-14-37		130.3	299	1840	0.16	0.0539	0.0012	0.4661	0.0134	0.0616	0.0011	365	48	389	9	385	7	99%
YK1412-14-38		41.37	10.7	1165	0.009	0.0499	0.0025	0.2369	0.0119	0.0344	0.0003	191	114	216	10	218	2	99%
YK1412-14-39		55.50	24.0	1497	0.016	0.0487	0.0017	0.2415	0.0086	0.0358	0.0005	132	81	220	7	227	3	96%
YK1412-14-40		46.78	9.16	1253	0.007	0.0502	0.0019	0.2485	0.0093	0.0359	0.0004	211	82	225	8	227	2	99%
YK1412-14-41		57.43	18.4	1519	0.012	0.0509	0.0021	0.2493	0.0101	0.0355	0.0003	235	94	226	8	225	2	99%
YK1412-14-42		44.45	15.6	1184	0.013	0.0515	0.0020	0.2524	0.0094	0.0356	0.0004	261	87	229	8	226	2	98%
YK1412-14-43		42.19	15.4	1109	0.014	0.0510	0.0019	0.2528	0.0096	0.0360	0.0005	239	87	229	8	228	3	99%
YK1412-14-44		66.89	27.0	1801	0.015	0.0501	0.0017	0.2463	0.0086	0.0354	0.0003	198	80	224	7	224	2	99%
YK1412-14-45	Overgrowth	51.32	36.0	1362	0.026	0.0499	0.0018	0.2456	0.0091	0.0356	0.0005	191	114	223	7	225	3	98%
YK1412-14-46	rims	32.70	9.99	933	0.011	0.0509	0.0027	0.2373	0.0126	0.0337	0.0004	235	122	216	10	213	2	98%
YK1412-14-47		46.18	16.3	1222	0.013	0.0520	0.0022	0.2566	0.0106	0.0359	0.0004	283	96	232	9	227	3	97%
YK1412-14-48		47.35	18.5	1251	0.015	0.0510	0.0018	0.2469	0.0087	0.0350	0.0003	243	77	224	7	222	2	98%
YK1412-14-49		39.58	13.0	1067	0.012	0.0507	0.0020	0.2423	0.0094	0.0347	0.0003	228	93	220	8	220	2	99%
YK1412-14-50		71.23	49.0	1877	0.026	0.0520	0.0016	0.2513	0.0073	0.0351	0.0003	283	70	228	6	223	2	97%
YK1412-14-51		48.63	19.3	1296	0.015	0.0520	0.0019	0.2519	0.0097	0.0352	0.0006	283	83	228	8	223	4	97%
YK1412-14-52		52.69	16.4	1416	0.012	0.0510	0.0018	0.2519	0.0091	0.0357	0.0004	243	77	228	7	226	2	99%
YK1412-14-53		53.24	16.5	1426	0.012	0.0512	0.0021	0.2488	0.0099	0.0352	0.0003	250	86	226	8	223	2	98%

Gneiss YK156-4

Spot No.	Domain	Element Content (ppm)			Th/U	Isotopic ratio						Ages						
		Pb	Th	U		$^{206}Pb/^{207}Pb$	1σ	$^{207}Pb/^{235}U$	1σ	$^{206}Pb/^{238}U$	1σ	$^{206}Pb/^{207}Pb$	1σ	$^{207}Pb/^{235}U$	1σ	$^{206}Pb/^{238}U$	1σ	Concordance
YK156-4-01		145.3	546	874	0.62	0.0638	0.0013	1.1267	0.0301	0.1279	0.0023	744	44	766	14	776	13	98%
YK156-4-02		102.0	429	693	0.62	0.0656	0.0016	0.9537	0.0220	0.1056	0.0011	794	51	680	11	647	6	95%

YK156-4-03	Core	152.1	708	962	0.74	0.0655	0.0011	1.0404	0.0182	0.1144	0.0011	791	40	724	9	698	6	96%
YK156-4-04		286.6	1235	1631	0.76	0.0644	0.0009	1.1622	0.0209	0.1290	0.0014	767	31	783	10	782	8	99%
YK156-4-05		131.8	1222	949	1.29	0.0605	0.0017	0.6996	0.0187	0.0838	0.0012	633	59	539	11	519	7	96%
YK156-4-06		35.3	157	198	0.79	0.0653	0.0030	1.1482	0.0512	0.1274	0.0021	787	96	776	24	773	12	99%
YK156-4-07		51.7	129	746	0.17	0.0581	0.0023	0.4291	0.0155	0.0539	0.0009	532	87	363	11	339	5	93%
YK156-4-08		172.7	838	970	0.86	0.0634	0.0016	1.1259	0.0293	0.1274	0.0018	724	22	766	14	773	10	99%
YK156-4-09		93.7	632	583	1.09	0.0622	0.0021	0.8758	0.0281	0.1013	0.0014	681	70	639	15	622	8	97%
YK156-4-10		95.5	422	640	0.66	0.0636	0.0018	1.1361	0.0411	0.1276	0.0032	728	27	771	20	774	18	99%
YK156-4-11		111.7	562	667	0.84	0.0623	0.0015	1.0575	0.0257	0.1220	0.0014	683	56	733	13	742	8	98%
YK156-4-12		160.4	433	1419	0.30	0.0584	0.0012	0.7661	0.0241	0.0930	0.0019	546	44	578	14	573	11	99%
YK156-4-13		61.6	88.3	931	0.09	0.0553	0.0020	0.4186	0.0136	0.0550	0.0006	433	80	355	10	345	4	97%
YK156-4-14		52.0	41.5	1027	0.04	0.0489	0.0021	0.2997	0.0122	0.0442	0.0005	146	100	266	10	279	3	95%
YK156-4-15		108.9	301	691	0.44	0.0651	0.0017	1.1487	0.0289	0.1282	0.0017	776	54	777	14	778	10	99%
YK156-4-16		161.6	458	1097	0.42	0.0620	0.0014	1.1160	0.0305	0.1287	0.0022	676	48	761	15	781	13	97%
YK156-4-17		91.2	675	580	1.16	0.0642	0.0020	0.9665	0.0333	0.1090	0.0020	750	65	687	17	667	11	97%
YK156-4-18		58.0	342	314	1.09	0.0654	0.0022	1.1681	0.0398	0.1290	0.0019	787	71	786	19	782	11	99%
YK156-4-19		122.4	521	996	0.52	0.0622	0.0017	0.8226	0.0310	0.0942	0.0025	680	62	610	17	580	15	95%
YK156-4-20		70.3	271	562	0.48	0.0612	0.0017	0.8340	0.0228	0.0980	0.0011	656	59	616	13	603	6	97%
YK156-4-21		108.9	174	1536	0.11	0.0570	0.0014	0.4855	0.0133	0.0611	0.0010	500	54	402	9	382	6	95%
YK156-4-22		35.2	218	187	1.17	0.0694	0.0027	1.2067	0.0460	0.1279	0.0022	909	80	804	21	776	13	96%
YK156-4-23		105.5	743	512	1.45	0.0642	0.0018	1.1536	0.0326	0.1293	0.0016	746	59	779	15	784	9	99%
YK156-4-24		63.3	116	1296	0.09	0.0546	0.0017	0.3219	0.0108	0.0423	0.0005	394	70	283	8	267	3	94%
YK156-4-25		66.6	84.9	1179	0.07	0.0566	0.0019	0.3824	0.0123	0.0490	0.0006	476	40	329	9	308	3	93%
YK156-4-26		135.7	947	690	1.37	0.0627	0.0015	1.1249	0.0282	0.1294	0.0017	700	47	765	13	784	10	97%
YK156-4-27		61.6	130	1022	0.13	0.0552	0.0017	0.3950	0.0133	0.0518	0.0009	420	75	338	10	325	6	96%
YK156-4-28		116.2	375	948	0.40	0.0616	0.0017	0.8416	0.0233	0.0984	0.0014	661	55	620	13	605	8	97%
YK156-4-29		240.1	2083	1671	1.25	0.0632	0.0015	0.9092	0.0293	0.1030	0.0022	717	50	657	16	632	13	96%
YK156-4-30		77.5	258	917	0.28	0.0587	0.0017	0.5903	0.0204	0.0722	0.0015	554	65	471	13	449	9	95%
YK156-4-31		25.8	121	274	0.44	0.0578	0.0035	0.5654	0.0312	0.0723	0.0014	520	136	455	20	450	9	98%
YK156-4-32		176.4	976	948	1.03	0.0644	0.0011	1.1474	0.0199	0.1280	0.0010	755	35	776	9	776	6	99%
YK156-4-33		53.3	31.5	1165	0.03	0.0517	0.0016	0.2887	0.0089	0.0403	0.0005	272	66	258	7	255	3	98%
YK156-4-34		43.9	57.4	859	0.07	0.0541	0.0018	0.3203	0.0112	0.0431	0.0006	376	76	282	9	272	3	96%
YK156-4-35	Overgrowth rims	38.54	46.7	879	0.053	0.0542	0.0022	0.2619	0.0101	0.0356	0.0005	389	89	236	8	225	3	95%
YK156-4-36		31.08	6.43	764	0.008	0.0530	0.0030	0.2520	0.0137	0.0351	0.0005	328	131	228	11	222	3	97%
YK156-4-38		37.48	14.6	984	0.015	0.0484	0.0017	0.2288	0.0079	0.0343	0.0004	120	90	209	7	218	3	96%
YK156-4-39		46.47	16.2	1219	0.013	0.0499	0.0016	0.2419	0.0076	0.0353	0.0004	191	71	220	6	223	3	98%
YK156-4-40		42.39	23.7	1141	0.021	0.0486	0.0022	0.2361	0.0113	0.0351	0.0005	128	109	215	9	222	3	96%
YK156-4-41		39.64	34.3	1036	0.033	0.0511	0.0019	0.2510	0.0110	0.0353	0.0007	243	87	227	9	223	4	98%
YK156-4-42		46.97	19.2	1213	0.016	0.0466	0.0016	0.2243	0.0072	0.0349	0.0005	33.4	72.2	205	6	221	3	92%
YK156-4-43		71.44	21.3	1895	0.011	0.0515	0.0016	0.2537	0.0081	0.0357	0.0005	261	72	230	7	226	3	98%
YK156-4-44		37.65	10.9	1014	0.011	0.0541	0.0024	0.2483	0.0106	0.0348	0.0008	376	100	225	9	221	5	98%
YK156-4-45		73.85	34.9	1947	0.018	0.0503	0.0016	0.2378	0.0073	0.0340	0.0004	209	40	217	6	216	2	99%
YK156-4-47		51.87	26.4	1306	0.020	0.0517	0.0017	0.2539	0.0082	0.0354	0.0004	272	76	230	7	224	2	97%
YK156-4-48		42.50	12.5	1095	0.011	0.0489	0.0016	0.2330	0.0073	0.0348	0.0004	143	78	213	6	221	2	96%
YK156-4-49		41.85	13.4	1071	0.012	0.0557	0.0025	0.2668	0.0121	0.0350	0.0005	439	128	240	10	222	3	91%
YK156-4-50		34.01	21.0	815	0.026	0.0549	0.0029	0.2700	0.0136	0.0362	0.0006	406	119	243	11	229	4	94%
YK156-4-37		36.99	66.1	879	0.075	0.0637	0.0025	0.3031	0.0123	0.0349	0.0007	731	85	269	10	221	4	80%
YK156-4-46		42.00	14.8	1163	0.013	0.0667	0.0037	0.3447	0.0291	0.0347	0.0009	831	109	301	22	220	5	68%
YK156-4-51		32.15	13.1	774	0.017	0.0695	0.0036	0.3358	0.0170	0.0351	0.0005	922	-93	294	13	222	3	72%

Note: values in red color represent individual analysis with <90% concordance.

Table S6a. LA-ICP-MS zircon trace element compositions (ppm) of the host eclogites.

Eclogite YK1412-13

Spot No.	Domain	Ti	Y	Nb	La	Ce	Pr	Nd	Sm	Eu	Gd	Tb	Dy	Ho	Er	Tm	Yb	Lu	Hf	Ta	Pb	Th	U	ΣREE	ΣHREE	Ce/Ce*	Eu/Eu*	(Gd/Lu)$_N$	Th/U	Hf/Y	T (°C) 2.5 GPa
YK1412-13-01	Core	17.8	4053	5.76	0.022	90.1	0.25	3.28	10.4	3.20	57.2	21.3	305	110	575	122	1357	223	31847	2.51	313	721	766	2878	2770	300.3	0.40	0.212	0.941	7.9	*n.c.*
YK1412-13-02		140	9397	4.84	0.39	111	1.27	20.3	33.8	10.1	185	57.1	764	265	1314	265	2848	460	23235	2.44	399	893	579	6336	6159	38.5	0.39	0.331	1.543	2.5	*n.c.*
YK1412-13-03		48.4	15096	6.73	31.1	251	8.02	57.9	65.7	18.8	306	96.0	1266	419	2041	418	4390	655	24769	2.71	617	1415	788	10024	9591	3.9	0.41	0.385	1.796	1.6	*n.c.*
YK1412-13-04		34.3	12342	5.94	0.16	141	1.57	25.4	53.3	15.1	243	77.0	1029	349	1678	345	3676	547	27635	2.55	514	1163	715	8180	7944	69.7	0.40	0.367	1.626	2.2	*n.c.*
YK1412-13-05		6.93	545	1.38	*b.d.*	12.7	0.019	0.56	1.36	0.87	12.5	3.40	44.7	15.8	72.4	14.8	163	26.8	35157	0.50	133	155	254	369	354	*n.a.*	0.64	0.386	0.613	64.5	*n.c.*
YK1412-13-06		19.6	8047	5.45	0.016	116	0.80	12.7	28.4	8.47	148	48.1	639	220	1129	236	2562	424	27235	3.11	544	1172	1063	5573	5407	252.7	0.40	0.288	1.103	3.4	*n.c.*
YK1412-13-07		22.9	7922	7.27	0.063	131	0.49	7.25	20.1	5.67	121	42.2	595	211	1109	236	2598	435	26290	3.32	655	1321	1202	5513	5349	183.3	0.35	0.230	1.099	3.3	*n.c.*
YK1412-13-08		6.14	3178	3.35	*b.d.*	60.0	0.19	3.25	5.83	2.20	44.7	16.1	224	87.0	467	103	1209	208	30549	2.70	284	428	1024	2430	2358	*n.a.*	0.42	0.177	0.417	9.6	*n.c.*
YK1412-13-09		180	21295	13.0	3.59	205	3.93	59.5	112	35.7	543	157	1931	614	2825	557	5794	862	20722	3.04	894	2130	971	13702	13283	13.4	0.44	0.520	2.194	1.0	*n.c.*
YK1412-13-10		3.67	3176	3.96	0.021	79.3	0.18	3.35	6.18	2.20	45.0	16.5	224	83.8	463	104	1240	212	28307	2.90	393	713	1334	2478	2387	315.1	0.40	0.175	0.535	8.9	*n.c.*
YK1412-13-11		13.9	2624	1.75	0.045	34.3	0.34	5.56	9.78	3.23	45.6	15.5	202	72.3	371	78.1	835	133	34061	0.84	167	297	454	1806	1753	67.9	0.47	0.282	0.654	13.0	*n.c.*
YK1412-13-12		85.7	13190	8.61	1.50	213	1.82	30.0	49.7	13.6	243	78.1	1047	365	1782	368	3950	596	28768	4.15	956	2277	1259	8737	8428	31.5	0.38	0.337	1.809	2.2	*n.c.*
YK1412-13-13		10.2	2405	2.69	0.039	44.2	0.20	2.31	5.73	1.82	36.8	11.8	176	64.8	343	74.7	830	146	30405	1.68	173	304	582	1737	1682	121.9	0.38	0.208	0.523	12.6	*n.c.*
YK1412-13-14		23.8	6152	3.89	0.052	80.3	0.19	8.41	21.5	7.24	111	34.9	482	171	840	176	1982	292	28424	2.04	240	518	525	4205	4088	200.4	0.45	0.313	0.986	4.6	*n.c.*
YK1412-13-15		24.3	6906	3.83	0.11	86.4	0.80	15.2	25.7	8.47	133	42.5	568	194	960	202	2280	324	25560	1.77	254	553	463	4842	4705	73.1	0.44	0.340	1.195	3.7	*n.c.*
YK1412-13-16		22.3	8698	4.53	0.074	138	1.04	16.6	34.4	9.09	166	54.7	711	242	1173	244	2576	397	26955	2.36	457	962	730	5763	5564	122.2	0.37	0.345	1.318	3.1	*n.c.*
YK1412-13-17		442	2084	2.48	0.014	34.1	0.14	1.62	6.34	1.53	29.8	11.8	156	56.1	296	64.7	721	121	30225	1.40	115	201	754	1500	1456	193.9	0.34	0.204	0.266	14.5	*n.c.*
YK1412-13-18		6.98	725	0.71	0.060	12.6	0.049	0.69	2.59	1.11	16.0	5.31	59.1	18.7	93.1	19.7	225	35.5	32592	0.42	143	163	382	490	473	57.0	0.53	0.372	0.427	44.9	*n.c.*
YK1412-13-19	Overgrowth rims and new zircon grains	13.0	245	0.27	0.021	1.07	*b.d.*	0.087	0.10	0.45	4.42	2.28	23.4	5.60	22.7	3.52	35.3	5.73	34741	0.17	15.8022	1.32	195	105	103	*n.a.*	2.02	0.636	0.007	142.0	846
YK1412-13-20		12.1	182	0.40	*b.d.*	0.60	*b.d.*	0.31	0.51	0.41	4.07	1.53	17.9	4.87	18.8	2.89	26.8	3.64	34173	0.18	10.0410	0.68	173	82	80	*n.a.*	0.87	0.923	0.004	187.3	839
YK1412-13-21		14.0	313	0.35	0.011	2.32	*b.d.*	0.14	1.06	0.85	9.91	2.63	33.8	8.92	32.8	5.73	55.6	7.72	35126	0.091	16.2808	4.69	311	161	157	*n.a.*	0.80	1.059	0.015	112.2	853
YK1412-13-22		11.5	148	0.26	*b.d.*	1.35	0.017	0.28	0.43	0.55	4.42	1.50	15.2	3.74	15.4	2.68	26.8	4.18	36291	0.15	19.83	5.67	187	77	74	*n.a.*	1.22	0.873	0.030	244.6	834
YK1412-13-23		9.61	234	0.24	*b.d.*	1.12	0.0066	0.12	0.29	0.40	3.97	1.74	20.8	5.69	23.9	4.19	41.4	5.66	33901	0.24	17.0299	1.25	219	109	107	*n.a.*	1.14	0.579	0.006	145.0	817
YK1412-13-24		*b.d.*	200	0.30	*b.d.*	1.07	0.028	0.22	0.88	0.65	4.78	1.98	21.4	5.23	17.7	3.06	30.5	4.56	36464	0.13	16.69	1.06	195	92	89	*n.a.*	0.97	0.865	0.005	182.0	*n.a.*
YK1412-13-25		*b.d.*	314	0.20	0.022	1.30	0.030	0.22	0.63	0.50	6.90	2.54	28.4	8.02	30.2	5.70	57.1	8.22	34852	0.26	17.7422	3.37	203	150	147	12.1	0.74	0.692	0.017	110.9	*n.a.*
YK1412-13-26		*b.d.*	170	0.44	*b.d.*	1.66	0.023	0.047	1.12	0.68	4.62	2.23	18.1	4.20	15.5	2.37	23.0	2.94	34149	0.17	21.6103	1.78	266	76	73	*n.a.*	0.91	1.295	0.007	200.4	*n.a.*
YK1412-13-27		16.8	219	0.36	0.0073	0.82	0.0099	0.030	0.32	0.46	4.60	1.81	21.1	5.73	21.7	4.12	35.1	5.08	34861	0.14	12.91	0.81	183	101	99	23.6	1.16	0.747	0.004	159.4	872
YK1412-13-28		10.2	248	0.31	0.038	0.81	0.0086	0.052	0.44	0.57	4.80	1.93	20.9	6.26	24.6	3.86	37.8	6.55	33290	0.19	24.30	1.58	211	109	107	10.9	1.20	0.605	0.007	134.5	823
YK1412-13-29		12.0	203	0.40	b.d.	1.96	b.d.	0.25	0.83	0.88	8.95	2.18	22.0	5.05	19.8	3.29	34.2	4.79	35908	0.18	5.72	2.52	237	104	100	*n.a.*	0.98	1.542	0.011	176.7	839
YK1412-13-30		8.82	144	0.24	0.015	1.26	0.0099	0.091	0.47	0.67	5.57	1.83	14.0	3.74	11.3	1.50	18.5	2.71	34015	0.14	10.2039	1.80	229	62	59	25.6	1.27	1.697	0.008	236.8	809
YK1412-13-31		10.9	174	0.35	*b.d.*	1.20	b.d.	0.030	0.57	0.51	4.72	1.45	16.7	4.22	15.9	3.03	27.2	4.08	35379	0.14	8.84	3.32	237	80	77	*n.a.*	0.96	0.954	0.014	203.4	829
YK1412-13-32		3.20	169	0.32	*b.d.*	1.07	0.011	0.13	0.70	0.54	5.12	1.73	16.2	4.30	15.6	2.59	22.8	3.12	33625	0.10	7.3160	1.30	216	74	71	*n.a.*	0.87	1.354	0.006	198.6	724
YK1412-13-33		*b.d.*	172	0.20	0.031	0.84	0.021	0.063	0.45	0.34	4.44	1.67	17.6	4.39	16.4	2.59	22.8	3.22	34649	0.19	7.8814	0.93	170	75	73	8.1	0.74	1.137	0.005	200.9	*n.a.*
YK1412-13-34		8.66	170	0.23	b.d.	0.72	0.018	0.056	0.47	0.26	3.14	1.64	17.5	4.66	13.7	2.38	19.7	2.99	33703	0.12	11.35	1.17	180	67	66	*n.a.*	0.67	0.866	0.006	198.5	808
YK1412-13-35		12.3	196	0.31	0.0083	2.36	0.017	0.14	0.81	0.87	7.43	1.96	20.9	5.22	18.7	3.44	29.9	4.55	33424	0.17	10.72	3.08	378	96	92	49.1	1.09	1.347	0.008	170.4	840
YK1412-13-36		6.55	170	0.34	b.d.	0.66	0.0000	0.073	0.52	0.59	3.94	1.70	17.1	4.41	14.4	2.35	22.2	3.00	33451	0.096	5.80	1.11	196	71	69	*n.a.*	1.26	1.085	0.006	196.4	783
YK1412-13-37		10.3	189	0.043	b.d.	1.16	0.0061	0.074	0.18	0.49	5.09	1.67	16.4	4.99	19.4	3.44	35.6	4.88	31088	0.11	6.20	3.07	210	93	91	*n.a.*	1.57	0.862	0.015	164.2	824

Eclogite YK156-3

Spot No.	Domain	Ti	Y	Nb	La	Ce	Pr	Nd	Sm	Eu	Gd	Tb	Dy	Ho	Er	Tm	Yb	Lu	Hf	Ta	Pb	Th	U	ΣREE	ΣHREE	Ce/Ce*	Eu/Eu*	(Gd/Lu)$_N$	Th/U	Hf/Y	T (°C) 2.5 GPa
YK156-3-01	Core	23.0	9264	3.74	0.20	96.6	1.99	28.8	46.7	10.6	208	59.7	770	258	1220	236	2382	383	26605	1.48	266	569	365	5702	5517	37.5	0.33	0.449	1.560	2.9	*n.c.*
YK156-3-02		26.3	11201	5.01	0.14	111	1.71	26.8	48.2	15.1	226	70.0	920	304	1465	278	2849	459	25541	1.93	391	903	473	6774	6571	55.0	0.44	0.406	1.909	2.3	*n.c.*
YK156-3-03		19.5	5040	3.32	0.030	63.3	0.25	4.29	10.7	3.93	64.5	24.2	345	130	692	144	1575	273	33271	1.97	373	818	761	3331	3248	176.3	0.46	0.195	1.074	6.6	*n.c.*
YK156-3-04		18.5	6297	45.2	15.3	257	3.17	13.3	8.39	1.44	45.0	19.5	331	146	902	210	2501	425	34805	10.3	510	1156	1164	4877	4578	9.0	0.23	0.087	0.993	5.5	*n.c.*
YK156-3-05		*b.d.*	505	2.49	0.0084	18.1	0.0057	0.17	0.28	*b.d.*	1.66	1.06	19.4	12.5	97.8	31.1	479	110	30265	2.72	120	167	554	771	752	641.9	*n.a.*	0.012	0.301	59.9	*n.c.*
YK156-3-06		4.41	310	0.30	0.028	9.45	*b.d.*	0.039	0.28	0.14	2.05	0.79	16.6	6.47	46.7	13.1	207	51.9	31002	0.15	124	204	593	354	344	*n.a.*	0.57	0.033	0.343	100.2	*n.c.*
YK156-3-07		3.57	3034	4.65	0.019	65.1	0.11	2.92	6.10	1.53	38.2	14.1	208	79.3	432	96.7	1128	213	41429	2.46	455	628	2513	2284	2209	351.4	0.31	0.148	0.250	13.7	*n.c.*
YK156-3-08		21.7	9772	4.01	0.14	92.0	1.17	24.8	40.3	11.5	199	61.8	801	271	1300	253	2625	412	26863	1.79	332	732	426	6092	5922	56.1	0.39	0.398	1.718	2.7	*n.c.*
YK156-3-09		15.7	11472	5.15	0.27	160	1.41	25.2	40.0	13.3	209	65.0	872	304	1529	311	3382	543	28313	2.30	1018	2282	1484	7454	7214	63.6	0.44	0.318	1.537	2.5	*n.c.*
YK156-3-10		25.7	3084	4.37	0.32	63.6	0.12	3.30	6.43	1.80	45.5	15.1	219	77.7	406	85.0	899	152	30969	1.78	287	460	741	1975	1899	79.1	0.32	0.248	0.621	10.0	*n.c.*
YK156-3-11		16.1	446	1.30	0.011	10.2	0.050	0.17	1.07	0.83	9.00	2.00	27.9	11.2	67.6	18.1	250	52.3	39477	1.61	130.1	101	1304	450	438	109.5	0.81	0.142	0.077	88.6	*n.c.*
YK156-3-12		14.7	4566	22.8	24.7	117	6.18	32.6	15.8	3.97	67.2	21.1	321	123	661	144	1646	273	34731	10.4	386	734	1056	3455	3254	2.3	0.37	0.203	0.695	7.6	*n.c.*
YK156-3-13		12.8	456	0.57	*b.d.*	7.41	0.032	*b.d.*	1.28	0.65	7.88	2.39	30.2	11.7	62.5	15.3	174	29.4	38482	0.36	53.5	46.8	311	343	334	*n.a.*	0.63	0.221	0.151	84.4	*n.c.*
YK156-3-14	Overgrowth rims and new zircon grains	6.82	107	0.40	*b.d.*	2.11	*b.d.*	0.10	0.58	0.72	5.90	1.34	11.0	2.85	10.0	1.65	14.9	2.43	38092	0.32	17.51	2.77	297	54	50	*n.a.*	1.18	2.001	0.009	355.7	786
YK156-3-15		3.70	201	0.41	0.022	2.53	0.0074	0.090	0.69	0.84	8.49	2.29	20.8	4.82	17.8	2.79	25.0	4.12	32219	0.14	9.30	2.07	379	90	86	48.9	1.06	1.698	0.005	160.3	735
YK156-3-16		9.24	102	0.37	0.017	2.86	*b.d.*	0.14	0.41	0.51	5.43	1.21	11.3	2.64	9.10	1.45	15.1	1.80	39836	0.35	14.09	3.51	470	52	48	*n.a.*	1.05	2.485	0.007	389.2	814
YK156-3-17		*b.d.*	95.9	0.33	0.017	2.33	*b.d.*	0.070	0.46	0.54	4.53	1.42	10.6	2.49	9.32	1.42	14.7	2.00	39965	0.38	10.72	3.53	382	50	46	*n.a.*	1.15	1.864	0.009	416.6	*n.a.*
YK156-3-18		37.7	99.9	0.45	0.10	4.38	0.13	0.81	1.62	0.77	6.36	1.28	12.5	2.47	9.64	1.53	14.3	1.99	38431	0.17	8.0371	4.46	333	58	50	9.2	0.73	2.636	0.013	384.6	963
YK156-3-19		12.6	146	0.49	*b.d.*	2.53	0.024	0.11	0.65	0.81	7.89	1.95	17.4	3.29	12.0	1.85	19.0	2.47	40415	0.29	21.41	4.43	800	70	66	*n.a.*	1.09	2.637	0.006	276.5	843
YK156-3-20		*b.d.*	102	0.40	0.0082	2.14	0.011	0.034	0.52	0.56	5.65	0.85	11.4	2.45	9.05	1.38	12.1	1.89	36442	0.20	8.24	2.60	314	48	45	54.9	1.00	2.472	0.008	358.8	*n.a.*
YK156-3-21		7.17	188	0.34	*b.d.*	2.35	0.0081	0.15	0.99	0.86	6.94	2.29	20.4	4.91	19.0	3.09	32.9	4.90	39064	0.22	10.05	6.35	340	99	95	*n.a.*	1.00	1.168	0.019	207.7	791
YK156-3-22		10.7	76.6	0.22	0.024	2.14	0.0054	0.066	0.47	0.48	3.88	1.08	9.54	1.84	6.38	1.21	9.16	1.59	36634	0.27	16.18	1.96	270	38	35	46.1	1.10	2.020	0.007	478.0	827
YK156-3-23		6.42	125	0.32	0.022	2.63	*b.d.*	0.045	0.59	0.54	4.31	1.25	11.9	3.11	12.2	2.27	26.8	3.71	38467	0.15	14.98	6.54	314	69	66	*n.a.*	1.04	0.958	0.021	307.9	781
YK156-3-24		9.11	136	0.41	*b.d.*	2.96	0.0062	0.11	1.37	1.07	8.75	1.96	16.8	3.34	12.2	1.78	17.8	2.77	34665	0.25	19.48	1.40	365	71	65	*n.a.*	0.94	2.609	0.004	255.5	812
YK156-3-25		9.83	114	0.33	*b.d.*	1.46	0.021	0.042	0.69	0.60	5.34	1.30	11.5	3.01	10.6	1.58	17.2	2.66	36061	0.15	8.57	1.58	222	56	53	*n.a.*	0.96	1.655	0.007	316.2	819
YK156-3-26		6.13	156	0.27	0.031	2.98	0.032	0.36	1.06	0.99	9.26	2.16	17.1	4.08	13.9	2.19	19.3	2.64	34349	0.15	12.30	3.39	356	76	71	23.1	0.96	2.898	0.010	220.1	777
YK156-3-27		8.35	103	0.14	*b.d.*	2.19	*b.d.*	0.19	0.45	0.64	3.84	1.19	11.3	2.25	8.94	1.54	13.5	1.89	36993	0.042	14.43	2.28	241	48	44	*n.a.*	1.49	1.678	0.009	359.0	804
YK156-3-28		2.25	114	0.34	0.018	1.64	0.024	0.075	0.57	0.57	5.15	1.37	13.7	3.02	9.72	1.59	14.8	2.13	34660	0.11	21.8	2.48	263	54	51	19.1	1.01	1.991	0.009	303.8	698
YK156-3-29		6.19	132	0.29	0.039	1.44	*b.d.*	0.11	*b.d.*	0.85	5.93	1.41	14.9	3.33	11.6	1.81	17.3	2.09	37210	0.094	6.50	2.69	244	61	58	*n.a.*	*n.a.*	2.341	0.011	282.9	778

Table S6b. LA-ICP-MS zircon trace element compositions (ppm) of the granite of the composite granite–quartz veins.

Granite YK1412-12

Spot No.	Domain	Ti	Y	Nb	La	Ce	Pr	Nd	Sm	Eu	Gd	Tb	Dy	Ho	Er	Tm	Yb	Lu	Hf	Ta	Pb	Th	U	ΣREE	ΣHREE	Ce/Ce*	Eu/Eu*	(Gd/Lu)$_N$	Th/U	Hf/Y	T (°C) 2.5 GPa
YK1412-12-01		16.0	364	1.92	*b.d.*	8.95	0.14	0.58	2.28	0.18	4.79	2.46	30.7	11.7	53.4	11.4	124	22.9	13365	1.08	52.6	68.4	151	274	262	*n.a.*	0.16	0.172	0.453	36.7	*n.c.*
YK1412-12-02		16.7	868	1.21	*b.d.*	9.99	0.14	1.69	3.41	0.95	14.9	5.40	68.9	27.2	138	29.8	315	59.8	9907	0.54	22.8	33.7	63.7	675	659	*n.a.*	0.41	0.206	0.529	11.4	*n.c.*
YK1412-12-03		*b.d.*	328	2.55	0.14	4.16	0.028	0.25	0.43	0.13	4.77	1.83	25.3	9.43	53.3	13.7	169	34.2	12822	1.18	57.8	79.1	192	317	311	16.1	0.27	0.115	0.413	39.1	*n.c.*
YK1412-12-04		11.5	1659	8.49	*b.d.*	49.5	0.0051	2.46	4.74	0.93	31.7	11.0	146	54.4	256	54.7	562	97.8	12068	3.09	191.6	371	323	1271	1213	*n.a.*	0.23	0.267	1.147	7.3	*n.c.*
YK1412-12-05		*b.d.*	1710	12.0	*b.d.*	33.2	0.23	1.23	4.09	0.54	25.4	9.69	135	53.2	267	59.3	634	113	12965	4.34	231.6	435	499	1335	1296	*n.a.*	0.16	0.186	0.872	7.6	*n.c.*
YK1412-12-06		14.0	1183	3.16	*b.d.*	24.2	0.14	2.04	3.92	0.82	21.9	7.84	100	38.0	183	38.4	405	72.0	10231	1.09	74.8	140	109	898	867	*n.a.*	0.27	0.251	1.288	8.6	*n.c.*
YK1412-12-07		11.1	1832	13.1	0.59	52.8	0.42	5.01	6.24	1.02	29.3	10.8	145	57.9	289	64.8	685	123	11725	4.29	101.7	162	288	1471	1405	25.8	0.23	0.197	0.561	6.4	*n.c.*
YK1412-12-08		6.05	1077	6.76	0.24	15.2	0.16	2.18	2.80	0.43	14.9	5.63	81.7	33.1	171	39.9	456	88.4	12699	3.38	76.5	120	318	912	891	19.1	0.21	0.139	0.377	11.8	*n.c.*
YK1412-12-09		20.0	190	0.80	0.053	2.40	0.0012	*b.d.*	1.29	0.20	4.94	1.39	17.2	5.62	26.8	5.76	57.7	10.4	12646	0.43	14.4	14.9	101	134	130	73.0	0.24	0.391	0.147	66.5	*n.c.*

YK1412-12-10		5.82	1297	7.10	0.17	17.0	*b.d.*	1.55	2.84	0.62	16.8	6.69	99.0	40.0	206	46.6	511	92.0	13158	2.76	78.6	122	231	1041	1019	*n.a.*	0.27	0.151	0.530	10.1	*n.c.*
YK1412-12-11		4.64	1043	5.83	1.13	26.2	0.14	1.86	2.24	0.43	14.5	5.75	78.5	31.6	161	35.9	382	69.4	13659	2.73	71.9	119	174	810	778	16.1	0.23	0.173	0.686	13.1	*n.c.*
YK1412-12-12		30.5	1011	7.45	0.36	23.5	*b.d.*	*b.d.*	1.47	0.36	13.2	5.85	74.3	31.1	156	35.9	379	68.1	12432	2.92	84.0	143	225	789	763	*n.a.*	0.25	0.159	0.636	12.3	*n.c.*
YK1412-12-13		*b.d.*	360	2.71	*b.d.*	9.53	0.12	1.04	1.03	0.20	4.40	2.11	28.5	11.5	53.6	12.1	134	24.9	11690	1.77	29.6	45.3	101	283	271	*n.a.*	0.28	0.146	0.448	32.5	*n.c.*
YK1412-12-14		*b.d.*	1058	7.84	2.16	50.7	0.44	2.61	2.25	0.23	11.5	4.31	67.5	29.6	165	41.4	522	108	12326	1.74	102.2	182	288	1007	949	12.8	0.14	0.087	0.631	11.7	*n.c.*
YK1412-12-15		*b.d.*	2363	14.2	10.6	130	2.59	11.7	6.77	1.54	37.2	14.1	190	74.6	356	73.9	739	125	10605	3.00	162.0	300	220	1772	1609	6.1	0.30	0.246	1.366	4.5	*n.c.*
YK1412-12-16		2.07	522	4.31	0.15	8.63	*b.d.*	0.094	0.99	0.31	9.30	3.04	41.1	15.9	80.4	18.0	197	35.9	12650	2.72	39.9	64.3	206	410	400	*n.a.*	0.31	0.214	0.312	24.2	*n.c.*
YK1412-12-17	Core	42.0	928	2.48	*b.d.*	19.1	*b.d.*	1.73	3.70	0.42	19.2	6.25	80.7	29.8	137	28.9	296	51.5	11234	1.17	61.7	112	106	674	649	*n.a.*	0.15	0.307	1.061	12.1	*n.c.*
YK1412-12-18		6.40	1442	4.22	0.45	30.8	0.38	3.07	6.05	1.27	27.0	9.32	123	45.6	217	44.9	465	79.8	8976	1.06	53.2	88.0	71.5	1053	1011	18.4	0.30	0.280	1.230	6.2	*n.c.*
YK1412-12-19		3.64	1721	11.3	4.02	52.7	0.90	5.08	5.00	1.40	29.0	10.6	139	53.3	257	55.1	575	99.8	11618	3.81	222.2	386	389	1289	1219	6.8	0.36	0.240	0.992	6.8	*n.c.*
YK1412-12-20		8.33	2292	19.2	0.23	44.9	0.098	1.34	4.46	0.98	35.7	13.7	188	71.0	343	73.4	756	131	11325	5.44	321.2	591	555	1664	1612	73.9	0.24	0.224	1.066	4.9	*n.c.*
YK1412-12-21		15.8	3174	8.57	0.16	74.0	0.32	4.30	11.3	2.68	55.6	18.8	245	101	490	109	1070	223	30639	4.00	60.2	353	366	2405	2313	80.1	0.33	0.206	0.963	9.7	*n.c.*
YK1412-12-22		*b.d.*	4509	43.7	*b.d.*	70.4	0.21	0.49	8.68	1.72	63.1	24.4	350	147	710	159	1532	308	37812	16.3	201.9	1009	1393	3376	3294	*n.a.*	0.22	0.169	0.724	8.4	*n.c.*
YK1412-12-23		11.2	5732	27.6	0.41	195	0.42	7.58	18.9	4.72	110	39.3	484	189	871	183	1680	335	31802	8.91	168.1	1473	912	4117	3890	115.9	0.32	0.270	1.616	5.5	*n.c.*
YK1412-12-24		55.2	6193	50.6	0.70	127	0.13	5.00	9.78	2.03	94.2	38.8	504	206	967	212	2006	394	37670	15.8	240.5	1386	1518	4566	4421	102.2	0.20	0.197	0.913	6.1	*n.c.*
YK1412-12-25		21.5	624	8.51	0.59	7.94	*b.d.*	0.050	5.46	0.22	9.18	3.37	46.2	19.0	95.5	24.6	265	60.9	39959	3.39	37.8	87.5	515	538	523	*n.a.*	0.10	0.124	0.170	64.0	*n.c.*
YK1412-12-26		*b.d.*	602	4.65	0.091	5.50	*b.d.*	1.47	*b.d.*	1.06	6.75	3.55	43.6	18.7	96.4	24.2	241	52.9	38590	2.74	19.0	52.6	327	495	487	*n.a.*	*n.a.*	0.105	0.161	64.1	*n.c.*
YK1412-12-27		*b.d.*	2496	15.7	1.81	48.0	0.80	6.14	6.07	2.09	39.4	14.6	201	82.0	395	86.7	819	166	36966	6.79	87.7	413	603	1869	1804	9.8	0.41	0.196	0.685	14.8	*n.c.*
YK1412-12-28		*b.d.*	4443	31.9	0.45	81.7	0.83	5.77	10.4	1.03	70.9	26.6	353	145	690	154	1478	295	38633	12.3	169.9	865	1055	3313	3212	32.8	0.12	0.199	0.820	8.7	*n.c.*
YK1412-12-29		33.5	4749	31.7	5.11	124	2.90	21.7	19.5	5.54	90.0	30.9	395	158	724	153	1451	290	36820	12.4	207.7	1429	1214	3469	3290	7.9	0.40	0.256	1.177	7.8	*n.c.*
YK1412-12-30		21.4	7297	34.7	4.76	186	1.76	12.8	20.1	4.90	119	43.2	569	229	1053	227	2097	421	29332	9.69	142.6	800	780	4990	4760	15.7	0.31	0.233	1.025	4.0	*n.c.*
YK1412-12-31		24.9	3927	28.8	0.45	66.8	0.23	3.52	7.47	1.69	55.4	22.8	300	122	581	129	1235	252	32043	10.6	158.2	622	940	2778	2697	50.8	0.25	0.181	0.661	8.2	*n.c.*
YK1412-12-32		49.1	3746	30.6	1.02	70.9	0.49	4.29	7.27	2.66	55.3	19.3	283	118	565	127	1235	252	33504	12.2	200.7	856	1192	2741	2654	24.6	0.40	0.181	0.718	8.9	*n.c.*
YK1412-12-33		97.4	3361	26.5	2.46	74.6	0.94	7.69	7.14	1.65	49.0	19.7	257	105	493	111	1084	221	32266	10.4	152.7	767	1004	2434	2340	12.0	0.27	0.182	0.764	9.6	*n.c.*
YK1412-12-34		*b.d.*	1802	8.26	0.10	81.8	0.20	1.52	4.10	0.27	26.6	10.2	126	52.9	273	68.0	724	168	32606	2.56	61.4	306	360	1537	1449	142.4	0.08	0.131	0.850	18.1	*n.c.*
YK1412-12-35		11.7	29.4	0.23	*b.d.*	0.29	0.063	0.25	*b.d.*	*b.d.*	1.35	0.21	3.56	0.75	3.42	0.86	9.14	1.56	13946	0.16	2.9	0.17	58.4	21	21	*n.a.*	*n.a.*	0.715	0.003	473.9	908
YK1412-12-36		1.79	53.8	0.19	0.023	0.44	0.026	0.010	0.45	0.33	1.68	0.50	5.67	1.51	6.54	1.72	23.2	4.35	13057	0.17	1.7	0.49	76.3	46	45	4.4	1.16	0.318	0.006	242.6	733
YK1412-12-37		9.17	58.6	*b.d.*	*b.d.*	0.60	*b.d.*	*b.d.*	0.95	0.17	3.02	0.68	6.74	1.80	5.66	1.18	11.7	1.49	12573	0.0036	2.5	1.49	77.7	34	32	*n.a.*	0.31	1.679	0.019	214.6	881
YK1412-12-38		*b.d.*	63.5	0.18	0.014	1.30	0.12	0.18	*b.d.*	0.57	2.61	0.88	6.81	1.88	6.60	1.18	10.5	1.83	12246	0.17	4.4	1.25	161	34	32	7.6	*n.a.*	1.179	0.008	192.9	*n.a.*
YK1412-12-39		14.5	36.9	0.16	*b.d.*	0.18	0.0076	*b.d.*	0.94	0.22	0.94	0.43	4.23	1.21	4.52	0.89	9.87	1.68	11675	0.14	3.0	0.30	52.5	25	24	*n.a.*	0.73	0.459	0.006	316.2	932
YK1412-12-40		*b.d.*	59.9	0.083	*b.d.*	0.60	0.055	*b.d.*	*b.d.*	0.45	2.13	0.82	6.17	1.60	6.49	1.38	15.5	2.90	10950	0.070	2.3	0.20	60.8	38	37	*n.a.*	*n.a.*	0.606	0.003	182.7	*n.a.*
YK1412-12-41		4.69	135	0.63	*b.d.*	1.25	0.053	1.22	1.54	1.33	5.77	1.76	15.1	3.84	13.4	2.53	21.7	4.09	35751	0.26	6.4	1.12	175	74	68	*n.a.*	1.36	1.164	0.006	264.2	815
YK1412-12-42		1.05	99.9	*b.d.*	0.22	1.22	*b.d.*	2.10	2.82	0.11	4.81	1.11	9.90	2.93	10.5	2.27	20.4	4.12	38474	0.55	6.6	1.22	168	62	56	*n.a.*	0.09	0.964	0.007	385.3	693
YK1412-12-43	Overgrowth	*b.d.*	236	1.48	*b.d.*	1.09	0.067	1.35	*b.d.*	0.45	1.94	2.14	23.9	7.16	31.0	7.33	72.7	16.4	36271	0.68	5.5	0.90	158	166	163	*n.a.*	*n.a.*	0.097	0.006	153.5	*n.a.*
YK1412-12-44	rims and	6.19	133	0.0000	0.43	0.78	*b.d.*	2.02	0.70	0.83	3.47	1.55	13.4	4.31	15.7	3.08	28.1	6.45	37377	1.41	5.2	0.60	139	81	76	*n.a.*	1.63	0.443	0.004	280.4	841
YK1412-12-45	new zircon	*b.d.*	172	*b.d.*	1.25	2.11	*b.d.*	2.96	4.85	0.94	11.0	2.09	20.2	5.51	16.4	2.89	28.6	6.44	38038	0.53	9.4	1.48	261	105	93	*n.a.*	0.39	1.405	0.006	221.5	*n.a.*
YK1412-12-46	grains	22.9	222	1.53	0.37	1.39	0.28	0.71	2.27	1.21	9.74	3.33	24.7	7.01	21.4	3.18	27.8	5.50	34898	0.28	11.5	1.49	329	109	103	1.1	0.79	1.461	0.005	157.5	987
YK1412-12-47		*b.d.*	130	0.12	0.23	1.04	*b.d.*	*b.d.*	0.42	0.31	4.06	1.70	12.8	3.89	13.0	2.44	20.8	3.79	38261	0.34	6.6	1.07	180	65	63	*n.a.*	0.71	0.886	0.006	295.1	*n.a.*
YK1412-12-48		29.4	360	0.16	*b.d.*	1.72	0.042	1.06	*b.d.*	2.16	19.8	5.94	44.5	10.7	35.6	6.50	51.9	10.0	38203	0.0000	10.2	2.59	281	190	185	*n.a.*	*n.a.*	1.636	0.009	106.2	1020
YK1412-12-49		16.0	263	0.40	*b.d.*	0.80	0.11	0.89	1.49	0.68	7.52	2.48	27.9	7.61	28.8	4.74	38.2	6.86	40151	0.70	5.3	0.61	145	128	124	*n.a.*	0.62	0.906	0.004	152.5	943
YK1412-12-50		17.5	123	0.35	0.21	2.81	*b.d.*	0.40	1.81	0.70	4.62	1.24	13.4	3.77	14.1	2.30	19.4	4.05	29854	0.0000	13.6	2.34	360	69	63	*n.a.*	0.74	0.942	0.006	241.8	954
YK1412-12-51		12.4	123	*b.d.*	0.060	0.71	*b.d.*	0.45	*b.d.*	1.07	6.15	1.59	13.9	3.66	12.0	2.18	16.6	2.94	31041	0.057	7.4	1.34	193	61	59	*n.a.*	*n.a.*	1.724	0.007	252.5	914
YK1412-12-52		33.2	201	0.63	0.67	1.81	0.51	*b.d.*	*b.d.*	0.85	5.42	0.99	16.7	5.92	26.1	6.27	56.2	12.9	34861	0.042	6.2	4.03	149	134	131	0.8	*n.a.*	0.346	0.027	173.7	1036
YK1412-12-53		12.2	67.3	1.10	0.17	0.52	0.17	0.48	1.31	0.39	3.33	0.76	5.40	1.97	7.50	2.13	19.3	3.45	32243	0.19	4.2	0.88	108	47	44	0.7	0.57	0.798	0.008	479.3	912
YK1412-12-54		*b.d.*	114	1.02	*b.d.*	2.33	0.24	1.94	*b.d.*	0.40	5.54	1.44	11.4	3.50	10.2	2.01	15.3	2.91	29490	0.26	7.0	3.31	181	57	52	*n.a.*	*n.a.*	1.569	0.018	258.9	*n.a.*
YK1412-12-55		33.3	140	0.10	0.40	2.89	0.53	1.48	3.31	1.41	6.36	1.37	17.5	3.87	14.1	2.39	22.2	3.85	29090	0.31	12.7	1.99	321	82	72	1.5	0.94	1.364	0.006	208.5	1037

Granite YK156-2

Spot No.	Domain	Ti	Y	Nb	La	Ce	Pr	Nd	Sm	Eu	Gd	Tb	Dy	Ho	Er	Tm	Yb	Lu	Hf	Ta	Pb	Th	U	ΣREE	ΣHREE	Ce/Ce*	Eu/Eu*	(Gd/Lu)$_N$	Th/U	Hf/Y	T (°C) 2.5 GPa
YK156-2-01		12.1	3368	6.80	0.0082	48.2	0.33	7.34	11.6	2.65	68.5	24.3	304	119	530	122	1234	212	22726	2.76	40.2	213	208	2684	2614	229.0	0.29	0.266	1.023	6.7	*n.c.*
YK156-2-02		11.1	2366	7.21	*b.d.*	62.1	0.24	3.80	8.25	2.30	44.6	17.1	201	80.0	376	88.0	909	157	25889	4.50	56.7	312	353	1949	1872	*n.a.*	0.37	0.235	0.883	10.9	*n.c.*
YK156-2-03		26.9	4320	8.02	0.088	71.1	0.69	9.33	19.8	3.71	100	33.5	403	155	674	149	1452	237	21089	2.83	65.8	640	320	3309	3204	70.7	0.25	0.348	2.000	4.9	*n.c.*
YK156-2-04		16.0	1671	29.2	0.43	23.8	0.23	2.01	3.57	0.78	22.9	9.77	134	54.0	264	65.6	691	114	34484	29.2	92.3	393	890	1386	1355	18.5	0.26	0.165	0.442	20.6	*n.c.*
YK156-2-05		12.4	2788	5.13	0.011	53.8	0.37	5.44	12.9	2.64	59.1	21.5	253	95.6	437	101	1029	171	22841	2.15	41.0	234	206	2242	2167	205.3	0.29	0.285	1.138	8.2	*n.c.*
YK156-2-06		14.3	1836	7.77	*b.d.*	29.1	0.15	3.22	6.93	1.29	30.5	12.0	154	61.1	293	70.9	731	130	28827	4.35	33.7	159	363	1523	1482	*n.a.*	0.27	0.194	0.438	15.7	*n.c.*
YK156-2-07		5.72	1038	6.53	0.045	11.7	0.085	1.86	3.24	0.94	16.8	5.99	82.4	34.7	172	42.6	462	101	35303	5.28	40.92	79.0	451	936	918	46.2	0.39	0.137	0.175	34.0	*n.c.*
YK156-2-08		21.8	9706	37.0	0.043	273	0.54	8.78	31.5	2.04	202	79.2	974	340	1417	288	2507	343	26672	15.8	93.7	563	485	6465	6150	438.1	0.08	0.485	1.161	2.7	*n.c.*
YK156-2-09		15.9	3788	31.2	0.037	87.5	0.070	2.79	8.65	0.92	60.6	24.5	316	125	587	143	1417	238	32865	13.5	164.4	904	1005	3012	2912	421.0	0.12	0.210	0.899	8.7	*n.c.*
YK156-2-10	Core	35.6	12669	10.1	0.57	473	4.68	78.7	130	14.3	505	149	1502	488	1831	361	3209	485	16167	2.07	36.0	392	141	9231	8530	71.1	0.17	0.858	2.781	1.3	*n.c.*
YK156-2-11		15.0	727	19.3	0.018	5.43	0.012	0.33	0.30	0.066	6.60	3.07	47.8	22.0	121	34.0	369	71.5	36772	12.7	59.5	204	687	681	675	90.4	0.14	0.076	0.296	50.6	*n.c.*
YK156-2-12		14.6	3719	27.1	0.100	75.5	0.21	3.56	9.26	0.93	63.0	23.6	310	124	583	138	1395	261	30912	13.8	143.1	766	1145	2987	2897	126.5	0.12	0.200	0.669	8.3	*n.c.*
YK156-2-13		10.2	5074	33.5	1.72	118	0.84	6.33	11.6	2.48	88.7	33.5	434	170	796	180	1766	303	31948	12.6	207.9	1204	1089	3913	3772	24.0	0.24	0.241	1.106	6.3	*n.c.*
YK156-2-14		*b.d.*	4495	18.3	2.39	61.8	1.55	13.0	14.6	4.01	82.6	29.8	382	153	712	163	1633	298	28585	6.55	121.9	472	696	3551	3454	7.9	0.35	0.229	0.678	6.4	*n.c.*
YK156-2-15		7.22	3968	24.5	0.023	86.4	0.15	2.98	10.3	1.72	67.9	25.3	336	133	628	145	1455	245	32379	10.7	158.7	798	895	3137	3035	362.6	0.20	0.229	0.891	8.2	*n.c.*
YK156-2-16		31.1	3834	33.7	*b.d.*	80.0	0.12	2.63	8.15	1.77	61.7	25.4	335	132	609	143	1467	259	33755	15.9	162.9	767	1169	3124	3031	*n.a.*	0.24	0.197	0.656	8.8	*n.c.*
YK156-2-17		17.2	5171	47.5	*b.d.*	74.8	0.15	3.09	6.58	1.41	68.6	28.8	419	173	843	202	2026	351	32024	15.6	205.5	720	1175	4197	4110	*n.a.*	0.20	0.161	0.613	6.2	*n.c.*
YK156-2-18		16.3	3269	33.7	5.72	54.7	0.88	4.03	6.11	1.08	43.3	17.5	261	110	543	135	1429	243	33463	14.6	149.0	479	948	2854	2781	6.0	0.20	0.147	0.505	10.2	*n.c.*
YK156-2-19		27.1	4838	51.4	3.90	89.8	2.59	19.4	18.0	4.40	78.0	30.2	415	162	784	182	1816	307	33094	19.0	256.1	1286	1594	3912	3774	6.9	0.36	0.209	0.807	6.8	*n.c.*
YK156-2-20		7.64	166	0.87	0.071	0.99	0.036	0.11	0.67	0.88	8.06	2.64	21.2	4.41	15.4	2.87	26.3	4.78	33602	0.35	7.0467	1.58	177	88	86	4.8	1.16	1.392	0.009	201.9	862
YK156-2-21		*b.d.*	105	0.55	*b.d.*	0.84	0.011	0.097	0.60	0.28	4.81	1.74	13.6	3.08	9.22	1.85	16.8	2.18	32301	0.30	8.20	0.94	210	55	53	*n.a.*	0.50	1.817	0.004	308.5	*n.a.*
YK156-2-22		7.14	260	0.62	*b.d.*	1.23	0.0040	0.071	0.50	0.74	8.60	3.14	31.5	7.15	24.1	4.29	36.0	5.40	31120	0.56	9.526	1.72	254	123	120	*n.a.*	1.09	1.315	0.007	119.7	856
YK156-2-23		9.56	251	0.71	*b.d.*	1.27	0.0058	*b.d.*	0.77	0.47	6.47	2.66	31.5	7.64	23.4	3.90	35.0	5.30	30402	0.36	9.2552	1.78	239	118	116	*n.a.*	0.65	1.008	0.007	121.0	886
YK156-2-24		7.33	186	0.51	0.010	1.28	0.021	0.043	0.44	0.47	5.30	2.35	21.4	5.27	17.0	2.87	24.7	3.70	31220	0.42	9.83	2.07	248	85	83	21.2	0.94	1.184	0.008	168.0	858
YK156-2-25		2.22	240	6.46	*b.d.*	0.50	0.022	*b.d.*	*b.d.*	0.15	1.64	0.79	13.0	6.58	36.8	12.5	173	43.5	32348	10.3	4.49	0.43	117	288	287	*n.a.*	*n.a.*	0.031	0.004	135.0	750
YK156-2-26	Overgrowth	7.01	171	2.29	0.020	0.49	0.0067	*b.d.*	0.14	0.22	1.91	1.00	15.4	5.01	22.1	5.70	74.7	17.0	36927	4.81	4.92	0.47	126	144	143	10.3	1.29	0.093	0.004	215.7	854
YK156-2-27	rims and	13.3	123	0.54	*b.d.*	0.93	*b.d.*	0.056	0.39	0.58	6.23	1.84	14.1	3.74	11.0	2.17	19.2	2.97	30164	0.36	8.5285	1.21	224	63	61	*n.a.*	1.13	1.730	0.005	244.9	922
YK156-2-28	new zircon	*b.d.*	176	0.77	0.023	1.22	*b.d.*	0.093	0.75	0.70	6.11	2.18	21.2	5.67	16.1	3.42	31.0	6.00	30267	0.23	9.06	1.42	230	95	92	*n.a.*	0.99	0.839	0.006	171.8	*n.a.*
YK156-2-29	grains	5.91	107	0.46	*b.d.*	0.57	*b.d.*	0.12	0.47	0.33	3.81	1.36	13.3	2.91	9.07	1.66	14.7	2.82	31849	0.45	5.30	0.68	140	51	50	*n.a.*	0.75	1.116	0.005	297.0	837
YK156-2-30		*b.d.*	354	1.12	0.010	1.12	*b.d.*	0.043	0.50	0.53	5.17	2.60	31.1	10.7	47.5	9.52	92.7	16.5	31528	2.60	9.12	0.86	240	218	216	*n.a.*	1.01	0.258	0.004	89.1	*n.a.*
YK156-2-31		11.9	418	0.92	*b.d.*	0.97	0.012	0.11	0.47	0.45	6.29	3.22	38.5	12.9	54.9	11.1	108	16.4	31900	2.33	7.1454	0.76	191	253	251	*n.a.*	0.79	0.317	0.004	76.3	909
YK156-2-32		10.9	333	1.72	*b.d.*	4.22	0.016	0.063	2.27	1.76	17.4	4.94	41.4	10.6	34.5	6.06	49.3	8.35	34567	1.77	29.82	4.22	761	181	173	*n.a.*	0.85	1.718	0.006	103.7	900
YK156-2-33		9.20	105	1.46	*b.d.*	1.96	*b.d.*	0.11	0.69	0.41	3.96	1.12	11.4	3.10	9.88	1.99	16.5	2.36	34488	1.64	10.3120	2.33	266	54	50	*n.a.*	0.77	1.388	0.009	327.3	882
YK156-2-34		7.60	117	1.05	0.0081	2.30	0.0055	0.20	0.27	0.53	3.53	1.39	11.2	3.44	10.4	1.71	15.6	2.15	35608	1.08	7.25	2.67	194	53	50	84.1	1.67	1.352	0.014	304.2	862
YK156-2-35		6.00	93.1	0.86	0.0086	4.42	0.0059	0.21	0.86	0.65	5.58	1.35	11.4	3.06	9.37	2.08	18.5	3.17	33922	0.84	15.94	5.86	410	61	55	152.1	0.91	1.452	0.014	364.2	838
YK156-2-36		13.1	155	1.42	0.073	3.22	*b.d.*	0.19	0.96	0.92	7.00	2.05	18.0	4.55	15.7	3.36	26.5	4.84	36536	3.12	16.89	5.80	442	87	82	*n.a.*	1.08	1.193	0.013	235.8	920
YK156-2-37		3.74	85.5	0.43	0.044	1.21	0.0075	*b.d.*	0.47	0.41	4.03	0.91	9.27	2.54	7.77	1.46	12.3	1.70	35046	0.34	6.32	0.73	154	42	40	16.4	0.91	1.958	0.005	409.7	794

Table S6c. LA-ICP-MS zircon trace element compositions (ppm) of the vein quartz of the composite granite–quartz veins.
Vein quartz YK1412-11

Spot No.	Domain	Ti	Y	Nb	La	Ce	Pr	Nd	Sm	Eu	Gd	Tb	Dy	Ho	Er	Tm	Yb	Lu	Hf	Ta	Pb	Th	U	ΣREE	ΣHREE	Ce/Ce*	Eu/Eu*	(Gd/Lu)$_N$	Th/U	Hf/Y	T (°C) 2.5 GPa
YK1412-11-1		2.29	546	4.21	0.071	9.93	0.088	*b.d.*	1.36	0.32	8.73	3.14	41.4	15.7	78.7	17.8	192	35.1	11325	2.40	62.3	107	245	404	392	30.8	0.28	0.205	0.435	20.8	*n.c.*
YK1412-11-2		9.37	1881	2.63	0.11	25.3	0.28	4.68	7.34	1.57	42.4	13.3	165	60.0	268	55.3	546	96.8	7878	0.98	77	147	118	1285	1246	35.6	0.27	0.362	1.250	4.2	*n.c.*
YK1412-11-3		4.05	1972	13.7	1.15	51.0	0.74	5.64	5.04	1.05	31.2	11.7	154	59.0	282	60.8	630	113	9884	4.26	238	415	415	1406	1341	13.5	0.26	0.228	0.998	5.0	*n.c.*
YK1412-11-4		*b.d.*	549	0.78	0.024	13.3	0.12	1.40	3.06	0.73	11.2	3.36	46.0	17.4	86.3	20.0	210	40.4	13928	0.36	139	255	215	453	434	62.0	0.38	0.228	1.189	25.3	*n.c.*
YK1412-11-5		0.17	2176	17.6	0.29	63.0	0.47	4.54	7.81	2.01	42.5	14.9	193	73.4	342	72.2	730	129	11293	4.42	333	578	452	1675	1597	41.6	0.34	0.271	1.277	5.2	*n.c.*
YK1412-11-6		12.9	1763	9.67	0.39	65.6	*b.d.*	1.90	2.22	0.57	25.8	10.4	143	57.3	284	62.6	639	114	12031	2.63	157	272	334	1407	1336	*n.a.*	0.23	0.186	0.815	6.8	*n.c.*
YK1412-11-7		14.4	1573	2.13	0.21	23.3	0.32	5.36	7.40	1.55	34.4	11.6	142	53.0	247	51.9	536	95.6	8995	0.81	92	153	107	1211	1173	22.2	0.30	0.297	1.432	5.7	*n.c.*
YK1412-11-8		3.39	1326	10.4	0.027	17.1	0.26	1.79	4.69	0.45	22.5	8.28	112	43.4	224	49.4	532	96.3	14709	4.38	119	185	366	1112	1088	49.6	0.13	0.193	0.506	11.1	*n.c.*
YK1412-11-9		6.95	2267	10.1	0.092	39.8	0.17	3.66	7.52	1.24	41.7	15.1	195	74.2	360	80.3	856	152	13099	3.36	166	279	394	1826	1774	77.5	0.21	0.227	0.708	5.8	*n.c.*
YK1412-11-10		7.72	2242	2.45	0.11	21.2	0.43	6.82	10.2	2.42	54.9	18.3	218	77.2	344	71.2	709	124	11205	0.97	77	142	131	1658	1617	23.6	0.31	0.365	1.081	5.0	*n.c.*
YK1412-11-11		1.69	321	3.04	*b.d.*	6.10	0.043	0.44	0.62	0.30	4.92	1.86	24.8	10.2	50.6	11.6	123	22.2	13353	1.56	47.0	62.1	154	257	249	*n.a.*	0.53	0.183	0.403	41.6	*n.c.*
YK1412-11-12		2.09	842	1.72	*b.d.*	14.4	0.13	2.49	2.91	0.53	15.7	5.59	73.7	27.5	133	27.9	301	54.0	11168	0.65	31.9	54.7	80.6	659	638	*n.a.*	0.24	0.240	0.679	13.3	*n.c.*
YK1412-11-13		*b.d.*	69.2	0.64	0.12	0.90	*b.d.*	0.24	0.47	0.21	1.34	0.84	6.52	2.04	9.08	1.98	25.6	5.50	12797	0.33	11.0	5.63	108	55	53	*n.a.*	0.80	0.200	0.052	185.0	*n.c.*
YK1412-11-14		29.1	2303	13.1	b.d.	44.3	b.d.	4.97	5.66	1.26	41.8	15.2	188	75.5	362	82.8	826	190	41027	12.1	75.0	290	758	1837	1781	*n.a.*	0.25	0.181	0.382	17.8	*n.c.*
YK1412-11-15		16.3	1039	5.93	0.40	30.2	0.060	2.10	4.76	1.00	20.5	6.87	91.2	34.5	163	36.5	384	88.4	37684	3.63	29.5	185	337	863	824	47.6	0.31	0.191	0.549	36.3	*n.c.*
YK1412-11-16	Core	45.7	3689	27.2	0.38	85.5	0.18	5.50	7.33	0.31	62.2	23.1	297	122	582	134	1332	285	37218	7.76	103.3	710	829	2937	2838	81.0	0.04	0.180	0.857	10.1	*n.c.*
YK1412-11-17		46.8	6366	10.8	0.43	179	0.96	17.1	29.1	4.79	160	50.9	591	216	931	189	1684	329	34669	3.94	128.2	1370	757	4383	4151	68.5	0.21	0.402	1.811	5.4	*n.c.*
YK1412-11-18		10.5	1074	*b.d.*	0.41	17.9	0.37	1.85	5.61	1.96	25.8	8.83	95.3	35.7	157	32.2	286	56.5	38356	0.88	22.05	111	341	725	697	11.3	0.50	0.376	0.327	35.7	*n.c.*
YK1412-11-19		45.0	1055	0.24	*b.d.*	21.7	*b.d.*	1.15	2.92	0.73	24.5	6.90	82.3	34.8	160	36.3	333	70.8	39024	1.18	30.03	102	365	775	748	*n.a.*	0.26	0.286	0.279	37.0	*n.c.*
YK1412-11-20		*b.d.*	6055	29.2	*b.d.*	157	0.71	13.0	8.98	2.25	108	39.4	515	203	932	200	1858	375	38782	11.8	150.2	929	1071	4412	4230	*n.a.*	0.22	0.238	0.868	6.4	*n.c.*
YK1412-11-21		190	5891	38.6	4.15	156	1.45	11.9	14.1	4.98	103	37.9	479	192	892	195	1806	366	34663	12.8	211	1555	1290	4262	4070	15.6	0.40	0.231	1.205	5.9	*n.c.*
YK1412-11-22		18.5	2102	8.88	0.65	56.9	0.54	4.61	10.7	0.81	46.0	15.6	188	70.4	309	62.3	580	113	40500	5.02	35.5	259	429	1458	1383	23.6	0.11	0.336	0.604	19.3	*n.c.*
YK1412-11-23		*b.d.*	7294	15.9	0.074	154	1.02	17.1	30.0	3.56	157	55.2	642	249	1115	228	2043	397	31607	5.50	97.8	816	587	5093	4887	137.3	0.16	0.327	1.389	4.3	*n.c.*
YK1412-11-24		*b.d.*	323	2.31	b.d.	3.50	*b.d.*	0.13	*b.d.*	*b.d.*	4.42	1.88	22.2	10.2	52.7	13.1	138	31.2	42088	3.24	12.26	32.6	145	277	274	*n.a.*	*n.a.*	0.117	0.225	130.3	*n.c.*
YK1412-11-25		33.2	2330	1.25	0.95	46.2	0.34	6.79	9.61	2.53	54.0	16.8	203	76.1	346	75.7	685	136	33289	0.95	47.8	253	747	1659	1592	19.8	0.34	0.328	0.339	14.3	*n.c.*
YK1412-11-26		129	3732	5.61	*b.d.*	64.8	0.21	12.0	11.8	5.84	82.3	25.0	306	124	558	120	1098	220	31713	1.55	78.1	452	695	2627	2533	*n.a.*	0.57	0.310	0.650	8.5	*n.c.*
YK1412-11-27		18.2	2900	14.8	b.d.	83.5	0.27	3.55	14.1	1.52	64.2	20.9	250	97.9	443	92.0	840	166	36778	6.53	88.9	840	610	2077	1974	*n.a.*	0.15	0.319	1.376	12.7	*n.c.*
YK1412-11-28		7.69	1551	10.9	*b.d.*	24.7	0.51	0.38	3.16	*b.d.*	21.1	9.08	110	47.7	256	63.6	694	160	38671	6.67	43.63	107	504	1390	1361	*n.a.*	*n.a.*	0.109	0.211	24.9	*n.c.*
YK1412-11-29		127	6593	49.9	0.79	181	0.84	4.27	20.1	5.15	119	43.2	528	211	948	205	1900	388	24251	12.6	231	1780	1260	4555	4342	54.6	0.32	0.252	1.413	3.7	*n.c.*
YK1412-11-30		35.1	6024	41.5	0.90	191	0.25	8.08	19.1	3.29	125	43.4	532	201	903	188	1751	342	30430	13.2	256	1846	1316	4306	4084	99.1	0.21	0.302	1.402	5.1	*n.c.*
YK1412-11-31		58.9	4457	41.5	0.52	114	0.53	8.01	10.8	1.46	76.9	29.4	373	147	683	147	1396	276	32192	13.8	214.3	1093	1274	3263	3129	53.1	0.15	0.230	0.858	7.2	*n.c.*
YK1412-11-32		7.37	6967	28.7	0.17	132	0.30	7.92	19.7	2.80	119	45.2	571	229	1073	229	2221	433	32276	10.3	264	1528	1627	5083	4920	144.5	0.18	0.226	0.939	4.6	*n.c.*
YK1412-11-33		0.56	78.8	1.25	*b.d.*	0.84	0.064	0.42	0.11	0.23	1.51	0.47	5.49	1.93	11.4	3.12	46.0	11.6	10873	0.75	3.83	2.04	97.9	83	82	*n.a.*	1.71	0.107	0.021	137.9	650
YK1412-11-34		4.56	42.4	*b.d.*	*b.d.*	0.42	0.012	0.056	0.22	0.26	1.48	0.49	4.72	1.13	4.09	0.69	6.18	1.09	10059	0.040	2.0162	0.45	63.8	21	20	*n.a.*	1.39	1.127	0.007	237.4	812
YK1412-11-35		0.22	156	0.70	*b.d.*	0.24	*b.d.*	0.095	0.071	0.13	1.56	0.55	9.79	4.03	22.4	5.47	59.4	11.6	10895	0.89	1.14	0.80	37.2	115	115	*n.a.*	1.24	0.111	0.022	69.9	594
YK1412-11-36		2.73	54.8	0.25	*b.d.*	0.74	*b.d.*	*b.d.*	0.10	0.40	2.37	0.68	5.40	1.64	6.97	1.40	12.0	2.31	13483	0.20	2.9408	1.42	124	34	33	*n.a.*	2.47	0.848	0.011	246.0	767
YK1412-11-37		12.2	63.8	0.16	0.062	0.68	0.097	0.43	*b.d.*	0.17	3.11	0.49	6.73	1.87	7.72	1.33	14.2	2.63	13963	0.22	2.90	1.45	118	40	38	2.1	*n.a.*	0.975	0.012	218.9	912
YK1412-11-38		*b.d.*	63.9	0.0016	*b.d.*	0.93	*b.d.*	*b.d.*	0.19	0.44	2.31	0.80	8.20	1.99	6.74	1.33	11.0	1.80	13581	0.095	4.21	1.23	135	36	34	*n.a.*	2.03	1.060	0.009	212.6	*n.a.*
YK1412-11-39		5.28	67.3	*b.d.*	*b.d.*	1.22	0.11	0.027	0.12	0.57	2.48	0.78	7.39	1.86	7.67	1.33	12.1	1.95	14041	*b.d.*	10.7	2.16	141	38	36	*n.a.*	3.15	1.049	0.015	208.7	826
YK1412-11-40		5.04	76.6	0.54	*b.d.*	0.53	*b.d.*	0.39	0.43	0.18	2.35	0.71	6.84	2.28	10.3	2.67	30.0	5.97	14437	0.70	5.37	0.80	107	63	61	*n.a.*	0.54	0.325	0.007	188.5	822
YK1412-11-41		*b.d.*	74.7	0.27	*b.d.*	0.43	0.022	*b.d.*	0.11	0.37	1.40	0.81	7.99	2.26	8.65	1.51	12.2	2.45	13976	0.23	4.61	0.38	108	38	37	*n.a.*	2.94	0.471	0.003	187.1	*n.a.*
YK1412-11-42		14.0	60.2	0.71	*b.d.*	0.29	*b.d.*	*b.d.*	0.72	0.21	1.59	0.43	5.42	1.62	8.08	1.83	17.8	3.45	13602	0.85	2.52	0.40	54.3	41	40	*n.a.*	0.58	0.382	0.007	226.1	928
YK1412-11-43		11.4	65.4	0.100	0.077	0.50	*b.d.*	0.026	0.63	0.18	3.11	0.95	6.99	1.87	5.74	1.03	9.81	1.43	12962	0.13	2.4024	0.46	104	32	31	*n.a.*	0.39	1.795	0.004	198.2	905
YK1412-11-44		*b.d.*	157	0.34	0.50	1.31	0.10	*b.d.*	0.54	0.98	5.60	1.96	16.7	4.87	16.1	2.81	24.5	4.53	37693	0.40	8.6765	1.36	254	80	77	1.4	1.73	1.021	0.005	239.7	*n.a.*
YK1412-11-45		*b.d.*	167	*b.d.*	0.58	1.56	0.28	1.15	1.30	0.68	0.90	1.38	16.8	5.15	20.0	3.99	38.8	8.51	39424	0.42	5.32	1.16	152	101	96	1.0	1.92	0.087	0.008	236.7	*n.a.*
YK1412-11-46		51.8	278	1.27	*b.d.*	1.49	0.40	1.32	2.81	1.36	6.60	2.31	24.8	8.30	28.1	5.43	48.9	9.86	44474	1.15	7.69	4.46	200	142	134	*n.a.*	0.97	0.552	0.022	160.0	1101
YK1412-11-47	Overgrowth	*b.d.*	110	0.46	*b.d.*	1.51	*b.d.*	1.48	1.36	0.72	5.75	2.05	13.5	3.06	10.4	1.98	13.3	2.89	37390	*b.d.*	7.4912	0.97	215	58	53	*n.a.*	0.79	1.644	0.004	338.8	*n.a.*
YK1412-11-48	rims and	11.2	127	0.80	0.20	2.98	0.100	*b.d.*	0.97	0.47	5.30	1.84	14.7	4.01	12.4	2.34	18.9	3.46	37823	*b.d.*	11.6516	2.38	332	68	63	5.1	0.64	1.264	0.007	298.4	903
YK1412-11-49	new zircon	*b.d.*	158	1.29	0.29	1.39	*b.d.*	0.23	*b.d.*	0.88	3.15	1.62	18.6	4.83	16.1	3.17	24.1	4.44	39135	0.31	6.86	4.08	189	79	76	*n.a.*	*n.a.*	0.585	0.022	247.3	*n.a.*
YK1412-11-50	grains	*b.d.*	151	0.36	*b.d.*	1.47	0.17	0.82	0.70	0.43	5.00	1.33	14.2	4.44	17.6	3.65	32.1	6.78	39439	0.27	6.565	1.30	186	89	85	*n.a.*	0.69	0.609	0.007	261.4	*n.a.*
YK1412-11-51		*b.d.*	221	0.086	0.83	0.78	0.036	3.44	*b.d.*	0.49	4.96	2.01	23.5	7.18	24.4	5.35	39.2	7.03	40528	0.40	8.5677	1.74	244	119	114	1.1	*n.a.*	0.582	0.007	183.1	*n.a.*
YK1412-11-52		*b.d.*	162	*b.d.*	*b.d.*	0.71	*b.d.*	*b.d.*	2.37	1.11	8.69	1.81	19.7	4.55	17.7	4.03	32.5	6.85	39454	*b.d.*	6.2066	1.33	175	100	96	*n.a.*	0.75	1.047	0.008	242.9	*n.a.*
YK1412-11-53		64.7	232	0.48	*b.d.*	1.11	*b.d.*	*b.d.*	0.73	1.13	5.36	2.98	25.5	6.70	24.2	4.62	36.5	6.19	40532	0.42	7.22	1.92	191	115	112	*n.a.*	1.75	0.715	0.010	175.0	1136
YK1412-11-54		2.52	249	0.92	*b.d.*	2.42	0.016	0.81	1.65	1.03	8.95	2.68	26.7	7.49	27.5	5.46	52.9	10.8	37953	1.34	10.95	4.91	303	148	142	*n.a.*	0.82	0.686	0.016	152.4	760
YK1412-11-55		2.19	217	*b.d.*	0.016	1.65	*b.d.*	*b.d.*	*b.d.*	0.62	8.89	2.44	23.6	6.58	20.9	4.18	34.3	6.49	35657	0.41	6.38	1.34	180	110	107	*n.a.*	*n.a.*	1.132	0.007	164.0	749
YK1412-11-56		*b.d.*	208	1.76	0.43	2.25	*b.d.*	0.67	1.98	0.91	10.7	2.99	25.3	6.84	21.2	3.65	29.5	4.71	38272	0.17	9.297	1.99	266	111	105	*n.a.*	0.60	1.873	0.007	183.8	*n.a.*
YK1412-11-57		*b.d.*	117	0.57	*b.d.*	1.27	0.013	*b.d.*	0.62	0.78	1.78	1.35	13.2	3.48	10.6	1.93	17.0	3.02	35806	*b.d.*	5.64	0.55	159	55	52	*n.a.*	2.27	0.485	0.003	306.3	*n.a.*
YK1412-11-58		27.3	139	0.35	*b.d.*	4.20	0.020	0.91	3.26	1.71	10.2	2.28	17.3	4.22	13.6	2.37	18.8	3.43	31877	0.10	11.02	6.65	300	82	72	*n.a.*	0.91	2.447	0.022	229.1	1010
YK1412-11-59		36.8	132	*b.d.*	0.52	0.77	0.57	*b.d.*	*b.d.*	*b.d.*	2.32	2.02	17.0	4.32	13.7	3.00	17.1	3.25	29833	*b.d.*	8.1937	2.34	210	65	63	0.3	*n.a.*	0.588	0.011	226.7	1051
YK1412-11-60		45.9	206	1.06	*b.d.*	3.26	*b.d.*	*b.d.*	1.91	0.89	9.96	1.86	22.4	6.04	25.5	4.97	47.5	11.3	33023	*b.d.*	9.90	7.31	251	136	130	*n.a.*	0.63	0.727	0.029	160.4	1083
YK1412-11-61		*b.d.*	219	0.98	*b.d.*	2.26	0.14	*b.d.*	3.66	0.46	7.22	3.18	23.1	6.45	22.5	4.26	37.2	5.94	31626	0.27	8.3177	2.70	228	116	110	*n.a.*	0.27	1.002	0.012	144.2	*n.a.*
YK1412-11-62		19.6	196	0.43	0.17	2.40	*b.d.*	*b.d.*	0.70	0.63	5.47	1.90	20.9	6.06	25.2	5.79	63.1	13.7	31914	0.23	9.2588	3.79	263	146	142	*n.a.*	0.99	0.328	0.014	163.0	968
YK1412-11-63		*b.d.*	200	0.94	0.041	1.38	0.087	*b.d.*	*b.d.*	0.55	6.31	1.67	20.4	5.68	25.7	6.01	59.7	12.0	33116	1.27	7.67	2.88	199	140	138	5.7	*n.a.*	0.433	0.014	165.8	*n.a.*
YK1412-11-64		8.83	171	0.64	*b.d.*	1.71	*b.d.*	*b.d.*	*b.d.*	1.24	7.30	1.99	18.6	5.03	17.8	3.74	32.4	5.81	32165	0.080	6.11	4.40	157	96	93	*n.a.*	*n.a.*	1.036	0.028	188.4	877
YK1412-11-65		10.6	401	1.72	*b.d.*	2.13	0.48	1.23	2.07	1.85	13.3	4.59	41.0	11.9	42.9	7.70	71.9	13.9	35598	1.23	15.79	7.02	430	215	207	*n.a.*	1.08	0.784	0.016	88.9	897

Vein quartz YK156-1

Spot No.	Domain	Ti	Y	Nb	La	Ce	Pr	Nd	Sm	Eu	Gd	Tb	Dy	Ho	Er	Tm	Yb	Lu	Hf	Ta	Pb	Th	U	ΣREE	ΣHREE	Ce/Ce*	Eu/Eu*	(Gd/Lu)$_N$	Th/U	Hf/Y	T (°C) 2.5 GPa
YK156-1-01		*b.d.*	4810	5.83	*b.d.*	156	0.25	5.31	18.3	7.93	91.3	29.9	380	160	791	185	1958	448	32071	4.91	623	5107	3287	4231	4043	*n.a.*	0.59	0.168	1.553	6.7	*n.c.*
YK156-1-02		16.0	3799	21.5	1.56	136	1.07	6.20	11.3	2.27	65.5	24.2	316	126	601	134	1298	266	33762	7.30	105.2	500	620	2989	2830	25.9	0.25	0.203	0.807	8.9	*n.c.*
YK156-1-03		47.7	4857	16.2	0.76	76.3	0.083	9.97	7.81	2.41	89.6	31.6	404	162	770	172	1659	338	32050	6.06	111.5	545	834	3723	3626	74.2	0.28	0.219	0.654	6.6	*n.c.*
YK156-1-04		*b.d.*	2013	15.4	2.16	85.3	0.86	7.20	6.25	*b.d.*	27.5	11.4	145	60.7	318	73.3	784	175	27417	4.58	73.5	294	596	1697	1595	15.4	*n.a.*	0.129	0.492	13.6	*n.c.*
YK156-1-05		19.6	4042	23.4	1.56	101	0.80	9.96	11.4	3.70	72.7	26.4	338	134	609	131	1234	247	28392	7.83	121.4	741	679	2921	2792	22.1	0.39	0.242	1.092	7.0	*n.c.*
YK156-1-06		8.47	523	0.90	0.24	11.8	0.27	1.84	2.53	1.30	13.5	4.09	46.8	17.4	74.6	16.5	153	31.6	33487	0.41	16.39	49.8	316	375	357	11.3	0.68	0.352	0.158	64.0	*n.c.*
YK156-1-07		29.7	1047	3.29	*b.d.*	20.6	0.33	5.07	8.21	2.38	31.0	8.84	94.7	34.7	157	33.4	321	69.4	35190	2.01	30.75	80.9	500	786	750	*n.a.*	0.46	0.369	0.162	33.6	*n.c.*
YK156-1-08		96.2	10576	11.5	*b.d.*	255	2.37	29.9	55.6	17.3	254	78.4	898	332	1489	315	2901	571	27288	3.54	403	5073	2853	7199	6839	*n.a.*	0.44	0.366	1.778	2.6	*n.c.*
YK156-1-09		19.7	6908	24.1	4.46	142	2.53	19.3	23.7	4.15	114	42.4	556	222	1056	232	2209	444	28869	8.60	208.7	1086	1219	5071	4875	10.3	0.24	0.212	0.891	4.2	*n.c.*
YK156-1-10	Core	19.5	2171	19.0	0.14	54.9	0.69	4.07	5.49	1.85	35.7	12.2	163	67.2	340	78.4	811	184	35522	8.53	114.2	635	1136	1759	1691	43.7	0.41	0.160	0.559	16.4	*n.c.*
YK156-1-11		12.9	1099	5.99	0.062	16.0	*b.d.*	1.71	2.36	1.15	14.2	5.81	79.5	33.8	168	40.7	410	89.3	35017	4.06	97.8	259	1090	863	842	*n.a.*	0.61	0.132	0.238	31.9	*n.c.*
YK156-1-12		30.0	7925	48.7	0.12	146	0.93	6.73	16.5	2.55	119	47.4	623	254	1217	268	2574	522	32036	15.3	307	1788	2310	5799	5626	105.6	0.18	0.189	0.774	4.0	*n.c.*
YK156-1-13		*b.d.*	4030	4.34	0.70	129	1.26	10.4	17.0	6.56	86.7	29.2	323	127	594	130	1270	261	29050	2.83	166	1732	1039	2985	2821	33.7	0.52	0.275	1.667	7.2	*n.c.*
YK156-1-14		18.7	5649	14.2	0.025	75.7	0.41	6.74	15.8	3.23	90.0	30.5	404	152	794	165	1844	308	30044	5.10	349	584	638	3891	3789	184.1	0.26	0.241	0.915	5.3	*n.c.*
YK156-1-15		8.11	5446	41.1	0.16	86.2	0.29	4.92	10.8	1.55	74.9	30.8	415	155	766	163	1762	275	33290	12.4	527	1060	1082	3745	3641	98.2	0.17	0.225	0.980	6.1	*n.c.*
YK156-1-16		30.4	7588	42.5	0.51	143	0.56	7.33	15.0	3.69	109	40.4	554	208	1052	228	2584	378	30673	12.5	767	1259	1255	5323	5153	65.8	0.28	0.239	1.003	4.0	*n.c.*
YK156-1-17		14.3	6695	25.6	0.040	83.6	0.38	6.93	17.9	2.61	98.9	35.8	497	182	908	198	2238	326	34057	11.2	406	748	1033	4596	4485	166.1	0.19	0.250	0.724	5.1	*n.c.*
YK156-1-18		20.1	6990	8.60	0.10	62.5	0.87	15.8	27.9	6.68	146	47.4	585	202	956	190	2056	299	26606	3.04	197	399	331	4595	4482	51.3	0.32	0.402	1.206	3.8	*n.c.*
YK156-1-19		10.8	3678	13.6	0.064	73.5	0.29	5.88	11.4	2.74	58.1	20.5	282	103	523	115	1359	208	26505	4.65	182	293	352	2764	2670	132.9	0.32	0.231	0.833	7.2	*n.c.*

YK156-1-20		18.6	3967	5.69	0.049	44.8	0.35	7.18	14.2	2.98	68.4	23.0	306	113	554	119	1356	208	24421	1.86	123	240	221	2817	2747	84.1	0.29	0.271	1.086	6.2	*n.c.*
YK156-1-21		9.15	196	0.54	0.050	2.04	*b.d.*	*b.d.*	0.032	0.73	8.39	2.39	20.8	6.24	22.0	3.79	34.1	6.22	38213	0.15	10.9024	2.06	298	107	104	*n.a.*	4.30	1.113	0.007	194.5	806
YK156-1-22		18.7	175	0.70	*b.d.*	3.99	0.024	0.68	1.34	1.73	11.7	2.88	21.5	5.64	17.9	2.87	21.6	3.89	33554	0.33	22.29	5.39	628	96	88	*n.a.*	1.33	2.489	0.009	192.2	887
YK156-1-23		18.2	128	0.42	0.11	2.67	*b.d.*	*b.d.*	1.65	1.11	7.89	1.84	18.1	4.30	12.3	2.43	18.0	3.42	34652	0.12	18.13	3.62	494	74	68	*n.a.*	0.94	1.903	0.007	270.0	883
YK156-1-24		6.94	182	0.66	0.15	3.09	0.30	1.91	2.49	2.16	13.3	2.95	23.5	5.57	17.8	3.20	23.7	4.59	35027	0.084	17.54	3.46	479	105	95	3.5	1.15	2.396	0.007	191.9	778
YK156-1-25		3.13	99.3	0.18	0.028	1.56	0.070	0.44	*b.d.*	0.83	5.55	1.12	12.2	2.67	9.73	1.65	14.7	2.33	37478	*b.d.*	7.831	2.17	219	53	50	8.6	*n.a.*	1.966	0.010	377.5	704
YK156-1-26		0.63	97.9	0.012	*b.d.*	2.88	*b.d.*	0.62	0.17	0.89	5.53	1.48	12.4	3.35	9.66	1.64	10.9	2.11	34951	0.080	12.22	3.25	326	52	47	*n.a.*	2.79	2.163	0.010	357.2	583
YK156-1-27		9.61	111	0.31	0.23	3.27	*b.d.*	2.36	1.26	1.41	5.06	1.65	12.8	3.54	10.7	2.44	20.2	3.51	36579	*b.d.*	13.41	13.2	327	68	60	*n.a.*	1.70	1.188	0.041	329.3	811
YK156-1-28		15.0	201	0.37	0.19	1.89	0.24	1.18	*b.d.*	0.64	8.67	2.62	23.6	5.77	20.8	4.12	33.2	5.82	35928	0.51	13.79	6.88	367	109	105	2.2	*n.a.*	1.229	0.019	179.0	861
YK156-1-29		31.8	92.8	0.019	0.15	0.94	0.047	3.26	1.18	*b.d.*	3.94	1.99	9.34	2.98	9.26	1.65	11.5	2.29	33547	*b.d.*	9.06	2.39	235	48	43	2.8	*n.a.*	1.424	0.010	361.5	955
YK156-1-30		17.4	120	0.060	*b.d.*	3.99	0.040	0.84	3.29	1.97	11.8	2.67	17.8	3.80	11.7	2.06	13.8	2.70	35553	0.042	21.58	21.4	560	76	66	*n.a.*	0.96	3.609	0.038	295.1	879
YK156-1-31		5.42	239	0.14	0.031	3.94	0.0029	1.85	3.73	2.72	19.5	4.02	33.0	7.79	25.2	4.22	34.2	6.24	35478	0.037	17.26	7.41	458	146	134	101.7	0.97	2.578	0.016	148.2	754
YK156-1-32		6.37	118	0.54	0.70	5.11	0.61	3.91	6.21	3.09	9.70	2.06	15.6	3.78	14.3	2.13	22.3	4.46	33236	*b.d.*	15.14	22.5	374	94	74	1.9	1.22	1.795	0.060	281.4	769
YK156-1-33		13.0	107	1.03	*b.d.*	*b.d.*	0.25	*b.d.*	*b.d.*	0.026	0.44	0.39	8.07	3.23	13.1	2.80	32.7	6.59	42919	0.44	2.7327	2.23	77.3	68	67	*n.a.*	*n.a.*	0.056	0.029	400.9	845
YK156-1-34	Overgrowth	10.5	269	*b.d.*	0.22	2.30	*b.d.*	2.12	1.04	0.93	9.10	3.12	28.8	8.30	29.4	5.86	58.0	11.5	35582	0.42	11.27	3.90	298	161	154	*n.a.*	0.92	0.652	0.013	132.4	821
YK156-1-35	rims and	*b.d.*	166	0.46	0.13	2.28	0.044	*b.d.*	1.19	1.09	5.60	1.84	18.9	5.08	17.5	3.02	24.8	4.40	34161	0.16	10.6441	3.28	282	86	81	7.4	1.29	1.049	0.012	206.2	*n.a.*
YK156-1-36	new zircon	14.5	94.4	0.15	*b.d.*	3.31	0.012	0.81	0.51	0.85	7.18	1.73	12.0	2.79	9.70	1.67	12.8	2.21	34311	0.068	16.01	3.17	417	56	50	*n.a.*	1.37	2.679	0.008	363.3	857
YK156-1-37		9.94	197	*b.d.*	*b.d.*	2.07	*b.d.*	*b.d.*	0.66	1.34	6.85	2.17	22.1	5.79	19.5	4.21	35.1	6.17	33438	0.26	12.88	2.69	337	106	102	*n.a.*	1.93	0.915	0.008	169.8	815
YK156-1-38	grains	*b.d.*	208	0.47	*b.d.*	3.19	0.043	0.12	0.72	2.34	14.8	3.51	26.5	6.34	21.2	3.66	27.6	5.57	35928	0.072	16.71	5.94	452	116	109	*n.a.*	2.20	2.198	0.013	172.9	*n.a.*
YK156-1-39		8.79	285	0.57	0.24	3.94	*b.d.*	0.30	1.43	1.54	9.49	3.21	28.6	8.74	37.9	7.76	79.7	17.4	36307	0.77	14.54	12.3	383	200	193	*n.a.*	1.28	0.450	0.032	127.5	802
YK156-1-40		3.37	240	0.42	0.040	3.69	*b.d.*	1.50	2.65	2.71	19.5	4.00	31.0	7.52	21.8	3.69	28.3	5.13	33931	0.14	16.683	3.84	458	132	121	*n.a.*	1.15	3.140	0.008	141.2	710
YK156-1-41		11.9	166	*b.d.*	0.18	1.18	0.18	*b.d.*	*b.d.*	0.87	4.71	2.16	19.0	4.84	15.5	3.32	24.9	4.11	34485	0.20	13.04	1.81	342	81	79	1.6	*n.a.*	0.946	0.005	208.1	834
YK156-1-42		*b.d.*	210	*b.d.*	*b.d.*	1.68	*b.d.*	1.05	2.04	1.06	6.89	2.54	24.1	6.21	22.7	3.81	33.6	6.31	33385	0.15	14.77	1.83	393	112	106	*n.a.*	0.86	0.902	0.005	159.1	*n.a.*
YK156-1-43		12.2	176	0.87	*b.d.*	3.27	*b.d.*	*b.d.*	1.15	1.60	11.5	2.88	21.9	5.47	17.4	2.85	24.2	4.46	31369	0.18	17.81	4.60	479	97	91	*n.a.*	1.34	2.134	0.010	178.4	837
YK156-1-44		7.26	92.3	0.24	*b.d.*	2.19	0.099	0.25	0.48	0.55	5.24	1.37	11.3	2.92	8.55	1.56	11.9	2.32	33561	0.11	8.8960	2.67	250	49	45	*n.a.*	1.05	1.865	0.011	363.6	857
YK156-1-45		6.60	322	0.54	0.028	2.56	0.16	0.85	1.18	1.40	12.3	3.18	32.7	9.21	34.2	6.81	60.7	11.2	32822	0.13	9.45	10.7	255	176	170	9.5	1.12	0.900	0.042	102.0	848
YK156-1-46		*b.d.*	152	0.093	0.13	2.27	*b.d.*	*b.d.*	0.47	0.64	5.43	1.76	15.7	4.30	15.8	2.85	23.8	4.58	35068	0.23	9.98	3.44	276	78	74	*n.a.*	1.22	0.979	0.012	230.6	*n.a.*
YK156-1-47		*b.d.*	218	0.055	0.27	2.30	0.18	*b.d.*	3.81	2.40	13.5	3.18	23.5	5.75	23.3	3.68	29.1	5.96	29904	*b.d.*	23.35	4.36	644	117	108	2.6	1.02	1.868	0.007	137.1	*n.a.*
YK156-1-48		20.6	133	*b.d.*	*b.d.*	3.87	*b.d.*	0.11	2.32	1.50	10.9	2.15	16.4	4.01	12.3	2.23	16.8	2.65	31269	0.070	17.48	4.27	460	75	67	*n.a.*	0.91	3.394	0.009	235.2	974
YK156-1-49		3.00	149	0.092	*b.d.*	2.37	*b.d.*	0.83	1.20	1.17	6.19	2.14	17.9	4.46	14.3	2.58	20.6	3.15	32435	0.42	11.76	2.55	315	77	71	*n.a.*	1.31	1.624	0.008	217.6	775
YK156-1-50		9.72	181	0.19	*b.d.*	1.60	0.10	*b.d.*	0.24	0.72	7.43	2.06	19.6	5.54	18.5	3.42	28.4	5.53	30812	0.26	11.61	3.02	313	93	90	*n.a.*	1.63	1.108	0.010	170.0	887
YK156-1-51		6.32	183	0.54	*b.d.*	4.32	0.10	0.27	1.25	1.65	10.0	2.70	21.0	5.59	17.4	3.07	23.4	3.99	31497	0.18	22.08	5.62	618	95	87	*n.a.*	1.42	2.075	0.009	172.1	843

Table S6d. LA-ICP-MS zircon trace element compositions (ppm) of the surrounding gneisses.
Gneiss YK1412-14

Spot No.	Domain	Ti	Y	Nb	La	Ce	Pr	Nd	Sm	Eu	Gd	Tb	Dy	Ho	Er	Tm	Yb	Lu	Hf	Ta	Pb	Th	U	ΣREE	ΣHREE	Ce/Ce*	Eu/Eu*	(Gd/Lu)$_N$	Th/U	Hf/Y	T (°C) 2.5 GPa
YK1412-14-01		33.6	4452	43.5	*b.d.*	40.9	0.71	6.45	*b.d.*	1.58	51.8	21.7	301	139	711	169	1729	383	43615	17.8	255.8	770	2882	3554	3504	*n.a.*	*n.a.*	0.112	0.267	9.8	*n.c.*
YK1412-14-02		*b.d.*	4375	9.65	0.096	47.4	0.17	11.6	17.3	3.55	101	34.4	391	153	655	130	1146	229	33241	3.56	55.4	319	874	2920	2840	90.9	0.26	0.363	0.365	7.6	*n.c.*
YK1412-14-03		131	3763	16.0	*b.d.*	62.9	*b.d.*	9.80	8.10	3.70	61.4	22.3	293	122	594	135	1285	273	38125	6.64	74.4	381	568	2871	2786	n.a.	0.51	0.186	0.670	10.1	*n.c.*
YK1412-14-04		61.8	5349	43.1	1.81	96.9	0.68	5.51	12.4	2.41	76.8	33.4	422	172	832	180	1689	344	40389	16.3	231.6	1321	1402	3869	3749	21.3	0.24	0.184	0.942	7.6	*n.c.*
YK1412-14-05		*b.d.*	718	4.42	0.17	10.6	*b.d.*	*b.d.*	1.12	0.067	8.12	3.75	44.7	18.7	101	24.2	250	57.3	46420	4.02	53.13	71.8	1145	520	508	*n.a.*	0.07	0.117	0.063	64.6	*n.c.*
YK1412-14-06		*b.d.*	4561	9.00	0.25	67.7	0.55	4.81	6.56	2.16	77.4	27.6	357	148	728	158	1494	312	34699	4.41	62.9	336	387	3384	3302	45.0	0.29	0.205	0.867	7.6	*n.c.*
YK1412-14-07		1.32	24641	21.0	0.36	354	3.64	73.4	130	20.1	677	218	2404	870	3704	713	5975	1121	29901	6.40	257	2483	1266	16263	15682	75.6	0.21	0.499	1.962	1.2	*n.c.*
YK1412-14-08		*b.d.*	5179	2.74	0.27	41.6	0.36	10.4	22.5	4.40	135	42.8	473	180	783	156	1378	273	31976	1.97	34.8	225	203	3501	3421	32.2	0.24	0.408	1.108	6.2	*n.c.*
YK1412-14-09		42.8	8012	75.9	2.63	124	1.95	14.7	*b.d.*	2.62	107	45.9	613	260	1258	280	2635	536	39173	23.6	380	2743	2862	5880	5734	13.5	n.a.	0.164	0.958	4.9	*n.c.*
YK1412-14-10		90.9	3271	32.5	*b.d.*	39.4	1.21	1.59	*b.d.*	*b.d.*	43.8	17.1	233	101	519	123	1196	255	45522	17.0	189.5	692	2041	2529	2487	*n.a.*	*n.a.*	0.142	0.339	13.9	*n.c.*
YK1412-14-11		126	7798	106	1.96	102	2.37	15.7	21.8	4.57	87.9	44.1	591	252	1238	281	2650	546	35774	32.5	377	2367	3414	5839	5691	11.6	0.32	0.133	0.693	4.6	*n.c.*
YK1412-14-12		9.17	3762	26.5	*b.d.*	67.7	0.048	2.61	7.02	0.97	53.9	20.4	292	121	600	135	1297	263	42739	10.9	126.3	651	808	2861	2783	*n.a.*	0.15	0.169	0.806	11.4	*n.c.*
YK1412-14-13		8.19	6564	36.4	*b.d.*	99.0	0.41	8.76	12.8	2.42	122	45.4	573	223	1022	210	1879	371	37833	13.9	225	1486	1286	4569	4445	*n.a.*	0.19	0.272	1.155	5.8	*n.c.*
YK1412-14-14		13.5	4788	27.6	0.071	61.7	0.20	5.11	8.92	1.49	68.0	25.9	362	155	782	177	1727	359	36944	11.9	127.2	473	827	3733	3655	127.2	0.19	0.156	0.572	7.7	*n.c.*
YK1412-14-15		45.2	4253	22.7	*b.d.*	86.7	0.73	7.64	16.2	2.59	70.0	25.1	334	138	672	149	1440	290	39202	11.0	183.3	1100	1124	3231	3118	*n.a.*	0.24	0.200	0.979	9.2	*n.c.*
YK1412-14-16		14.7	1126	16.6	0.68	13.9	*b.d.*	2.49	*b.d.*	*b.d.*	11.9	5.38	72.2	31.4	178	44.7	479	114	50294	11.8	117.57	215	2352	953	936	*n.a.*	*n.a.*	0.087	0.091	44.7	*n.c.*
YK1412-14-17		0.0000	1166	10.8	0.21	18.7	0.010	*b.d.*	*b.d.*	*b.d.*	12.3	6.03	83.8	34.4	182	43.1	440	93.7	47481	5.64	66.45	170	1043	915	896	99.5	*n.a.*	0.109	0.163	40.7	*n.c.*
YK1412-14-18		25.4	2926	27.8	0.36	25.3	0.021	*b.d.*	5.00	0.46	27.7	14.0	200	91.1	484	116	1174	249	44909	12.5	125.2	332	1169	2386	2355	71.6	0.12	0.092	0.284	15.3	*n.c.*
YK1412-14-19	Core	*b.d.*	2643	13.5	*b.d.*	37.9	*b.d.*	3.84	4.47	0.60	32.6	13.7	195	83.4	425	96.2	955	201	40403	5.31	84.9	265	938	2049	2002	*n.a.*	0.15	0.134	0.283	15.3	*n.c.*
YK1412-14-20		12.7	5884	7.38	0.046	49.7	0.71	12.1	20.5	6.84	115	41.6	502	198	908	193	1739	344	26782	2.10	36.7	257	256	4130	4040	67.2	0.43	0.275	1.002	4.6	*n.c.*
YK1412-14-21		2.84	1981	19.1	0.56	22.9	*b.d.*	3.07	1.81	1.41	28.5	11.5	156	63.3	303	69.5	675	128	45178	8.67	154.4	586	1882	1466	1436	n.a.	0.60	0.183	0.312	22.8	*n.c.*
YK1412-14-22		*b.d.*	2064	18.3	*b.d.*	25.5	*b.d.*	4.57	*b.d.*	0.77	24.8	11.4	155	65.9	327	79.0	776	158	46421	13.2	130.4	316	1469	1628	1597	n.a.	*n.a.*	0.129	0.215	22.5	*n.c.*
YK1412-14-23		33.9	7669	24.1	0.92	224	1.53	15.5	27.4	6.53	164	56.5	676	262	1171	246	2232	428	31399	8.61	174	1453	906	5512	5236	46.3	0.30	0.317	1.603	4.1	*n.c.*
YK1412-14-24		47.2	4275	25.8	*b.d.*	69.1	0.21	2.73	7.96	0.93	61.9	24.6	329	137	671	153	1456	292	40016	11.7	175.5	845	1117	3206	3125	*n.a.*	0.13	0.175	0.756	9.4	*n.c.*
YK1412-14-25		*b.d.*	2449	5.86	*b.d.*	60.5	0.32	4.25	6.04	2.24	43.3	16.1	198	79.6	379	83.5	796	162	33277	3.66	61.5	344	398	1830	1757	*n.a.*	0.42	0.221	0.864	13.6	*n.c.*
YK1412-14-26		5.72	6519	46.0	1.20	126	0.83	8.51	16.0	3.82	108	41.4	537	218	1020	225	2111	396	35308	14.8	191.4	1140	1216	4814	4657	31.1	0.28	0.226	0.938	5.4	*n.c.*
YK1412-14-27		26.9	8855	87.1	0.28	126	0.18	4.37	12.7	2.54	122	52.7	692	290	1372	309	2868	554	39017	25.9	425	2372	2654	6405	6259	136.8	0.20	0.182	0.894	4.4	*n.c.*
YK1412-14-28		*b.d.*	2414	3.68	0.071	57.9	*b.d.*	4.21	6.24	2.76	46.8	16.3	199	77.7	375	85.9	830	172	29942	2.40	20.90	127	130	1874	1803	*n.a.*	0.49	0.224	0.981	12.4	*n.c.*
YK1412-14-29		32.1	6010	12.1	0.36	102	0.93	15.0	28.3	5.45	139	47.5	556	204	923	200	1798	340	28470	6.54	74.1	445	426	4359	4207	43.2	0.27	0.338	1.046	4.7	*n.c.*
YK1412-14-30		70.6	5994	38.1	*b.d.*	79.5	*b.d.*	1.52	8.52	2.95	79.3	31.3	442	189	951	222	2128	428	36018	13.1	174.6	879	1081	4563	4470	*n.a.*	0.35	0.153	0.813	6.0	*n.c.*
YK1412-14-31		85.9	1925	13.5	*b.d.*	20.7	*b.d.*	*b.d.*	1.61	*b.d.*	16.7	10.7	140	61.7	298	66.6	652	130	46028	6.24	79.29	184	1672	1398	1375	*n.a.*	n.a.	0.106	0.110	23.9	*n.c.*
YK1412-14-32		0.91	3860	23.9	12.3	105	9.95	63.7	29.8	5.51	84.9	26.1	301	120	588	132	1274	262	40152	11.2	181.2	853	1482	3014	2788	2.3	0.33	0.268	0.576	10.4	*n.c.*
YK1412-14-33		9.48	10378	74.5	1.10	179	0.98	11.2	28.3	3.63	193	71.6	895	350	1587	334	3005	577	36499	21.3	444	3470	2456	7236	7012	42.3	0.15	0.276	1.413	3.5	*n.c.*
YK1412-14-34		16.8	1860	14.7	*b.d.*	38.7	0.51	0.39	1.87	0.34	30.6	11.5	146	59.9	275	60.5	554	109	35447	5.40	63.5	168	868	1289	1247	*n.a.*	0.14	0.231	0.193	19.1	*n.c.*
YK1412-14-35		3.73	673	7.78	0.13	7.08	0.25	0.075	2.01	0.32	7.44	3.02	44.8	19.0	92.2	21.4	217	47.0	38530	3.39	75.92	113	1371	462	452	9.6	0.25	0.131	0.082	57.2	*n.c.*
YK1412-14-36		30.6	5283	25.6	5.54	105	3.18	19.2	21.7	3.87	105	35.2	435	171	790	177	1762	383	34831	8.07	211.9	803	2546	4016	3858	6.1	0.25	0.226	0.315	6.6	*n.c.*
YK1412-14-37		11.8	1914	27.2	0.59	24.6	0.053	*b.d.*	2.18	0.85	19.5	8.66	130	58.3	296	71.3	726	157	38408	9.45	130.3	299	1840	1496	1467	34.1	0.40	0.103	0.162	20.1	*n.c.*
YK1412-14-38		104	476	1.79	*b.d.*	2.59	*b.d.*	0.19	2.38	0.39	2.66	1.91	27.5	10.7	60.4	13.7	145	33.1	45871	1.44	41.3746	10.7	1165	300	295	*n.a.*	0.47	0.066	0.009	96.4	outlier (*n.a.*)
YK1412-14-39		0.67	496	3.26	0.35	3.62	*b.d.*	*b.d.*	*b.d.*	1.83	2.65	2.95	33.9	13.8	60.9	13.8	136	29.8	48164	1.51	55.50	24.0	1497	300	294	*n.a.*	*n.a.*	0.073	0.016	97.0	661
YK1412-14-40		1.90	511	2.77	0.31	2.55	*b.d.*	*b.d.*	0.19	*b.d.*	2.62	2.06	31.3	13.2	63.6	14.5	146	31.6	45254	1.01	46.775	9.16	1253	308	305	*n.a.*	*n.a.*	0.068	0.007	88.6	737
YK1412-14-41		4808	487	42.5	3.76	29.8	4.58	23.8	13.0	2.14	10.8	2.96	36.9	12.3	51.3	11.9	111	26.1	43715	5.95	57.43	18.4	1519	340	263	1.8	0.55	0.341	0.012	89.8	outlier (*n.a.*)
YK1412-14-42		1.00	180	3.50	*b.d.*	3.16	*b.d.*	*b.d.*	2.45	*b.d.*	3.85	0.79	11.9	4.43	22.9	5.31	51.2	11.9	45546	2.43	44.45	15.6	1184	118	112	*n.a.*	*n.a.*	0.267	0.013	253.4	689
YK1412-14-43		59.6	509	0.77	*b.d.*	3.67	*b.d.*	*b.d.*	5.50	1.77	3.06	1.85	29.8	13.7	64.1	16.2	151	33.6	45507	0.64	42.19	15.4	1109	324	313	*n.a.*	1.32	0.075	0.014	89.4	1122
YK1412-14-44	Overgrowth	*b.d.*	737	2.52	*b.d.*	6.90	0.40	3.30	*b.d.*	1.19	9.12	3.24	46.6	18.8	92.5	21.8	236	52.6	42444	2.74	66.89	27.0	1801	492	481	*n.a.*	*n.a.*	0.143	0.015	57.6	*n.a.*
YK1412-14-45	rims	11.9	465	2.42	0.39	5.62	*b.d.*	0.35	0.14	*b.d.*	7.52	2.57	32.4	12.7	58.2	13.3	126	26.9	44536	1.32	51.32	36.0	1362	286	280	*n.a.*	*n.a.*	0.231	0.026	95.7	909
YK1412-14-46		*b.d.*	330	2.94	0.52	1.20	*b.d.*	*b.d.*	0.89	*b.d.*	3.07	1.62	17.8	8.13	43.0	11.2	118	28.4	42828	1.72	32.70	9.99	933	234	232	*n.a.*	*n.a.*	0.089	0.011	129.7	*n.a.*
YK1412-14-47		9.29	522	1.41	0.22	2.91	*b.d.*	0.99	0.89	*b.d.*	7.63	2.19	32.5	13.9	64.6	14.4	148	31.0	44961	1.20	46.18	16.3	1222	319	314	*n.a.*	*n.a.*	0.203	0.013	86.1	883
YK1412-14-48		*b.d.*	362	2.67	0.12	3.79	*b.d.*	*b.d.*	0.56	*b.d.*	2.84	1.48	21.4	8.57	44.0	9.41	103	23.1	38862	1.45	47.35	18.5	1251	218	213	*n.a.*	*n.a.*	0.101	0.015	107.3	*n.a.*
YK1412-14-49		10.5	330	2.65	*b.d.*	4.04	0.21	1.22	*b.d.*	*b.d.*	3.77	1.05	16.6	8.10	39.2	9.83	104	23.4	37856	1.78	39.579	13.0	1067	211	206	*n.a.*	*n.a.*	0.133	0.012	114.8	896
YK1412-14-50		44.6	601	6.05	2.02	17.2	2.04	13.1	6.35	1.84	15.6	4.14	41.9	15.9	69.7	15.9	159	36.1	35974	2.86	71.23	49.0	1877	401	358	2.1	0.56	0.356	0.026	59.9	1078

YK1412-14-51		*b.d.*	361	2.89	0.26	3.32	0.11	0.86	0.78	0.44	2.51	1.24	22.9	8.88	45.2	10.7	107	23.5	40664	1.86	48.63	19.3	1296	228	222	4.8	0.96	0.088	0.015	112.8	*n.a.*
YK1412-14-52		1.14	270	3.30	0.11	3.65	0.074	*b.d.*	0.016	0.090	3.22	1.36	17.5	6.97	31.5	6.76	72.5	15.1	37891	1.49	52.69	16.4	1416	159	155	9.8	1.23	0.176	0.012	140.3	698
YK1412-14-53		11.6	463	5.03	*b.d.*	4.67	0.51	*b.d.*	*b.d.*	*b.d.*	4.49	2.14	26.3	11.4	54.8	12.3	141	32.1	34835	2.72	53.24	16.5	1426	290	285	*n.a.*	*n.a.*	0.115	0.012	75.3	907
Gneiss YK156-4																														
Spot No.	Domain	Ti	Y	Nb	La	Ce	Pr	Nd	Sm	Eu	Gd	Tb	Dy	Ho	Er	Tm	Yb	Lu	Hf	Ta	Pb	Th	U	ΣREE	ΣHREE	Ce/Ce*	Eu/Eu*	(Gd/Lu)$_N$	Th/U	Hf/Y	T (°C) 2.5 GPa
YK156-4-01	Core	11.5	3441	22.0	0.22	68.4	0.31	4.63	9.03	1.34	57.5	21.4	279	116	551	133	1347	232	31050	9.25	145.3	546	874	2821	2737	64.4	0.18	0.205	0.625	9.0	*n.c.*
YK156-4-02		8.30	4054	11.8	0.073	54.4	0.25	4.55	10.4	2.63	73.8	27.4	355	139	652	150	1454	269	30333	5.42	102.0	429	693	3192	3120	99.7	0.29	0.227	0.619	7.5	*n.c.*
YK156-4-03		11.0	3098	19.6	0.063	62.1	0.086	3.17	6.43	1.08	49.8	18.9	256	104	501	119	1203	216	31542	8.91	152.1	708	962	2542	2469	207.4	0.19	0.190	0.735	10.2	*n.c.*
YK156-4-04		9.72	4967	43.6	6.19	101	4.10	25.8	17.4	3.62	87.5	31.6	409	165	789	190	1905	322	33428	17.1	287	1235	1631	4057	3899	4.9	0.28	0.224	0.757	6.7	*n.c.*
YK156-4-05		26.6	8939	27.0	1.04	243	2.62	42.6	61.0	11.6	252	78.6	865	316	1354	295	2783	479	22326	6.13	131.8	1222	949	6785	6423	36.0	0.29	0.433	1.287	2.5	*n.c.*
YK156-4-06		7.64	3697	7.29	*b.d.*	51.4	0.25	6.32	14.1	3.24	75.1	25.6	319	126	602	138	1341	247	22943	3.03	35.3	157	198	2949	2874	*n.a.*	0.30	0.251	0.794	6.2	*n.c.*
YK156-4-07		6.30	1301	7.53	0.018	26.0	0.048	1.16	4.04	0.82	22.5	8.25	108	44.4	204	48.1	480	85.2	32005	2.99	51.7	129	746	1033	1000	218.5	0.26	0.217	0.172	24.6	*n.c.*
YK156-4-08		1.87	3411	23.4	0.020	75.7	0.14	2.85	8.66	1.32	55.3	21.9	292	116	546	129	1263	224	30712	10.4	172.7	838	970	2736	2647	347.3	0.18	0.204	0.864	9.0	*n.c.*
YK156-4-09		15.7	3719	36.5	3.22	172	0.54	5.38	7.14	1.12	45.6	17.6	259	117	585	139	1394	248	27732	7.32	93.7	632	583	2995	2806	31.8	0.19	0.152	1.086	7.5	*n.c.*
YK156-4-10		11.7	4569	21.9	4.02	90.5	2.14	18.2	20.3	1.64	104	34.8	432	166	715	151	1409	238	27635	6.06	95.5	422	640	3388	3251	7.6	0.11	0.361	0.659	6.0	*n.c.*
YK156-4-11		9.18	4098	20.6	0.53	89.1	0.67	6.63	11.6	2.46	70.9	27.9	354	140	653	154	1526	258	31315	7.77	111.7	562	667	3295	3184	36.7	0.26	0.227	0.842	7.6	*n.c.*
YK156-4-12		9.09	2701	27.1	0.15	29.3	0.19	1.32	3.42	0.73	32.5	14.6	196	87.7	448	112	1182	218	34260	10.4	160.4	433	1419	2326	2291	42.0	0.21	0.123	0.305	12.7	*n.c.*
YK156-4-13		2.56	595	5.23	*b.d.*	7.30	0.0074	0.37	0.69	0.31	7.58	3.23	45.1	18.9	88.0	20.4	195	36.1	31301	2.02	61.59	88.3	931	423	415	*n.a.*	0.41	0.173	0.095	52.6	*n.c.*
YK156-4-14		*b.d.*	348	3.25	*b.d.*	4.78	0.028	0.26	0.39	0.28	4.36	1.89	25.8	9.85	43.1	10.9	109	22.8	33226	1.03	51.99	41.5	1027	233	227	*n.a.*	0.67	0.158	0.040	95.4	*n.c.*
YK156-4-15		10.3	2445	20.0	0.26	37.1	0.26	3.90	4.73	0.85	36.0	13.9	197	81.8	397	97.1	1023	177	32819	10.2	108.9	301	691	2069	2022	34.6	0.20	0.168	0.436	13.4	*n.c.*
YK156-4-16		11.1	3808	37.3	0.065	49.2	0.13	1.59	6.15	1.07	45.1	19.3	276	125	630	161	1677	312	31140	13.0	161.6	458	1097	3305	3247	130.6	0.20	0.119	0.417	8.2	*n.c.*
YK156-4-17		19.7	7645	16.6	0.046	138	1.25	19.9	38.3	8.27	196	63.8	736	269	1155	251	2323	382	23734	5.18	91.2	675	580	5582	5376	141.0	0.29	0.424	1.163	3.1	*n.c.*
YK156-4-18		13.2	3718	8.45	0.022	72.0	0.28	5.78	12.8	3.23	78.1	26.6	321	130	581	130	1272	225	25086	3.64	58.0	342	314	2858	2764	227.2	0.31	0.286	1.089	6.7	*n.c.*
YK156-4-19		8.98	2150	16.7	0.055	35.8	0.037	1.60	5.37	0.74	33.5	13.1	169	72.2	338	79.5	763	139	30409	6.29	122.4	521	996	1650	1606	194.6	0.17	0.199	0.523	14.1	*n.c.*
YK156-4-20		5.52	2781	13.9	0.37	45.7	0.40	3.98	6.39	1.04	38.7	15.5	212	89.7	451	113	1187	219	31126	6.56	70.3	271	562	2383	2326	29.1	0.20	0.146	0.482	11.2	*n.c.*
YK156-4-21		4.08	660	12.7	0.10	14.4	0.050	0.44	1.14	0.40	7.58	3.40	48.8	20.5	102	25.8	284	54.8	35549	4.75	108.9	174	1536	564	547	50.1	0.41	0.114	0.113	53.8	*n.c.*
YK156-4-22		22.2	3118	6.29	0.79	58.3	0.66	6.99	13.1	2.86	70.4	22.3	279	109	495	111	1084	192	23177	2.39	35.2	218	187	2446	2363	19.8	0.29	0.303	1.168	7.4	*n.c.*
YK156-4-23		18.8	5126	19.1	2.12	134	2.28	19.4	22.7	4.90	119	39.4	470	179	774	171	1612	261	26648	5.14	105.5	743	512	3811	3626	14.9	0.29	0.377	1.452	5.2	*n.c.*
YK156-4-24		4.42	691	6.19	0.026	8.55	0.036	0.61	1.21	0.53	8.53	4.08	51.0	21.3	102	25.9	274	52.5	35671	2.93	63.31	116	1296	550	539	68.1	0.51	0.134	0.089	51.6	*n.c.*
YK156-4-25		2.19	656	8.79	0.040	8.32	0.032	0.16	0.53	0.31	7.23	3.00	43.5	19.6	103	27.5	316	69.4	38575	6.98	66.62	84.9	1179	599	590	56.7	0.48	0.086	0.072	58.8	*n.c.*
YK156-4-26		6.53	4104	15.3	1.09	131	1.16	11.6	14.6	3.76	83.3	28.2	358	138	630	138	1384	247	26499	6.32	135.7	947	690	3170	3007	28.7	0.33	0.278	1.373	6.5	*n.c.*
YK156-4-27		1.70	621	5.07	0.040	11.0	0.031	0.43	1.50	0.43	9.56	3.55	46.3	19.4	95.2	23.7	242	46.8	35229	3.27	61.56	130	1022	500	486	76.1	0.35	0.168	0.127	56.7	*n.c.*
YK156-4-28		4.96	3621	31.1	0.062	43.3	0.077	1.40	4.97	0.90	45.0	17.8	249	116	597	147	1529	308	34921	12.5	116.2	375	948	3059	3008	153.3	0.18	0.120	0.396	9.6	*n.c.*
YK156-4-29		21.1	5099	48.5	2.55	113	1.80	15.5	19.1	3.57	98.7	35.9	434	172	760	168	1549	278	29399	17.1	240	2083	1671	3652	3496	13.0	0.25	0.293	1.246	5.8	*n.c.*
YK156-4-30		6.81	2140	17.9	*b.d.*	30.7	0.043	0.48	3.12	0.57	21.4	9.77	141	67.0	353	88.4	975	194	32087	7.72	77.5	258	917	1884	1849	*n.a.*	0.21	0.091	0.281	15.0	*n.c.*
YK156-4-31		12.5	2016	3.99	0.10	39.3	0.30	3.71	5.75	1.88	42.6	13.6	170	67.6	318	74.6	728	140	22871	1.86	25.82	121	274	1606	1555	54.6	0.37	0.250	0.442	11.3	*n.c.*
YK156-4-32		8.01	4077	35.9	0.37	110	0.38	4.39	10.7	2.21	72.0	27.5	343	138	631	144	1403	252	30527	11.9	176.4	976	948	3137	3010	71.3	0.24	0.236	1.030	7.5	*n.c.*
YK156-4-33		*b.d.*	354	2.83	*b.d.*	5.54	0.029	0.16	0.49	0.28	6.14	2.10	27.4	10.5	44.4	10.1	103	19.3	31724	1.40	53.26	31.5	1165	229	223	*n.a.*	0.49	0.263	0.027	89.7	*n.c.*
YK156-4-34		5.10	463	4.01	0.044	12.0	0.030	0.33	0.84	0.37	7.04	3.01	37.5	14.3	64.9	15.3	154	27.9	35792	1.45	43.87	57.4	859	338	324	80.8	0.46	0.209	0.067	77.3	*n.c.*
YK156-4-35	Overgrowth rims	38.8	426	4.17	1.71	14.6	0.55	2.23	1.00	0.39	6.59	2.59	33.8	12.7	59.6	14.4	146	27.4	34610	1.47	38.54	46.7	879	324	303	3.7	0.46	0.199	0.053	81.2	1058
YK156-4-36		*b.d.*	193	1.13	0.012	2.29	*b.d.*	0.25	0.37	0.28	2.83	0.97	15.4	5.55	21.8	5.08	49.0	9.75	33547	0.46	31.08	6.43	764	114	110	*n.a.*	0.83	0.240	0.008	174.2	*n.a.*
YK156-4-37		8.86	279	7.94	0.55	11.5	0.071	0.80	0.62	0.059	4.86	1.30	19.4	8.55	48.5	14.2	193	44.6	30700	3.09	36.99	66.1	879	349	335	14.2	0.10	0.090	0.075	110.1	878
YK156-4-38		2.23	235	1.65	0.0070	5.10	0.029	0.26	0.64	0.28	3.80	1.44	19.0	6.33	27.6	5.58	59.8	11.5	36018	0.39	37.48	14.6	984	141	135	87.4	0.55	0.274	0.015	153.1	750
YK156-4-39		5.22	236	2.22	0.027	3.91	0.0047	0.028	0.46	0.40	3.42	1.60	18.1	6.91	29.4	6.51	66.6	11.8	32388	1.02	46.47	16.2	1219	149	144	85.0	0.98	0.238	0.013	137.4	825
YK156-4-40		4.81	420	3.96	0.62	5.08	0.17	0.83	0.96	0.63	7.57	3.14	34.8	12.0	50.5	11.4	105	18.0	34422	1.21	42.39	23.7	1141	251	242	3.9	0.72	0.347	0.021	82.0	817
YK156-4-41		3.17	366	3.43	*b.d.*	10.0	*b.d.*	*b.d.*	0.95	0.54	5.33	2.25	30.6	10.2	44.7	9.89	98.7	18.8	34434	1.27	39.64	34.3	1036	232	221	*n.a.*	0.73	0.234	0.033	94.0	780
YK156-4-42		*b.d.*	363	2.20	0.014	2.70	0.023	0.17	0.65	0.42	5.36	2.29	28.5	10.4	44.3	9.66	99.6	19.3	33490	0.87	46.97	19.2	1213	223	220	37.3	0.69	0.229	0.016	92.1	*n.a.*
YK156-4-43		1.61	591	5.13	0.18	5.31	0.040	0.48	1.71	0.45	10.0	3.59	45.4	16.9	67.6	14.9	147	26.1	33626	1.21	71.44	21.3	1895	340	331	15.2	0.33	0.316	0.011	56.9	725
YK156-4-44		3.64	287	1.72	0.029	3.13	0.025	0.045	0.18	0.34	4.27	1.80	22.1	7.39	34.1	6.77	69.5	13.8	35508	0.68	37.65	10.9	1014	163	160	28.3	1.21	0.255	0.011	123.9	792
YK156-4-45		4.46	734	3.26	*b.d.*	9.04	*b.d.*	0.16	0.85	0.90	12.4	5.21	60.3	21.0	86.9	17.1	166	30.3	32079	0.89	73.85	34.9	1947	410	399	*n.a.*	0.85	0.337	0.018	43.7	810
YK156-4-46		6.02	391	2.00	0.060	4.48	0.0033	0.15	0.38	0.34	5.70	1.99	28.8	10.5	47.2	10.3	102	19.4	35041	0.61	42.00	14.8	1163	232	226	77.8	0.70	0.242	0.013	89.5	839
YK156-4-47		*b.d.*	417	2.78	*b.d.*	5.75	0.0055	*b.d.*	1.05	0.64	9.66	2.92	33.9	11.8	48.4	9.76	95.4	17.7	36128	0.63	51.87	26.4	1306	237	229	*n.a.*	0.62	0.451	0.020	86.6	*n.a.*
YK156-4-48		*b.d.*	222	2.10	*b.d.*	3.02	*b.d.*	*b.d.*	0.29	0.26	3.64	1.35	17.7	6.12	25.8	5.65	54.6	10.0	35341	0.77	42.50	12.5	1095	128	125	*n.a.*	0.78	0.299	0.011	159.3	*n.a.*
YK156-4-49		2.76	380	2.59	0.22	4.28	0.049	0.54	0.74	0.43	4.77	1.99	25.4	10.1	45.0	10.8	97.3	18.3	32350	0.54	41.85	13.4	1071	220	214	10.2	0.70	0.215	0.012	85.1	768
YK156-4-50		*b.d.*	270	3.58	*b.d.*	5.18	*b.d.*	0.12	0.49	0.25	2.66	1.22	15.9	7.70	38.7	10.7	121	28.6	30746	0.90	34.01	21.0	815	233	227	*n.a.*	0.68	0.077	0.026	113.8	*n.a.*
YK156-4-51		171	283	3.77	*b.d.*	3.03	0.018	0.25	0.59	0.21	4.21	1.67	19.2	7.32	33.7	7.42	73.8	14.2	34752	0.96	32.15	13.1	774	166	161	*n.a.*	0.40	0.244	0.017	122.7	outlier (*n.a.*)

Note: *b.d.* represents "below detection"; *n.a.* represents "not applicable"; *n.c.* represents "not calculated". (Gd/Lu) $_N$, Chondrite normalized ratio; $Ce/Ce^{*}=Ce_N/(La_N\times Pr_N)^{0.5}$; $Eu/Eu^{*}=Eu_N/(Sm_N\times Gd_N)^{0.5}$

Table S7. LA-MC-ICP-MS zircon Lu–Hf isotope compositions of the composite granite–quartz veins, the host eclogite and the surrounding gneiss.

Spot No.	Domain	Spot Age (Ma)	$^{176}Hf/^{177}Hf$	1σ	$^{176}Lu/^{177}Hf$	1σ	$^{176}Yb/^{177}Hf$	1σ	Calculation Age (Ma)	$(^{176}Hf/^{177}Hf)i$	1σ	$\varepsilon_{Hf}(t)$	1σ	T_{DM1} (Ma)	1σ	$f_{Lu/Hf}$	T_{DM2} (Ma)	1σ
Granite YK1412-12																		
YK1412-12-01		661	0.281880	0.000019	0.001707	0.000031	0.042289	0.000754	780	0.281855	0.000019	-15.2	0.9	1964	52	-0.95	2628	82
YK1412-12-02		784	0.281925	0.000019	0.000813	0.000012	0.017063	0.000288	780	0.281913	0.000019	-13.2	0.9	1856	52	-0.98	2501	83
YK1412-12-03		469	0.282007	0.000017	0.001310	0.000038	0.030292	0.000883	780	0.281987	0.000017	-10.5	0.8	1766	47	-0.96	2337	75
YK1412-12-04		606	0.281988	0.000018	0.001197	0.000014	0.028703	0.000370	780	0.281971	0.000018	-11.1	0.9	1787	50	-0.96	2374	79
YK1412-12-05		783	0.282003	0.000024	0.001562	0.000038	0.036716	0.000942	780	0.281981	0.000024	-10.8	1.0	1782	67	-0.95	2351	106
YK1412-12-06		782	0.281970	0.000016	0.000894	0.000024	0.021244	0.000652	780	0.281957	0.000016	-11.6	0.8	1797	43	-0.97	2403	69
YK1412-12-07		753	0.282054	0.000014	0.000560	0.000015	0.012843	0.000373	780	0.282045	0.000014	-8.5	0.8	1667	39	-0.98	2209	63
YK1412-12-08		778	0.281939	0.000023	0.001472	0.000023	0.036171	0.000651	780	0.281917	0.000023	-13.0	1.0	1869	64	-0.96	2490	100
YK1412-12-09		717	0.281869	0.000015	0.001108	0.000044	0.028254	0.001253	780	0.281853	0.000015	-15.3	0.8	1948	41	-0.97	2633	65
YK1412-12-10		770	0.281882	0.000020	0.001278	0.000009	0.033662	0.000237	780	0.281863	0.000020	-14.9	0.9	1938	56	-0.96	2610	89
YK1412-12-11	Core	747	0.281845	0.000023	0.001778	0.000013	0.047655	0.000397	780	0.281819	0.000023	-16.5	1.0	2016	65	-0.95	2706	102
YK1412-12-12		421	0.281850	0.000024	0.001554	0.000006	0.042084	0.000229	780	0.281827	0.000024	-16.2	1.0	1998	67	-0.95	2689	106
YK1412-12-13		333	0.282039	0.000012	0.000355	0.000009	0.008787	0.000212	780	0.282034	0.000012	-8.9	0.7	1678	33	-0.99	2234	54
YK1412-12-14		699	0.281899	0.000019	0.001075	0.000030	0.028645	0.000781	780	0.281883	0.000019	-14.2	0.9	1904	53	-0.97	2566	85
YK1412-12-15		786	0.281916	0.000022	0.001353	0.000023	0.035961	0.000534	780	0.281896	0.000022	-13.8	1.0	1895	60	-0.96	2538	95
YK1412-12-16		767	0.281902	0.000021	0.001247	0.000006	0.032693	0.000308	780	0.281884	0.000021	-14.2	0.9	1909	59	-0.96	2564	93
YK1412-12-17		784	0.282044	0.000018	0.000442	0.000020	0.010647	0.000417	780	0.282038	0.000018	-8.8	0.9	1675	49	-0.99	2226	79
YK1412-12-18		772	0.282026	0.000019	0.000985	0.000014	0.021702	0.000518	780	0.282011	0.000019	-9.7	0.9	1724	51	-0.97	2284	82
YK1412-12-19		764	0.282005	0.000019	0.000668	0.000017	0.016894	0.000395	780	0.281995	0.000019	-10.3	0.9	1738	51	-0.98	2319	82
YK1412-12-20		673	0.281987	0.000023	0.000743	0.000046	0.018733	0.001120	780	0.281977	0.000023	-10.9	1.0	1766	62	-0.98	2360	100
YK1412-12-21		777	0.282022	0.000021	0.001568	0.000022	0.041663	0.000526	780	0.281999	0.000021	-10.1	0.9	1757	60	-0.95	2311	94
YK1412-12-22		218	0.282207	0.000020	0.000014	0.000000	0.000383	0.000020	221	0.282207	0.000020	-15.1	0.9	1436	53	-1.00	2206	87
YK1412-12-23		214	0.282015	0.000018	0.000307	0.000012	0.005606	0.000207	221	0.282013	0.000018	-22.0	0.8	1709	49	-0.99	2634	80
YK1412-12-24		224	0.282228	0.000016	0.000028	0.000001	0.000705	0.000018	221	0.282228	0.000016	-14.4	0.8	1408	44	-1.00	2160	72
YK1412-12-25		219	0.282071	0.000016	0.000300	0.000034	0.007423	0.000881	221	0.282069	0.000016	-20.0	0.8	1633	45	-0.99	2510	73
YK1412-12-26		221	0.282149	0.000030	0.000030	0.000001	0.000924	0.000035	221	0.282149	0.000030	-17.2	1.2	1515	80	-1.00	2334	131
YK1412-12-27		225	0.282114	0.000014	0.000159	0.000006	0.003265	0.000134	221	0.282113	0.000014	-18.5	0.7	1568	39	-1.00	2414	63
YK1412-12-28		221	0.282029	0.000016	0.000903	0.000020	0.023941	0.000636	221	0.282025	0.000016	-21.6	0.8	1716	43	-0.97	2607	69
YK1412-12-29		221	0.282245	0.000020	0.000113	0.000007	0.002392	0.000151	221	0.282244	0.000020	-13.8	0.9	1388	53	-1.00	2123	87
YK1412-12-30	Overgrowth rims and new zircon grains	224	0.282239	0.000022	0.000015	0.000000	0.000448	0.000016	221	0.282239	0.000022	-14.0	0.9	1392	60	-1.00	2135	98
YK1412-12-31		222	0.282209	0.000012	0.000043	0.000005	0.001017	0.000117	221	0.282209	0.000012	-15.1	0.7	1434	33	-1.00	2201	54
YK1412-12-32		232	0.282032	0.000013	0.000101	0.000013	0.002470	0.000319	221	0.282032	0.000013	-21.3	0.7	1676	35	-1.00	2593	57
YK1412-12-33		229	0.282091	0.000016	0.000131	0.000008	0.003499	0.000211	221	0.282091	0.000016	-19.3	0.8	1598	43	-1.00	2464	70
YK1412-12-34		222	0.282041	0.000022	0.000207	0.000028	0.005241	0.000705	221	0.282040	0.000022	-21.0	0.9	1669	60	-0.99	2575	97
YK1412-12-35		216	0.282082	0.000014	0.000017	0.000000	0.000482	0.000011	221	0.282082	0.000014	-19.6	0.7	1606	37	-1.00	2484	61
YK1412-12-36		223	0.282096	0.000014	0.000019	0.000000	0.000616	0.000015	221	0.282096	0.000014	-19.1	0.7	1586	37	-1.00	2451	60
YK1412-12-37		226	0.282127	0.000015	0.000024	0.000000	0.000748	0.000016	221	0.282127	0.000015	-18.0	0.7	1544	40	-1.00	2382	66
YK1412-12-38		211	0.282070	0.000014	0.000017	0.000000	0.000489	0.000008	221	0.282069	0.000014	-20.0	0.7	1622	37	-1.00	2510	60
YK1412-12-39		227	0.282065	0.000014	0.000012	0.000000	0.000344	0.000008	221	0.282065	0.000014	-20.2	0.7	1629	38	-1.00	2521	62
Vein quartz YK1412-11																		
YK1412-11-01		562	0.282143	0.000024	0.000695	0.000102	0.015827	0.002389	780	0.282132	0.000024	-5.4	1.1	1550	67	-0.98	2016	107
YK1412-11-02		725	0.281881	0.000025	0.001546	0.000046	0.036788	0.001190	780	0.281858	0.000025	-15.1	1.1	1953	70	-0.95	2620	110
YK1412-11-03		794	0.282043	0.000024	0.001468	0.000027	0.035363	0.000692	780	0.282022	0.000024	-9.3	1.0	1722	68	-0.96	2261	106
YK1412-11-04		557	0.282146	0.000024	0.000466	0.000048	0.011601	0.001222	780	0.282139	0.000024	-5.2	1.0	1537	66	-0.99	2002	106
YK1412-11-05		772	0.282053	0.000015	0.000469	0.000006	0.008927	0.000230	780	0.282046	0.000015	-8.5	0.8	1664	41	-0.99	2207	66
YK1412-11-06		583	0.281923	0.000012	0.000712	0.000006	0.012686	0.000139	780	0.281912	0.000012	-13.2	0.7	1854	34	-0.98	2502	55
YK1412-11-07		781	0.281989	0.000016	0.000534	0.000015	0.010312	0.000440	780	0.281981	0.000016	-10.8	0.8	1755	43	-0.98	2350	70
YK1412-11-08		670	0.282046	0.000020	0.000752	0.000014	0.018792	0.000437	780	0.282035	0.000020	-8.8	0.9	1685	56	-0.98	2230	90

YK1412-11-09		675	0.282010	0.000020	0.000858	0.000020	0.020794	0.000489	780	0.281998	0.000020	-10.2	0.9	1740	56	-0.97	2313	89
YK1412-11-10		774	0.282107	0.000020	0.000876	0.000012	0.022618	0.000299	780	0.282094	0.000020	-6.8	0.9	1607	55	-0.97	2101	87
YK1412-11-11		659	0.282064	0.000015	0.001491	0.000050	0.037614	0.001249	780	0.282042	0.000015	-8.6	0.8	1694	41	-0.96	2215	64
YK1412-11-12	Core	576	0.281836	0.000019	0.001867	0.000015	0.047832	0.000351	780	0.281808	0.000019	-16.9	0.9	2034	54	-0.94	2730	84
YK1412-11-13		372	0.282097	0.000019	0.000893	0.000055	0.022964	0.001521	780	0.282083	0.000019	-7.1	0.9	1622	53	-0.97	2124	85
YK1412-11-14		530	0.282139	0.000024	0.000443	0.000041	0.011186	0.001031	780	0.282133	0.000024	-5.4	1.0	1545	65	-0.99	2015	105
YK1412-11-15		422	0.282178	0.000024	0.000455	0.000012	0.011639	0.000305	780	0.282171	0.000024	-4.0	1.0	1492	65	-0.99	1930	105
YK1412-11-16		587	0.282193	0.000026	0.001735	0.000103	0.046628	0.002942	780	0.282168	0.000026	-4.2	1.1	1522	75	-0.95	1938	117
YK1412-11-17		631	0.282027	0.000024	0.000883	0.000025	0.022318	0.000657	780	0.282014	0.000024	-9.6	1.0	1718	66	-0.97	2277	106
YK1412-11-18		328	0.281861	0.000017	0.001680	0.000028	0.042055	0.000762	780	0.281836	0.000017	-15.9	0.8	1989	48	-0.95	2669	76
YK1412-11-19		440	0.282108	0.000017	0.000470	0.000015	0.012787	0.000405	780	0.282101	0.000017	-6.5	0.8	1589	47	-0.99	2086	76
YK1412-11-20		667	0.282080	0.000023	0.000238	0.000017	0.005691	0.000374	780	0.282077	0.000023	-7.4	1.0	1617	64	-0.99	2139	103
YK1412-11-21		720	0.281925	0.000024	0.001101	0.000020	0.028611	0.000709	780	0.281909	0.000024	-13.3	1.0	1870	66	-0.97	2510	105
YK1412-11-22		389	0.281990	0.000021	0.002185	0.000044	0.064453	0.001521	780	0.281958	0.000021	-11.6	0.9	1832	59	-0.93	2401	91
YK1412-11-23		695	0.282017	0.000027	0.000902	0.000077	0.022701	0.001930	780	0.282004	0.000027	-9.9	1.1	1732	75	-0.97	2299	120
YK1412-11-24		224	0.282202	0.000020	0.000022	0.000002	0.000556	0.000044	221	0.282202	0.000020	-15.3	0.9	1443	54	-1.00	2218	88
YK1412-11-25		231	0.282230	0.000035	0.000143	0.000029	0.003561	0.000693	221	0.282230	0.000035	-14.3	1.4	1409	96	-1.00	2156	157
YK1412-11-26		223	0.282181	0.000028	0.000070	0.000006	0.001374	0.000102	221	0.282180	0.000028	-16.1	1.1	1474	76	-1.00	2265	124
YK1412-11-27		223	0.282168	0.000019	0.000187	0.000022	0.004317	0.000539	221	0.282167	0.000019	-16.5	0.9	1495	53	-0.99	2294	86
YK1412-11-28		215	0.282182	0.000015	0.000032	0.000004	0.000876	0.000105	221	0.282182	0.000015	-16.0	0.8	1471	41	-1.00	2262	67
YK1412-11-29		220	0.282027	0.000022	0.000762	0.000094	0.019552	0.002378	221	0.282024	0.000022	-21.6	1.0	1713	61	-0.98	2611	98
YK1412-11-30		229	0.281991	0.000016	0.000712	0.000024	0.016102	0.000685	221	0.281988	0.000016	-22.9	0.8	1761	45	-0.98	2690	72
YK1412-11-31		223	0.282045	0.000023	0.001000	0.000070	0.023844	0.001687	221	0.282041	0.000023	-21.0	1.0	1698	63	-0.97	2573	101
YK1412-11-32	Overgrowth	220	0.282113	0.000022	0.000536	0.000054	0.013362	0.001417	221	0.282111	0.000022	-18.5	1.0	1585	61	-0.98	2418	98
YK1412-11-33	rims and new zircon grains	225	0.282033	0.000018	0.000379	0.000032	0.009915	0.000857	221	0.282031	0.000018	-21.4	0.8	1688	50	-0.99	2595	81
YK1412-11-34		221	0.282079	0.000018	0.000251	0.000018	0.005505	0.000372	221	0.282078	0.000018	-19.7	0.8	1619	50	-0.99	2491	82
YK1412-11-35		222	0.282070	0.000019	0.000642	0.000071	0.016564	0.001835	221	0.282068	0.000019	-20.1	0.9	1648	52	-0.98	2514	83
YK1412-11-36		224	0.282075	0.000017	0.000504	0.000024	0.012963	0.000713	221	0.282073	0.000017	-19.9	0.8	1635	47	-0.98	2502	76
YK1412-11-37		224	0.282149	0.000020	0.000191	0.000009	0.004621	0.000204	221	0.282148	0.000020	-17.2	0.9	1522	54	-0.99	2337	88
YK1412-11-38		221	0.282254	0.000027	0.000028	0.000001	0.000711	0.000024	221	0.282254	0.000027	-13.5	1.1	1373	73	-1.00	2102	119
YK1412-11-39		218	0.282258	0.000019	0.000020	0.000000	0.000591	0.000019	221	0.282258	0.000019	-13.3	0.9	1366	52	-1.00	2092	86
YK1412-11-40		222	0.282179	0.000025	0.000325	0.000022	0.008099	0.000537	221	0.282178	0.000025	-16.2	1.0	1485	68	-0.99	2270	110
YK1412-11-41		221	0.282114	0.000028	0.000395	0.000007	0.007906	0.000138	221	0.282112	0.000028	-18.5	1.1	1578	76	-0.99	2416	123
Eclogite YK1412-13																		
YK1412-13-01		518	0.281991	0.000014	0.003385	0.000044	0.086553	0.001213	780	0.281941	0.000014	-12.2	0.8	1892	42	-0.90	2438	63
YK1412-13-02		642	0.281856	0.000015	0.001661	0.000026	0.039575	0.000655	780	0.281831	0.000015	-16.1	0.8	1995	43	-0.95	2679	67
YK1412-13-03		682	0.282067	0.000009	0.000841	0.000013	0.020313	0.000324	780	0.282055	0.000009	-8.2	0.6	1661	25	-0.97	2188	41
YK1412-13-04		658	0.281883	0.000010	0.001973	0.000082	0.048382	0.002152	780	0.281854	0.000010	-15.3	0.7	1973	28	-0.94	2630	44
YK1412-13-05		524	0.281853	0.000010	0.001315	0.000041	0.032401	0.001185	780	0.281834	0.000010	-16.0	0.7	1980	29	-0.96	2674	45
YK1412-13-06		666	0.282011	0.000014	0.002024	0.000040	0.050961	0.001059	780	0.281982	0.000014	-10.7	0.8	1793	40	-0.94	2349	62
YK1412-13-07	Core	731	0.281887	0.000013	0.001597	0.000024	0.039174	0.000660	780	0.281864	0.000013	-14.9	0.7	1947	37	-0.95	2608	58
YK1412-13-08		778	0.282169	0.000014	0.000347	0.000031	0.008301	0.000733	780	0.282164	0.000014	-4.3	0.7	1500	39	-0.99	1946	63
YK1412-13-09		587	0.281975	0.000020	0.001460	0.000075	0.035124	0.001840	780	0.281953	0.000020	-11.8	0.9	1818	57	-0.96	2412	90
YK1412-13-10		690	0.281921	0.000016	0.001544	0.000048	0.037727	0.001191	780	0.281898	0.000016	-13.7	0.8	1897	44	-0.95	2532	68

YK1412-13-11		455	0.281938	0.000015	0.000829	0.000058	0.019153	0.001369	780	0.281926	0.000015	-12.7	0.8	1838	41	-0.98	2472	66
YK1412-13-12		639	0.281975	0.000018	0.000868	0.000065	0.020701	0.001566	780	0.281962	0.000018	-11.4	0.9	1790	50	-0.97	2393	79
YK1412-13-13		535	0.281892	0.000013	0.000939	0.000009	0.023010	0.000253	780	0.281878	0.000013	-14.4	0.7	1908	37	-0.97	2578	59
YK1412-13-14		214	0.282211	0.000011	0.000016	0.000000	0.000506	0.000008	221	0.282211	0.000011	-15.0	0.7	1431	30	-1.00	2197	49
YK1412-13-15		223	0.282265	0.000013	0.000006	0.000000	0.000165	0.000009	221	0.282265	0.000013	-13.1	0.7	1356	36	-1.00	2076	59
YK1412-13-16		221	0.282251	0.000012	0.000102	0.000011	0.002176	0.000231	221	0.282251	0.000012	-13.6	0.7	1379	34	-1.00	2108	55
YK1412-13-17		220	0.282246	0.000012	0.000007	0.000000	0.000206	0.000009	221	0.282246	0.000012	-13.8	0.7	1383	33	-1.00	2120	54
YK1412-13-18		215	0.282244	0.000011	0.000014	0.000001	0.000375	0.000014	221	0.282244	0.000011	-13.9	0.7	1386	31	-1.00	2124	51
YK1412-13-19		215	0.282124	0.000019	0.001883	0.000114	0.055104	0.003083	221	0.282116	0.000019	-18.4	0.9	1627	53	-0.94	2407	82
YK1412-13-20		218	0.282160	0.000016	0.000014	0.000001	0.000413	0.000021	221	0.282160	0.000016	-16.8	0.8	1500	43	-1.00	2311	70
YK1412-13-21		215	0.282194	0.000011	0.000017	0.000001	0.000505	0.000025	221	0.282194	0.000011	-15.6	0.7	1454	30	-1.00	2235	49
YK1412-13-22	Overgrowth	218	0.282235	0.000015	0.000059	0.000010	0.001513	0.000286	221	0.282235	0.000015	-14.1	0.7	1399	41	-1.00	2143	66
YK1412-13-23	rims and new	218	0.282190	0.000015	0.000020	0.000000	0.000557	0.000011	221	0.282190	0.000015	-15.7	0.7	1459	41	-1.00	2243	67
YK1412-13-24	zircon grains	217	0.282165	0.000011	0.000013	0.000000	0.000382	0.000017	221	0.282165	0.000011	-16.6	0.7	1493	31	-1.00	2299	51
YK1412-13-25		215	0.282168	0.000012	0.000017	0.000000	0.000480	0.000013	221	0.282168	0.000012	-16.5	0.7	1489	33	-1.00	2293	54
YK1412-13-26		216	0.282203	0.000014	0.000013	0.000000	0.000380	0.000013	221	0.282203	0.000014	-15.3	0.7	1441	39	-1.00	2215	64
YK1412-13-27		217	0.282217	0.000010	0.000061	0.000008	0.001574	0.000214	221	0.282217	0.000010	-14.8	0.6	1424	28	-1.00	2184	45
YK1412-13-28		218	0.282206	0.000014	0.000032	0.000003	0.000860	0.000073	221	0.282205	0.000014	-15.2	0.7	1438	38	-1.00	2209	63
YK1412-13-29		218	0.282159	0.000017	0.000028	0.000000	0.000823	0.000017	221	0.282159	0.000017	-16.8	0.8	1501	45	-1.00	2312	74
YK1412-13-30		217	0.282196	0.000014	0.000228	0.000021	0.006085	0.000551	221	0.282195	0.000014	-15.5	0.7	1458	38	-0.99	2231	61
YK1412-13-31		214	0.282165	0.000014	0.000013	0.000001	0.000411	0.000023	221	0.282165	0.000014	-16.6	0.7	1493	37	-1.00	2298	61
YK1412-13-32		221	0.282196	0.000013	0.000075	0.000007	0.002021	0.000197	221	0.282196	0.000013	-15.5	0.7	1453	35	-1.00	2231	56
Gneiss YK1412-14																		
YK1412-14-01		557	0.281926	0.000030	0.000992	0.000012	0.027492	0.000441	780	0.281911	0.000030	-13.2	1.2	1863	82	-0.97	2504	130
YK1412-14-02		344	0.281900	0.000025	0.001520	0.000012	0.041842	0.000309	780	0.281877	0.000025	-14.4	1.1	1926	71	-0.95	2578	112
YK1412-14-03		774	0.281879	0.000020	0.001790	0.000007	0.050186	0.000292	780	0.281853	0.000020	-15.3	0.9	1969	57	-0.95	2633	89
YK1412-14-04	Core	282	0.281951	0.000019	0.001044	0.000013	0.028172	0.000308	780	0.281935	0.000019	-12.4	0.9	1832	53	-0.97	2451	85
YK1412-14-05		775	0.281832	0.000018	0.001320	0.000022	0.036347	0.000686	780	0.281813	0.000018	-16.7	0.9	2010	51	-0.96	2721	81
YK1412-14-06		779	0.281933	0.000017	0.001125	0.000026	0.030556	0.000660	780	0.281916	0.000017	-13.1	0.8	1860	48	-0.97	2493	76
YK1412-14-07		780	0.281807	0.000022	0.002155	0.000036	0.059556	0.001055	780	0.281776	0.000022	-18.0	1.0	2090	62	-0.94	2801	95
YK1412-14-08		527	0.281885	0.000020	0.001308	0.000036	0.034494	0.001153	780	0.281866	0.000020	-14.9	0.9	1936	56	-0.96	2605	88
YK1412-14-09		218	0.282005	0.000030	0.000115	0.000001	0.002889	0.000033	221	0.282005	0.000030	-22.3	1.2	1714	81	-1.00	2654	132
YK1412-14-10		227	0.281946	0.000014	0.000921	0.000072	0.024078	0.001821	221	0.281942	0.000014	-24.5	0.7	1832	38	-0.97	2790	61
YK1412-14-11		227	0.281894	0.000017	0.001061	0.000052	0.029149	0.001702	221	0.281890	0.000017	-26.4	0.8	1910	48	-0.97	2906	76
YK1412-14-12	Overgrowth	225	0.281990	0.000016	0.000505	0.000018	0.012293	0.000444	221	0.281988	0.000016	-22.9	0.8	1751	44	-0.98	2689	71
YK1412-14-13	rims	226	0.282027	0.000016	0.000203	0.000020	0.004781	0.000479	221	0.282026	0.000016	-21.5	0.8	1688	43	-0.99	2606	71
YK1412-14-14		228	0.281960	0.000026	0.001077	0.000036	0.026002	0.001008	221	0.281956	0.000026	-24.0	1.1	1820	73	-0.97	2761	116
YK1412-14-15		224	0.281947	0.000018	0.000616	0.000017	0.015275	0.000394	221	0.281944	0.000018	-24.4	0.8	1816	49	-0.98	2786	79
YK1412-14-16		225	0.281952	0.000015	0.000761	0.000019	0.019160	0.000484	221	0.281949	0.000015	-24.3	0.7	1816	40	-0.98	2776	65
YK1412-14-17		213	0.282005	0.000019	0.000626	0.000038	0.015571	0.000961	221	0.282002	0.000019	-22.4	0.9	1737	51	-0.98	2658	83

$\varepsilon_{Hf}(t)=[(^{176}Hf/^{177}Hf_Z/^{176}Hf/^{177}Hf_{CHUR}(t)-1]\times10000$;

$(^{176}Hf/^{177}Hf)_i=[(^{176}Hf/^{177}Hf)z - (^{176}Lu/^{177}Hf)z \times (e^{\lambda t} - 1)]$

$^{176}Hf/^{177}Hf_{CHUR}(t)=^{176}Hf/^{177}Hf_{CHUR}(0)-^{176}Lu/^{177}Hf_{CHUR}\times(e^{\lambda t}-1)$;

$T_{DM1}=(1/\lambda)\times\ln[1+(^{176}Hf/^{177}Hf_{DM}-^{176}Hf/^{177}Hf_Z)/(^{176}Lu/^{177}Hf_{DM}-^{176}Lu/^{177}Hf_Z)]$;

$T_{DM2}=T_{DM1}-(T_{DM1}-t)\times(f_{CC}-f_Z)/(f_{CC}-f_{DM})$;

$f_{Lu/Hf}=^{176}Lu/^{177}Hf_Z/^{176}Lu/^{177}Hf_{CHUR}-1$

Where f_{CC}, f_Z and f_{DM} are the $f_{Lu/Hf}$ values of the continental crust, zircon sample and the depleted mantle; subscript Z=analyzed zircon sample; CHUR=chondritic uniform reservoir; DM=depleted mantle; t=the formation age for zircon. t=221 Ma or 780 Ma, timing of the sample crystallization; $\lambda=1.867\times10^{-11}$ year^{-1}, decay constant of ^{176}Lu (Söderlund et al., 2004); $(^{176}Hf/^{177}Hf)_{DM}=0.28325$; $(^{176}Lu/^{177}Hf)_{DM}=0.0384$; present-day $^{176}Hf/^{177}Hf_{CHUR(0)}=0.282772$; $^{176}Lu/^{177}Hf_{CHUR}=0.0332$; $^{176}Lu/^{177}Hf_{CC}=0.015$.

REFERENCE

Söderlund, U., Patchett, J.P., Vervoort, J.D. & Isachsen, C.E., 2004. The Lu-176 decay constant determined by Lu−Hf and U−Pb isotope systematics of Precambrian mafic intrusions. *Earth and Planetary Science Letters*, **219,** 311−324.

Table S8. *In situ* SIMS zircon O isotope compositions of the composite granite–quartz veins, the host eclogite and the surrounding gneiss.

Granite YK1412-12			Vein quartz YK1412-11			Eclogite YK1412-13			Gneiss YK1412-14		
Spot No.	$\delta^{18}O$ (‰, VSMOW)	2σ SD	Spot No.	$\delta^{18}O$ (‰, VSMOW)	2σ SD	Spot No.	$\delta^{18}O$ (‰, VSMOW)	2σ SD	Spot No.	$\delta^{18}O$ (‰, VSMOW)	2σ SD
Zircon Core											
#1	5.70	0.28	#1	5.87	0.28	#1	6.06	0.17	#1	6.19	0.27
#2	6.26	0.28	#2	5.46	0.34	#2	5.94	0.17	#2	6.48	0.27
#3	6.11	0.28	#3	6.67	0.34	#3	5.94	0.17	#3	6.07	0.27
#4	5.70	0.15	#4	6.21	0.34	#4	5.79	0.17	#4	6.61	0.27
#5	5.88	0.15	#5	6.13	0.34	#5	5.75	0.26	#5	6.43	0.27
#6	6.25	0.15	#6	6.45	0.34	#6	5.78	0.26	#6	6.13	0.27
#7	6.41	0.15	#7	5.80	0.34	#7	5.72	0.26	#7	6.05	0.42
#8	6.51	0.15	#8	6.16	0.34	#8	5.83	0.26	#8	6.51	0.42
#9	6.09	0.15	#9	6.14	0.34	#9	5.88	0.21	#9	6.61	0.42
#10	5.88	0.15	#10	6.07	0.34	#10	5.71	0.21	#10	6.66	0.42
#11	6.19	0.15	#11	6.27	0.34	#11	5.61	0.21	#11	5.88	0.42
#12	5.41	0.25	#12	6.14	0.34	#12	6.58	0.21	#12	5.95	0.42
#13	6.27	0.25	#13	5.84	0.34	#13	6.66	0.21	#13	6.67	0.42
#14	5.79	0.25	#14	5.56	0.34	#14	6.30	0.21	#14	6.43	0.42
#15	5.73	0.25	#15	6.22	0.34	#15	5.94	0.18	#15	5.86	0.31
#16	5.83	0.25	#16	6.03	0.34	#16	5.70	0.18	#16	5.82	0.31
#17	5.73	0.28	#17	5.84	0.19	#17	5.77	0.18	#17	6.31	0.31
#18	5.86	0.28	#18	6.14	0.19	#18	6.82	0.18	#18	6.11	0.31
#19	5.54	0.28	#19	6.25	0.19	#19	5.65	0.18	#19	6.17	0.31
#20	5.53	0.28	#20	5.51	0.19	#20	5.71	0.18	#20	5.99	0.31
#21	6.08	0.23	#21	6.27	0.19	#21	5.83	0.18	#21	5.93	0.31
#22	5.47	0.23	#22	6.40	0.19	#22	6.04	0.18	#22	5.94	0.23
#23	6.36	0.23	#23	6.15	0.19	#23	6.03	0.27	#23	6.12	0.23
#24	6.28	0.23	#24	5.70	0.19	#24	6.03	0.27			
#25	6.11	0.23	#25	6.31	0.17						
Overgrowth rims and/or new zircon grains											
#26	5.49	0.28	#26	5.75	0.28	#25	5.59	0.17	#24	5.84	0.27
#27	5.69	0.28	#27	5.35	0.28	#26	5.65	0.17	#25	6.29	0.27
#28	5.46	0.28	#28	5.19	0.28	#27	5.65	0.17	#26	5.83	0.27
#29	5.39	0.28	#29	5.64	0.34	#28	5.54	0.17	#27	5.91	0.27
#30	5.39	0.28	#30	5.61	0.34	#29	5.44	0.17	#28	5.93	0.27
#31	5.39	0.28	#31	5.58	0.34	#30	5.76	0.17	#29	5.82	0.27
#32	5.65	0.28	#32	5.90	0.34	#31	5.38	0.26	#30	6.04	0.27
#33	5.70	0.28	#33	5.82	0.34	#32	5.57	0.26	#31	6.00	0.27
#34	5.69	0.15	#34	5.77	0.34	#33	5.33	0.26	#32	5.94	0.27
#35	5.61	0.15	#35	5.66	0.34	#34	5.47	0.26	#33	5.84	0.27
#36	5.54	0.15	#36	5.74	0.34	#35	5.70	0.26	#34	5.88	0.27
#37	5.65	0.15	#37	5.64	0.34	#36	5.34	0.26	#35	5.55	0.42
#38	5.54	0.15	#38	5.75	0.34	#37	5.73	0.21	#36	5.88	0.42
#39	5.75	0.15	#39	5.91	0.34	#38	5.70	0.21	#37	5.84	0.42
#40	5.71	0.15	#40	5.51	0.34	#39	5.64	0.21	#38	5.61	0.42
#41	5.56	0.25	#41	5.31	0.34	#40	5.72	0.21	#39	5.86	0.42

#42	5.66	0.25	#42	5.36	0.34	#41	5.47	0.21	#40	5.78	0.42
#43	5.65	0.25	#43	5.42	0.34	#42	5.55	0.21	#41	5.78	0.42
#44	5.55	0.25	#44	5.48	0.34	#43	5.72	0.21	#42	5.91	0.42
#45	5.38	0.25	#45	5.43	0.34	#44	5.60	0.21	#43	5.84	0.42
#46	5.58	0.25	#46	5.38	0.34	#45	5.48	0.21	#44	5.61	0.42
#47	5.41	0.25	#47	5.38	0.34	#46	5.88	0.21	#45	5.58	0.42
#48	5.38	0.25	#48	5.62	0.34	#47	5.55	0.18	#46	5.50	0.31
#49	5.59	0.25	#49	5.58	0.34	#48	5.72	0.18	#47	5.78	0.31
#50	5.72	0.25	#50	5.66	0.34	#49	5.70	0.18	#48	5.55	0.31
#51	5.57	0.25	#51	5.64	0.19	#50	5.64	0.18	#49	5.71	0.31
#52	5.48	0.25	#52	5.81	0.19	#51	5.58	0.18	#50	5.69	0.31
#53	5.43	0.25	#53	5.51	0.19	#52	5.50	0.18	#51	5.62	0.31
#54	5.72	0.25	#54	5.60	0.19	#53	5.53	0.18	#52	5.51	0.31
#55	5.59	0.25	#55	5.66	0.19	#54	5.60	0.18	#53	5.60	0.31
#56	5.91	0.28	#56	5.45	0.19	#55	5.66	0.18	#54	5.67	0.31
#57	5.81	0.28	#57	5.72	0.19	#56	5.58	0.18	#55	5.76	0.31
#58	5.46	0.28	#58	5.70	0.19	#57	5.85	0.18	#56	5.52	0.31
#59	5.46	0.28	#59	5.69	0.19	#58	5.93	0.18	#57	5.79	0.31
#60	5.15	0.28	#60	5.54	0.19	#59	5.92	0.27	#58	5.60	0.23
#61	5.49	0.28	#61	5.81	0.19	#60	5.81	0.27	#59	5.30	0.42
#62	5.60	0.28	#62	5.57	0.19				#60	5.43	0.31
#63	5.32	0.28	#63	5.53	0.19				#61	5.58	0.31
#64	5.42	0.28	#64	5.41	0.17						
#65	5.53	0.28	#65	5.74	0.17						
#66	5.25	0.28	#66	5.44	0.17						
#67	5.36	0.28	#67	6.02	0.34						
#68	5.96	0.23	#68	6.00	0.34						
#69	5.71	0.23	#69	6.06	0.19						
#70	5.98	0.23									
#71	5.85	0.23									
#72	5.29	0.23									
#73	5.37	0.23									
#74	5.36	0.23									
#75	5.55	0.23									
#76	5.60	0.23									